

# UC Riverside

## UC Riverside Electronic Theses and Dissertations

### Title

Investigation of Flow, Turbulence, and Dispersion within Built Environments

### Permalink

<https://escholarship.org/uc/item/5w44s7hh>

### Author

Pan, Hansheng

### Publication Date

2011

Peer reviewed|Thesis/dissertation

UNIVERSITY OF CALIFORNIA  
RIVERSIDE

Investigation of Flow, Turbulence, and Dispersion within Built Environments

A Dissertation submitted in partial satisfaction  
of the requirements for the degree of

Doctor of Philosophy

in

Mechanical Engineering

by

Hansheng Pan

December 2011

Dissertation Committee:

Dr. Marko Princevac, Chairperson

Dr. Akula Venkatram

Dr. Guillermo Aguilar

Copyright by  
Hansheng Pan  
2011

The Dissertation of Hansheng Pan is approved:

---

---

---

Committee Chairperson

University of California, Riverside

## ACKNOWLEDGEMENTS

I gratefully acknowledge my advisor Professor Marko Princevac who gave advice and support in the course of the present study. He originally raised my interest in experimental research through hands-on work in the Laboratory for Environmental Flow Modeling. And he always had an open door when problems were to be discussed or decisions to be made. I am especially grateful that he always encouraged me to attend conferences and present my research. This dissertation would not have been possible without his help and support.

I would like to thank Professor Akula Venkatram for serving on my committee and for reviewing the paper manuscript. I am very grateful for his valuable comments and suggestions that led to significant improvements of the dissertation. I would also like to thank Professor Guillermo Aguilar for serving on my committee and his lecture on Fundamentals of Fluid Mechanics. Special thanks go to Professor Rufus Edwards, Professor Marlon Boarnet, Professor Douglas Houston and Professor Jun Wu. They gave advice and support on the field experiments in summer 2008 and shared countless discussions on data analysis and other scientific problems. I would like to thank Professor Jong-Jin Baik from Seoul National University and his doctoral student Seung-Bu Park for running the CFD model simulations of flow through cubical arrays.

I would like to thank several professors who expand my knowledge and experience in Mechanical Engineering. My thanks go to Professor Shankar Mahalingam for his kind discussion in mathematics and combustion problems, Professor Wayne Miller for

mentoring in emission testing, Professor Douglas Altshuler for advising in comparative biomechanics and Dr. Miodrag Micic for discussion related to microfluidics.

Many other people were important for the realization of this thesis: Dr. Xiangyi Li, who instructed me on both laboratory and field experiments; Mr. Neil Zimmerman, who shared his skills of meteorological tower installation with me; Mr. Christian Bartolome, who gave plenty of support and help to the research presented in this dissertation; Dr. Jesse Lozano, with whom I learned the Particle Image Velocimetry (PIV) and conducted several projects related to PIV. Mr. Shiyang Chen, Ms. Yanyan Zhang, Mr. Uzair Ahmed, Ms. Anh Nguyen, Mr. Eric Wittenmeier, Mr. Chai Yang and Ms. Anahita Sfazi, who offered great help to the field experiments under the hot Southern California sun; Mr. Sam Pournazeri who helped a lot with laboratory experiments; Mr. Eric Gutierrez, for carefully reading of my dissertation.

Great thanks go to my families: my husband Qiguo Jing, who is also my colleague in the micrometeorology area; and my parents, who supported me throughout my academic education.

My research was supported by the Los Alamos National Laboratory (Grant # 38510-001-006) and the University of California Transportation Center.

## ABSTRACT OF THE DISSERTATION

Investigation of Flow, Turbulence, and Dispersion within Built Environments

by

Hansheng Pan

Doctor of Philosophy, Graduate Program in Mechanical Engineering  
University of California, Riverside, December 2011  
Dr. Marko Princevac, Chairperson

The built environment surrounding arterials impacts the dispersion of vehicular emissions in urban areas, modifying the potential risks to public health, which are not incorporated in current models. In order to study the influence of urban morphometry on flow, turbulence and dispersion of vehicular fine particulate matter emissions, water channel experiments and field measurements were performed. The research started from the investigation of flows through urban-like rectangular arrays of cubical obstacles. Next, a mock downtown Los Angeles building cluster was built to simulate the dispersion of vehicular emissions within a complex built environment. Meanwhile, field experiments were carried out in five study areas in the Greater Los Angeles area.

For rectangular arrays, Particle Image Velocimetry (PIV) was used for comprehensive flow measurements. A novel flow feature, lateral channeling, was observed and quantitatively measured within regular  $3 \times 3$  and  $5 \times 5$  arrays. Low pressure in the wake region drew the fluid through the array, which led to formation of the strongest lateral inflow in front of the last row of buildings.

For the complex urban setup, simultaneous Particle Image Velocimetry/Planar Laser Induced Fluorescence (PIV/PLIF) technique was applied to study the impact of an individual tall building on flow characteristics and plume dispersion in built environment. The results suggested that the presence of the tall building increase 16% of vertical plume spread by adding  $0.02H^*$  to characteristic length  $H^*$ . The larger integral time scale of concentration fluctuations  $T_c$  below the height of  $H^*$  indicated that the speed of concentration decay is slow and the plume is persistent in the canyon because of the presence of the tall building.

Field measurements suggested that the observed meteorological data at surface level within the urban canopy has a reasonable agreement with the Monin-Obukhov similarity theory. The generalized additive models showed that neighborhood- or urban-scale background concentrations dominated the variation of roadside particle concentrations regardless of urban morphometry. The effects of variables other than background concentrations on DTFP concentrations vary with building morphometry. In Los Angeles, the increasing vertical velocity fluctuation and vertical mean wind speed reduced fine particle concentrations at street level. The estimated fine particle emission factor was  $0.021 \text{ g vehicle}^{-1} \text{ km}^{-1}$  in the Los Angeles area.



## CONTENTS

1	INTRODUCTION AND OBJECTIVES.....	1
1.1	Background.....	3
1.1.1	Dimensionless Analysis for Physical Modeling .....	3
1.1.2	Structure of Urban Boundary Layer .....	7
1.1.3	Previous Laboratory Experiments .....	10
1.1.4	Previous Field Experiments.....	17
1.1.5	Modeling Wind Flow and Dispersion.....	18
1.1.6	Analytical and Statistical Modeling for Analysis of Air Quality in Urban Areas...	19
1.1.7	The representation of fine particles monitoring sites.....	23
1.2	Objectives .....	24
1.3	Structure of the Dissertation .....	25
2	LABORATORY MEASUREMENTS .....	26
2.1	Laboratory Setup .....	27
2.1.1	Water Channel Facility .....	27
2.1.2	Scaling Method .....	30
2.1.3	Rectangular Arrays of Cubical Obstacles .....	32
2.1.4	Scaled Built Environments .....	34
2.1.5	Line Sources .....	36
2.1.6	Simultaneous PIV/PLIF system .....	38

2.2	Results of Flow through Rectangular Arrays of Cubical Obstacles.....	41
2.2.1	Flow Through a 3 × 3 array of cubes.....	41
2.2.2	Flow Through a 5 × 5 array of cubes.....	47
2.2.3	Measurement Uncertainty .....	49
2.2.4	Pressure Analysis .....	51
2.2.5	Discussions .....	54
2.3	Laboratory Simulation of Flow and Dispersion through a Scaled Built Environment	59
2.3.1	Plume Dispersion from a Line Source .....	59
2.3.2	Velocity and Concentration Distributions.....	60
2.3.3	Vertical Spread of Plume .....	65
2.3.4	Vertical Profiles of Velocity and Concentration .....	66
2.3.5	Analysis of Turbulent and Advective Fluxes of Plume .....	69
2.3.6	Summary .....	71
3	FIELD MEASUREMENTS.....	73
3.1	Site Description.....	73
3.2	Sampling Description .....	80
3.3	Micrometeorology .....	82
3.4	Statistical Methods .....	83
3.5	Results and Discussion .....	85
3.5.1	Mean Wind Observation .....	85
3.5.2	Turbulent Characteristic Observation.....	90
3.5.3	Generalized Additive Model Results.....	96

3.5.4	PM <sub>2.5</sub> Concentrations on Leeward Side and Windward Side .....	100
3.5.5	Analytical method .....	102
3.6	Summary .....	104
4	CONCLUSIONS .....	107
	REFERENCE.....	111
	APPENDIX I: Uncertainty analysis for PIV measurements.....	122
	APPENDIX II: Supplemental Field Measurement Figures .....	127
	APPENDIX III: GAM Parameters.....	146
	APPENDIX IV: Application of PIV for Flow Measurements around Hovering Hummingbirds.....	149
	APPENDIX V: Application of PIV for Measurements of Mixing Efficiency of a Micromixer.....	170
	APPENDIX VI: Marine Diesel Engine Emission Measurements.....	182

## LIST OF FIGURES

Figure 1.1 Structure of urban boundary layer. Modified after Oke (1988) and Bottema (1997).....	8
Figure 1.2 Definition of surface dimensions used in morphometric analysis (Grimmond and Oke, 1999).....	10
Figure 2.1 a) Schematic (side view) and b) photograph of the water channel.....	28
Figure 2.2 a) Approaching flow velocity profile, $u/U_e$ , measured in the test section together with Logarithmic profile given by Eq.2.1; b) the rms velocities in vertical, $\sigma_w$ and along the channel, $\sigma_u$ , directions.....	30
Figure 2.3 Schematics of tested building array configurations: a) $3 \times 3$ array of uniform height and with the tall central building (double height, shown in grey); b) $5 \times 5$ array of uniform height and with the tall central building (double height, shown in grey). .....	32
Figure 2.4 a) Acrylic models and b) a schematic of building cluster in downtown Los Angeles. ....	36
Figure 2.5 A schematic diagram of the measured (a golden rectangular) on the cross sectional plane ( $Y/H^* = 6$ ) of building cluster. ....	38
Figure 2.6 Measured flow field in the vertical plane at the centerline of the uniform height array. ....	42
Figure 2.7 Measured flow field in the vertical plane at the centerline of the array with tall central building. ....	42

Figure 2.8 Measured velocity field in the horizontal plane through a $3 \times 3$ building array of uniform height. ....	44
Figure 2.9 Measured velocity field in the horizontal plane through a $3 \times 3$ building array with a central building of double height. ....	45
Figure 2.10 Velocity field through a $3 \times 3$ building array of uniform height produced by a CFD model. ....	46
Figure 2.11 Velocity field through a $3 \times 3$ building array with a central building of double height produced by a CFD model. ....	46
Figure 2.12 a) Measured horizontal velocity field within a uniform height $5 \times 5$ cubical array and b) measured horizontal velocity field within a $5 \times 5$ cubical array with the central building of double height. Refer to Figure 2.3 for location schematic. Velocity scale is given in Figure 2.8 and Figure 2.9. ....	48
Figure 2.13 a) Streamlines calculated from velocity field in Figure 2.10a for $5 \times 5$ array of uniform height and b) streamlines calculated from velocity field in Figure 2.10b for $5 \times 5$ array with a central building of double height. ....	49
Figure 2.14 Integration routes used to integrate two-dimensional pressure. Two paths of integration follow either the dashed or solid arrows (Raffel et al. 2007). ....	52
Figure 2.15 Pressure profile along $Y$ axis at $X=70$ mm for $3 \times 3$ arrays with central building' height of a) $1H$ and b) $2H$ . ....	53
Figure 2.16 Pressure profile along $X$ axis at $Y=125$ and $225$ mm for $3 \times 3$ arrays with central building' height of a) $1H$ and b) $2H$ . ....	54
Figure 2.17 Schematic of streamlines (blue) of the flow around a $5 \times 5$ cubical array. .	57

Figure 2.18 Vertical plane of plume dispersion from a line source through an open terrain. Color bar shows dimensionless concentration. ....	59
Figure 2.19 Mean velocity (black arrows) and concentration (colorbar) fields on vertical plane with tall building .....	61
Figure 2.20 Mean velocity (black arrows) and concentration (colorbar) fields on vertical plane without tall building. ....	62
Figure 2.21 Contours of the logarithm of ratio of concentration distribution with tall building to that without tall building .....	62
Figure 2.22 Contours of unified two-dimensional turbulent kinetic energy on vertical plane with tall building .....	63
Figure 2.23 Contours of unified two-dimensional turbulent kinetic energy on vertical plane without the tall building. ....	64
Figure 2.24 Contours of the logarithm of ratio of normalized turbulent kinetic energy with tall building to that without tall building. ....	64
Figure 2.25 Comparison of vertical spread of plume with and without the tall building calculated by Eqs. 2.12 and 2.13.....	66
Figure 2.26 Vertical profiles of a) mean velocity $u/U_e$ and $w/U_e$ and b) rms velocity $\sigma_u/U_e$ and $\sigma_w/U_e$ for the cases with and without the tall building at the position $X/H^*=4.6$ . ....	67
Figure 2.27 Vertical profiles of a) the mean concentrations and b) the integral time scale of concentration fluctuations at the positions $X/H^* = 4.6$ . ....	69

Figure 2.28 Vertical profiles of dimensionless advective, turbulent and net flux components within the canyon with the tall building.....	70
Figure 3.1 Site distribution in low-rise low-dense settlement-Anaheim.....	75
Figure 3.2 Site distribution in low-rise settlement-Pasadena.....	76
Figure 3.3 Site distribution in mid-rise settlement-Long Beach.....	77
Figure 3.4 Site distribution in high-rise settlement-Los Angeles.....	78
Figure 3.5 Site distribution in strip mall settlement-Huntington Beach.....	79
Figure 3.6 Comparison of $\sigma_w$ calculated from the observed $u^*$ and $\overline{w'T'}$ using Eqs. 3.6 thru 3.9 with the observations for the sites LA6, HB6 and AN6.....	93
Figure 3.7 Nondimensional variability in $W$ , $\Phi_w$ as a function of $z/L$ .....	94
Figure 3.8 Nondimensional variability in $T$ , $\Phi_T$ as a function of $z/L$ .....	95
Figure 3.9 Estimated effects of wind direction (WD) on DTFP concentrations for the Anaheim (AN) and Long Beach (LB) models.....	98
Figure 3.10 Estimated effects of horizontal mean wind speed (WS) on DTFP concentrations for the Long Beach (LB) and Huntington Beach (LB) models....	98
Figure 3.11 Estimated effects of vertical velocity fluctuation ( $\sigma_w$ ) and vertical mean wind speed (W) on DTFP concentrations for the Los Angeles (LA) model.....	99
Figure 3.12 Estimated effects of traffic counts (TC) on DTFP concentrations for a) the Los Angeles (LA) and b) the Huntington Beach models.....	100
Figure 3.13 Time series (~ 10 minutes) of PM <sub>2.5</sub> concentration at site1 (windward side) and site 5 (leeward side) in Los Angeles during a) morning, b) noon and c)	

afternoon. (Note: data are collected on 06/19/2008 in a) and b), 06/30/2008 in c).)

..... 101

Figure 3.14 a) Comparison of predicted concentrations with measured DTFP concentration and b) comparison of road contribution with predicted concentrations calculated by Eq. 5.11..... 103

Figure A2.1 Urban- and neighborhood- scale monitoring stations and field measurement cities. .... 127

Figure A2.2 Meteorological variables observed in Los Angeles on 06/19/2008. .... 131

Figure A2.3 Meteorological variables observed in Los Angeles on 06/23/2008. .... 132

Figure A2.4 Meteorological variables observed in Los Angeles on 06/30/2008. .... 133

Figure A2.5 Meteorological variables observed in Anaheim on 07/30/2008..... 134

Figure A2.6 Meteorological variables observed in Anaheim on 07/31/2008..... 135

Figure A2.7 Meteorological variables observed in Anaheim on 08/01/2008..... 136

Figure A2.8 Meteorological variables observed in Huntington Beach on 07/16/2008. . 137

Figure A2.9 Meteorological variables observed in Huntington Beach on 07/18/2008. . 138

Figure A2.10 Meteorological variables observed in Huntington Beach on 07/21/2008. 139

Figure A2.11 Meteorological variables observed in Long Beach on 07/02/2008. .... 140

Figure A2.12 Meteorological variables observed in Long Beach on 07/07/2008. .... 141

Figure A2.13 Meteorological variables observed in Long Beach on 07/09/2008. .... 142

Figure A2.14 Meteorological variables observed in Pasadena on 07/23/2008..... 143

Figure A2.15 Meteorological variables observed in Pasadena on 07/25/2008..... 144

Figure A2.16 Meteorological variables observed in Pasadena on 07/29/2008..... 145



Figure A4.1 a) The experimental chamber used in hummingbird PIV experiments. b) The wings were visible in most of the raw images recorded from the camera located underneath the bird. ....	152
Figure A4.2 Representative analysis of the wake underneath a wing, using experiment 5 as an example.....	156
Figure A4.3 Along bird velocity plots in the wing domain.. ....	157
Figure A4.4 Perpendicular to bird velocity plots in the wing domain.....	159
Figure A4.5 Representative analysis of the wake underneath a tail, using experiment 1 as an example.....	160
Figure A4.6 Along bird velocity plots in the tail domain.....	161
Figure A4.7 Examples of prominent vortex loops. ....	162
Figure A4.8 Proposed model for the principal vortex wake structures of hovering Anna’s hummingbirds, with left lateral (a) and dorsal (b) views .....	166
Figure A5.1 Microfluidics mixer cartridge.....	172
Figure A5.2 Illustration of the experimental setup.....	174
Figure A5.3 Selected sequential planar laser induced fluorescence intensity maps obtained from processed video frames during different stages of mixing and corresponding histograms.....	179
Figure A5.4 a) Progression of the standard deviation of the pixel intensity; b) Schematic of the forces acting on the fluid elements in the mixer.....	180

Figure A6.1 Test engine map.....	186
Figure A6.2 Flow diagram of the hydrogen injection system and the sampling system.....	187
Figure A6.3 CO <sub>2</sub> emissions vs. H <sub>2</sub> volume percentage.....	190
Figure A6.4 Modal and overall emission factors for CO <sub>2</sub> .....	190
Figure A6.5 NO <sub>x</sub> emissions vs. equivalence ratio.....	191
Figure A6.6 NO <sub>x</sub> emissions vs. H <sub>2</sub> volume percentage.....	193
Figure A6.7 Modal and overall emission factors for NO <sub>x</sub> .....	194
Figure A6.8 CO emissions vs. H <sub>2</sub> volume percentage.....	195
Figure A6.9 Modal and overall emission factors for CO.....	195
Figure A6.10 PM emissions vs. H <sub>2</sub> volume percentage. ....	196
Figure A6.11 Modal and overall emission factors for weighted PM.....	197
Figure A6.12 Overall weighted average emission factors for gases and PM <sub>2.5</sub> with hydrogen flow rates of 0, 22 and 220 SLPM under the test cycle of E3. ....	199
Figure A6.13 Engine power efficiency vs. loads.....	200
Figure A6.14 Enthalpy of combustion vs. loads.....	201
Figure A6.15 Fuel consumption vs. CO <sub>2</sub> emission factors.....	202
Figure A6.16 Continuous monitoring of power during idle modes with hydrogen flow rates of a) 0 SLPM, b) 22 SLPM and c) 220 SLPM.....	205

Figure A6.17 Continuous monitoring of speed during idle modes with hydrogen flow rates of a) 0 SLPM, b) 22 SLPM and c) 220 SLPM.....206

## LIST OF TABLES

Table 2.1 Uncertainty for vertical plane measurements and free stream velocity of 8.2 cm s <sup>-1</sup> .....	50
Table 2.2 Uncertainty for 3 × 3 array horizontal measurements and free stream velocity of 8.2 cm s <sup>-1</sup> .....	51
Table 2.3 Uncertainty for 5 × 5 array horizontal measurements and free stream velocity of 8.2 cm s <sup>-1</sup> .....	51
Table 3.1 The classification of building arrangements .....	73
Table 3.2 Morphological and aerodynamic parameters for five city areas .....	80
Table 3.3 Summary of mean wind and turbulent characteristics .....	87
Table 3.4 R <sup>2</sup> of GAM and Relative importance of each variable for five models. Note: C <sub>bk</sub> -background concentrations; WS: horizontal mean wind speed; W-vertical mean wind speed; WD-wind direction; F <sub>t</sub> -momentum flux; F <sub>s</sub> -sensible heat flux; σ <sub>w</sub> -vertical velocity fluctuation; TC-traffic count .....	97
Table A1.1 Principal measurements for 3 × 3 arrays .....	122
Table A1.2 Uncertainty for each variable in velocity measurement .....	125
Table A1.3 Combined uncertainty for velocity measurement .....	126
Table A2.1 Specification of each site .....	128
Table A3.1 Parameter coefficients for Intercept and C <sub>bk</sub> in GAMs. ....	146
Table A3.2 Parameter coefficients for other variables in GAMs .....	147
Table A6.1 Engine properties .....	185
Table A6.2 Test modes and weighting factors for marine applications (ISO-8178 E3) .....	187

Table A6.3 Hydrogen measurements .....	198
Table A6.4 Percentage of increased fuel consumptions due to the increased electrical load of electrolysis for each engine load.....	203

## 1 INTRODUCTION AND OBJECTIVES

Particulate matter emissions from transportation have a significant contribution on ambient air pollution especially in urban area. Epidemiologic studies showed the evidence for increased mortality and morbidity associated with pollutions of particulate matter with aerodynamic diameter below 10  $\mu\text{m}$  ( $\text{PM}_{10}$ ) and especially the finer fraction with aerodynamic diameter below 2.5  $\mu\text{m}$  ( $\text{PM}_{2.5}$ ) (Dockery and Pope, 1994). The database for national  $\text{PM}_{2.5}$  emissions by source sector shows the  $\text{PM}_{2.5}$  emissions by on-road vehicles are 3% of the total national  $\text{PM}_{2.5}$  emissions in 2002. While for Los Angeles County case, the percentage is increased to 16% (EPA, 2002). In metropolitan cities, vehicular emissions are in close proximity to pedestrians, residences and local businesses. Current line source models based on the Gaussian diffusion equation are commonly applied to evaluate the air quality impact of freeways or highways passing through an open terrain (Gokhale et al., 2008; Venkatram et al., 2009). Those models consider factors such as particle size classes, source emission rate, atmospheric stability, vehicle wake effect as well as increased emission factors or 'idle' emission factors relevant to intersection situations. However, their application in predicting the air quality in built environments surrounding major arterials is more challenging since they still cannot accurately incorporate building influence on dispersion. In the past several decades numerous studies were conducted to address potential factors that could impact the dispersion of pollutants in urban areas.

Urban areas can be considered as inhomogeneous entities. The pollution levels are high in street canyons where pollutions from vehicle exhaust are trapped by the presence

of buildings. Based on empirical understanding of flow and dispersion within street canyons a parameterized semi-empirical model, Operational Street Pollution Model (OSPM) was created (Berkowicz, 2000a). Evaluation and application of OSPM for traffic pollution assessment have been done for several European cities (Berkowicz et al., 2000b; Mensink et al., 2006; Vardoulakis et al., 2007; Kumar et al., 2009). OSPM was also applied in studying population exposure to traffic related primary pollutants in densely populated street canyons in mid-town Manhattan (Zhou and Levy, 2008). However, for most urban areas in the United States, there are both suburban areas with low building density and dense urban environments with deep urban canyons. For example, for the Greater Los Angeles Area, idealized street canyons seldom exist, but street networks composed of several street canyons flanked by buildings of different heights are common in the downtown configuration. Hence, investigation of flow and dispersion in a wider variety of streets are still needed.

Flow and dispersion of transportation emissions are affected by building geometry. The objective of this dissertation is to achieve the physical modeling of flow and dispersion within simple and complex building arrays, to investigate the influence of an individual tall building on flow and dispersion within a complex building array, and to analyze the impact of background concentrations, meteorological and traffic related variables on middle-scale fine particle concentrations in varying built environments. Therefore, the research in this thesis begins with laboratory experiments for studying mean flows and turbulent characteristics within simple regular arrays. Next, a near source study of transportation emissions in built environments surrounding major

arterials was carried out in the summer of 2008. Field experiments were conducted in five southern Californian cities to investigate a wider range of urban morphometry and more urban-like rough surfaces. Scaled urban-like models were created, and water channel simulations were carried on in a laboratory. Some background and previous studies related to the research in this dissertation are described in the next section.

## 1.1 Background

### 1.1.1 Dimensionless Analysis for Physical Modeling

To study mechanical phenomena, a series of mathematics equations are supposed to be established. These equations usually present the natural process of mechanics. The idea case is that differential equations, which can be solved by a suitable scheme, are determined for the quantities characterizing the phenomenon. However, in most cases, no satisfactory scheme can be supplied to solve a complicated problem.

Similarity requirement for physical modeling of flow and dispersion in the atmospheric boundary layer and over complex terrain (Cermak, 1984) have been presented in several publications.

The governing equations are conservation of mass, momentum, and energy (Lumley and Panofsky, 1964),

$$\frac{\partial u_i}{\partial t} + U_j \frac{\partial u_i}{\partial x_j} + 2\varepsilon_{ijk} u_k \Omega_j = -\frac{1}{\rho_0} \frac{\partial \Delta P}{\partial x_i} + \frac{g}{T_0} \Delta T \delta_{3i} + \nu \frac{\partial^2 u_i}{\partial x_k \partial x_k} \quad 1.1$$

$$\frac{\partial u_i}{\partial x_i} = 0 \quad 1.2$$



$$\frac{\partial \Delta T}{\partial t} + \frac{\partial \Delta T}{\partial x_i} u_i = \kappa \frac{\partial^2 \Delta T}{\partial x_i \partial x_i} \quad 1.3$$

where the  $x_3$  axis is taken vertically upward,  $u_i$  is instantaneous velocity,  $\Delta P$  and  $\Delta T$  are deviation of pressure and temperature from those of a neutral atmosphere,  $\rho_0$  and  $T_0$  are density and temperature of a neutral atmosphere (functions of height),  $\nu$  is kinematic viscosity,  $\kappa$  is thermal diffusivity,  $\varepsilon_{ijk}$  is the alternating tensor,  $\delta_{ij}$  is Kroneker delta and the summation convention is used here.

The scaled variables in dimensional method are presented as follows:  $x_i^* = x_i/L$ ,  $u_i^* = u_i/U_R$ ,  $t^* = U_R t/L$ ,  $\rho^* = \rho_0/\rho_R$ ,  $\Delta P^* = \Delta P/\rho_R U_R^2$ ,  $\Delta T^* = \Delta T/\Delta T_R$ ,  $\Omega_j^* = \Omega_j/\Omega_R$ . Here subscripts  $R$  represent reference quantities. Substitute the scaled variables into Eq. 1.1 to 1.3, the non-dimensional equations are obtained

$$\frac{\partial u_i^*}{\partial t^*} + u_j^* \frac{\partial u_i^*}{\partial x_j^*} + \frac{1}{\text{Ro}} 2\varepsilon_{ijk} u_k^* \Omega_j^* = -\frac{1}{\rho^*} \frac{\partial \Delta P^*}{\partial x_i^*} + \frac{1}{\text{Fr}^2} \Delta T^* \delta_{3i} + \frac{1}{\text{Re}} \nu \frac{\partial^2 u_i^*}{\partial x_k^* \partial x_k^*} \quad 1.4$$

$$\frac{\partial u_i^*}{\partial x_i^*} = 0 \quad 1.5$$

$$\frac{\partial \Delta T^*}{\partial t^*} + \frac{\partial \Delta T^*}{\partial x_i^*} u_i^* = \frac{1}{\text{Pe}} \kappa \frac{\partial^2 \Delta T^*}{\partial x_i^* \partial x_i^*} \quad 1.6$$

where  $\text{Ro} = U_R/L\Omega_R$  is the Rossby number,  $\text{Fr} = U_R/(gL\Delta T_R/T_0)^{1/2}$  is the densimetric Froude number,  $\text{Re} = U_R L/\nu$  is the Reynolds number and  $\text{Pe} = U_R L/\kappa$  is the Peclet number.

Any two flows within the same general category will be similar if and only if they are described by identical solutions to the given set of Eqs. 1.4 to 1.6. Solutions to this

set of equations will be identical if and only if the coefficients  $Ro$ ,  $Fr$ ,  $Re$  and  $Pe$  and the non-dimensional boundary conditions are identical. The final statement, then, as it applies to laboratory modeling of atmospheric motion becomes: any atmospheric flow which can be describe by Eqs. 1.4 to 1.6 may be modeled by any other flow which can also be described by the same set of equations, provided that the Rossby, Froude, Reynolds and Peclet numbers are identical and provided that the non-dimensional boundary conditions are identical.

When the dispersion of a pollutant within the system is considered, the contaminant is assumed to be completely passive in the sense that it is without effect on the governing equation and undergoes no transformations in the fluid. Its dynamic behavior must be the same as that of the air. Hence, the similarity criteria describing its dynamic behavior have already been specified. The dimensionless diffusion equation is

$$\frac{\partial C}{\partial t} + u_i \frac{\partial C}{\partial x_i} = \alpha \frac{\partial^2 C}{\partial x_i \partial x_i} \quad 1.7$$

where  $C$  represents the instantaneous concentration and  $\alpha$  is the molecular mass diffusivity. By introducing dimensionless concentration  $C^*=C/C_R$  (the subscript  $R$  represents a reference quantity), Eq. 1.7 can be written in a dimensionless form as

$$\frac{\partial C^*}{\partial t^*} + u_i^* \frac{\partial C^*}{\partial x_i^*} = \frac{1}{\text{ReSc}} \frac{\partial^2 C^*}{\partial x_i^* \partial x_i^*} \quad 1.8$$

where  $\text{Sc}=\nu/\alpha$  is the Schmidt number.

Eqs. 1.4 to 1.6 and 1.8 form a complete set of equations that govern the dispersion of a dynamically passive contaminant in the atmosphere and in a model. If and only if

the non-dimensional coefficients in these equations and the boundary conditions are identical, the dispersion of the contaminant in a model will be identical to that in the atmosphere.

For length scale in urban areas, the Coriolis force may be neglected and the Rossby number can generally be eliminated from the requirements for similarity. The scale reductions commonly used result in model Reynolds numbers three to four orders of magnitude smaller than found in the atmosphere. Various arguments have been presented which attempt to justify the use of smaller Reynolds number in a model. Reynolds number independence is based on the hypothesis that in the absence of thermal and Coriolis effects and for a specified flow system, whose boundary conditions are expressed non-dimensionally in terms of a characteristic length  $L$  and velocity  $U_R$ , the turbulent flow structure is similar at all sufficiently high Reynolds number. To avoid the effects of viscosity at the boundaries, one way is to roughen the surface of the model. If water is used as the medium for modeling, the Prandtl number at ordinary room temperatures is a factor of about 10 larger than it is in air, and it varies rather greatly with temperature. The Schmidt number for most gases in air is about one. When water is used as the medium for modeling, salt water or alcohol is typically used to simulate the buoyancy of a plume. The Schmidt number for sodium chloride or alcohol in water is approximately 800. If the flow is of sufficiently high Reynolds number, then the main structure of the turbulence will be almost totally responsible for the transport of the contaminant. In the absence of buoyancy forces, this leaves Reynolds number as the most important number in physical modeling.

### 1.1.2 Structure of Urban Boundary Layer

Figure 1.1 was created after Oke (1988) and Bottema (1997). The two layer model recognizing the urban canopy layer (UCL) and urban boundary layer (UBL) was first proposed by Oke (1976). Furthermore, three distinct regions, roughness sub-layer (RSL), inertial sub-layer (ISL) and mixed layer (ML) were proposed by Grimmond and Oke (2002). Roth (2000) discussed each layer as following: UCL is produced by microscale effects of site characteristics. Here dynamic and thermal processes are dominated by the immediate surroundings, flow and scalar structure are generally very complex. RSL is also called the transition layer, interfacial layer or wake layer, includes UCL. It is mechanically and thermally influenced by the length-scales associated with the roughness and is thought of as a region in which the underlying buildings lead to a spatial horizontal inhomogeneity of the flow (Britter and Hanna, 2003). ISL is also called the constant-flux layer and for neutral stratification a mean velocity profile follows a logarithmic wind law.

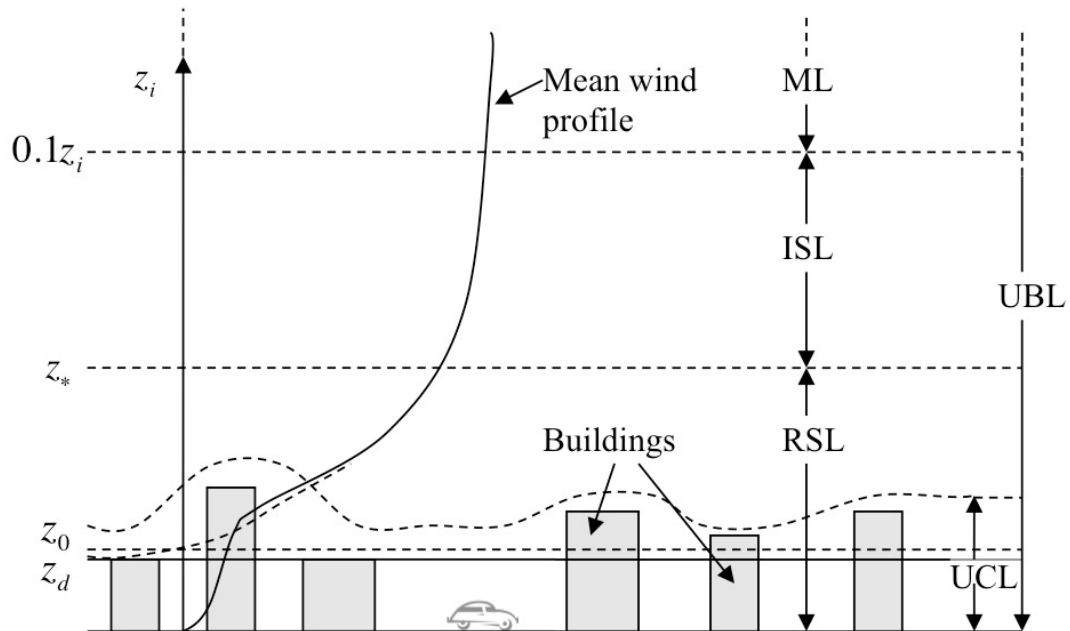


Figure 1.1 Structure of urban boundary layer. Modified after Oke (1988) and Bottema (1997).

The depth of RSL,  $z_*$ , is usually related to the values of roughness element's height,  $z_H$ . Wind tunnel experiments and field observations found that  $z_*/z_H$  are in the range of 2-5 for momentum RSL and about 10 for heat RSL (Raupach and Legg, 1984).

There are two aerodynamic properties, such as roughness length ( $z_0$ ) and displacement height ( $z_d$ ) used for generalizing the character of roughness. Roughness length  $z_0$  describes the height above displacement level where the downward extrapolated wind speed profiles reach zero (Garratt, 1994). Displacement height  $z_d$  represents the asymptotic lower limit, where the near-logarithmic profiles of atmospheric quantities (concentrations, temperature, wind speed, etc.) of the inertial sub-layer converge to, if they are extrapolated downwards into the roughness sub-layer or canopy layer. The

effective aerodynamic height ( $z$ ) of roughness elements is described by  $z = z_H - z_d$ . In order to make the published data from sites with different surface characteristics comparable, Roth (2000) suggested that all work should include a detailed description of the overall setting of the observation site and the characteristics of the fetch (average height of buildings, aerodynamic roughness length and zero-plane displacement height as a minimum).

Two classes of approach are available to assign values of  $z_0$  and  $z_d$ : morphometric methods and micrometeorological methods (Grimmond and Oke, 1999). Morphometric methods were used widely because values can be achieved without field observations of wind or turbulence from tall meteorological towers. The dimensions used to characterize the surface geometry in the morphometric methods are defined in Figure 1.2 and non-dimensional ratios are defined as follow

$$\overline{\lambda_P} = \overline{A_P} / \overline{A_T} = \overline{L_x L_y} / \overline{D_x D_y} \quad 1.9$$

$$\overline{\lambda_F} = \overline{A_F} / \overline{A_T} = \overline{z_H L_y} / \overline{D_x D_y} \quad 1.10$$

$$\overline{\lambda_S} = \overline{z_H} / \overline{W_x} = \overline{z_H} / \overline{(D_x - L_x)} \quad 1.11$$

$$\overline{\lambda_C} = \left[ \overline{L_x L_y} + 2 \overline{(L_y z_H)} + 2 \overline{(L_x z_H)} \right] / \overline{D_x D_y} \quad 1.12$$

There are several morphometric methods, such as height-based approach (Hanna and Chang, 1992), methods that use height and plan area fraction ( $\lambda_P$ ) (Counihan, 1971) and methods that consider height and frontal area fraction ( $\lambda_F$ ) (Lettau, 1969; Raupach, 1994; Bottema, 1997; MacDonald et al., 1998b). The MacDonald's model (MacDonald

et al., 1998b) is an attractive alternative given its good performance and more readily available data requirements (Grimmond and Oke, 1999).

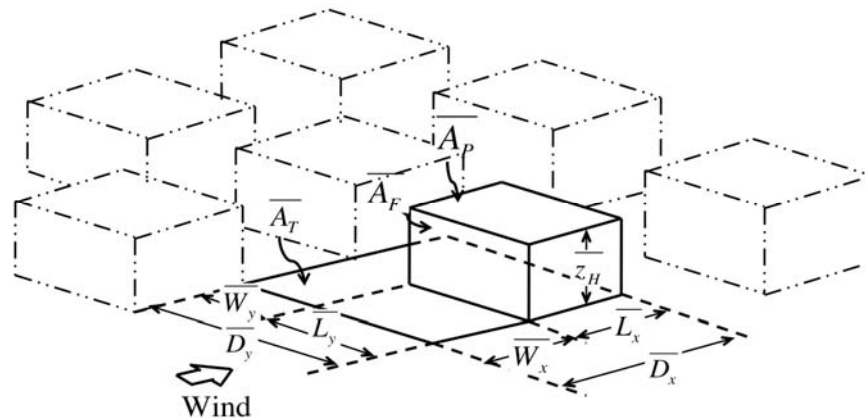


Figure 1.2 Definition of surface dimensions used in morphometric analysis (Grimmond and Oke, 1999)

### 1.1.3 Previous Laboratory Experiments

Detailed laboratory experiments with a focus on the flow readjustment to a different surface roughness were conducted by Cheng and Castro (2002a). Using wind-tunnel experiments, Cheng and Castro (2002b) investigated the spatially averaged mean velocity and turbulent stresses above an urban-like surface. This study pointed out some difficulties in applying the fore mentioned results of flows over vegetative canopies to flows above urban canopies.

Hosker (1980) provided a review of studies related to isolated buildings. Extensive investigations of flows around single building and flows in complex scaled city blocks were conducted in a wind tunnel (e.g. Pavageau and Schatzmann, 1999; Schatzmann et al., 2000). Those studies examined the turbulent characteristics of the flows and the

statistical properties of concentration fields associated with steady releases at street level. Similar studies were conducted to examine flow and dispersion around scaled model buildings using EPA's fluid modeling facility (Brown et al., 2001).

Some studies of flow and dispersion within the urban canopy have modeled the canopy as a series of urban street canyons. Oke (1987) summarized the nature of this flow in terms of the ratio of the spacing between buildings,  $S$ , to the building height,  $H$ . Based on past studies conducted in wind tunnels and water flumes, Oke defines three types of flow regimes depending on  $S/H$ : isolated roughness flow regime for  $S/H > 4$ , wake interference flow regime for  $2 < S/H < 4$  and the skimming flow regime for  $S/H < 2$ .

Other studies have focused on individual street canyons and street intersections, where complex flow patterns can occur. Kastner-Klein et al. (2001) used a wind tunnel, while Macdonald et al. (2002) used a water flume to study the details of such flows. Yamartino and Wiegand (1986), Gavze et al. (2002). Rotach et al. (2005) conducted field studies in which turbulence intensities and flow velocities were measured with sonic anemometers and the associated concentration patterns were studied using tracer releases. Such studies have provided useful insight into urban street canyon flows. In a narrow street canyon ( $S/H > 1$ ), a single vertically rotating horizontally-aligned in-canyon vortex develops, while a smaller counter-rotating vortex may develop next to the larger in-canyon vortex in a wider canyon ( $S/H \sim 1.5$ ). Baik et al. (2000) and Eliasson et al. (2004) tried to elucidate the vertical structure of the flow inside deep canyons ( $S/H > 0.5$ ). Different studies have looked at the effect of roof shape and relative building heights on



vertical transport and dispersion (e.g. Rafailidis and Schatzmann, 1995; Kastner-Klein et al., 1997; Macdonald et al., 1998a). A number of wind tunnel tracer experiments have shown that concentrations for releases in the street canyon are particularly sensitive to the approaching wind direction (Wedding et al., 1977; Hoydysh and Dabberdt, 1988; Kastner-Klein and Plate, 1999). Dabberdt and Hoydysh (1991) found that concentrations within the street canyon vary significantly with block shape (rectangular vs. square) and with the relative width of streets versus avenues.

The influence of street architecture on the wind and turbulence patterns in street canyons and the associated effects on local air quality were also studied (Kastner-Klein et al., 2004; Kastner-Klein and Rotach, 2004; etc.). The results suggest that small-scale features of the building architecture (e.g. roof) may play an important role in determining canyon flow patterns.

Reduced-scale field experiments and water flumes were used to study the interaction of a tracer plume with the internal boundary layer created over the obstacle array (Macdonald et al., 2000a,b; Macdonald, 2000). Compared to plumes in the open terrain, the plumes in the arrays were typically wider and the plume width was closely related to the width of the obstacles. It was found that the lateral concentration profiles were Gaussian in all cases when the wind was perpendicular to the obstacle array. However, plumes were deflected along street canyons when the wind direction was not normal to the array.

Yee et al. (2006) compared results from field tracer measurements with corresponding simulations using a water channel and a wind tunnel. They found that the

field measurements agree better with the water channel measurements than with the wind tunnel results. The better performance of the water channel might be related to the more precise flow control and conditioning that is possible in the water channel.

Theurer et al. (1996) made the wind tunnel investigation of several hierarchical, idealized, arrangements of buildings to obtain the parameters required in a semi-empirical urban dispersion model. The wind tunnel experiments showed that the influence of individual obstacles becomes negligible at downwind distances larger than the radius of homogenization (ROH). At distances larger than ROH, for the dispersion calculation, buildings can be considered as homogeneous roughness. Theurer (1999) proposed a classification scheme for urban environments which consists of nine typical building arrangements. The effect of each building arrangement on local concentration of pollutants was investigated through wind tunnel experiments and numerical modeling. However, due to the complex interactions of the flow and buildings no explicit formula for the concentration in terms of different building parameters was possible.

In simplified obstacle arrays studies, urban areas are described by several parameters, such as street aspect ratio  $L/W$  (building length/street width) and  $H/W$  (building height/street width), or area aspect ratio  $\lambda_P$  (plan area fraction) and  $\lambda_F$  (frontal area fraction) (Grimmond and Oke 1999). There were several field and laboratory experiments focusing on the plume dispersion from ground level point sources through obstacle arrays and their comparison with open-terrain dispersion. Davidson et al. (1996) conducted field experiments to study the plume dispersion through the staggered arrays and aligned arrays. Macdonald et al. (1997) studied urban dispersion through three

groups of regular arrays with  $\lambda_P = \lambda_F = 0.06, 0.16$  and  $0.44$ , respectively. Their field experiments displayed the effect of the arrays on the diffusion as follow: horseshoe vortices around the individual buildings produce vertical mixing and downwash of plume in the front rows of the array resulting in non-Gaussian distributions; the deflection of mean streamlines over the arrays causes an effective lifting of the plume and an enhancement of vertical mixing; lateral dispersion is enhanced in the denser arrays and sheltered in sparse arrays compared to open-terrain. As Macdonald pointed out the details of the dependence of  $\sigma_y$ ,  $\sigma_z$  and mean advection velocity on building lay-out and wind direction are still needed for the model applications. Furthermore, the effect of obstacle width on the dispersion in large obstacle arrays was investigated (Macdonald et al., 1998b). Both field and wind tunnel experiments revealed that an increase by a factor of 1 in obstacle width could produce an increase by a factor of 2-4 in the plume width, and the initial dispersion of the plume is greater for a release inside the array than a release upwind of the array. Yee et al. (2006) investigated a case of ground level point source release upstream of the arrays with wide obstacles ( $W \times L \times H = 4.8 \times 0.95 \times 1.0$ ) in both water channel and wind tunnel experiments. Mean plume dispersion, internal plume structure and concentration fluctuations in the obstacle array were comparable with that in the open terrain and were related to the turbulence integral length scale, the turbulence intensity, the concentration fluctuation intensity and the integral time scale of concentration fluctuations within the obstacle array.

Building height variation was considered as another important parameter affecting air exchange flux, exchange velocity and the residence time of pollutant, finally

determining the air exchange mechanism and the dispersion process (Britter and Hanna, 2003). Bentham and Britter (2003) derived a characteristic in-canopy velocity  $U_C$  and an exchange velocity  $U_E$ , both of which are expressed by friction velocity  $u_*$  and could be used for intermediate scale dispersion problem. Pascheke et al. (2008) conducted a wind-tunnel study to measure transfer velocity ( $w_T$ ) and dispersion from an area source within an uniform height urban canopy and a non-uniform height urban canopy, with both  $\lambda_P$  and  $\lambda_F$  equal to 25%. By introducing transfer velocity, which is relevant for momentum transfer into and out of the canopy, canopy ventilation may be analyzed quantitatively. It was found that the non-uniform height urban canopy had a larger transfer coefficient defined as a ratio of transfer velocity and incoming wind speed ( $w_T/U$ ) indicating enhanced ventilation efficiency. However, although enhanced vertical momentum exchange due to the building height variability was observed, the dispersion from a limited area source within the canopy was not enhanced (Pascheke et al., 2008). In the Comprehensive Outdoor Scale MOdel (COSMO) experiments, it was found that building height variations enhanced the momentum flux, but had little influence on sensible heat flux (Kanda and Moriizumi, 2009). Laboratory simulations indicated that the dimensionless residence time defined as  $H = \tau U/L$ , where  $\tau$  is the time constant for the concentration decay,  $U$  the free-stream velocity and  $L$  is a characteristic dimension for the urban geometry is independent of Reynolds number (Re) in an investigated urban geometry case (Gomes et al., 2007) and is also independent of atmospheric stability in an isolated obstacle case (Mavroidis et al., 1999). Their studies revealed that the residence time depends on the type of urban geometry. The transfer process and street canyon

ventilation were also investigated by numerical methods by different groups (Hamlyn et al., 2007; Solazzo and Britter, 2007; Cheng et al., 2008).

Several studies addressed the dispersion of transportation related pollutants. Meroney et al. (1996) used a stable and laterally homogeneous line source to simulate vehicular pollution in a street canyon. They compared different flow characteristics within an isolated street canyon in the middle of open country roughness and another in urban environment. Unstable vortex existed in the canyon amidst open country while stable vortex was developed inside the urban environment. Ahmad et al. (2005) reviewed wind tunnel simulation studies on dispersion at urban street canyons and intersections have been reviewed. They concluded that vortices do not significantly contribute to the removal of exhaust gases in deep canyons and better ventilation exists at corners of relatively short canyons. Wind vortices, low-pressure zones and channeling effects may cause pollutants trapping within urban street intersections. Vincont et al. (2000) conducted simultaneous measurements of the velocity and concentration fields of the plume emitting from a two-dimensional source. In this study, Particle Image Velocimetry (PIV) was used for the velocity field measurements, Laser-Induced Fluorescence (LIF) and Mie Scattering Diffusion (MSD) were used for the concentration measurements in the water flow and in the air flow, respectively. By introducing PIV/LIF and PIV/MSD, data were collected simultaneously in a substantial portion of the illuminated plane rather than at single point (Vincont et al., 2000). Recently, PIV/MSD technique was applied to observe the dispersion of smoke released from a two-

dimensional slot in the wall within a street canyon perpendicular to an approaching flow (Simoëns et al., 2007; Simoëns and Wallace, 2008).

#### 1.1.4 Previous Field Experiments

In recent years, there are series of field experiments conducted to study turbulent flow and dispersion in urban areas. URBAN 2000 (Allwine et al., 2002) investigate the urban nocturnal boundary layer (stable to neutral atmospheric condition) in Salt Lake City, Utah. Joint Urban 2003 (JU2003) field campaign was designed to investigate the daytime boundary layer (neutral to unstable) in Oklahoma City (Allwine et al., 2004a and 2004b; Klein and Clark, 2007). Velocity data obtained within a street canyon were used to explore the directional dependence of the mean flow and turbulence within a realistic street canyon (Allwine and Flaherty, 2006; Nelson et al., 2007a and 2007b). The Madison Square Garden July 2004 (MSG04) field experiment was conducted to understand the atmospheric circulations and rapid vertical dispersion in the deep canyons of very large cities such as New York City. Mean flow and turbulent characteristics near street level were obtained from field experiments in these cities (Hanna et al., 2007). Tracer dispersion data were mainly used to evaluate dispersion models. These experiments were not focusing on environmental pollutants and their impact factors. There are several other field experiments including Basel Urban Boundary-Layer Experiment (BUBBLE) in Basel, Switzerland (Rotach et al., 2004), Dispersion of Air Pollution and its Penetration into the Local Environment (DAPPLE) in London, UK (Arnold et al., 2004; Dobre et al., 2005; Patra et al., 2008) and Canyon Particle

Experiment (CAPAREX) in Essen, Germany (Weber et al., 2006). These experiments were mostly interested in a specific street canyon or a certain urban area.

### 1.1.5 Modeling Wind Flow and Dispersion

The governing equations for modeling wind flow are the continuity equation and the steady state momentum conservation equation

$$\frac{\partial u_i}{\partial x_i} = 0 \quad 1.13$$

$$u_i \frac{\partial u_j}{\partial x_i} = \frac{\partial}{\partial x_i} \left( \nu \frac{\partial u_j}{\partial x_i} - \overline{u_i' u_j'} \right) - \frac{1}{\rho} \frac{\partial P}{\partial x_j} \quad 1.14$$

The eddy-viscosity concept can be applied for flows in urban areas. This concept assumes that in analogy to molecular diffusion the turbulent stresses are proportional to the local velocity gradients as

$$\overline{u_i' u_j'} = -\nu_t \left( \frac{\partial u_j}{\partial x_i} + \frac{\partial u_i}{\partial x_j} \right) \quad 1.15$$

where  $\nu_t$  is the eddy-viscosity which needs to be parameterized.

The eddy viscosity can be modeled by  $k$ - $\varepsilon$  method, which has a wide application in modeling flow in urban areas. Here  $k$  is the turbulent kinetic energy and  $\varepsilon$  is the rate of dissipation of the turbulent kinetic energy. Eqs 1.16 to 1.18 describe  $k$ - $\varepsilon$  method

$$k = \frac{1}{2} \overline{u_i' u_i'} \quad 1.16$$

$$\varepsilon = \nu \overline{\frac{\partial u_i'}{\partial x_j} \frac{\partial u_i'}{\partial x_j}} \quad 1.17$$

$$\nu_t = c_\mu \frac{k^2}{\varepsilon} \quad 1.18$$

where  $c_\mu$  is an empirical proportionality constant.

The governing equation for modeling dispersion of pollutants in streets is the steady state mass conservation equation

$$u_i \frac{\partial C}{\partial x_i} = - \frac{\partial C}{\partial x_i} \overline{C' u_i'} \quad 1.19$$

where  $C'$  denotes the deviation from the mean value. The turbulent flux term is determined by the eddy diffusivity concept as

$$\overline{C' u_i'} = -K_t \frac{\partial C}{\partial x_i} \quad 1.20$$

where  $K_t$  is the eddy diffusivity coefficient, usually assumed to be equal to the eddy viscosity  $\nu_t$ .

#### 1.1.6 Analytical and Statistical Modeling for Analysis of Air Quality in Urban Areas

The pollution models for street transportation emissions are usually derived based on pollution measurements in typical street canyon. The pollution concentrations at a receptor are composed of emissions from the local street traffic (street contribution  $C_s$ ) and the pollution present in the air that enters from roof level (background concentration  $C_b$ ).



The STREET model (Johnson et al., 1973) solved the concentrations for the leeward side and windward side respectively. The model considered parameters such as the emission rate  $Q$  ( $\text{g m}^{-1}\text{s}^{-1}$ ), wind speed  $u$ , the distance from the traffic lane to the receptor  $x$ , the height of the street canyon  $H$  and the width of the canyon  $W$ . Hotchkiss and Harlow model (Hotchkiss and Harlow, 1973) also considered the parameter such as the eddy diffusivity  $\nu_t$  and the canyon ventilation velocity  $u_w$ . The Canyon Plume-Box Model (CPBM) calculated the concentrations by combining a plume model for the direct impact of vehicle emitted pollutants with a box model that enables computation of the additional impact due to pollutants recirculated within the street by the vortex flow (Yamartino and Wiegand, 1986). In CPBM, the plume dispersion is calculated according to Gaussian plume formulas. The dispersion parameters  $\sigma_z$  and the turbulence parameters  $\sigma_u$ ,  $\sigma_v$  and  $\sigma_w$  were introduced.

The Operational Street Pollution Model (OSPM) is a simple dispersion model based on similar principles as the CPBM. OSPM makes use of a very simplified parameterization of flow and dispersion conditions in a street canyon. This parameterization was deduced from extensive analysis of experimental data and model tests (Berkowicz, 1997). The direct contribution of traffic emissions can be calculated using a simple plume model for the street canyon. The assumption is that the traffic emissions are treated as a number of infinitesimal line source aligned perpendicular to the wind direction at the street level and with thickness  $dx$ . The emission density for such a line source can be expressed as

$$dQ = \frac{Q}{W} dx \quad 1.21$$

where  $W$  is the width of the street canyon. The contribution to the concentration at a point located at a distance  $x$  from the line source is given by

$$dC_d = \sqrt{\frac{2}{\pi}} \frac{dQ}{u_b \cdot \sigma_z(x)} \quad 1.22$$

where  $u_b$  is the wind speed at the street level and  $\sigma_z(x)$  is the vertical dispersion parameter at a downwind distance  $x$ . Then Eq. 1.22 was integrated through a finite street length. For the case of wind direction perpendicular to the street axis, the direct contribution of traffic emissions in OSPM is

$$C_d = \sqrt{\frac{2}{\pi}} \frac{Q}{W \cdot \sigma_w} \ln \frac{h_0 + (\sigma_w/u_b)W}{h_0} \quad 1.23$$

where  $\sigma_w$  is the vertical turbulent velocity fluctuation,  $C_d$  is the concentrations of fine particles from the direct contribution of traffic emissions,  $h_0$  is the initial mixing of pollutants. In Eq. 1.14,  $Q = b \cdot TC \cdot 10^6$ , where parameter  $b$  is the fine particle emission factor in  $\text{g vehicle}^{-1} \text{ km}^{-1}$ .

Mensink et al. (2003) applied the OSPM to evaluate the concentration levels of  $\text{NO}_x$ ,  $\text{SO}_2$ ,  $\text{PM}_{10}$ ,  $\text{CO}$  and benzene in one of the main passage roads in Antwerp, Belgium. It was found that the OSPM provide very good estimates of the annual averages for the pollutants considered. Higher percentiles are underestimated, probably because of the lack of variation in the background concentrations. Kumar et al. (2009) compared particle number concentrations (PNCs) at different heights in a canyon between

measured, OSPM modelled and Computational Fluid Dynamics (CFD) modeled. The measured PNCs were between a factor of two and three of those from both models. It was found that larger PNC differences at the upper sampling heights existed between OSPM and CFD modeling results when compared to the PNC differences near to the road level. It was caused by the weaker exchange of street and above-roof in the upper part of the canyon in CFD models. However, the actual flow conditions in the street canyon are expected to be more complex than assumed idealist condition in CFD models.

In addition to analytical methods, a generalized additive model (GAM) can be used to quantify the effects of various predictor variables on the concentration of air pollution variables. GAM is a generalization of the usual linear regression model, which replaces the linear form of the regression model with a sum of smooth functions of covariates (Hastie and Tibshirani, 1990). It can be described as

$$Y = \sum_{j=1}^p s_j(X_j) + \varepsilon \quad 1.24$$

where  $Y$  is an independent variable,  $s_j(X_j)$  is a smooth function of covariate,  $p$  is the total number of covariates and  $\varepsilon$  is the error.

The application of statistical models, such as generalized additive model (GAM) in analyzing air quality data has been already used in recent studies. Hourly data of PM<sub>10</sub>, PM<sub>2.5</sub>, NO<sub>2</sub> and NO<sub>x</sub> concentration, with corresponding traffic volume and meteorological conditions, collected in 2001-2003, were used to develop separate models (Aldrin, 2005). The relative contribution of each predictor variable to pollution was estimated in each model. The results showed that traffic volume and wind were the most

important variables for all pollutants. Relative humidity also has an impact on the PM concentration. The effects of other predictor variables such as temperature or snow cover on the ground are less important. GAM was also used to model daily NO<sub>x</sub> and CO concentrations in a busy street canyon during the period 1998-2005 (Carslaw et al., 2007). GAM models of Carslaw et al. (2007) also showed that the reduction of overall traffic and meteorological factors appeared to account for reduced NO<sub>x</sub> concentrations. In the most recent study, vehicle type (diesel or gasoline), driving style (passing or idling) and background pollution were also considered as predictor variables (Richmond-Bryant et al., 2009). Our study examines the impacts of mean wind, temperature, turbulence as well as traffic volume variables on fine particulate concentrations with varying urban morphometry and estimates the relative importance of those variables corresponding to each urban morphometry.

#### 1.1.7 The representation of fine particles monitoring sites

The fine particles concentrations measured at any site result from contributions of emissions from nearby and distant sources and the zone of representation of a monitoring site depends on the relative amounts contributed by sources on different spatial scales (Watson et al., 1997). EPA has given a standard 40 CFR part 58 for the dimensions of a monitoring site which indicate the diameter of a circle, or the length and width of a grid square, with a monitor at its center as: 1) collocated Scale (1 to 10 m); 2) microscale (10 to 100 m); 3) middle scale (100 to 500 m); 4) neighborhood scale (500 to 4 km); 5) urban scale (4 to 100 km); 6) regional-scale background (100 to 1000 km); 7) continental-scale background (1000 to 10000 km); and 8) global-scale background (>10000 km).

## **1.2 Objectives**

The previous laboratory experiments were focus mostly on regular arrays of obstacles. What is lacking is a systematic study of flow in building clusters of varying complexity. To address this gap we initiated a systematic experimental program in the newly established Laboratory for Environmental Flow Modeling (LEFM) at UCR. As a part of the study, a new mean flow pattern through regular arrays of cubical obstacles in the skimming regime is presented in this thesis.

The laboratory experiment on simulating dispersion in real city needs to be developed. Therefore, scaled urban-like models were created and water channel simulations were carried on in the laboratory. The model configurations are based on the real building dimensions in the areas we are interested in. The influence of an individual building on velocity and concentration fields was investigated by comparing cases with and without the tall building.

In the Greater Los Angeles Area, there are both suburban area with lower building density and deep urban canyons forming dense urban environments. Hence, a near source study of transportation emissions in built environments surrounding major arterials has been carried out since summer 2008. Field experiments were conducted in five southern Californian cities to investigate a wider range of urban morphometry and more urban-like rough surface. The current study presents field experiments in four aspects. The first aspect is to analyze mean wind speed and direction and be compared with nearby automated airport weather stations data. The second aspect is to identify turbulence characteristics at both street and roof levels in built environments. The third

aspect is to evaluate the influence of a wide range of meteorological and traffic-related variables on roadside fine particulate concentrations by using a statistical model (GAM). The fourth aspect is to estimate the contribution of traffic emission on neighborhood-scale fine particle concentrations using a simple analytical model based on the OSPM and evaluate the model performance.

### **1.3 Structure of the Dissertation**

Chapter 2 describes laboratory experiments for modeling flow through regular arrays and complex urban-like arrays as well as dispersion through a scaled built environment. To explain these lab studies with real world data, field measurements were conducted. Chapter 3 describes the field investigation of roadside particulate matter concentration surrounding major arterials in five Southern Californian cities. Chapter 4 provides the major conclusions.

Appendix I through III explain uncertainty analysis for PIV measurements and give supplemental field data and GAM parameters.

Throughout my graduate studies, I applied the same experimental techniques to different problems. An example of PIV application for flow measurements around hovering hummingbirds is given in Appendix IV. Application of PLIF for measurements of mixing efficiency of a micro-mixer is given in Appendix V. Appendix VI explains measurements of H<sub>2</sub> impact on emissions from a two-stroke marine diesel engine.

## 2 LABORATORY MEASUREMENTS

Water channel experiments were conducted with the goal of obtaining better understanding of flows through urban-like arrays of buildings. Particle Image Velocimetry (PIV) was used for comprehensive flow measurements within modeled simple rectangular arrays and a complex urban setup. Building arrays were modeled using acrylic blocks whose refractive index is the same as that of salty water. Such a setup allowed for undisturbed laser sheet illumination through the obstacles enabling detailed flow measurements between the obstacles/buildings. Building array size, measurement plane and flow conditions were varied.

For rectangular arrays, a novel flow feature, lateral channeling, observed and quantitatively measured within regular  $3 \times 3$  and  $5 \times 5$  arrays of cubes is reported here. A sideways mean outflow from the building array was observed behind the first row of buildings followed by the mean inflow in the lee of all succeeding rows of buildings. When the central building in a  $3 \times 3$  array was replaced by a building of double height, due to the strong downdraft caused by this tall building, the lateral outflow becomes significantly more intense. When the central building in a  $5 \times 5$  array is replaced by a building of double height, the building downdraft blocks the lateral inflow to the array. This was the first time that such detailed measurements are available for a mock urban array of finite size – a real three-dimensional case. The newly identified mean flow pattern may be accountable for the initial plume spread within an array of obstacles.

For a complex urban setup, an urban area in downtown Los Angeles with complex building configurations and traffic arterials were simulated in the water channel. Tracer

plumes were released from ground level line sources to simulate pollutants emitted from vehicles in arterials. Simultaneous Particle Image Velocimetry/Planar Laser Induced Fluorescence (PIV/PLIF) technique was applied to acquire the flow velocity and plume concentration data in selected vertical planes. The impact of an individual tall building on flow characteristics and plume dispersion in built environment was investigated. The nondimensional concentration  $C^*$  of plume was compared between the configurations with a tall building and without a tall building. The comparison of vertical spread of plume with and without the tall building showed that the presence of the tall building will amplify the vertical plume spread. In order to understand the variation of turbulent and plume structures, the vertical profiles of mean velocity, root mean square velocity, mean concentration and the integral time scale of concentration fluctuations,  $T_c$ , was calculated. The influence of building configurations and the physical mechanisms governing ground level concentrations is presented.

## **2.1 Laboratory Setup**

### **2.1.1 Water Channel Facility**

A custom-designed circulating water channel with a test section that is 1.5 m long, 1 m wide and 0.5 m deep (Figure 2.1) was utilized for the experiments. Water is circulated through the test section using a 20 HP axial pump, which produces a maximum mean velocity of  $0.5 \text{ m s}^{-1}$  in the test section. A variable frequency controller allows flow control with a resolution of 1/100 Hz (from 0 to 60 Hz) that corresponds to the mean velocity change resolution of only  $0.08 \text{ mm s}^{-1}$ . Flow conditioning is achieved with the



profiled honeycombs and the custom-built perforated screens. The perforated screens are used to generate desired inflow velocity profiles as a part of the flow conditioning. The channel flow is steady and becomes fully developed before reaching the test section.

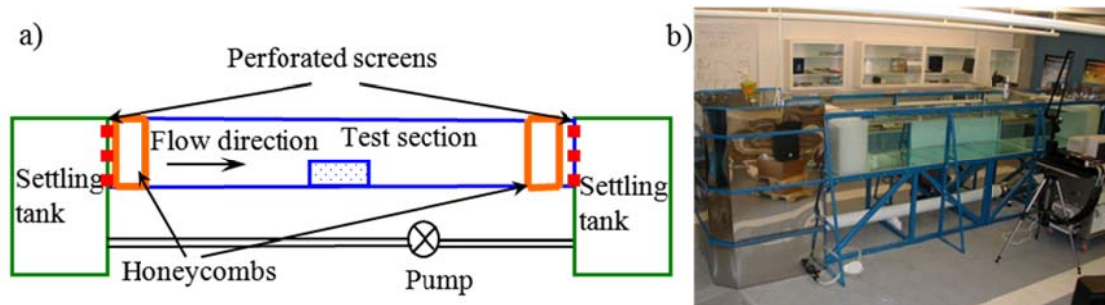


Figure 2.1 a) Schematic (side view) and b) photograph of the water channel.

The LEFM is equipped with the Particle Image Velocimetry (PIV) system for velocity measurements. Detailed velocity field can be measured in the vertical or horizontal plane. PIV measurement technique is well established and widely used for fluid flow investigations (Adrian, 1988, 1991, 1997; Prasad, 1992).

The channel has flow control capability to maintain desired velocity profile starting from the classical logarithmic to the linear profile. As needed, the channel can also maintain well defined jets at desired height. Experiments presented in this paper are all with the logarithmic mean velocity profile. Vertical profiles of the standard deviations of vertical and horizontal velocities,  $\sigma_u$  and  $\sigma_w$ , were maintained constant (around 0.028 and 0.018 m s<sup>-1</sup>, respectively) with  $\sigma_u$  exhibiting a slight peak (0.032 m s<sup>-1</sup>) at 1 cm from the ground. The flow becomes Reynolds number independent for the pump setting larger than 30 Hz (50% of the pump capacity), which corresponds to the Reynolds number, based on the obstacle height,  $Re = 5000$ .

The model buildings are made of highly polished acrylic. Flow is seeded with the Pliolite® particles with the median diameter of 50 μm. The particles are rendered neutrally buoyant by adding filtered and re-crystallized salt of high purity (Morton Culinox 999) to the water. In addition to increasing the density, the salt brings the refractive index of the water closer to that (Aly and Esmail, 1993) of the acrylic used to construct the model buildings. This minimizes the refraction of the laser sheet, which depending on the experimental configuration, has to pass through several building rows. This study is the first that reports results of detailed PIV measurements through and within arrays of obstacles and cover the whole horizontal field at once with no blind spots.

The free stream velocity of the flow through the test section,  $U_e$ , was maintained at 0.09 m s<sup>-1</sup> and neutral condition was simulated in this study. The vertical velocity profile of the approaching flow is shown in Figure 2.2. The equation for logarithmic profile in Figure 2.2a is as follow

$$u(z) = u_{ref} \frac{\ln(z/z_0)}{\ln(z_{ref}/z_0)} \quad 2.1$$

where  $z_{ref}$  is a reference height,  $u_{ref}$  is the wind speed at a reference height,  $z_0$  is roughness length, for center of large city, the value is 0.6-0.8 m (Snyder, 1981).

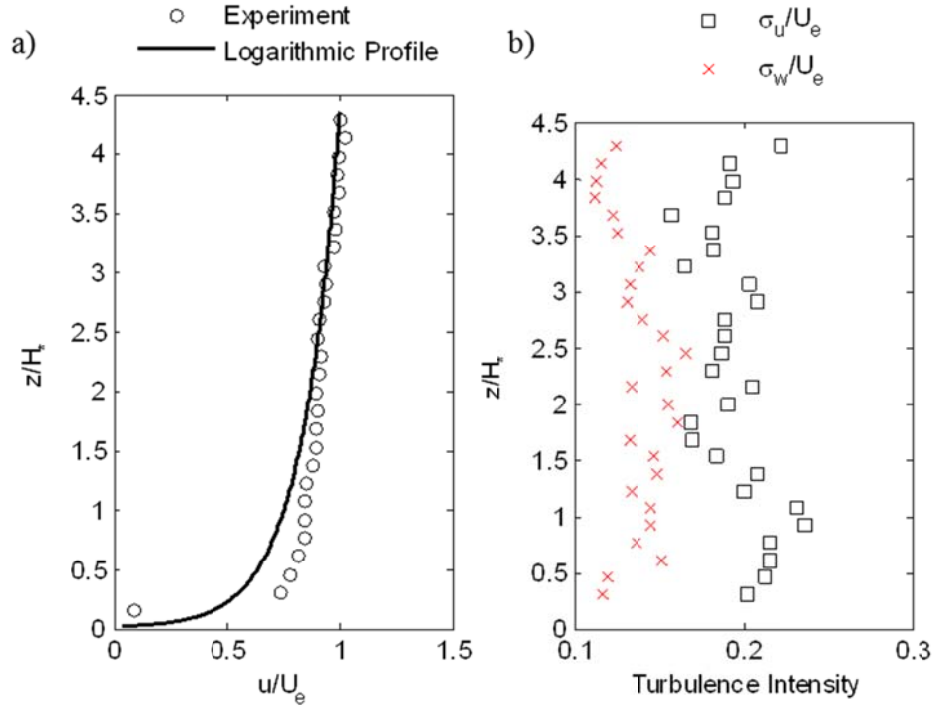


Figure 2.2 a) Approaching flow velocity profile,  $u/U_e$ , measured in the test section together with Logarithmic profile given by Eq.2.1; b) the rms velocities in vertical,  $\sigma_w$  and along the channel,  $\sigma_u$ , directions

### 2.1.2 Scaling Method

Prior to creating a laboratory model to be tested in the water channel, it is necessary to introduce several scaling factors. A dimensionless length scale factor  $\Phi_L$  is defined as

$$\Phi_L = \frac{[L]_{field}}{[L]_{lab}} \quad 2.2$$

where  $L$  is the length scale.

Considering kinematic similarity, or equality of time scales  $t^* = tU/L$ , the dimensionless time scale factor  $\Phi_T$  is defined as

$$\Phi_T = \frac{[t]_{field}}{[t]_{lab}} = \frac{\left[\frac{L}{U_e}\right]_{field}}{\left[\frac{L}{U_e}\right]_{lab}} = \frac{[L]_{field}}{[L]_{lab}} \frac{[U_e]_{lab}}{[U_e]_{field}} = \frac{\Phi_L}{\Phi_U} \quad 2.3$$

where  $U_e$  is velocity of ambient flow;  $\Phi_U$  is a velocity scale factor.

The ambient concentration,  $C_e$ , of well mixed passive contaminant can be written as

$$C_e = \frac{Q_m \cdot t}{V} \quad 2.4$$

where  $Q_m$  is the source mass flow rate,  $\text{mg s}^{-1}$ ;  $t$  is the travel time of contaminant;  $V$  is the control volume. A control volume, which can be understood as ambient space occupied by released contaminant, is approximated with a cube of a characteristic length scale,  $L$ .

A concentration scale factor is introduced as

$$\Phi_C = \frac{[C_e]_{field}}{[C_e]_{lab}} = \frac{\left[\frac{Q \cdot t}{V}\right]_{field}}{\left[\frac{Q \cdot t}{V}\right]_{lab}} = \frac{\left[\frac{Q \cdot t}{L^3}\right]_{field}}{\left[\frac{Q \cdot t}{L^3}\right]_{lab}} = \frac{[Q]_{field}}{[Q]_{lab}} \frac{\Phi_T}{\Phi_L^3} \quad 2.5$$

Eq. 2.5 can be rewritten as

$$\Phi_C = \frac{[C_e]_{field}}{[C_e]_{lab}} = \frac{[Q]_{field} [U_e L^2]_{lab}}{[Q]_{lab} [U_e L^2]_{field}} \quad 2.6$$

and the similarity of normalized dimensionless concentration is expressed as

$$C_* = \left[ \frac{C_e U_e L^2}{Q} \right]_{field} = \left[ \frac{C_e U_e L^2}{Q} \right]_{lab} \quad 2.7$$

which is consistent with the dimensionless similarity relation used by other researchers (Snyder, 1981; Meroney et al., 1996; Hanna et al., 2007).

### 2.1.3 Rectangular Arrays of Cubical Obstacles

Simple experimental series with a single cubical obstacle were used to validate the newly built water channel setup since these are well known canonical flows. These measurements did not bring any new results but served to confirm the validity of the PIV measurements by comparing them with already known flow patterns. An investigation of the vertical flow field through and above a  $3 \times 3$  cubical array also did not convey anything new. However, when we initiated the measurements of the horizontal flow field through a regular  $3 \times 3$  array of cubes an interesting mean flow pattern was observed.

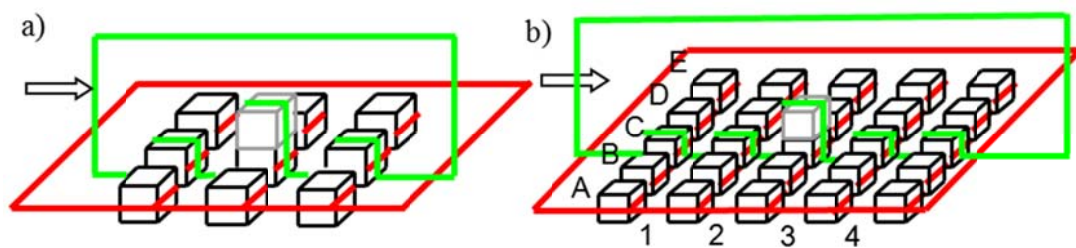


Figure 2.3 Schematics of tested building array configurations: a)  $3 \times 3$  array of uniform height and with the tall central building (double height, shown in grey); b)  $5 \times 5$  array of uniform height and with the tall central building (double height, shown in grey). Green lines delineate vertical measurement plane and red lines delineate horizontal measurement plane. Arrows show the approaching flow direction. Capital letters A-E refer to array columns and numbers 1-4 refer to rows as used in Figure 2.12 and Figure 2.13.

In this communication we focus on the mean flow feature which was first noticed while investigating a regular  $3 \times 3$  array of cubical obstacles in the skimming regime. Results of the mean flow measurements through a regular  $5 \times 5$  array are also presented and discussed. For both array sizes we investigated the configuration when all obstacles are of uniform height and when the central obstacle is of double height. See Figure 2.3 for schematics of the tested configurations and locations of the laser sheets for PIV measurements. The PIV technique measures velocity by correlating images of the particle-seeded flow. The neutrally buoyant Pliolite® particles (median diameter  $50 \mu\text{m}$ ) were illuminated in a plane using a laser sheet with a wavelength of  $532 \text{ nm}$  (with energy of  $388 \text{ mJ pulse}^{-1}$ ) generated by a double-pulsed Nd:YAG laser (Big Sky Laser Technologies, Inc, model CFR400). The Q-switch was set to  $120 \mu\text{s}$  corresponding to approximately medium laser power. The laser beam was expanded into a diverging light sheet using sheet-forming optics, which included the laser arm with three cylindrical lenses (each lens with  $15 \text{ mm}$  focal length) to achieve wide enough laser sheet to cover whole  $3 \times 3$  array. A larger,  $5 \times 5$  array had to be covered in parts. A LASERPULSE Synchronizer (TSI Inc., model 610034) was utilized to trigger the laser pulse and the camera with correct sequences and timing through a  $2.66 \text{ GHz}$  dual-processor workstation (Intel ®Xeon™). The laser sheet was synchronized with a high resolution ( $1600 \times 1192$  pixels) POWERVIEW 2M CCD camera (TSI Inc., model 630157) with a  $50 \text{ mm f/1.8}$  Nikkor lens and an exposure time of  $260 \mu\text{s}$ . The fields of view of the camera were  $320 \times 238 \text{ mm}$  for the measurement in vertical plane,  $380 \times 283 \text{ mm}$  for horizontal plane measurement of  $3 \times 3$  arrays and  $190 \times 142 \text{ mm}$  for horizontal plane

measurement of  $5 \times 5$  arrays ( $5 \times 5$  arrays were covered part by part). Actual regions of interest in  $3 \times 3$  arrays (Figure 2.6 -Figure 2.9) in which PIV was performed were slightly smaller to avoid lens distorted edge image parts. The regions of interest for PIV processing of  $5 \times 5$  arrays were only  $60 \times 60$  mm (Figure 2.12 and Figure 2.13). Camera aperture was set to  $f/5.6$ . Time difference between the two images in a pair was optimized for the best PIV quality to  $\Delta t = 1100 \mu\text{s}$ . A grid for the PIV processing was formed using the Nyquist Grid Engine over  $32$  by  $32$  pixels interrogation regions. Fast Fourier Transform Correlation was used with the Gaussian Peak Engine. TSI Insight 3G software was used for the image conditioning and processing.

#### 2.1.4 Scaled Built Environments

The highly polished acrylic models which can minimize effects of refraction and attenuation of the laser sheet utilized for the Planar Laser-Induced Fluorescence (PLIF) and Particle Image Velocimetry (PIV) measurements were used to create the model of downtown Los Angeles (Figure 2.4). The entire model was fixed on a black flat board which then was put in the center of test section in water channel facility (Figure 2.1). Urban morphology was obtained from the Los Alamos National Laboratory urban database. A  $480 \text{ m} \times 480 \text{ m}$  area including two major arterials perpendicular to the approaching wind direction was scaled down to a  $0.6 \text{ m} \times 0.6 \text{ m}$  (1: 800) area. The average height ( $\bar{H}$ ) of model obstacles is approximately  $0.059 \pm 0.055 \text{ m}$ . The height of tallest obstacle is approximately  $0.324 \text{ m}$ . Reynolds number based on the average height,  $\bar{H} = 0.059 \text{ m}$ , the approaching flow velocity,  $U_e = 0.09 \text{ m s}^{-1}$  and the kinematic viscosity

of water,  $\nu=1.06\times 10^{-6} \text{ m}^2 \text{ s}^{-1}$ ,  $\text{Re}_{\bar{H}} = U_e \bar{H} / \nu$  is approximately 5000 and Reynolds number based on the height of tallest obstacle  $\text{Re}_{H_{tall}}$  is approximately 28000. As it is argued by Yee et al. (2006), a more relevant characteristic length scale ( $H^*$ ) instead of  $\bar{H}$  for the flow interaction with the obstacles could be used for Reynolds number estimation. Here  $H^* \equiv A_f^{1/2}$ , that is the square root of the projected frontal area of the obstacle. In our study,  $H^*$  is calculated as 0.058 m and  $\text{Re}_{H^*} = 4925$ . Castro and Robins (1977) concluded that Reynolds number independence was applicable in the shear flow when  $\text{Re} > 4000$  from an investigation on the highly turbulent flow through a suburban area with a simulated roughness length of 1.3 m. Yee also stated that the criteria that the lower limit of 4000 for Reynolds number independence of shear flow around surface mounted cubes fit for water channel study. Thus, in our study, for physical modeling of flows around sharp-edged obstacles,  $\text{Re}_{H^*} = 4925$  is acceptable.

Roughness length,  $z_0$ , and displacement height,  $d$ , were calculated by *Ma* method (MacDonald et al., 1998b) as

$$\frac{d}{H} = 1 + \alpha^{-\lambda_p} (\lambda_p - 1) \quad 2.8$$

$$\frac{z_0}{H} = \left(1 - \frac{d}{H}\right) \exp \left\{ - \left[ 0.5 \beta \frac{C_D}{k^2} \left(1 - \frac{d}{H}\right) \lambda_F \right]^{-0.5} \right\} \quad 2.9$$

where  $\lambda_p$  and  $\lambda_F$  are plan area density and frontal area density of obstacles respectively,  $H$  is the height of building,  $\alpha$  is an empirical coefficient,  $C_D$  is a drag coefficient ( $\approx 1.2$ ),  $k$



is von Karman's constant ( $\approx 0.4$ ) and  $\beta$  is a correction factor for the drag coefficient (the net correction for several variables, including velocity profile shape, incident turbulence intensity, turbulence length scale, and incident wind angle and for rounded corners). Macdonald (1998b) provides a graphical sensitivity analysis that demonstrates responses to changes in these values. For square arrays of cubes,  $\alpha = 2.3$  and  $\beta = 0.55$ . For staggered arrays,  $\alpha = 4.43$  and  $\beta = 1.0$ . In this study, we are using the latter. For the height of building, we are using  $H^*$  instead of  $\bar{H}$ . The mean values of  $\lambda_P$  and  $\lambda_F$  are 0.40 and 0.45, respectively. The calculated  $d$  is 0.038 m and  $z_0$  is 0.0002 m for our water channel setup.

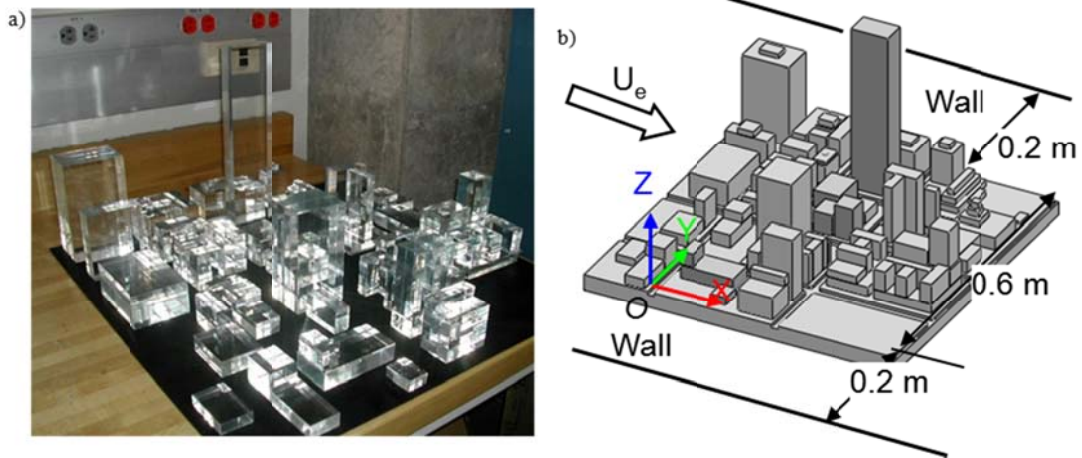


Figure 2.4 a) Acrylic models and b) a schematic of building cluster in downtown Los Angeles. Both sides of the model are 0.2 m away from the side walls of water channel. The origin and X, Y and Z axis are labeled.

### 2.1.5 Line Sources

Vehicle exhaust can be treated as: 1) a source of low vertical momentum since most vehicle exhausts are directed horizontally; 2) neutrally buoyant gas, since buoyancy

forces effects are small compared to traffic produced turbulence and street canyon circulations; and 3) constant traffic flow induces uniform gas flow distribution along the line source (Meroney *et al.*, 1996).

One design for line source is drilling regularly spaced holes along pipes or tubes (Schatzmann *et al.*, 2000). The difficulty of this design is producing laterally homogeneous source in the near field. We selected homogeneous porous tubing which produces laterally homogeneous flow when the pressure drop across the tubing is sufficiently large.

A dye is pumped by digital gear pump (Cole-Parmer Instrument Company) into a soaker tubing inserted in the flat board to simulate a continuous line source. No buoyancy effect was considered and constant traffic flow was simulated. The tubing, line source, perpendicular to the free stream represented 7<sup>th</sup> street, which is a four lane-two way arterial. Rhodamine 610 Chloride, one of the most common PLIF dyes, was used as the source dye. It is a fluorescent dye with a peak absorption wavelength of 555 nm and broad absorption spectrum permitting excitation at 532 nm.

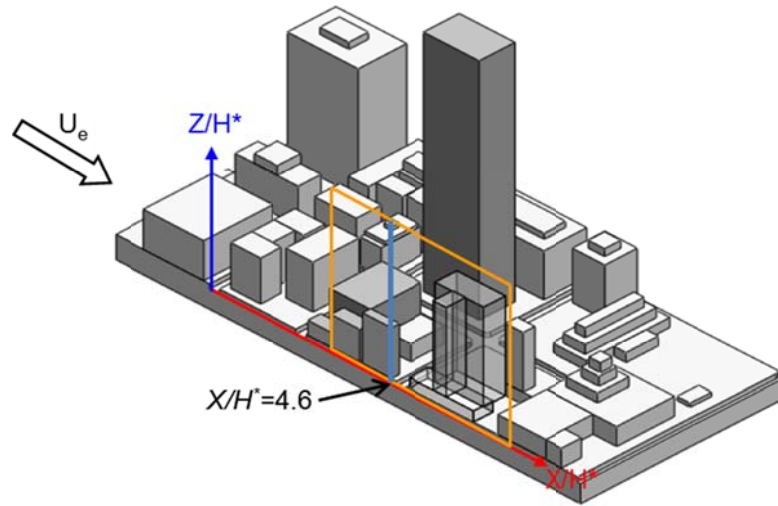


Figure 2.5 A schematic diagram of the measured (a golden rectangular) on the cross sectional plane ( $Y/H^* = 6$ ) of building cluster. Refer to Figure 2.4 for a view of the whole building cluster and the coordinate origin. The tall building is shown as a translucent block.

#### 2.1.6 Simultaneous PIV/PLIF system

Two-dimensional velocity field was measured by PIV. Fluorescent emission of the laser illuminated dye measured by PLIF system provided concentration field. PIV/PLIF system includes a 400 mJ double-pulsed Nd-YAG laser (Big Sky Laser Technologies, Inc, model CFR400), a LASERPULSE Synchronizer (TSI Inc.), a high resolution (1600 pixel $\times$ 1192 pixel) POWERVIEW Plus 2M CCD camera (TSI Inc., model 630157) for PLIF measurement, a high resolution (4008 pixel $\times$ 2672 pixel) POWERVIEW Plus 11M CCD camera (TSI Inc., model 630162) for PIV measurement, and CameraLink frame grabber (TSI Inc.). Particles (specific gravity 1.02) used to seed the channel were Pliolite Ultra 100 (Eliokem). Insight 3G (TSI Inc.) software was utilized for data collection and TecPlot (Tecplot, Inc.) and the MatLab were used for the velocity vector field and concentration field visualizations.

A double pulsed laser beams of 532 nm wavelength were generated with a frequency of 1 Hz and expanded into laser sheets by sheet-forming optics, which included two cylindrical lenses (-15 mm focal length). The time interval between two laser pulses was set to  $\Delta t = 1800 \mu\text{s}$ . The particles illuminated by laser sheets were recorded by CCD camera. The velocity of particles was calculated by cross correlation of consecutive images. PIV. PIV measurement technique is well established and widely used for fluid flow investigations (Adrian, 1988, 1991, 1997; Prasad et al., 1992) and details will not be discussed here. In addition to illuminating the particles for PIV measurement, laser was exciting the fluorescent dye. When fluorescent dye is illuminated by the laser sheet, it absorb incident light at around 532 nm and re-emits light at around 580 nm, which is the peak emission wavelength of Rhodamine 610 (Coppeta and Rogers, 1998). The re-emitted light intensity recorded by CCD camera is proportional to the concentration of the fluorescent dye. This proportionality is expressed by the Beer-Lambert law and it is linear for dilute solutions (Vincont, et al., 2000; Crimaldi, 2008).

A filter with a 10 nm bandwidth centered on the 580 nm dye wavelength was used together with the CCD camera in order to remove the 532 nm wavelength of the YAG lasers. A LASERPULSE Synchronizer (TSI Inc.) was used to trigger the laser pulse and the CCD camera with correct sequences and timing through a 2.66 GHz dual-processor workstation (Intel  $\text{\textcircled{C}}$ Xeon<sup>TM</sup>). An aperture opening of 1.4 was chosen for optimal brightness. Before each experimental sequence, 20 images of background light intensity were captured. The average intensity was calculated and used in post-processing for

background subtraction from the images of the fluorescent dye. An 8 pixel  $\times$  8 pixel grid size was chosen, which corresponds to a grid size of 1.20 mm  $\times$  1.20 mm. Total of 60 images (one minute sampling time) were captured and averaged per each experimental sequence.

Grid by grid concentration calibration was applied to entire camera image in concentration measurements. Two separated calibration curves were made. One is for mean intensity smaller than 80 and the other for mean intensity greater than 80. Polynomial coefficients for each grid were found by least square fitting. The background intensity is subtracted from the measured concentration for each grid.

The plume dispersion from a line source over an open terrain was measured. The length of the line source is 0.6 m. The flow rate was set at 100 ml min<sup>-1</sup>, which is sufficiently small so that the vertical momentum from the source has less influence on the dispersion.

A case study was made to investigate the role played by an individual building in built environment. The velocity vectors and concentrations distribution on a vertical plane at the downstream distances from  $X/H^*=2.6$  to  $X/H^*=7.4$  were investigated. This plane cut through the tall building at  $Y/H^*=6$  as shown in Figure 2.5. Data were acquired with tall building and without tall building separately. The comparison of flow characteristics, concentrations distribution, turbulent kinetic energy and vertical plume spread for two cases were made. Vertical profiles of mean velocity, turbulent intensity and concentration were obtained.

## **2.2 Results of Flow through Rectangular Arrays of Cubical Obstacles**

### **2.2.1 Flow Through a $3 \times 3$ array of cubes**

An array of  $3 \times 3$  cubes was placed perpendicular to the flow in the channel test section. The cubes have  $H = 5$  cm long edges and the distance between cubes (“street width”) was  $S = 5$  cm. The schematic of the experimental arrays and the measurement planes for vertical and horizontal flow fields is given in Figure 2.3. The PIV measurements in the vertical plane confirmed well-known flow pattern. Flow field in the vertical plane through the array of uniform height, presented in Figure 2.6, reveals expected acceleration regions at the leading edge of the first building and vortices behind each building row. For the case of tall central building (Figure 2.7), in addition to the acceleration regions at the leading edges of the first building and the tall building, the blocking effect of the tall building is evident which results in intense downdraft and stronger vortex behind the first building.

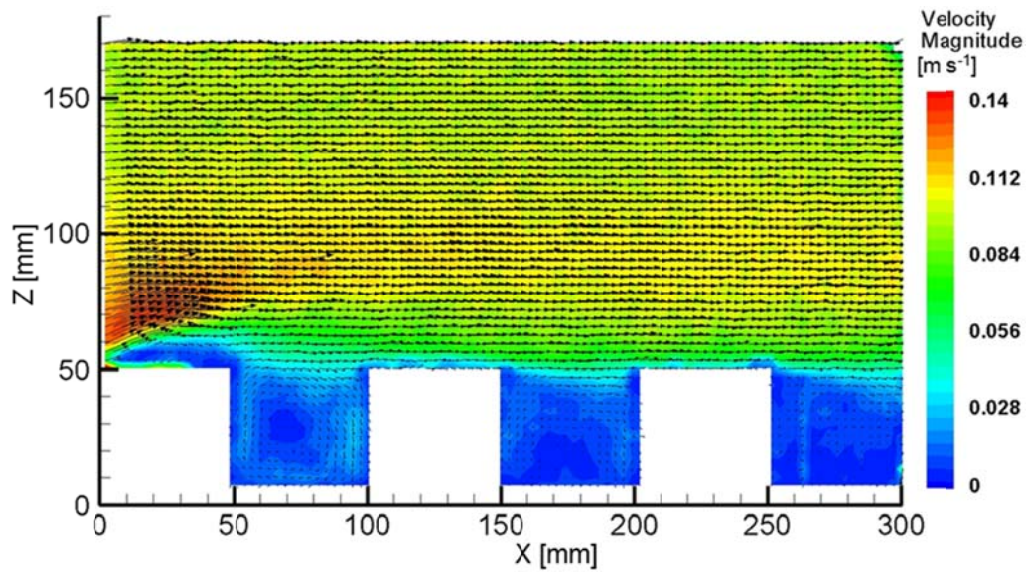


Figure 2.6 Measured flow field in the vertical plane at the centerline of the uniform height array. Velocity magnitude color bar is given on the right.

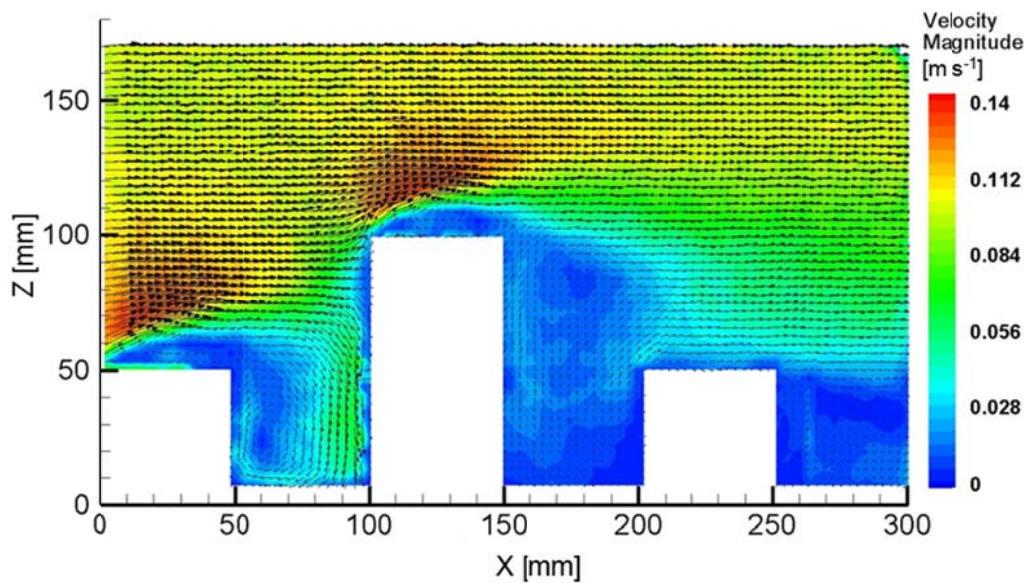


Figure 2.7 Measured flow field in the vertical plane at the centerline of the array with tall central building. Note the strong downdraft caused by the tall building.

A surprise came as we started to look at the detailed velocity field in the horizontal plane. The flow pattern through an array of regular obstacles is not something un-

published. The typical published flow pattern would consist of the acceleration regions in the streets that are parallel to the incoming flow and the counter-rotating vortex pairs behind each building. However, that idealized picture does not match the actual flow through the three dimensional array. Here by “three dimensional” we refer to a finite array, not bounded with a wall on any side. The measured horizontal flow pattern is given in Figure 2.8. As fluid enters the array it is partially deflected sideways after the first building row. It flows back into the array behind the second building row. This pattern, thereafter referred to as the ‘lateral channeling’, was very surprising, and we suspected that there may be some problem in the experimental setup. The building alignment was checked and even the experiments with intentionally misaligned buildings in a way to oppose this pattern were performed. The influence of the channel walls was investigated and the buildings of half the original size ( $H = 2.5$  cm) were used to form the array. A range of Reynolds numbers was covered from  $Re = 1000$  to  $Re = 7000$ . The pattern persisted and turned out to be insensitive to the building alignment imperfections and the incoming flow conditions (i.e. velocity profile and background turbulence).



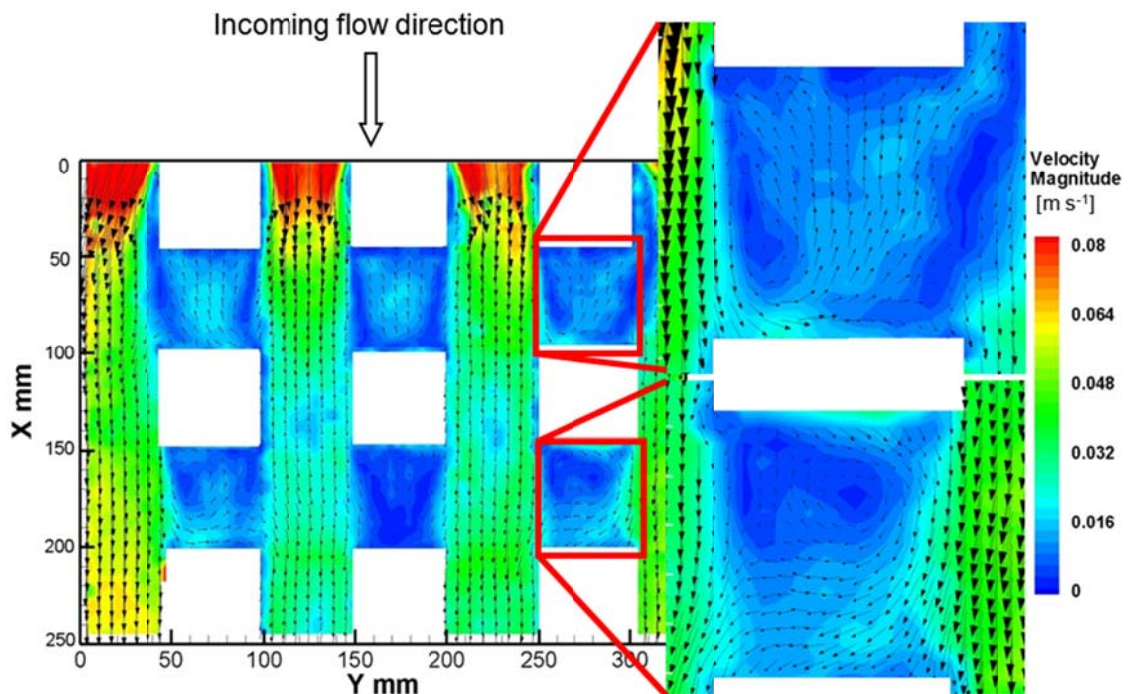


Figure 2.8 Measured velocity field in the horizontal plane through a  $3 \times 3$  building array of uniform height.

The presented flow field in Figure 2.8 is measured at  $1/3H$  (1.6 cm) from the ground. The measurements were also performed at  $1/2H$  and  $2/3H$  from the ground level. The lateral channeling patterns, on both sides of the arrays, are symmetric along the array centerline and are independent of the measurement height. Since these measurements are close to the ground level (at  $1/3H$ ), the back flow of the horizontal wake vortex can be seen in the lee of the central buildings.

The next step was to look at the influence of tall ( $2H$ ) central building. Figure 2.9 presents the flow pattern measured at the same location and under the same incoming flow conditions as the one given in Figure 2.8 with the only difference being the tall central building. Note how the tall building causes more intense lateral outflow in the lee

of the first row of buildings. This is a consequence of a strong downdraft caused by the blocking effect of the tall building (see Figure 2.9). The volumetric flow rate in the outflow region is three times larger than that in the outflow from the uniform height array.

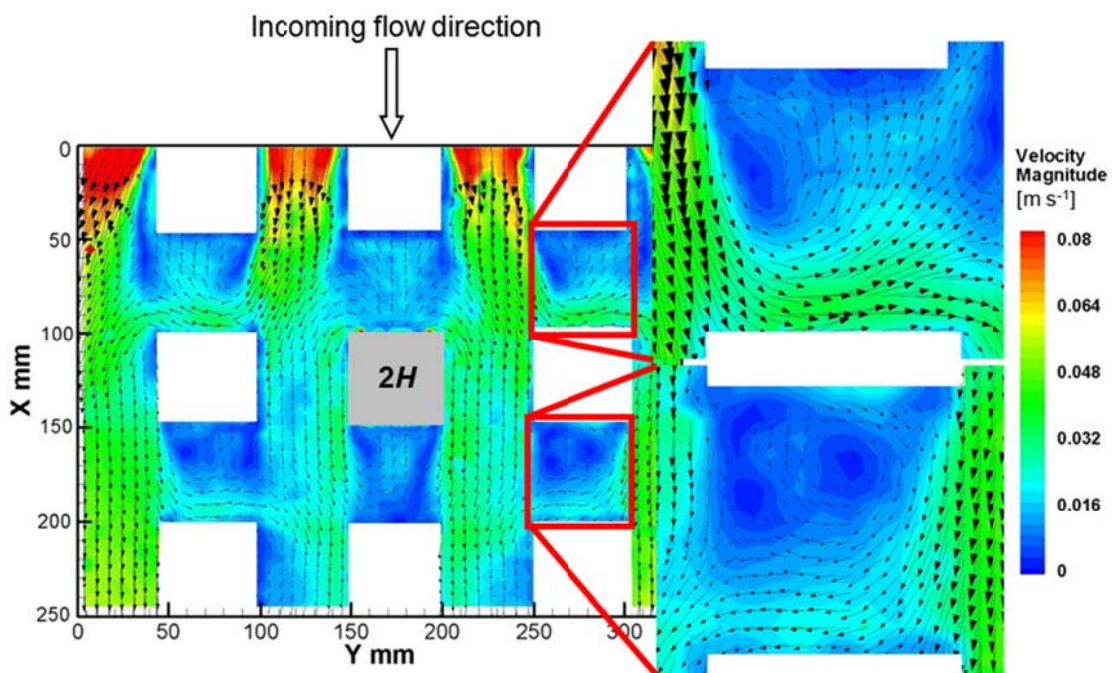


Figure 2.9 Measured velocity field in the horizontal plane through a  $3 \times 3$  building array with a central building of double height.

The CFD model with the  $k-\varepsilon$  turbulence closure scheme (Baik et al., 2003) was deployed to the same building configuration as the laboratory experiments. Assuming neutral atmosphere, logarithmic velocity profile with a roughness length of 0.05 m is used as the incoming wind. Reference velocity was  $10 \text{ m s}^{-1}$  at the 10 m height. Cubical building height is also 10 m. Zero shear condition is used at the domain boundaries. Model results for the flow through the uniform height array and flow pattern through the

array with tall central building are given in Figure 2.10 and 2.11, respectively. The model reproduced the measured flow patterns. The model was run at very high  $Re \sim 10^7$  eliminating any possibility that the observed pattern is some low  $Re$  artifact.

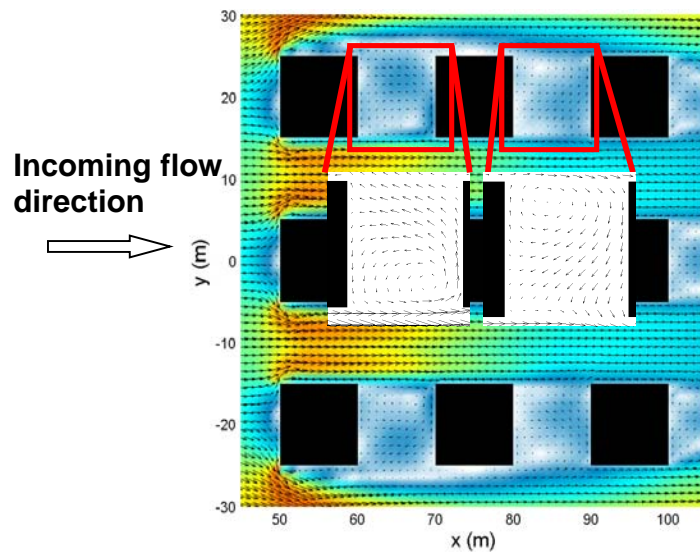


Figure 2.10 Velocity field through a  $3 \times 3$  building array of uniform height produced by a CFD model. (Park, S.-B., personal communication)

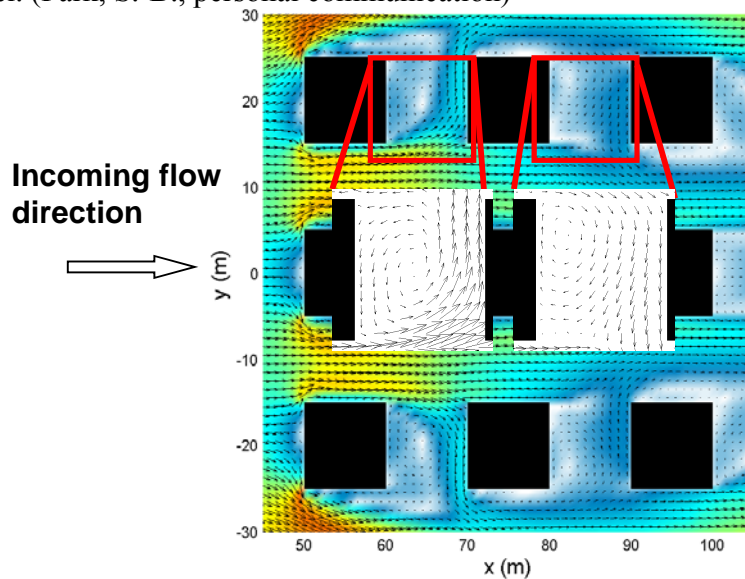


Figure 2.11 Velocity field through a  $3 \times 3$  building array with a central building of double height produced by a CFD model (Park, S.-B., personal communication).

### 2.2.2 Flow Through a $5 \times 5$ array of cubes

We proceeded with the same measurements for a  $5 \times 5$  array of cubes as presented by schematic in Figure 2.3. The measured flow fields in representative regions of the uniform height array are given in Figure 2.12a. Refer to schematic in Figure 2.3 for location notation. Note again the lateral channeling from the array behind the first row of buildings (location A1). This is followed by the lateral channeling into the array in all following rows. In this case the introduction of a tall central building (Figure 2.12b) could not significantly influence the lateral outflow channeling in the first row, which is one row upstream of it. However, as expected from our  $3 \times 3$  array results, the lateral spreading of the downdraft near the ground caused by the tall building did block the lateral channeling into the array at the second row. Actually this lateral spreading of the tall building downdraft was strong enough to completely block the inflow in location A2 and fully reverse the flow direction from inflow to outflow in the columns next to the tall building (location B2). For clarity, we include and plots of streamlines (Figure 2.13) calculated directly from velocity vectors (Figure 2.12).



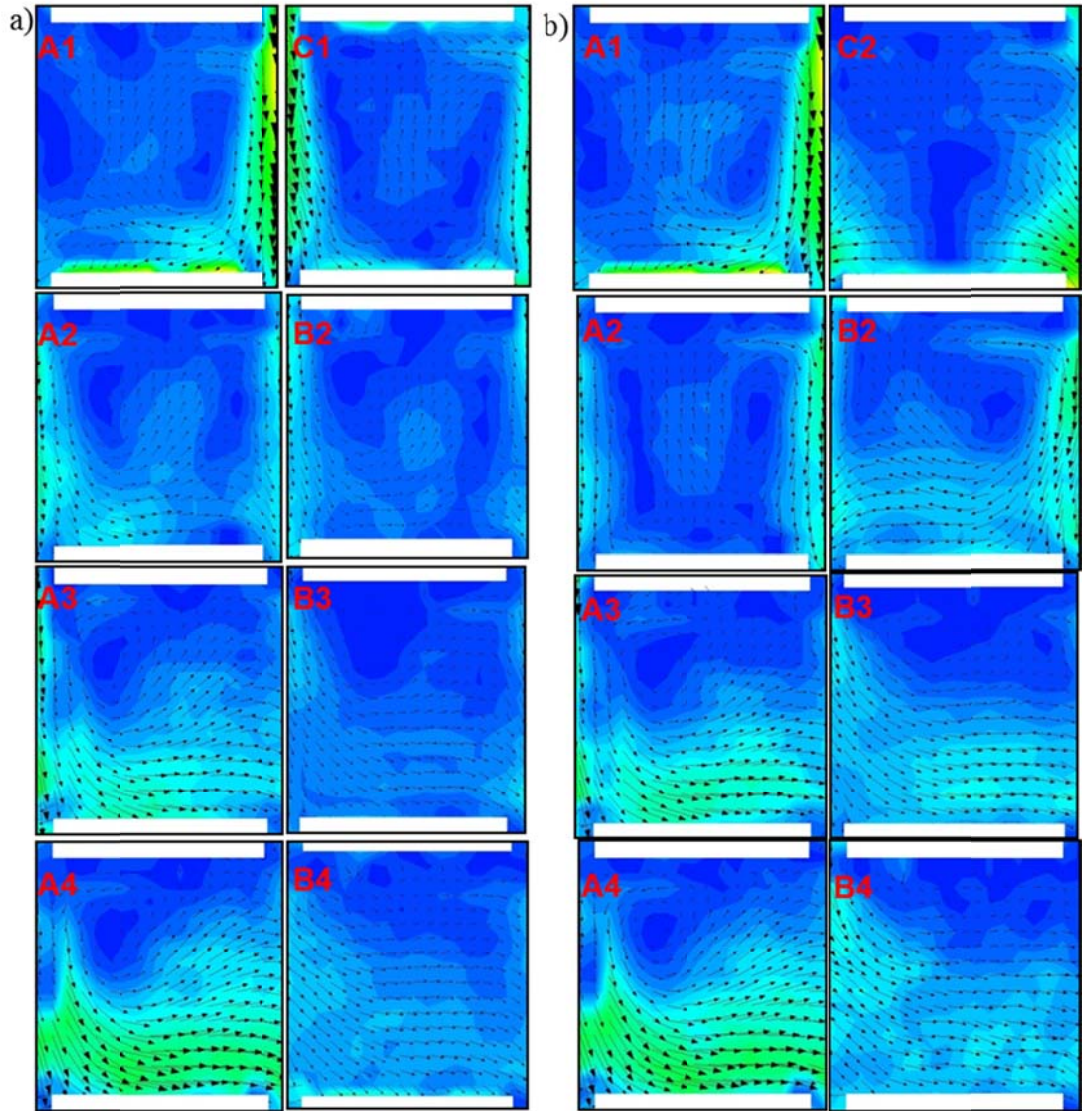


Figure 2.12 a) Measured horizontal velocity field within a uniform height  $5 \times 5$  cubical array and b) measured horizontal velocity field within a  $5 \times 5$  cubical array with the central building of double height. Refer to Figure 2.3 for location schematic. Velocity scale is given in Figure 2.8 and Figure 2.9.

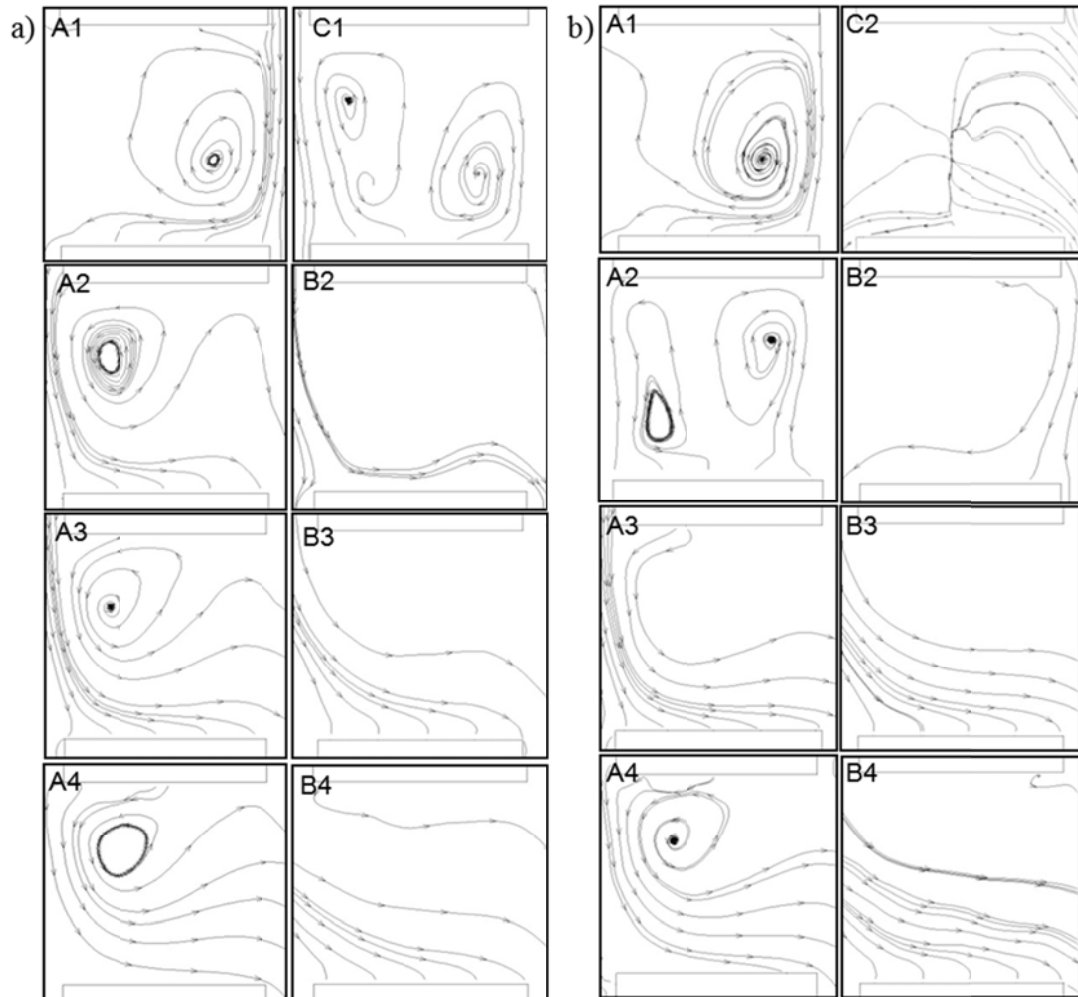


Figure 2.13 a) Streamlines calculated from velocity field in Figure 2.12a for  $5 \times 5$  array of uniform height and b) streamlines calculated from velocity field in Figure 2.12b for  $5 \times 5$  array with a central building of double height. Refer to Figure 2.3 for location schematic.

### 2.2.3 Measurement Uncertainty

The uncertainty analysis was performed according to ITTC (2008) recommendations for PIV measurements. The uncertainty for velocity measurement results from the calibration (magnification) factor,  $\alpha$ , image displacement  $\Delta X$ , time interval  $\Delta t$  and lag of the tracer particle from the flow field,  $\delta u$ . Note that  $\delta u$  also

accounts for measuring 3-D flow in 2-D plane. PIV velocity can be expressed as  $u = \alpha \Delta X / \Delta t + \delta u$ . From calibration images we determined  $\alpha$  (units of  $\alpha$  are mm pixel<sup>-1</sup>, or short mm pxl<sup>-1</sup>). Time interval  $\Delta t$  was optimized to 1.1 ms. Uncertainty in each of  $\alpha$ ,  $\Delta X$ ,  $\Delta t$  and  $\delta u$  results from several error sources (for details refer to ITTC, 2008 and Appendix A). Sensitivity coefficients ( $\partial u / \partial \Delta X$ ,  $\partial u / \partial \Delta t$ ,  $\partial u / \partial \alpha$ ,  $\partial u / \partial \delta u$ ) were calculated from measurements, taken from PIV software settings and our (TSI Inc) PIV hardware specifications. Summarized results of uncertainty analysis for three camera views (vertical plane, horizontal 3 × 3 and horizontal 5 × 5) are given in Table 2.1-Table 2.3. Root-sum-square is employed for the accumulation of uncertainties. The combined uncertainty was estimated to be approximately 11%, 12% and 8% for vertical plane measurements, 3 × 3 horizontal measurements and 5 × 5 horizontal measurements, respectively.

Table 2.1 Uncertainty for vertical plane measurements and free stream velocity of 8.2 cm s<sup>-1</sup>.

Parameter	Uncertainty ( $u$ )	Sensitivity coefficient ( $c$ )	$cu$
$\alpha$ [mm pxl <sup>-1</sup> ]	0.00114	41.0 [pxl s <sup>-1</sup> ]	0.05 [mm s <sup>-1</sup> ]
$\Delta X$ [pxl]	0.047	181.8 [mm pxl <sup>-1</sup> s <sup>-1</sup> ]	8.62 [mm s <sup>-1</sup> ]
$\Delta t$ [s]	5.39e-09	7.0 [m s <sup>-2</sup> ]	0.00 [mm s <sup>-1</sup> ]
$\delta u$ [mm s <sup>-1</sup> ]	0.158	1.0	0.16 [mm s <sup>-1</sup> ]
	Combined uncertainty (root-sum-square)		8.63 [mm s <sup>-1</sup> ]
	Percentage Uncertainty		10.52 %

Table 2.2 Uncertainty for  $3 \times 3$  array horizontal measurements and free stream velocity of  $8.2 \text{ cm s}^{-1}$ .

Parameter	Uncertainty (u)	Sensitivity coefficient (c)	$cu$
$\alpha$ [mm pxl <sup>-1</sup> ]	0.00136	34.5 [pxl s <sup>-1</sup> ]	0.05 [mm s <sup>-1</sup> ]
$\Delta X$ [pxl]	0.045	215.9 [mm pxl s <sup>-1</sup> ]	9.82 [mm s <sup>-1</sup> ]
$\Delta t$ [s]	5.39e-09	7.0 [m s <sup>-2</sup> ]	0.00 [mm s <sup>-1</sup> ]
$\delta u$ [mm s <sup>-1</sup> ]	0.189	1.0	0.19 [mm s <sup>-1</sup> ]
	Combined uncertainty (rms)		9.82 [mm s <sup>-1</sup> ]
	Percentage Uncertainty		11.98 %

Table 2.3 Uncertainty for  $5 \times 5$  array horizontal measurements and free stream velocity of  $8.2 \text{ cm s}^{-1}$ .

Parameter	Uncertainty (u)	Sensitivity coefficient (c)	$cu$
$\alpha$ [mm pxl <sup>-1</sup> ]	0.00068	69.1 [pxl s <sup>-1</sup> ]	0.05 [mm s <sup>-1</sup> ]
$\Delta X$ [pxl]	0.058	108.0 [mm pxl s <sup>-1</sup> ]	6.29 [mm s <sup>-1</sup> ]
$\Delta t$ [s]	5.39e-09	7.0 [m s <sup>-2</sup> ]	0.00 [mm s <sup>-1</sup> ]
$\delta u$ [mm s <sup>-1</sup> ]	0.093	1.0	0.09 [mm s <sup>-1</sup> ]
	Combined uncertainty (rms)		6.29 [mm s <sup>-1</sup> ]
	Percentage Uncertainty		7.68 %

#### 2.2.4 Pressure Analysis

With the assumption that the flow field is nearly two-dimensional, steady as well as incompressible, the pressure field can be estimated through the numerical integration of the steady Navier-Stokes equations in two-dimensional form



$$u \frac{\partial u}{\partial x} + v \frac{\partial u}{\partial y} = -\frac{1}{\rho} \frac{\partial P}{\partial x} + \nu \left( \frac{\partial^2 u}{\partial x^2} + \frac{\partial^2 u}{\partial y^2} \right) \quad 2.10$$

$$u \frac{\partial v}{\partial x} + v \frac{\partial v}{\partial y} = -\frac{1}{\rho} \frac{\partial P}{\partial y} + \nu \left( \frac{\partial^2 v}{\partial x^2} + \frac{\partial^2 v}{\partial y^2} \right) \quad 2.11$$

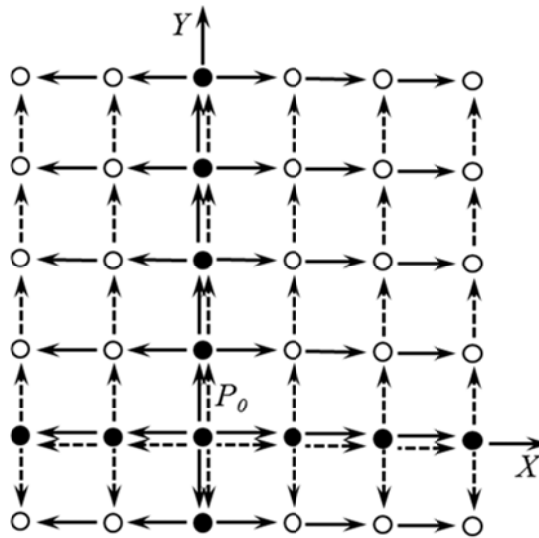


Figure 2.14 Integration routes used to integrate two-dimensional pressure. Two paths of integration follow either the dashed or solid arrows (Raffel et al. 2007).

To obtain the pressure field, the pressure gradients  $\partial P/\partial x$  and  $\partial P/\partial y$  are calculated using finite difference approximations of the velocity gradients. The pressure gradients are then integrated starting from a point near the center of an initial value of  $P_0$  using an integration scheme as shown in Figure 2.14. In principal, there are two integration methods: a column-major integration or a row-major integration (Raffel et al. 2007).

The pressure analysis was applied to flow fields obtained from  $3 \times 3$  arrays. Figure 2.15 shows the calculation results of pressure profile along  $Y$  axis at  $X=70$  mm. In Figure

2.15b, the introduction of a tall central building causes negative pressure zones where vortexes present (see Figure 2.9). Along the streets parallel to the flow direction, the magnitude of pressure decreases gradually (see Figure 2.16b).

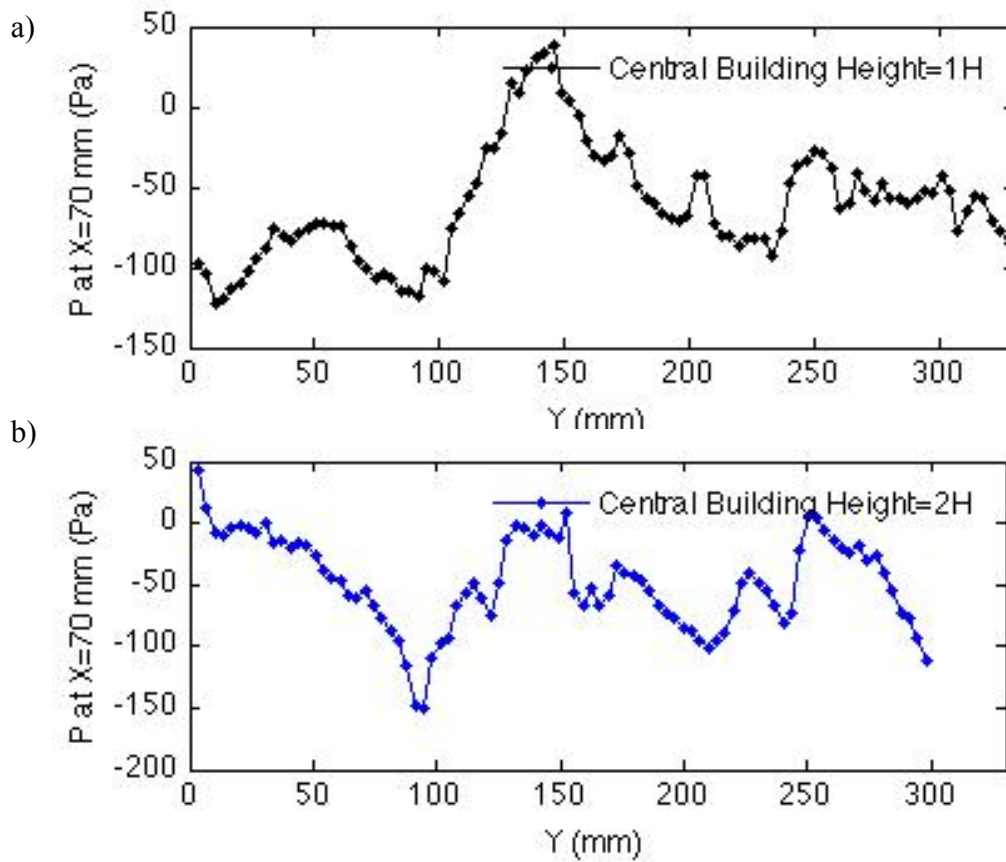


Figure 2.15 Pressure profile along  $Y$  axis at  $X=70$  mm for  $3 \times 3$  arrays with central building height of a)  $1H$  and b)  $2H$ .

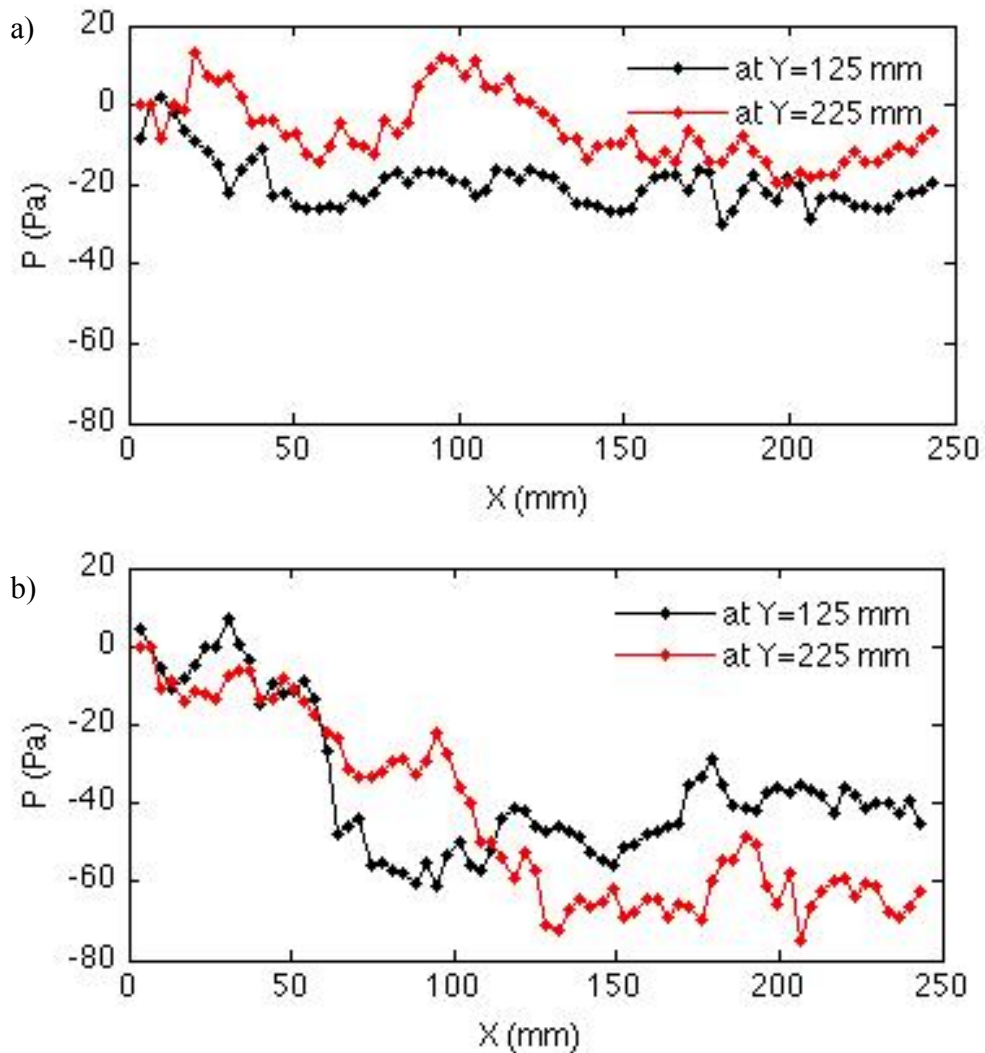


Figure 2.16 Pressure profile along  $X$  axis at  $Y=125$  and  $225$  mm for  $3 \times 3$  arrays with central building' height of a)  $1H$  and b)  $2H$ .

### 2.2.5 Discussions

A re-circulating water channel was utilized to create controlled flow field to model wind flows through simple mock urban environments. In this communication the flows through regular arrays of  $3 \times 3$  and  $5 \times 5$  cubical mock buildings are reported. A novel flow pattern within the array was observed in the horizontal plane. This flow pattern

shows regions of lateral channeling in the form of the mean outflow from the array and the mean inflow into the array. For the case of the tall central building in  $3 \times 3$  array this “sideway” flow is significantly enhanced, while the tall central building in  $5 \times 5$  array causes the blockage, and reversal, of the inflow to the array.

The unavoidable question is why this flow pattern was not reported by the previous studies? Most of previous wind tunnel and water flume studies focused on quasi 2-D arrays, arrays that would cover the whole width of the test section allowing the channel walls to block any possible lateral flow channeling. The same distortion can be done by imposing the periodic boundary conditions (e.g. Coceal et al., 2006; Lien and Yee, 2004), which emulates the infinite array in lateral direction, for numerical simulations. Also, none of the previous researchers had the laboratory capabilities to perform such detailed and precise measurements of the flow between the obstacles. Even when the building array was not from side to side of the experimental facility, most measurements were point measurements using hot wires, pressure transducers, Pitot tubes or line measurements using the scanning Laser Doppler Velocimetry (LDV) and none was able to “see-through” the obstacles/buildings.

This study shows that approximating even very simple 3-D flow configurations with a quasi 3-D (e.g. periodic boundaries in numerical simulations, or wall bounded arrays in experiments) can lead to deceptive results. Flow displacement, acceleration and separation occur not only above the array but also on the array sides, which become impossible for the sidewall bounded arrays. For the neutral atmosphere there is no reason to give preference neither to the array side acceleration nor above the array acceleration.

For the stable case the vertical rising would be blocked giving even more weight to the flow acceleration around the array rather than above it.

Purely physical explanation of the lateral channeling can be given in the following way:

*Outflow behind the first row of buildings:* One can imagine a second row of obstacles replaced with a single array-wide block. Obviously, the flow in this case would diverge around the block. Now, let us imagine a block with small gaps. If the gaps in the block are not big enough, in addition to the small amount of flow through the gaps, we will still have the flow divergence in front of the block. Following this logic one can see the second row of buildings as a big block with big gaps that still gives fairly strong longitudinal flow resistance to promote the lateral channeling: outflow in the first street. Further, as flow approaches the array, separation occurs at the leading edge of side buildings in the first row and reattachments occur further downstream (see measurements in Figure 2.8). This flow separation exposes the first lateral street to low-pressure regions on both array sides, which enhances the outflow (see schematic on Figure 2.17).

*Inflow in the remaining part of the array:* Streamlines that are deflected by the separation at the beginning of the array are converging back towards the array center to form inflows to the array (Figure 2.17). In addition, low pressure in the wake region draws the fluid through the array. This wake low pressure leads to formation of the strongest lateral inflow in front of the last row of buildings. As rows are further from the wake region inflow is less intense due to decreased pressure gradient.

In summary, pressure field caused by flow separation at the leading edge and in the array wake together with the increased flow resistance through the array leads to the lateral channeling. Presence of a tall central building will cause downdraft whose divergence at the ground level can completely overcome inflow to the array before the central row.

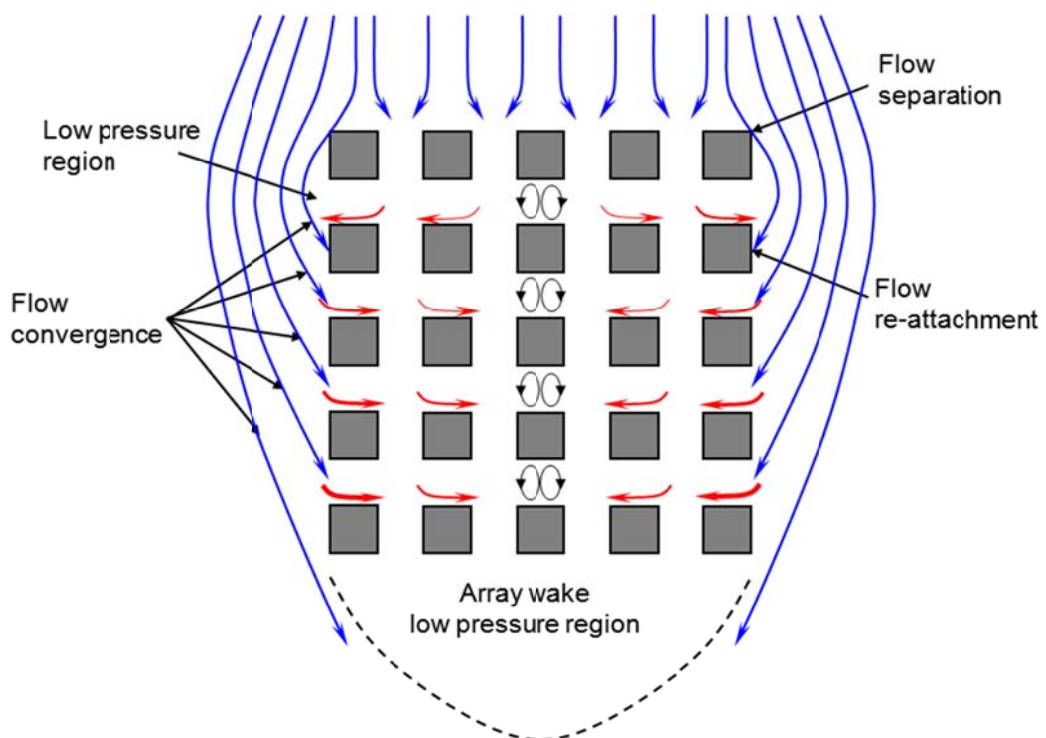


Figure 2.17 Schematic of streamlines (blue) of the flow around a  $5 \times 5$  cubical array. Red arrows represent the lateral channeling inside the array. Thickness of red lines corresponds to the relative flow intensity. Wake behind obstacles in the middle column consists of two counter rotating vortices. Case of uniform obstacle height is presented. For the case of tall central building flow behind the second row will change (refer to Figure 2.12b, locations A2 and B2).

With this physical explanation in mind, the current results allow us to speculate that the mean lateral flows into and out of the array will be prominent for arrays of regular

and equidistant obstacles with length (dimension parallel to the wind direction) comparable or larger than the array width (dimension perpendicular to the wind direction, i.e. lateral). Future work has to include the investigation of lateral channeling sensitivity to the array length/width parameter and  $S/H$  ratio. At this moment we can speculate that the lateral outflow in the first street is proportional to the array length/width ratio due to the increased flow resistance through the array for longer arrays. This should be valid for the skimming regime and it is probably not valid for the isolated and wake interference regimes. Due to the cost of laboratory experiments we plan to investigate this systematically using a computational fluid dynamics (CFD) model. It should be noted that the CFD model was already deployed to the same building configuration as the laboratory experiments. Assuming neutral atmosphere, logarithmic velocity profile with a roughness length of  $z_0 = 0.05$  m is used as the incoming wind. Reference velocity was  $U = 5 \text{ m s}^{-1}$  at the 10 m height. Cubical building height was also  $H = 10$  m for all simulations. Zero shear condition is used at the domain boundaries. In this way, the model was run at very high  $Re \sim 10^7$  eliminating any possibility that the observed pattern is some laboratory, low  $Re$  artifact. The model reproduced the measured flow patterns. Detailed comparisons of CFD and laboratory results will be presented separately.

As mentioned in the introduction, compared to plumes in the open terrain, the plumes in the arrays are wider (Macdonald 2000a, b and c), making initial spread very abruptly as entering the array. A question remains: Can this flow pattern, specifically the lateral outflow in the lee of the first building row, explain the sudden plume spread as it enters the array of obstacles? This is highly likely the case, but it is too early for such

conclusion. Dispersion experiments using simultaneous PIV and the Planar Laser Induced Fluorescence (PLIF) measurements are needed to investigate the actual plume spread through these arrays.

## 2.3 Laboratory Simulation of Flow and Dispersion through a Scaled Built Environment

### 2.3.1 Plume Dispersion from a Line Source

Figure 2.18 shows the plume dispersion from a line source over an open terrain. Color bar shows the dimensionless concentration after calibration. The length of the line source is 0.6 m. The flow rate was controlled at  $100 \text{ ml min}^{-1}$  so that the vertical momentum from the source has less influence on the dispersion.

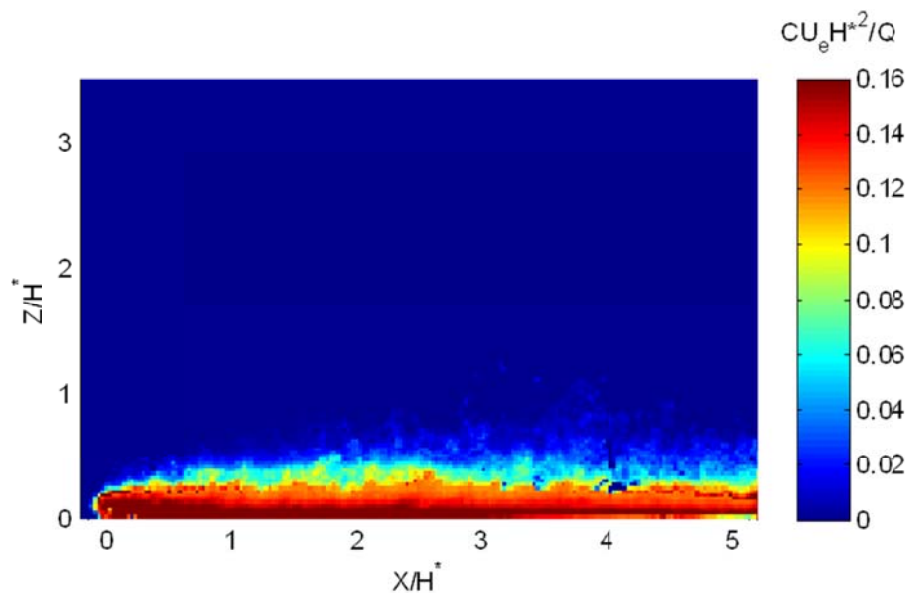


Figure 2.18 Vertical plane of plume dispersion from a line source through an open terrain. Color bar shows dimensionless concentration.



For the simultaneous PIV/PLIF measurements, mean velocity ( $u$ ,  $v$  and  $w$ ) and concentration fields are averaged over 60 seconds, which corresponds to 48 minutes in full field scale. The magnitudes of length, velocity and concentration are scaled to dimensionless quantity by being divided by characteristic length  $H^*$ , velocity  $U_e$  and concentration  $Q/U_e H^{*2}$  respectively. Two-dimensional turbulent kinetic energy is calculated as  $k=(u'^2+w'^2)/2$  for vertical plane. Here  $u'$  and  $w'$  are velocity fluctuation. Unified turbulent kinetic energy is turbulent kinetic energy divided by square of free stream velocity,  $k/U_e^2$ .

### 2.3.2 Velocity and Concentration Distributions

Figure 2.19 and Figure 2.20 show mean velocity and concentration fields in the cases with tall building and without tall building. In Figure 2.19, velocity vectors show acceleration region on the roof of the tall building, a clockwise vortex above the street upwind the tall building and updraft flow in the wake. Concentration field shows lifted plume to the roof level by the flow in the wake of tall building. In contrast, in Figure 2.20 the clockwise vortex above the street is much weaker and we can see that plume is more concentrated at the lower level and the magnitude of concentration is higher than when tall building is present. The diluted plume both upwind and downwind of the tall building shown in Figure 2.19 is caused by the rapid turbulent mixing of plume in the wakes. The recirculation region upwind of the tall building continuously lifts material from the ground surface. In the absence of tall building, plume tends to be trapped in the wake of the upstream building. Thus, due to the enhanced mixing caused by the tall

building (see Figure 2.19) the concentration distribution within building canopy is more uniform.

To compare two cases quantitatively, the ratio of concentration for the case with tall building ( $C_w$ ) to without tall building ( $C_{w/o}$ ) was taken and logarithm of ratio ( $\log(C_w/C_{w/o})$ ) was shown in Figure 2.21. The major concentration decay occurred below canopy, close to the ground surface (blue color) while the concentration was increased at the roof level of the tall building (yellow/red regions).

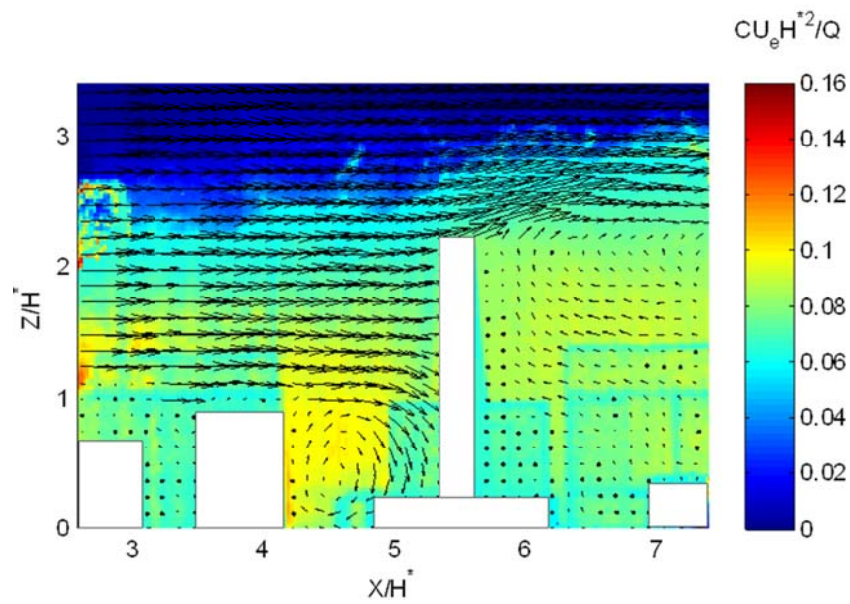


Figure 2.19 Mean velocity (black arrows) and concentration (colorbar) fields on vertical plane with tall building

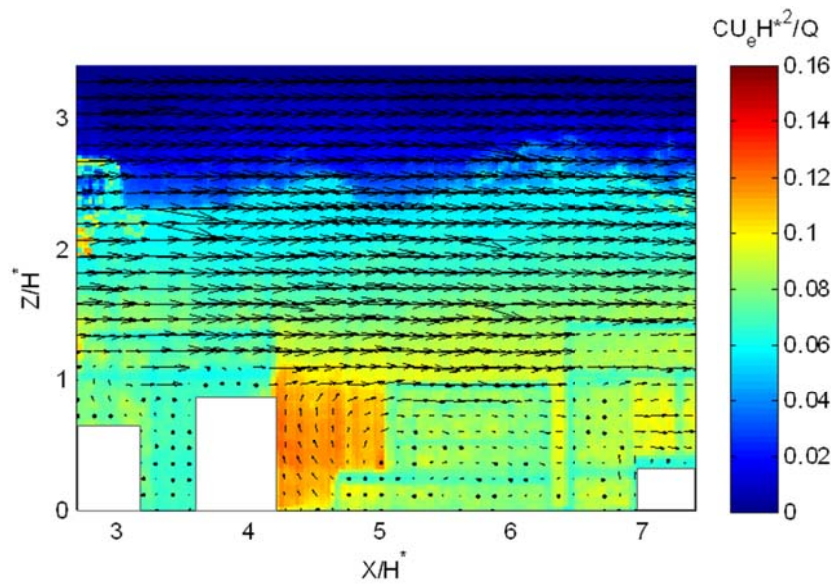


Figure 2.20 Mean velocity (black arrows) and concentration (colorbar) fields on vertical plane without tall building.

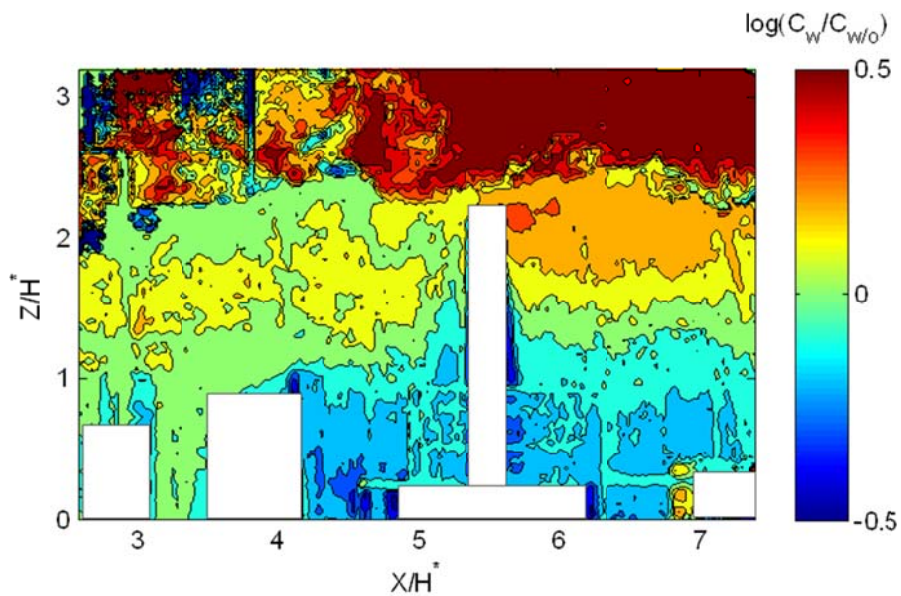


Figure 2.21 Contours of the logarithm of ratio of concentration distribution with tall building to that without tall building

Figure 2.22 and Figure 2.23 show turbulent kinetic energy in the case with tall building and without tall building, respectively. In Figure 2.22, perturbed high turbulent

region is formed at the roof level of tall building. In Figure 2.23 region of high turbulence is closer to the ground and has smaller magnitude compared with the tall building case. The region with low turbulence has high concentrations as seen in Figure 2.20. The ratio of normalized turbulent kinetic energy for the case with tall building to the case without tall building was taken and logarithm of ratio was shown in Figure 2.24. The major turbulent kinetic energy decrease occurred at the ground surface and the roof level (red color).

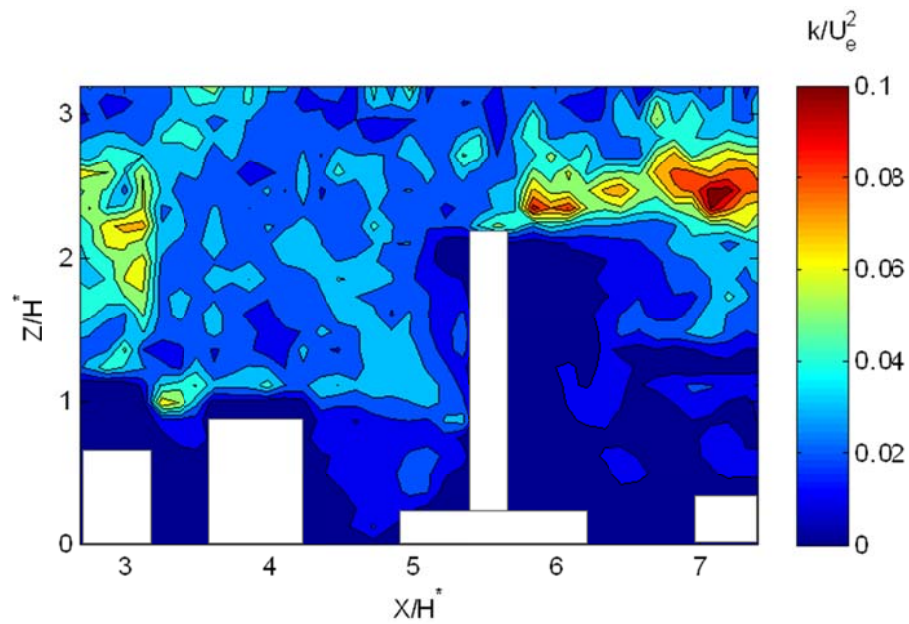


Figure 2.22 Contours of unified two-dimensional turbulent kinetic energy on vertical plane with tall building

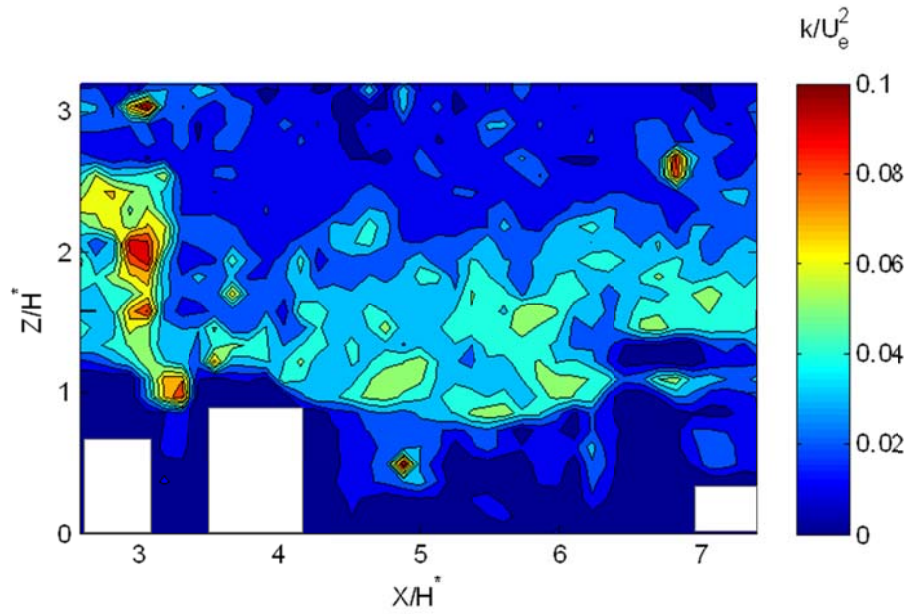


Figure 2.23 Contours of unified two-dimensional turbulent kinetic energy on vertical plane without the tall building.

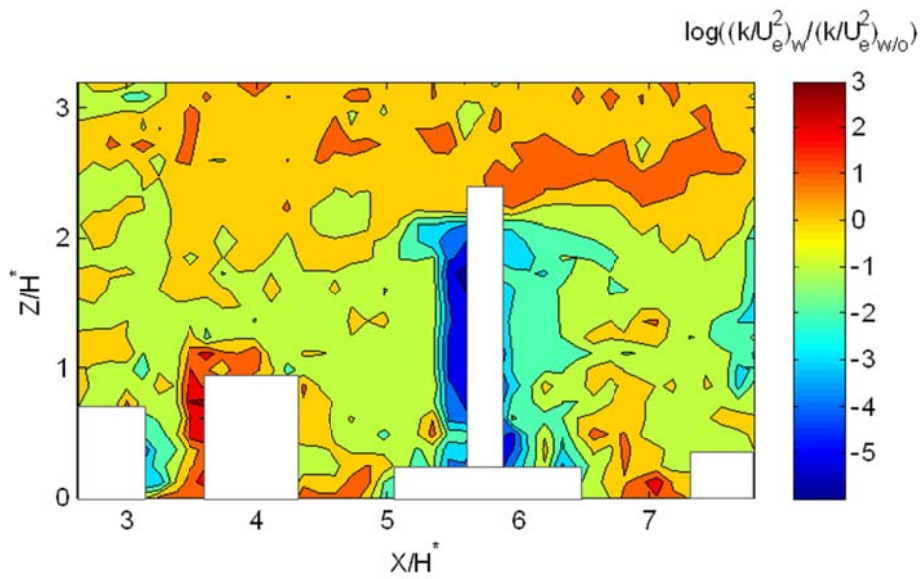


Figure 2.24 Contours of the logarithm of ratio of normalized turbulent kinetic energy with tall building to that without tall building.

### 2.3.3 Vertical Spread of Plume

The average height  $\bar{z}$  of the vertical plume spread can be found as

$$\bar{z} = \frac{\sum_{k=1}^N c_k \cdot z_k}{\sum_{k=1}^N c_k} \quad 2.12$$

and the standard deviation  $\sigma_z$  of concentration distribution is

$$\sigma_z^2 = \frac{\sum_{k=1}^N c_k \cdot (z_k - \bar{z})^2}{\sum_{k=1}^N c_k} \quad 2.13$$

Figure 2.25 shows the comparison of vertical spread of plume with the tall building and without the tall building. Without the tall building, the reduction in the characteristic height of building  $H^*$  is  $0.02H^*$ . This reduction leads to the maximum decay on vertical plume spread of  $0.34 H^*$ .

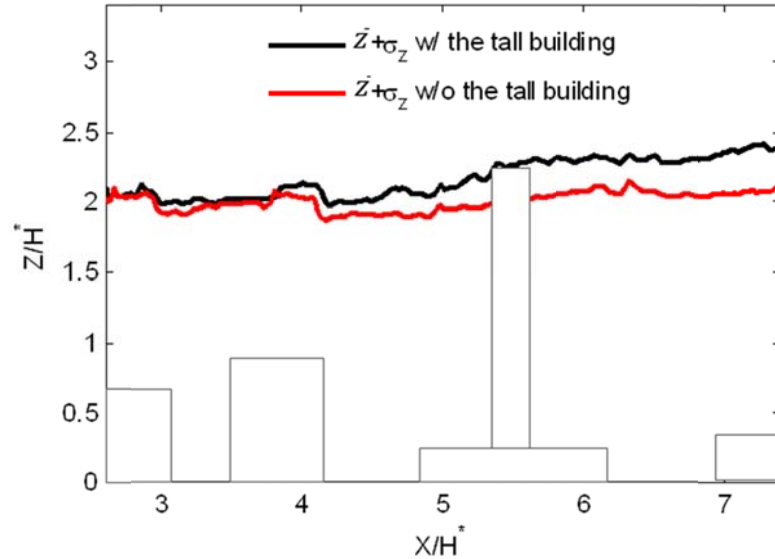


Figure 2.25 Comparison of vertical spread of plume with and without the tall building calculated by Eqs. 2.12 and 2.13.

### 2.3.4 Vertical Profiles of Velocity and Concentration

Figure 2.26a compares mean velocity components  $u/U_e$  and  $w/U_e$  profiles for the cases with and without the tall building at the downstream positions  $X/H^*=4.6$ . There is a transition point for  $u/U_e$  where velocity magnitude increases dramatically. This point is at about the height  $Z/H^*=1$ . In the case with the tall building,  $u/U_e$  have negative values and  $w/U_e$  are positive below  $Z/H^*=1$ . In the absence of the tall building,  $w/U_e$  are negative below  $Z/H^*=1$ . The presence of the tall building doesn't change the shape of vertical velocity profile because the tall building is narrow in width. Figure 2.26b shows turbulent components  $\sigma_u/U_e$  and  $\sigma_w/U_e$  profiles for the cases with and without the tall building. There is no significant change for turbulent components for two cases.



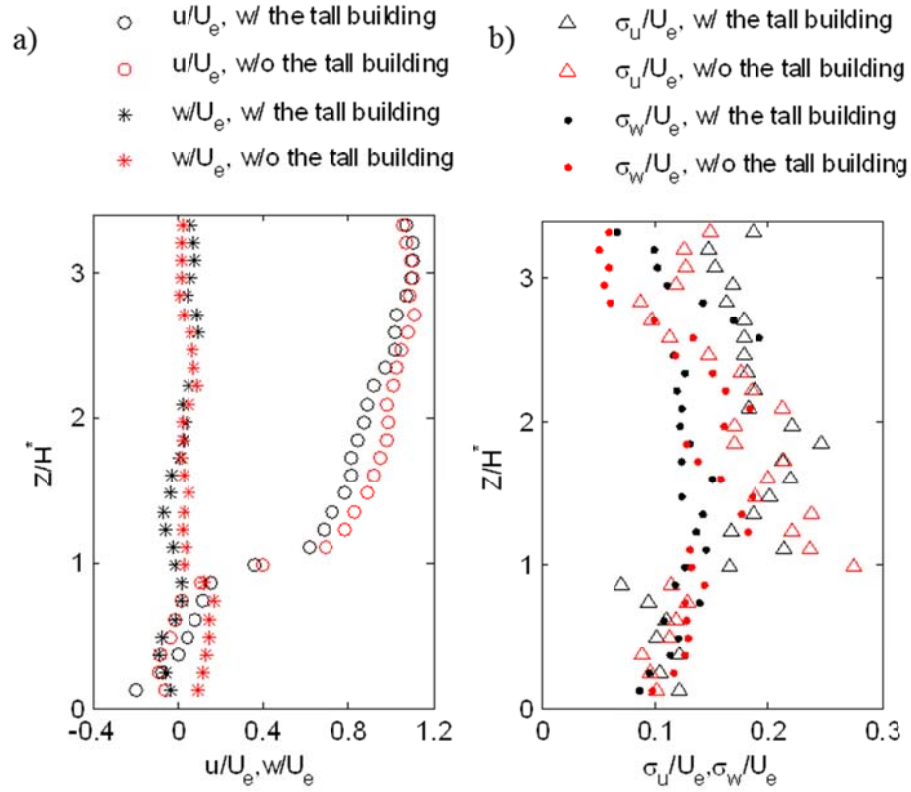


Figure 2.26 Vertical profiles of a) mean velocity  $u/U_e$  and  $w/U_e$  and b) rms velocity  $\sigma_u/U_e$  and  $\sigma_w/U_e$  for the cases with and without the tall building at the position  $X/H^*=4.6$ .

To study the influence of the tall building on plume dispersion, the integral time scale of concentration fluctuations  $T_c$  were calculated. The definition of  $T_c$  was determined by the following equations introduced by Yee et al. (2006):

$$T_c = \int_0^{\tau^*} R(\tau) d\tau \quad 2.14$$

where  $R(\tau) = \overline{c'(t)c'(t+\tau)} / \overline{c'^2(t)}$  is the autocorrelation function of the concentration time series,  $c'$  is concentration fluctuation and  $\tau^*$  is the lag time when  $R(\tau^*)=0.1$ .



In Figure 2.27a dimensionless concentration profiles  $CU_eH^{*2}/Q$  for two cases are compared at the downstream position  $X/H^*=4.6$ . Without the tall building, the concentration magnitudes below the transition point  $Z/H^*=1$  are greater than the values above the transition point. However, with the tall building, due to the vortex formed in the canyon, mixing of plume is more efficient, hence the concentrations above and below that height are more uniform.

Figure 2.27b shows vertical profiles of dimensionless  $T_c$  for the cases with and without the tall building at positions  $X/H^* = 4.6$ . The integral time scale  $T_c$  are larger below  $Z/H^* = 1.0$  than above for both cases. These trends are consistent with Yee's experiments in which vertical profiles of  $T_c$  at different downstream positions in the uniform height array plume were observed in a water channel. This time scale indicates the speed of concentration decay and how well the plume is persistent. The longer integral time scale demonstrates that the temporal structure of the plume was less fragmented because of the presence of obstacle array (Yee et al., 2006). In another word, it took longer for pollutants to escape from the canyon because of the presence of the vortex (see Figure 2.19) caused by the tall building. Also, because of the local mixing, the concentrations are more uniform within the canyon in the case when the tall building is present (see Figure 2.27).

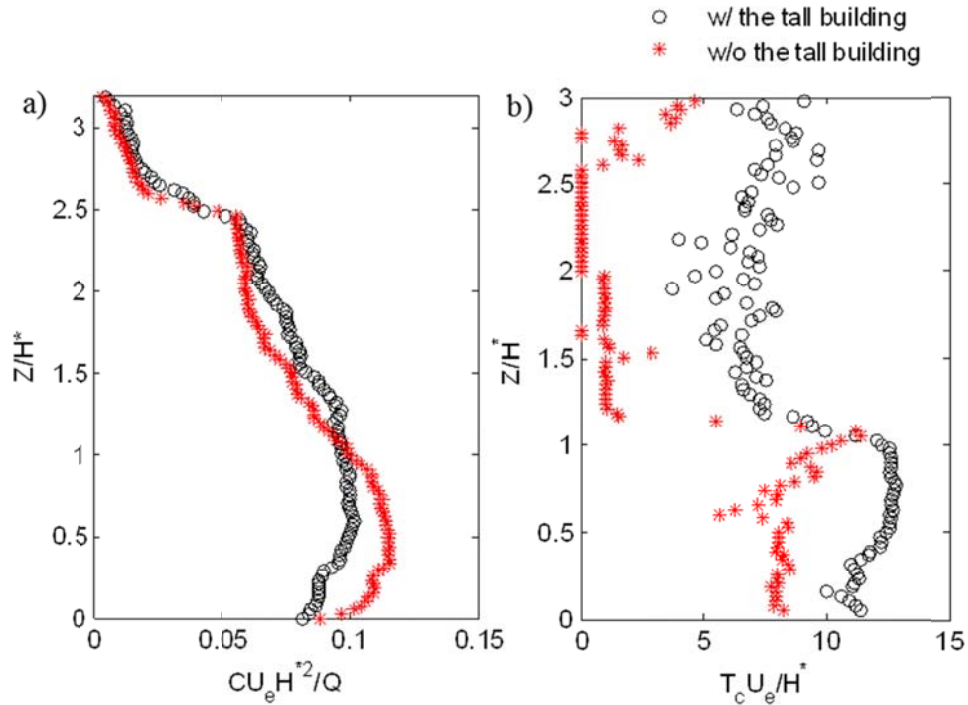


Figure 2.27 Vertical profiles of a) the mean concentrations and b) the integral time scale of concentration fluctuations at the positions  $X/H^* = 4.6$ .

### 2.3.5 Analysis of Turbulent and Advective Fluxes of Plume

As we see from Figure 2.27, the concentrations below  $Z/H^* = 1.0$  is lower when the tall building is present compared to when the tall building is absent. However, the rms velocities  $\sigma_w/U_e$  and  $\sigma_w'/U_e$  for two cases have no big difference. Hence, we evaluated both turbulent and advective fluxes to exam the plume venting from the canyon. Tay (2010) discussed the characterization of turbulent and advective aerosol flux components. The vertical plume flux due to mean flow is  $\overline{w\bar{c}}$ , where  $\bar{w}$  is the mean vertical velocity and  $\bar{c}$  is the mean plume concentration. The vertical flux of plume due to turbulent flows is  $\overline{w'c'}$ , where  $w'$  is the deviation from the mean vertical velocity and  $c'$  is the deviation

from the mean concentration. Integration of the flux across the horizontal direction yield the net flux due to advective flow,  $F_a = \int_L \overline{wc} dx$ , and turbulent flow  $F_t = \int_L \overline{w'c'} dx$ , where  $L$  is the canyon dimension. The sum of  $F_a$  and  $F_t$  is the net flux from both processes along the horizontal axis of the canyon. The positive flux represents a net venting from the canyon and a negative flux represents a net re-entry into the canyon. Figure 2.28 shows the vertical profiles of dimensionless advective, turbulent and net fluxes within the canyon with the presence of the tall building. The integral length  $L$  is from  $X/H^*=4.4$  to  $X/H^*=4.9$ . The advective flux  $F_a$  is an order of magnitude greater than the turbulent flux  $F_t$  from the surface level to the top of the tall building. Hence, the plume advective flux dominated the net flux. The removal of plume from the canyon was driven mainly by the advective process.

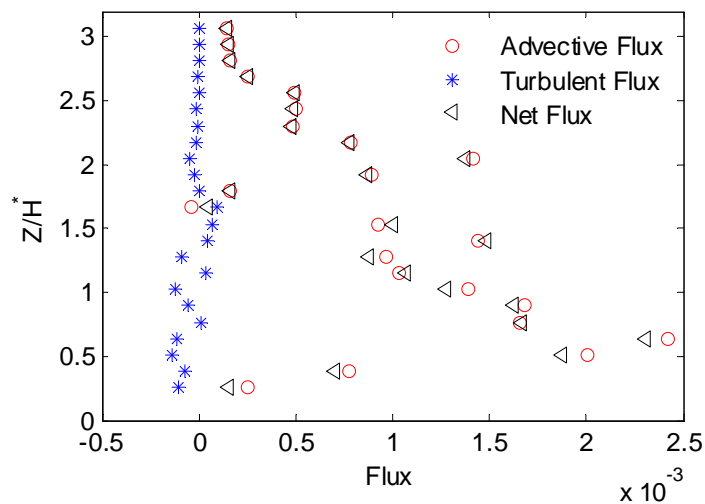


Figure 2.28 Vertical profiles of dimensionless advective, turbulent and net flux components within the canyon with the tall building.

### 2.3.6 Summary

This study is a part of the University of California Transportation Center sponsored project ‘Near source modeling of transportation emission in built environments surrounding major arterials’. A  $480\text{ m} \times 480\text{ m}$  area covering two arterials in downtown Los Angeles was chosen. The major buildings in this area were reproduced in 1:800 scale and vehicular emissions from one arterial were simulated as a line source in water channel. The flow through the building cluster was measured by PIV and the plume dispersion was measured by PLIF. The influence of an individual building on velocity and concentration fields was investigated by comparing cases with and without a tall building.

The recirculation flow was observed upwind tall building and updraft flow in the wake. Concentration measurements show the plume lifted to the top of the tall building by the wake recirculation. The plume within the wakes were mixed rapidly and distributed uniformly. Strong downdrafts at the upwind side of the tall building caused rapid flushing at the street level that resulted in lower concentrations. In the presence of this downdraft, when the tall building was removed, the plume was trapped in the wake of upstream building and the concentration at the ground level was higher. The ratio of the concentration for the case with the tall building to without the tall building was made and it was found that the peak decay regime occurred at the ground level and the enhancement regimes were at the top of the tall building. Regions of high turbulent intensity was observed at the top of a tall building and extended to ground level upwind.

The presence of building cluster resulted in a significant rise of plume compared with open terrain. The presence of the tall building adding  $0.02H^*$  to building height could lead to  $0.34H^*$  increase in vertical plume spread.

The integral time scale of concentration fluctuation  $T_c$  below  $Z/H^* = 1.0$  is much greater than above. That is consistent with Yee's observation in water channel. The longer integral time scale demonstrates that the speed of concentration decay is slow and the plume is persistent in the canyon. Comparing to the case without the tall building, it takes longer for pollutants to escape from the canyon in the case with the tall building. With the tall building, the advective flux of plume dominates the net flux. The removal of plume from the canyon was driven mainly by the advective process.

### 3 FIELD MEASUREMENTS

#### 3.1 Site Description

The classification of building arrangements is not well standardized. Theurer (1999) suggested a classification scheme for wider urban areas in German towns. In Theurer’s study, the building arrangements were divided into 9 types according to the function of buildings for urban air pollution modeling. Stewart and Oke (2009) suggested 9 thermal climate zones for studies of urban heat islands in cities. In our study, five typical building arrangements based on development patterns (Table 3.1) were selected from five southern Californian cities: 1) low density settlement, 1-2 stories; 2) low-rise settlement, 3-4 stories; 3) mid-rise settlement, 10-20 stories; 4) high-rise settlement, more than twenty stories and 5) commercial strip malls with surface parking separating the building and the arterial.

Table 3.1 The classification of building arrangements.






	Low density	Low rise	Mid-rise	High-rise	strip malls
Stories	1 to 2 stories	3 to 5 stories	10 to 20 stories	>20 stories	1 to 2 stories
City	Anaheim	Pasadena	Long Beach	Los Angeles	Huntington Beach
Arterials	Harbor Blvd.	E Colorado Blvd.	E Ocean Blvd.	6 <sup>th</sup> Ave.	Beach Blvd.
Typical buildings					

Figure 3.1 to Figure 3.5 show satellite maps of all five locations with measurement sites. Each location was equipped with one 3D sonic anemometer (CSAT3, Campbell Sci.) for measuring surface mean wind speed, turbulence and virtual air temperature; six DustTraks for measuring ambient fine particle concentration; and three digital cameras (JVC) for recording the traffic flow of the arterials. DustTraks can overestimate gravimetric concentrations (e.g. USDA, 2006) because measurement relies on light scattering. The measurement result is sensitive to the size distribution and nature of the particles. Hence, in this study, we refer to the measured particle concentrations as DustTrak Fine Particles (DTFP). Table A2.1 describes the specifics of each site showing the location of the instruments on the arterial streets. In selecting the measurement locations, an effort was made to avoid direct influence of industrial emissions on observation sites, such as power generation plants, mineral processes, or other industrial activities.

Figure 3.1 presents a residential block (400 m × 350 m) in Anaheim. The main arterial is Harbor Blvd. (in N-S direction), which is a six-lane two-way roadway with annual average daily traffic (ADT) of 28000-33000 vehicles day<sup>-1</sup>. The street width is about 25 m, and it is planted with bushes in between two ways. Lampson Ave. (in E-W direction) is a two-lane two-way roadway with ADT of about 8000-12000 vehicles day<sup>-1</sup>. Most of the buildings in this area are one-storey single-family houses. There are also several groceries and restaurants distributed along both sides of Harbor Blvd. The buildings are relatively uniform in height.

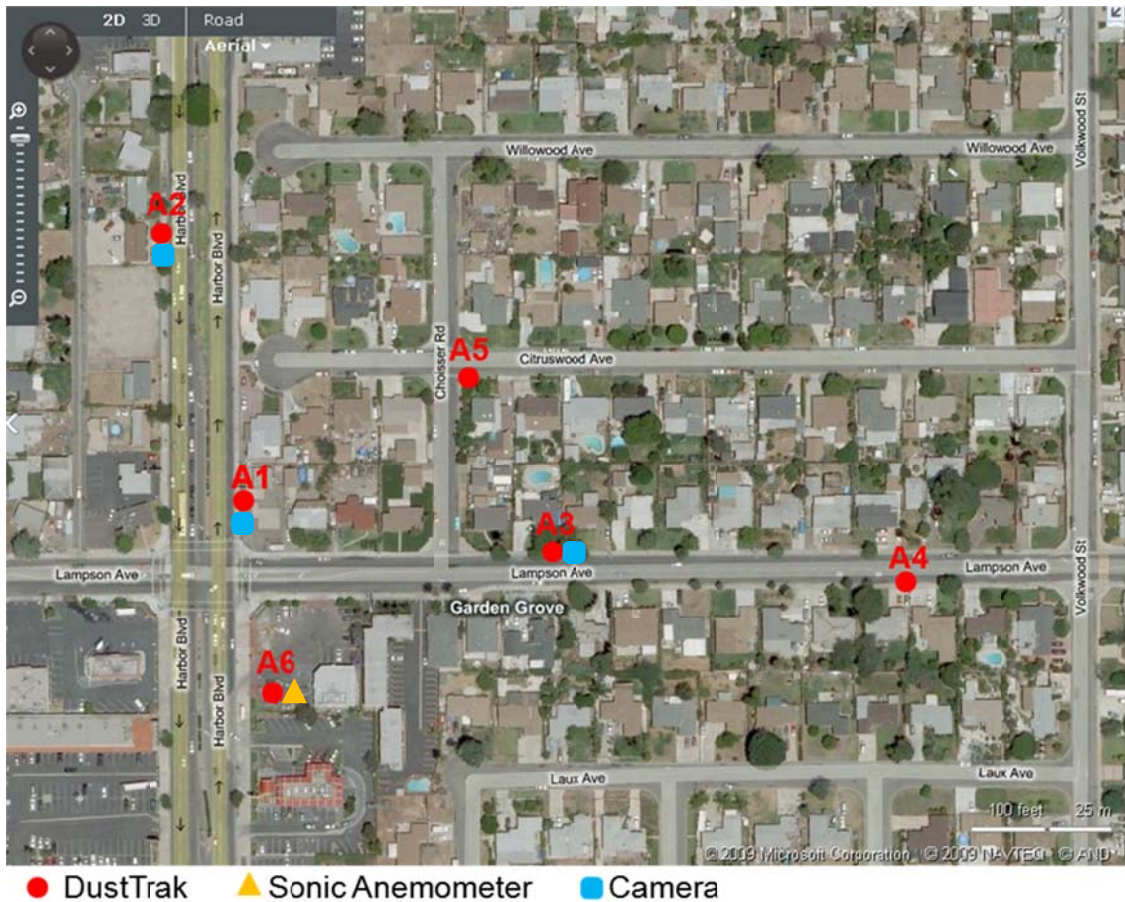


Figure 3.1 Site distribution in low-rise low-dense settlement-Anaheim.

Figure 3.2 presents a commercial area in Pasadena (400 m × 350 m). The approximate heights of the buildings are marked on the map. This area covers apartments, parking lots and garages, a church, a bookstore, restaurants and other commercial buildings. The major W-E arterial in this region is Colorado Blvd., which is a four-lane two-way roadway. The street width is about 15 m. Next arterial is El Molino (N-S), a two-lane one-way roadway. The ADT on Colorado Blvd., El Molino between Colorado Blvd and Playhouse Alley and El Molino between Colorado Blvd and Union

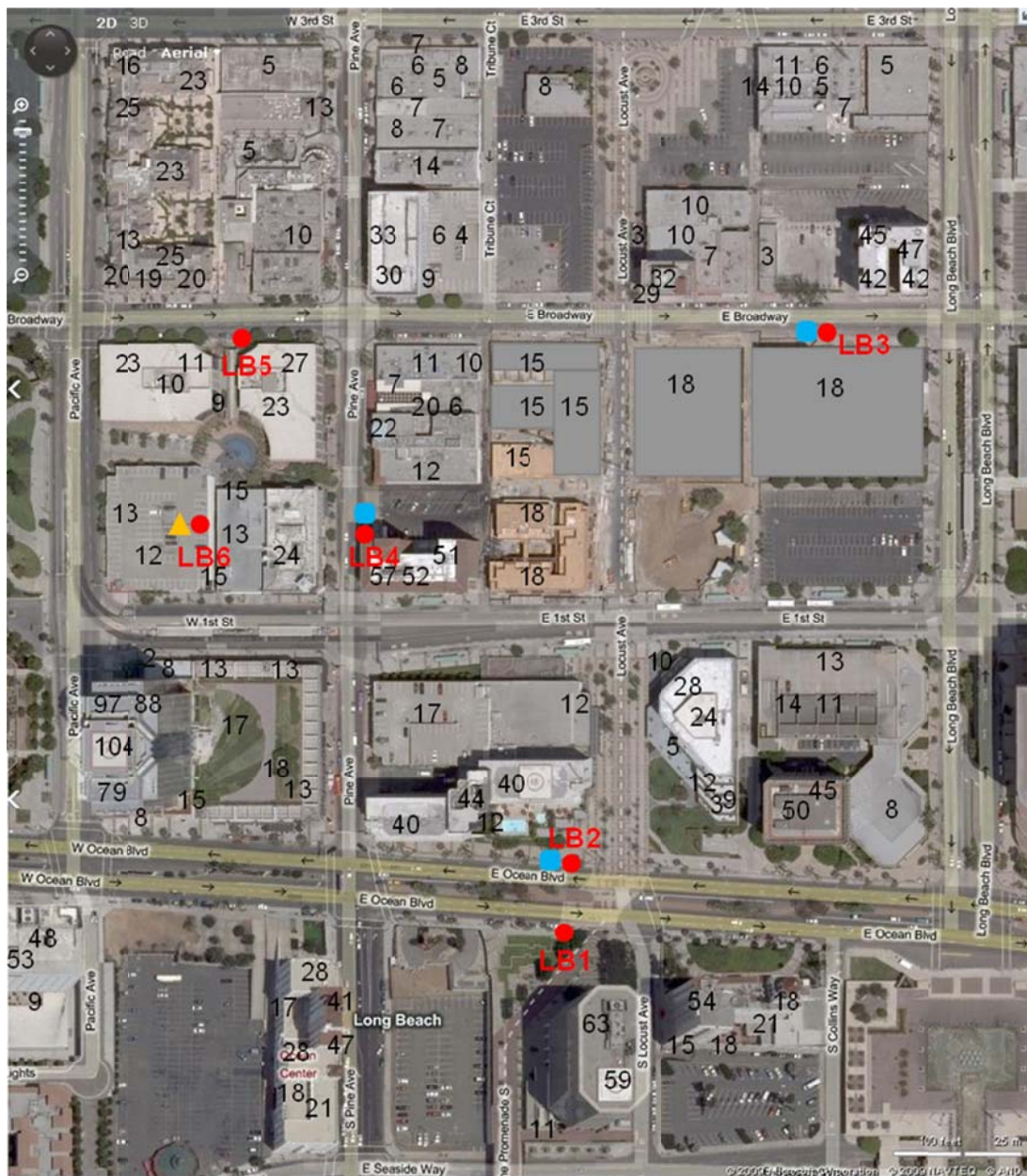


Street are 25842, 6528 and 7973 vehicles day<sup>-1</sup>, respectively (CALTRANS data). The buildings vary in height from 3 to 35 m.



Figure 3.2 Site distribution in low-rise settlement-Pasadena.

Figure 3.3 refers to a 400 m × 600 m area in Long Beach. There are hotels, banks, parking garages, business buildings and apartments in this area. The arterial Ocean Blvd. is a six-lane two-way roadway which is about 22 m wide. Broadway is a three-lane one-way roadway which is about 10 m wide. Traffic counts on Ocean Blvd. and Broadway are 37800 and 14200 vehicles day<sup>-1</sup>, respectively. The buildings vary significantly in height from 5 to 104 m.



● DustTrak    ▲ Sonic Anemometer    ● Camera

Figure 3.3 Site distribution in mid-rise settlement-Long Beach.



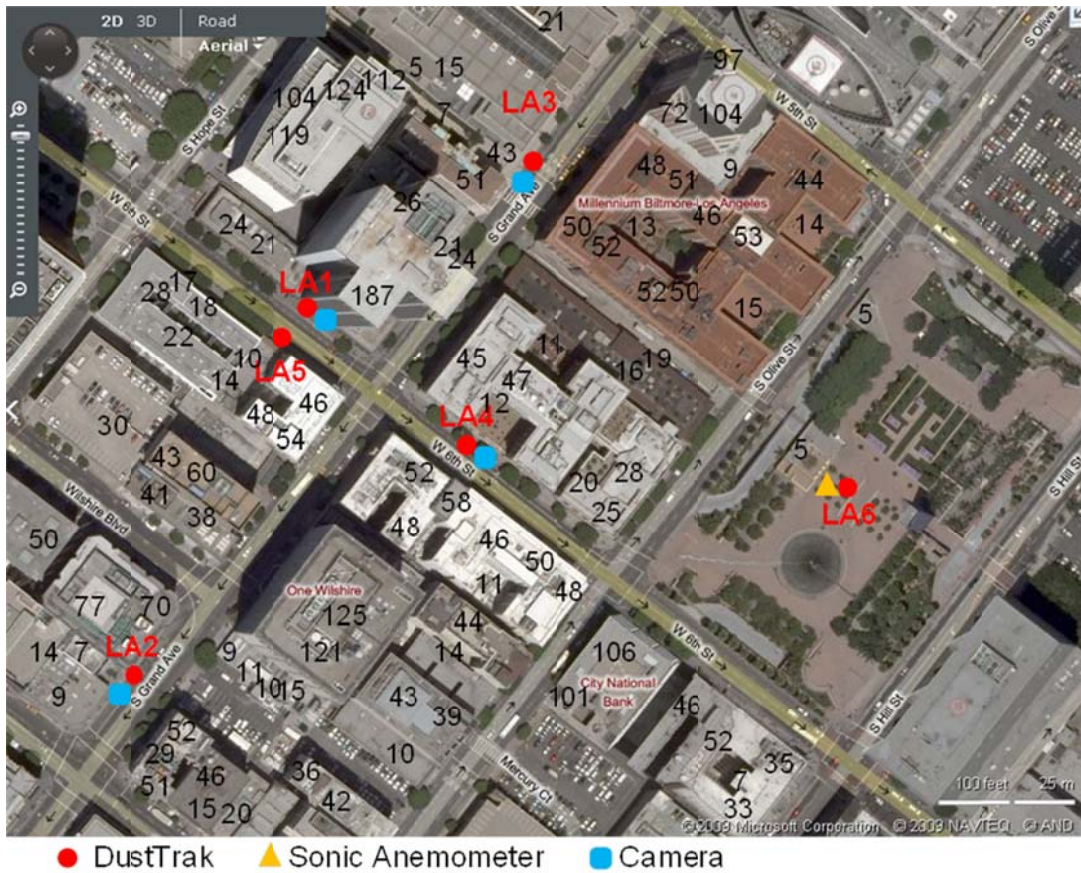


Figure 3.4 Site distribution in high-rise settlement-Los Angeles.

Figure 3.4 refers to a 400 m × 350 m area in downtown Los Angeles covering high-rise buildings and skyscrapers. The heights of the buildings vary from 5 to 187 m. The arterial 6th street is a three-lane one-way roadway. There are two parking lanes on both sides. The street width is about 13 m. The ADT is 20932 vehicles day<sup>-1</sup> on 6<sup>th</sup> street crossing Grand Ave. and 21127 vehicles day<sup>-1</sup> on 6<sup>th</sup> street crossing Olive Ave. The arterial Grand Ave. is also a three-lane, one-way roadway that is 13 m wide. The ADT is 15748 vehicles/day on Grand Ave. crossing 7<sup>th</sup> street and 16399 vehicles day<sup>-1</sup> crossing 5<sup>th</sup> street.



Figure 3.5 Site distribution in strip mall settlement-Huntington Beach.

Figure 3.5 refers to a 400 m × 600 m area in Huntington Beach. The arterial Beach Blvd. is a six-lane two-way roadway; plantings are located in the middle of the two-way

roadway . The street width is about 25 m. The ADT on Beach Blvd. is about 42000-51000 vehicles day<sup>-1</sup>. Garfield is a four-lane two-way roadway that is 15 m wide with an ADT of 12000-16000 vehicles day<sup>-1</sup>.

The displacement height ( $d$ ) and roughness length ( $z_0$ ) were calculated using the Eqs. 2.8 and 2.9. Table 3.2 listed morphological parameters,  $d$  and  $z_0$  for five city areas.

Table 3.2 Morphological and aerodynamic parameters for five city areas

City	H (m)	$\lambda_p$	$\lambda_f$	$z_0$ (m)	$d$ (m)
Anaheim	4	0.26	0.12	< 0.001	2.8
Pasadena	11	0.40	0.09	< 0.001	6.3
Long Beach	22	0.35	0.21	0.05	11.3
Los Angeles	42	0.38	0.41	0.07	23
Huntington Beach	7	0.26	0.06	< 0.001	2.8

### 3.2 Sampling Description

The field measurements were conducted during the weekdays from June 19, 2008 to August 1, 2008. In each city, experiments were conducted for three days. Meteorological measurements usually lasted 12 hours for each day from morning (about 7:00 a.m.) to late afternoon (about 7:00 p.m.). DustTraks covered the morning (7:00 a.m. ~ 9:00 a.m. local time), evening (5:00 p.m. ~ 7:00 p.m. local time) commute and lighter mid-day (11:00 a.m. ~ 1:00 p.m. local time) traffic. DustTraks collected 1 Hz data for 6 hours. All measurement sites, except PA6 (see Figure 3.2) and LB6 (see Figure 3.3),

were at ground level. For the sites near street level, the height of the DustTrak inlets was 2 m above the ground. The sonic anemometer was mounted at the height of 1.4 m at site 6, together with a DustTrak. Both PA6 and LB6 sites were at the roof of a parking garage. PA6 was 16 m above the ground, and LB6 was 24 m above the ground. Hence, meteorological data was collected at the street level for three sites (Huntington Beach, Anaheim and Los Angeles) and on the garage roof level at the other two (Long Beach and Pasadena). The locations of the sonic anemometers for all five cities were chosen to be far away from arterials to avoid being affected by traffic induced turbulence.

DTFP was monitored using DustTrak (Model 8520, TSI Inc., Shoreview, MN) factory-calibrated in January 2008, with a 2.5 $\mu$ m inlet. DustTraks correlate well with gravimetric instruments (Kingham et al., 2006), but rely on light scattering and when factory calibrated with Arizona road dust have been widely reported to overestimate gravimetric concentrations of urban aerosols by approximately factor 3 (Chung et al., 2001). The object of the study was to compare relative differences in simultaneously collected second by second particulate matter concentrations across different spatial locations in an urban environment as a result of built environment patterns, rather than absolute particulate matter concentrations. Hence, the DustTrak was selected because gravimetric methods do not give the precision required at this time scale, and other real time instruments are not suitable as portable instruments in field locations. To ensure comparability between the monitors, a quality assurance procedure was performed during each measurement period. Prior to the measurements, the DustTraks were zero calibrated and the internal clocks synchronized. In addition, in order to minimize between



instrument differences in sensitivity, all six DustTraks were sampled for ten minutes at the same time and place to derive linear adjustment factors.

Vehicle volume was recorded on videotape and manually counted in 20-second time intervals. Vehicles were classified into the following five categories: passenger cars, light trucks (including pickup trucks, SUVs, minivans and vans), other trucks (do not fit into the light trucks category), buses and motorcycles.

### 3.3 Micrometeorology

Fast response wind and temperature fluctuation data were measured by sonic anemometers at 10 Hz. Raw data files were used to calculate mean wind speed, wind direction and turbulent values, such as root mean square of wind velocity fluctuations and temperature fluctuations, friction velocity, vertical flux of momentum and sensible heat flux. The results were then averaged over thirty minutes. Overall mean values for each observational period were taken based on thirty-minute averaged data from 0730 to 1800, where OP is the operation period as shown in Table 3.3,  $\sigma$  is the root mean square (rms) of fluctuation components, subscripts  $u$ ,  $v$  and  $w$  correspond to three wind components (south-north, east-west and vertical direction), subscripts  $T$  and  $\theta$  correspond to temperature and wind direction, respectively and  $\sigma_h = (\sigma_u^2 + \sigma_v^2)^{1/2}$  corresponds to the horizontal wind fluctuation. We also examined the friction velocity  $u_*$  and the temperature scale  $T_*$  in the Monin-Obukhov similarity,  $u_* = \left[ \overline{(u'w')^2} + \overline{(v'w')^2} \right]^{1/4}$  and  $T_* = -\overline{(w'T')} / u_*$ , where the over bar denotes a time average. The variability in the

horizontal wind direction, vertical wind and temperature are presented as nondimensional forms as  $\phi_h = \sigma_h/u_*$ ,  $\phi_w = \sigma_w/u_*$  and  $\phi_T = \sigma_T/T_*$ , respectively. The stability parameter is presented by  $z/L$ , where  $L$  is the Monin-Obkuhov length  $L = -(u_*^2/k)/((g/\bar{T})T_*)$ ; here  $k$  is the von Karman constant 0.4 and  $g$  is the acceleration due to gravity. Since only one sonic anemometer was present in each city; spatial variability is not examined.

### 3.4 Statistical Methods

In this study, the models of the log-transform of one-minute averaged DTFP concentrations were developed on a wide range of variables, including background concentrations ( $C_{bk}$ ), horizontal mean wind speed ( $WS$ ), vertical mean wind speed ( $W$ ) due to tall building updrafts and downdrafts, wind direction ( $WD$ ), momentum flux ( $F_t = (\overline{u'w'^2} + \overline{v'w'^2})^{1/2}$ ), sensible heat flux ( $F_s = \rho C_p \overline{w'T'}$ ), turbulent intensity  $\sigma_w$  and traffic count ( $TC$ ) as follows

$$\begin{aligned} \log(\text{DTFP}) = & C_{bk} + s_2(WS) + s_3(W) + s_4(WD) + s_5(F_t) + s_6(F_s) \\ & + s_7(\sigma_w) + s_8(TC) + \varepsilon \end{aligned} \quad 3.1$$

Eq. 5.2 was applied for building a generalized additive model for each city. For the Los Angeles, Pasadena and Huntington Beach models, DTFP concentrations and traffic variables were site-averaged over five sites (LA1, LA2, LA3, LA4 and LA5 for Los Angeles; PA1, PA2, PA3, PA4 and PA5 for Pasadena; and HB1, HB2, HB3, HB4 and HB5 for Huntington Beach). For each of the Long Beach and Anaheim models, DTFP concentrations and traffic variables were site-averaged over four sites (LB1, LB2, LB3 and LB5 for Long Beach; and AN1, AN2, AN3 and AN4 for Anaheim). According to



the dimensions of the research areas for each city, the time series of site-averaged DTFP concentrations represented the variation of fine particle concentrations in middle-scale (~100-1000 m) (Watson and Chow, 2001).

Background  $PM_{2.5}$  concentration data was obtained from nearby monitoring stations managed by South Coast Air Quality Management District. A map of distribution of the monitoring stations is given in Figure A2.1. The hourly  $PM_{2.5}$  concentrations measured at these stations are derived from Beta Attenuation Monitors (BAM) samplers. Detailed information about the monitoring stations can be found in Boarnet et al.'s paper (2011). Linear interpolation was applied to 1-hour background  $PM_{2.5}$  concentration data to create 1-minute dataset of background concentrations,  $C_{bk}$ . In the Long Beach and Los Angeles models,  $C_{bk}$  represented neighborhood-scale (~1 to 5 km) (Watson, 2001) background concentrations since the distances between DustTrak sites and nearby monitoring stations are 2.4 and 3.3 km respectively. In the Anaheim, Pasadena and Huntington Beach models,  $C_{bk}$  represented urban-scale (~5-50 km) (Watson, 2001) background concentrations since the distances between DustTrak sites and nearby monitoring stations are 6.0, 11.7 and 23.4 km respectively.

In Eq. 3.1, linear regression of background concentrations,  $C_{bk}$ , and nonlinear regressions of other variables were included. Five separated models for five different cities are built using R programming language (R Development Core Team, 2006) with package 'mgcv' version 1.6-1 (Wood, 2006). The package mgcv uses a penalized spline regression approach with automatic smoothing to fit the models. Standard errors on

predictions and credible intervals are derived by a Bayesian approach. More details about mgcv could be found in Wood et al. (2002) and wood (2006).

The squared correlation coefficient  $R^2$  for each model is calculated by mgcv. The relative importance of the predictor variables are also calculated based on Aldrin's method (2005) as follows

$$P_i = 100 \times \frac{\sigma_{-i}^2 - \sigma^2}{\sum_{i=1}^p (\sigma_{-i}^2 - \sigma^2)} \quad 3.2$$

where  $\sigma^2 = \frac{1}{n} \sum_{t=1}^n (y_t - \hat{y}_t)^2$ ,  $\sigma_{-i}^2 = \frac{1}{n} \sum_{t=1}^n (y_t - \hat{y}_{t,-i})^2$ ,  $y_t$  is the observed values at time  $t$ ,

$\hat{y}_t$  is the predicted values at time  $t$  from the model,  $\hat{y}_{t,-i}$  is the predicted values at time  $t$  from a modified model in which smooth function  $s_i$  is based on the average values of variable  $i$  over time instead of on the time series data of variable  $i$ . Thus,  $P_i$  is the proportion of variation representing the relative importance of variable  $i$ . Note that the relative importance is distinguish from the contribution of variables. It indicated the sensitivity of variables in predicting DTFP concentrations.

### 3.5 Results and Discussion

#### 3.5.1 Mean Wind Observation

Although the sites of the sonic anemometer were chosen carefully to prevent the interference of buildings or other obstacles, wind speed and direction data from nearby automated airport weather stations were compared with the sonic anemometer to

determine how representative the sonic anemometer was of local meteorological conditions.

The time series of wind speed, temperature, turbulent flux and sensible heat flux and the wind rose are presented in Figures A2.2 to A2.16 in Appendix II. The mean wind speed and direction were calculated in both vector and scalar forms in Table 3.3. The vector forms indicate that the wind speed and direction components are summed and vector averaged at the end of the averaging time. The scalar forms indicate that simple arithmetic averages of the wind speed and direction are calculated over the averaging time independently. Large differences between vector and scalar wind speeds occurred in site LA6 due to very low wind speed conditions and large rms of wind direction during days 1 to 3. Vector wind speeds were about 40%, 31% and 49% of scalar wind speeds. The corresponding rms of wind directions were 84°, 103° and 80°. The possible reason for the large temporal variability in wind direction could be the location of site LA6, which is at a basin surrounded by tall buildings within the urban canopy. In addition, the speed and direction of the wind from the nearby airport shows that wind speeds around the downtown area were also very low. For all three days in LA, calm conditions in the morning and variable wind direction in the afternoon were observed. As an example, for day 1, 6 out of 11 hours are recorded as calm and 4 out of 11 hours are recorded as variable wind directions. Hence, the regional wind conditions dominated by mesoscale meteorology were also low wind conditions. For OPs 4 to 15, mean wind speeds observed at the nearby airport are also low (in the range of 2 to 3.8 m s<sup>-1</sup>) and mean rms

of wind direction are all greater than  $30^\circ$  (in the range of  $38^\circ$  to  $72^\circ$ ). Hence, it is better to use scalar wind speed and direction in later discussion.

Wind speed and direction in the automated airport weather stations are usually measured with wind vanes and cup anemometers, which are known to have a threshold below which the wind velocity is recorded as zero. Hence, airport data was likely to underestimate at low wind speeds compared to the sonic anemometer data. This explains why the mean scalar wind speed at street level in downtown Los Angeles is comparable to nearby airport data.

Five of six mean wind directions from our observation (OP 5-6 and 10-12) at roof level are consistent with the wind direction expressed by intermediate compass points at the airport. For OP 4, our roof level data shows WSW wind direction, while airport data shows SW. One reason for the difference is probably because zero wind is recorded at the airport from 0700 to 1000, which prevented accurate wind direction presentation. Mean wind directions observed at street level for OP 7-9 and 13-14 are not identical with airport data. For example, 30-min average wind directions at surface level from our observation are mostly from SSW during OP7 and SW during OP8 and 9. Wind direction data at the airport shows that most of the time, especially in the afternoon, steady S wind is observed during these three OPs. Since HB6 is located 12 m east of Beach blvd., traffic-induced flow from western arterials might affect the sonic anemometer measurements. For OP 13-15, the street level wind directions are similar to the airport wind directions.

Table 3.3 Summary of mean wind and turbulent characteristics

OP	Date	Site	Level	Vector	Vector	Scalar	Scalar	Wind	Wind	$T$	$\sigma_h$	$\sigma_w$	$\sigma_T$	$\sigma_\theta$	$u_*$	$-T_*$	$\frac{\sigma_h}{u_*}$	$\frac{\sigma_w}{u_*}$	$-\frac{\sigma_T}{T_*}$	$-z/L$	
				wind	wind	wind	wind	speed <sup>i</sup>	dir <sup>ii</sup>												
				speed	direction	speed	direction														
				m s <sup>-1</sup>	°	m s <sup>-1</sup>	°	m s <sup>-1</sup>		°C	m s <sup>-1</sup>	m s <sup>-1</sup>	°C	°	m s <sup>-1</sup>	°C					m
1	6/19	LA6	street	0.36	196	0.90	190	0.85	W	32	0.95	0.31	0.85	84	0.19	0.55	5.63	1.82	1.75	0.20	
2 <sup>iii</sup>	6/23	LA6	street	0.33	226	1.08	206	0.98	SE	30	1.16	0.35	0.94	103	0.27	0.40	4.74	1.38	2.44	0.09	
3	6/30	LA6	street	0.50	197	1.03	197	1.25	W	27	1.06	0.35	0.90	80	0.28	0.42	3.95	1.29	2.28	0.09	
4	7/2	LB6	roof	1.03	261	1.31	249	2.86	SW	24	1.04	0.56	0.98	60	0.35	0.44	3.13	1.69	3.26	0.52	
5	7/7	LB6	roof	0.71	219	1.15	217	2.32	SW	22	1.12	0.55	0.95	82	0.36	0.55	3.26	1.61	2.12	0.97	
6	7/9	LB6	roof	1.03	204	1.36	202	2.73	SSW	22	1.14	0.38	0.91	67	0.39	0.52	2.98	1.57	2.06	0.83	
7	7/16	HB6	street	1.13	215	1.32	217	3.76	S	25	0.95	0.41	1.00	38	0.29	0.58	4.08	1.56	1.83	0.10	
8 <sup>iv</sup>	7/18	HB6	street	1.03	228	1.22	226	3.35	S	23	0.93	0.40	1.19	38	0.25	0.73	3.41	1.46	1.65	0.20	
9	7/21	HB6	street	1.19	257	1.43	248	3.76	SSW	24	1.10	0.36	1.20	44	0.24	0.87	4.73	1.73	1.43	0.26	
10	7/23	PA6	roof	0.88	160	1.29	155	3.13	SSE	26	1.23	0.48	1.02	67	0.42	0.47	2.93	1.19	2.71	0.35	
11	7/25	PA6	roof	0.64	151	0.97	146	3.40	SE	29	0.97	0.44	0.93	71	0.35	0.33	2.76	1.28	3.93	0.38	
12	7/29	PA6	roof	0.77	183	1.20	173	2.95	S	25	1.17	0.50	1.04	72	0.44	0.44	2.64	1.20	2.67	0.36	

13	7/30	AN6	street	1.00	223	1.36	211	2.32	SW	25	1.12	0.39	0.83	62	0.20	0.60	6.45	2.27	2.44	0.07
14 <sup>v</sup>	7/31	AN6	street	1.16	225	1.47	212	2.06	SW	27	1.07	0.36	1.12	52	0.25	0.65	4.66	1.48	1.76	0.18
15	8/1	AN6	street	1.37	212	1.60	214	2.06	SSW	26	1.09	0.36	1.04	42	0.24	0.61	4.54	1.53	1.84	0.16

i Data were obtained from nearby airport (see <http://www.wunderground.com/history/>). Wind speed were recorded in mph and converted to  $\text{m s}^{-1}$  here. The mean of hourly data from the same IOPs were listed. Calm wind speed is treated as  $0 \text{ m s}^{-1}$ .

ii Data were obtained from nearby airport (see <http://www.wunderground.com/history/>). The mean of hourly data from the same IOPs were listed. Calm wind or Variable wind direction are not counted.

iii Data at 730 was not available

iv Data from 730 to 1030 were not available

v Data at 930 were not available

### 3.5.2 Turbulent Characteristic Observation

As shown in Table 3.3, the friction velocity,  $u_*$ , observed at street level in LA6 is in the range of 0.19 to 0.28  $\text{m s}^{-1}$ , with average of 0.25  $\text{m s}^{-1}$ . For HB6 and AN6, the average  $u_*$  values were 0.26 and 0.23  $\text{m s}^{-1}$ , respectively. During the sampling periods, variation in  $u_*$  at street level from site to site is not significant, although disparities exist within built environments surrounding the three sites; the average mean wind speed observed at LA6 is about 24% lower than that at HB6 and 32% lower than that at AN6. The friction velocity observed at LA6 is equivalent to the friction velocities at HB6 and AN6 due to the increased drag over the downtown Los Angeles area. Similarly, there were no significant differences between  $u_*$  values for LB6 and PA6, both of which were at the roof level. The average  $u_*$  at LB6 and PA6 is 0.37 and 0.40  $\text{m s}^{-1}$ , respectively. However, the variation in  $u_*$  with street and roof levels is obvious: The average  $u_*$  at roof level is about 1.6 times of street level.

The calculated mean stabilities  $z/L$  for all IOPs are between -1 and 0, which suggest that near neutral and slightly unstable conditions were observed at both surface level and roof level. Here, neutral condition refers to  $|z/L| \leq 0.05$  (Roth, 2000). According to the Monin-Obukhov similarity theory, non-dimensional variability of vertical velocity and temperature ( $\phi_w = \sigma_w/u_*$  and  $\phi_T = \sigma_T/T_*$ ) are presented as universal functions of  $z/L$ . Here  $\sigma_w$  can be treated as a combination of a shear-generated component and a buoyancy-

generated component (Qian et al., 2010). Based on Kansas data and other observations, the following accepted relations are given for plant canopy (Kaimal and Finnigan, 1994)

$$\phi_w = \begin{cases} 1.25(1 + 3|z/L|)^{1/3}, & -2 \leq z/L \leq 0 \\ 1.25(1 + 0.2z/L), & 0 \leq z/L \leq 1 \end{cases} \quad 3.3$$

$$\phi_r = \begin{cases} 2(1 + 9.5|z/L|)^{-1/3}, & -2 \leq z/L \leq 0 \\ 2(1 + 0.5z/L)^{-1}, & 0 \leq z/L \leq 1 \end{cases} \quad 3.4$$

Roth (2000) reviewed several field studies carried out in urban areas. The magnitudes of observation height above the ground normalized by the average height of the roughness for all reviewed studies are in the range of 0.7~6.3. Empirical functions are evaluated as follows

$$\phi_w = 1.12(1 + 2.48|z/L|)^{1/3}, \quad -6.2 \leq z/L \leq -0.05$$

$$\phi_r = 3.03(1 + 24.4|z/L|)^{-1/3}, \quad -5 \leq z/L \leq -0.02 \quad 3.5$$

The above similarity relations are fitted to data obtained from field experiments in cities with uniform height buildings that resulted in approximately horizontally homogeneous surface layer. However, for the case of non-uniform buildings data is expected to be scattered wider from the above relations.

In the Monin-Obukhov similarity theory, the displacement height  $d$  is subtracted from the observation height to get  $z$ . However, in our case displacement height can be higher than observation height. For example, the displacement height  $d$  and roughness length  $z_0$  for the Los Angeles area in Figure 3.4 were estimated to be 23 m and 0.07 m (in



Table 3.2). Hence, we used the observation height as  $z$  instead of subtracting  $d$  from the observation height.

Qian et al. (2010) presented the method to estimate  $\sigma_w$  by treating the variable as a combination of a shear-generated component,  $\sigma_{ws}$  and a buoyancy-generated component,  $\sigma_{wc}$  with the following equation:

$$\sigma_w = (\sigma_{ws}^3 + \sigma_{wc}^3)^{1/3} \quad 3.6$$

where the shear component,  $\sigma_{ws}$ , is taken to be

$$\sigma_{ws} = 1.3u_* \quad 3.7$$

and the convective component,  $\sigma_{wc}$ , is

$$\sigma_{wc} = 1.3 \left( \frac{g}{T} \overline{w'T'z} \right)^{1/3} \quad 3.8$$

where  $z$  is the measurement height,  $T$  is the temperature,  $g$  is the acceleration due to gravity. Eq. 3.8 can be rearranged to obtain

$$\sigma_w = 1.3u_* (1 + 2.5|z/L|)^{1/3} \quad 3.9$$

Eq. 3.9 is very similar to Roth's equation presented in Eq. 3.5. Figure 3.6 shows the correlation between  $\sigma_w$  calculated from Eq. 3.6 thru 3.9 and measured  $\sigma_w$ .

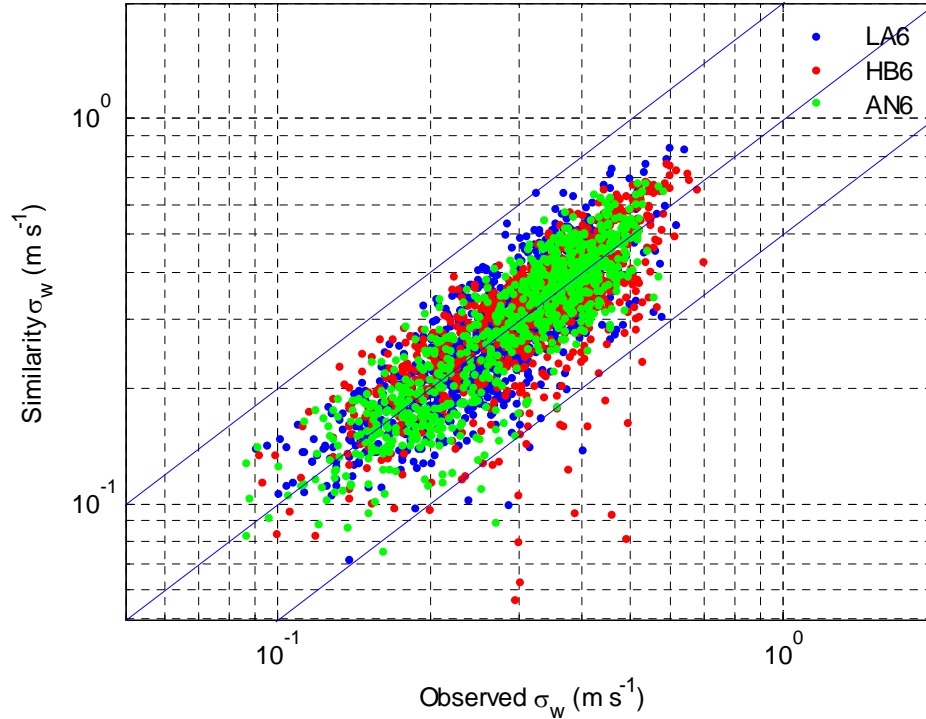


Figure 3.6 Comparison of  $\sigma_w$  calculated from the observed  $u_*$  and  $\overline{w'T'}$  using Eqs. 3.6 thru 3.9 with the observations for the sites LA6, HB6 and AN6.

Figure 3.7 shows  $\phi_w$  observed at the sites HB6, LA6 and AN6 as a function of  $z/L$ . The observed data follow the 1/3 relationship given by Qian et al. (2010), Roth (2000) or Kaimal and Finnigan's empirical functions (1994). The squared correlation coefficients,  $R^2$ , are 0.70 for both Qian and Roth's function and 0.73 between observed data and Kaimal and Finnigan's function. At low  $z/L$  (slightly unstable conditions), observed data appears to be shifted to the right from two empirical functions. Kaimal and Finnigan's equation predicts constant  $\phi_w$  at near neutral conditions; however, there is not enough data from our observations to show the trend at near neutral conditions ( $|z/L| \leq 0.05$ ).

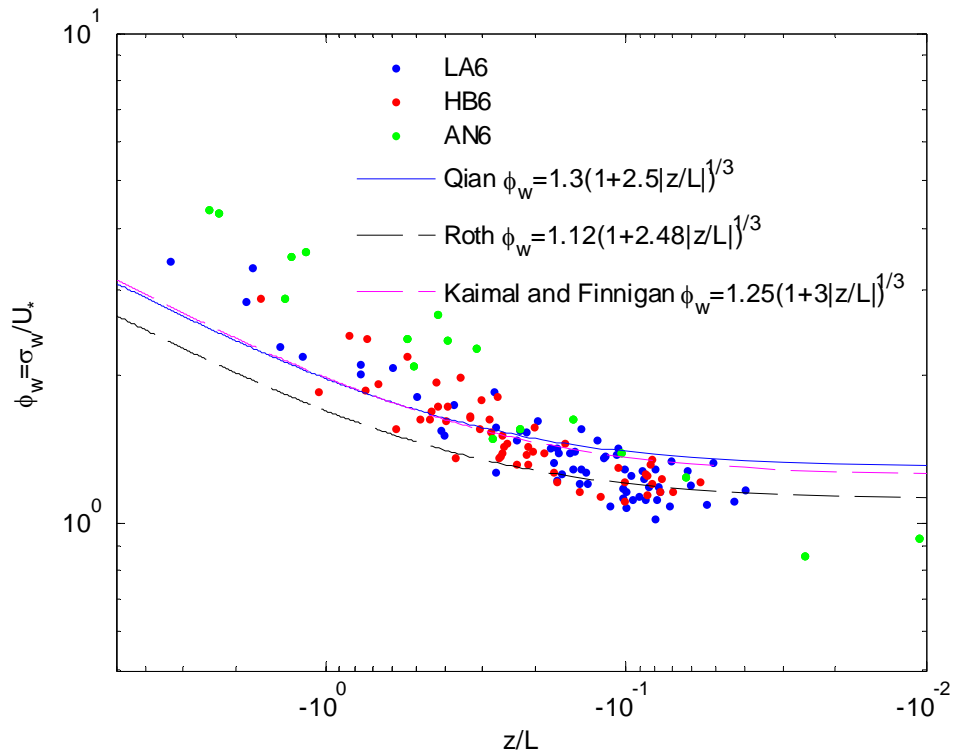


Figure 3.7 Non-dimensional variability in  $w$ ,  $\phi_w$  as a function of  $z/L$ . The scattered dots refer to observations at street level, the solid line refers to an empirical fit by Qian et al. (2010) a fitting curve on the observed data, the dash lines is an empirical fit on urban observations by Roth (1999) and the dotted line is an empirical fit on Kansas data by Kaimal and Finnigan (1994).

Figure 3.8 shows  $\phi_T$  observed at sites HB6, LA6 and AN6 as a function of  $z/L$ . Observed data are more consistent with Roth's equation than with other relationships, except at near neutral conditions observed data continues to increase. The  $R^2$  are 0.48 between observed data and Roth's function and 0.37 between observed data and Kaimal and Finnigan's function.

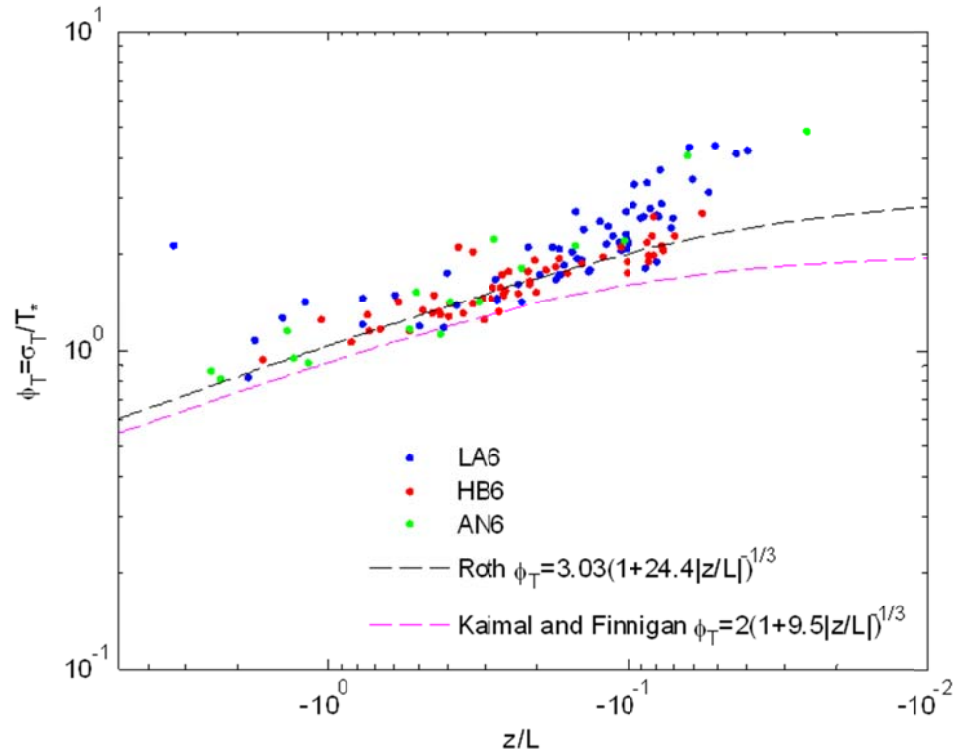


Figure 3.8 Non-dimensional variability in  $T$ ,  $\phi_T$  as a function of  $z/L$ . The scattered dots refer to observations at street level, the dash lines is an empirical fit on urban observations by Roth (1999) and the dotted line is an empirical fit on Kansas data by Kaimal and Finnigan (1994).

Although observations within the urban canopy have limits (i.e. the displacement height is higher than the measurement height and it is hard to find a representative place to mount instrumentation), our data still shows a reasonable agreement with proposed parameterizations as long as the measurements are from a relatively open area within the urban canopy. The agreement with roof level data was not good. Since  $\phi_w$  and  $\phi_T$  at sites LB6 and PA6 are very scattered we do not present them here.

□

### 3.5.3 Generalized Additive Model Results

The squared correlation coefficients  $R^2$  and the relative importance of each variable in each GAM model are listed in Table 3.4. The coefficients  $R^2$  for five models were in the range of 0.61 ~ 0.88. Among five models, the Anaheim, Long Beach and Los Angeles models had  $R^2$  greater than 0.8. The relative importance of urban- or neighborhood-scale background concentrations ( $C_{bk}$ ) in above three models were 91.2, 93.3 and 92.5%, respectively. The Pasadena and Huntington Beach models had lower  $R^2$  values, which were 0.62 and 0.61 respectively. The values for relative importance of urban-scale concentrations were 89.6 and 37.0%. Compared to other variables, background concentrations were the most important variables in all five models. Note that the calculation of relative importance in Eq. 3.2 implied the weighting of the variables in determining the fluctuation of the model prediction. Hence, we concluded that background concentration was the most correlated variable with the middle-scale fine particle concentrations. This indicated that urban mixing dominated the variation of roadside particle concentrations regardless of urban geometry. The distance from local sites to nearby monitoring stations affected model performance when neighborhood- or urban-scale concentrations were used to predict middle-scale concentrations by GAM. The  $R^2$  of five models showed that neighborhood-scale concentrations were more suitable to model middle-scale concentrations than urban-scale concentrations.

Table 3.4  $R^2$  of GAM and Relative importance of each variable for five models. Note:  $C_{bk}$ -background concentrations;  $WS$ : horizontal mean wind speed;  $W$ -vertical mean wind speed;  $WD$ -wind direction;  $F_t$ -momentum flux;  $F_s$ -sensible heat flux;  $\sigma_w$ -vertical velocity fluctuation;  $TC$ -traffic count.

Model	$R^2$	Relative Importance %							
		$C_{bk}$	$WS$	$W$	$WD$	$F_t$	$F_s$	$\sigma_w$	$TC$
Anaheim	0.84	91.2	1.1	1.2	4.8	0.4	0.9	0.3	0.1
Pasadena	0.62	89.6	0.0	0.1	4.3	1.2	2.4	0.1	2.2
Long Beach	0.88	93.3	0.7	0.2	2.2	0.5	1.8	0.7	0.5
Los Angeles	0.83	92.5	0.2	1.5	1.1	0.0	0.6	3.8	0.3
Huntington Beach	0.61	37.0	6.4	12.2	5.0	3.6	23.6	5.6	6.7

Figure 3.9 shows the estimated effects of wind direction on DTFP concentrations for the Anaheim and Long Beach models. For the Anaheim model, DTFP concentrations increased when the wind direction were in the range from  $300^\circ$  to  $360^\circ$  and from  $0^\circ$  to  $30^\circ$ . The high DTFP concentrations were probably associated with the emissions from a highway road located in the north direction of the observation areas in Anaheim. For the Long Beach model, a slightly decrease of DTFP concentrations appeared when wind direction are close to south (from  $160^\circ$  to  $200^\circ$ ) which is the direction of sea breeze comes from. The clean air from ocean flushed the observation areas and resulted in the reduction of pollution.

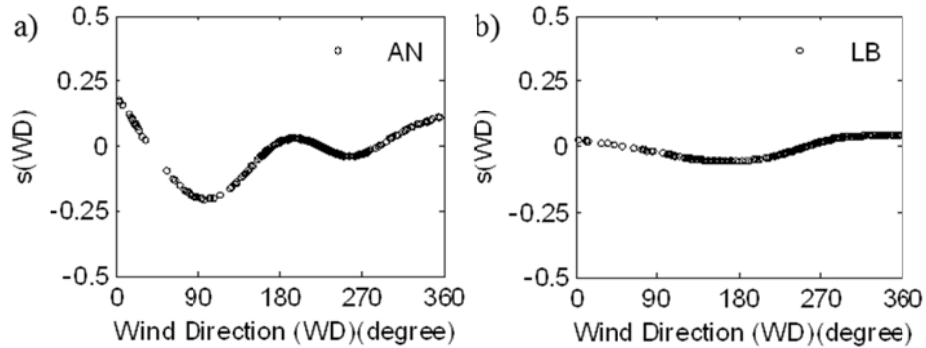


Figure 3.9 Estimated effects of wind direction ( $WD$ ) on DTFP concentrations for the Anaheim (AN) and Long Beach (LB) models

Figure 3.10 indicated the estimated effects of horizontal mean wind speed on DTFP concentrations for the Long Beach and Huntington Beach Models. For the Long Beach model, the meteorological data was obtained at roof level. We can see that when mean wind speed was in the range from 0 to  $1.2 \text{ m s}^{-1}$ , mean wind speed has no effect on eliminating pollutions. However, when mean wind speed was greater than  $1.2 \text{ m s}^{-1}$ , the increasing wind speed resulted in the reduction of pollutions. For the Huntington Beach model, this cutoff value is a little smaller than  $1.2 \text{ m s}^{-1}$ . That is because that meteorological tower was set up at street level.

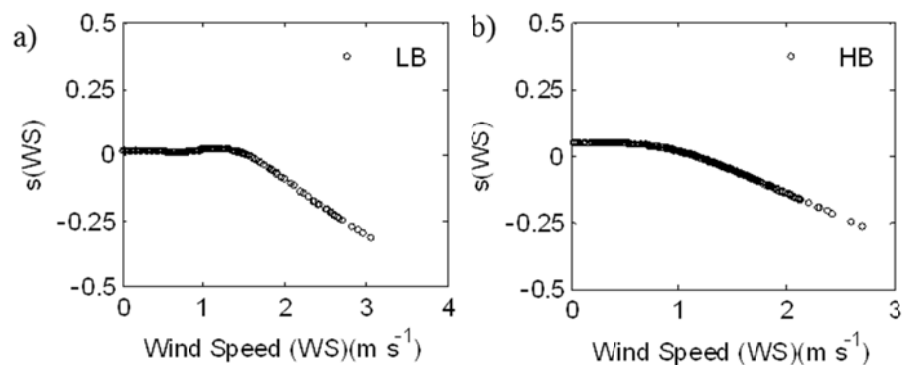


Figure 3.10 Estimated effects of horizontal mean wind speed ( $WS$ ) on DTFP concentrations for the Long Beach (LB) and Huntington Beach (LB) models

Figure 3.11 shows the estimated effects of vertical velocity fluctuation and vertical mean wind speed on DTFP concentrations for the Los Angeles model. It is obvious that the increase of both variables caused elimination of pollutions. As we know, the observation areas in Los Angeles have the most street-canyon-like configurations among all five areas. The role of vertical velocity fluctuation  $\sigma_w$  from GAM results is consistent with the simple analytical model (Eq. 1.23 in section 1.1.6) which was derived for street canyons. We also found that vertical mean wind speed had effects on DTFP for Los Angeles as shown in Figure 3.11b. This can be explained by the downdraft flow bringing the fresh air into the street level because of the presence of high-rise buildings.

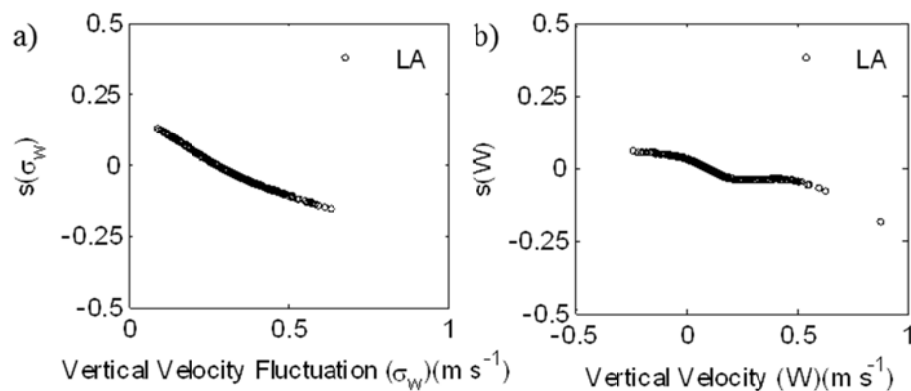


Figure 3.11 Estimated effects of vertical velocity fluctuation ( $\sigma_w$ ) and vertical mean wind speed ( $W$ ) on DTFP concentrations for the Los Angeles (LA) model.

Figure 3.12 shows the estimated effects of traffic counts on DTFP concentrations for the Los Angeles and Huntington Beach models. The difference between these two models was that the observation areas in Huntington Beach had much heavier traffic situations than that in Los Angeles. As we can see, the traffic counts in the Huntington Beach model was about 4-5 times of the Los Angeles model. Although there were no



records of vehicle speeds in these two areas during the observation periods, the vehicles were driven much faster for the Huntington Beach areas than the Los Angeles areas. Hence, traffic induced turbulence caused by passing vehicles in the Huntington Beach areas can reduce pollutions. However, for the Los Angeles model, increasing traffic counts slightly increased DTFP concentrations.

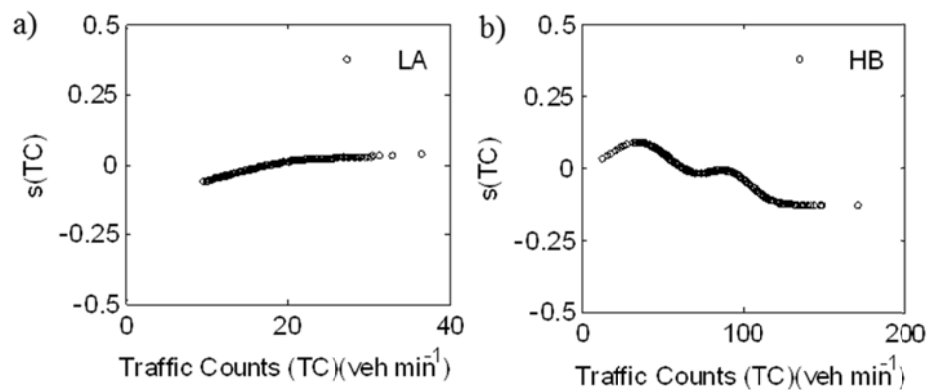


Figure 3.12 Estimated effects of traffic counts (TC) on DTFP concentrations for a) the Los Angeles (LA) and b) the Huntington Beach models.

### 3.5.4 Fine Particle Concentrations on Leeward Side and Windward Side

Figure 3.13 shows time series of Fine Particle concentration with 1 Hz sampling frequency measured in Los Angeles from two opposite sites. Black lines represent site LA1 which is located at the windward side on 6<sup>th</sup> street and red lines represent site LA5 which is located at the leeward side on the same street facing LA1. Fine Particle concentration peaks always appeared at leeward side. The performance of concentrations at windward side during the morning, noon and afternoon periods was different. In the morning (Figure 3.13a), concentration valley values appeared at windward side corresponding to the arising of concentration peaks at leeward side. At noon and in the

afternoon, the fluctuations of concentration at windward side were not as obvious as that in the morning. At this location, buildings height at windward side (the highest one is 188 m) was much higher than that at leeward side (the highest one is 54 m).

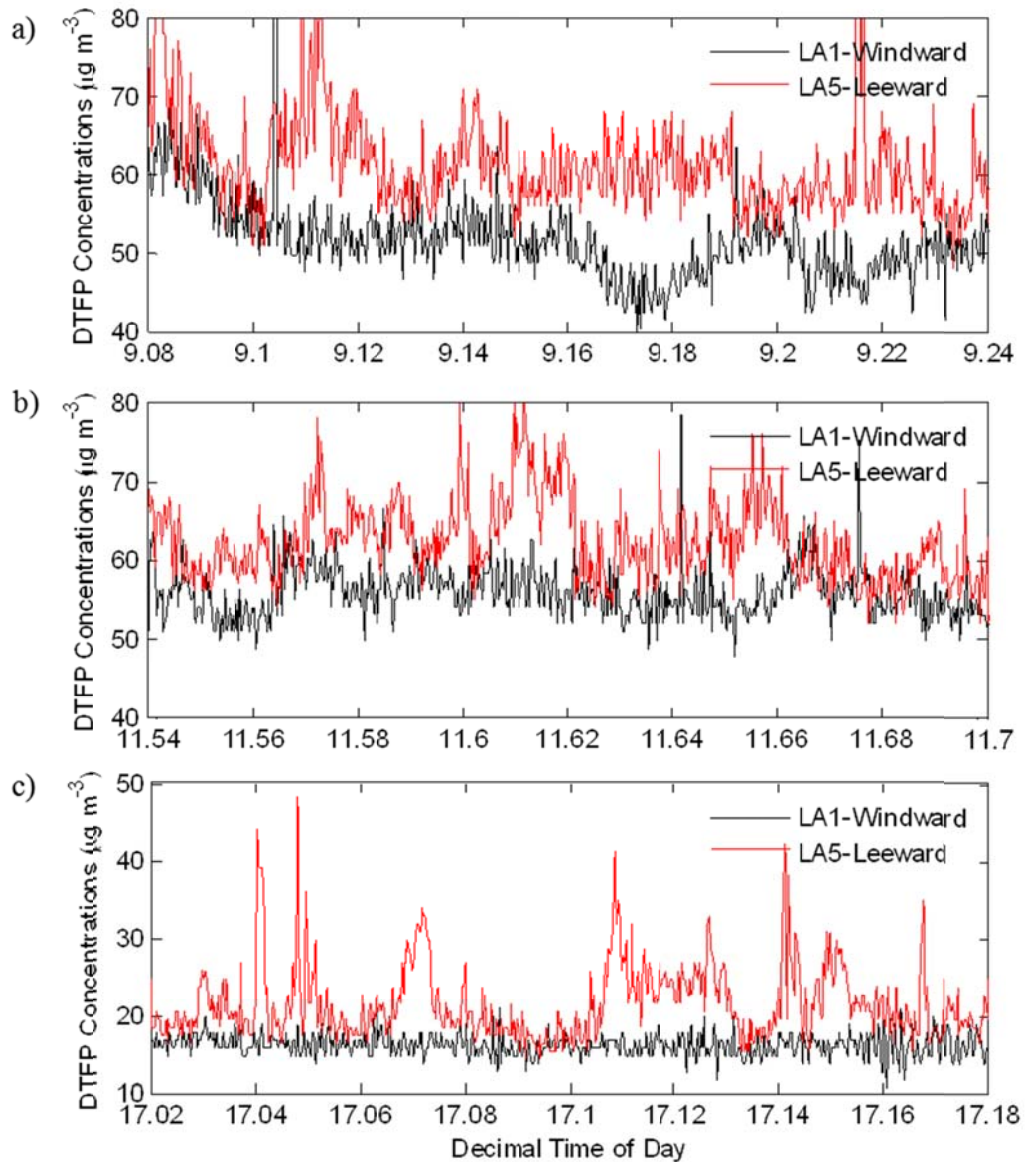


Figure 3.13 Time series (~ 10 minutes) of PM<sub>2.5</sub> concentration at site1 (windward side) and site 5 (leeward side) in Los Angeles during a) morning, b) noon and c) afternoon. (Note: data are collected on 06/19/2008 in a) and b), 06/30/2008 in c).)

### 3.5.5 Analytical method

Figure 3.13 shows the inverse trends of variation of DTFP concentrations at the LA1 site and LA5 site. The LA1 site was located at the windward side and LA5 site was located at the leeward side of the 6<sup>th</sup> street as shown in Figure 3.4. Those inverse trends indicated the evidence that a typical street canyon configuration exists at the 6<sup>th</sup> street. Also the estimated effects of vertical velocity fluctuation,  $\sigma_w$ , on DTFP concentrations show that the increasing  $\sigma_w$  eliminated pollutions from the street level in Figure 3.11. Hence, it is suitable to apply a simple analytical model (Eq. 1.23 in section 1.1.6) to predict DTFP concentrations for the leeward side site LA5. Based on Eq. 1.23, the direct contribution of traffic emissions are proportional to  $Q/(W \cdot \sigma_w)$ . The emission rate  $Q = b \cdot TC \cdot 10^6$ , where  $b$  is the emission factor from traffic emissions,  $TC$  is the traffic counts. We built a simple analytical model as

$$C_{DTFP} = a \cdot \left( C_{bk} + \sqrt{\frac{2}{\pi}} \frac{b \cdot TC \cdot 10^6}{W \cdot \sigma_w} \right) + c \quad 3.10$$

in which background concentrations are considered.

With the least square fitting of data set for LA5, parameters  $a$ ,  $b$  and  $c$  were calculated as 2.18, 0.07 and -27.24, respectively. Since the meaning of parameter  $b$  is the emission factor from traffic emissions, we get the fine particle emission factor of 0.021 g vehicle<sup>-1</sup> km<sup>-1</sup>. This value is comparable to the on-road PM<sub>2.5</sub> emission factors ranged from 0.016 ( $\pm 0.007$ ) to 0.115 ( $\pm 0.019$ ) g vehicle<sup>-1</sup> km<sup>-1</sup> in the Sepulveda Tunnel, Los Angeles for the mixed light-duty and heavy-duty fleet (Gillies et al., 2001). The

parameter  $a$  in Eq. 5.11 indicated the factor between DustTraks and BAM samplers and  $c$  indicated the intercept. Chung (2001) conducted the comparison of real-time instruments used to monitor airborne particulate matter. It was found that a DustTrak aerosol sampler overestimated  $PM_{10}$  concentrations by a factor of  $\sim 3$  compared to BAM and the intercept was  $-18.2$ . However, no report for comparison between  $PM_{2.5}$  DustTrak and BAM samplers was found.

Figure 3.14a compares estimates of fine particulate concentrations for the LA5 site corresponding to the measured DTFP concentrations. The  $R^2$  between predicted concentrations and observed concentrations is 0.76. Figure 5.14b shows the contributions from traffic emissions corresponding to the predicted fine particulate concentrations. The median value for road contributions was  $3.4 \mu\text{g m}^{-3}$ . Compared to the median value for predicted concentrations, the percentage is 7.4%.

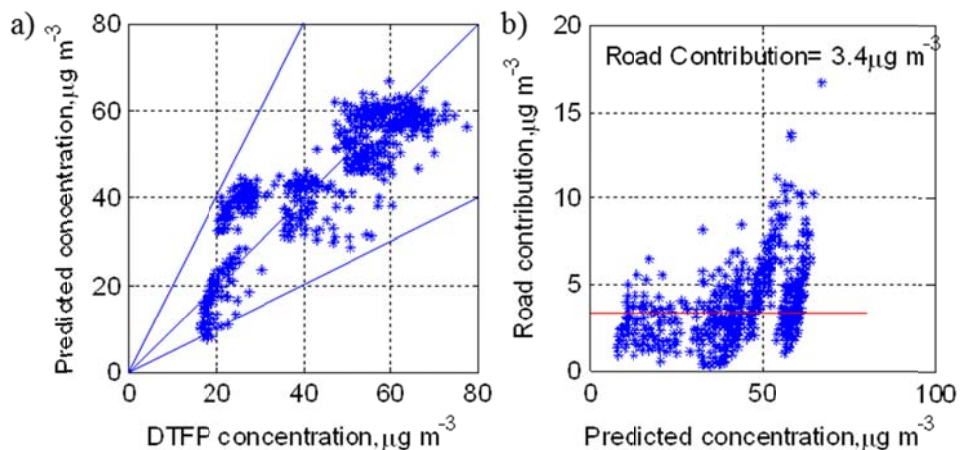


Figure 3.14 a) Comparison of predicted concentrations with measured DTFP concentration and b) comparison of road contribution with predicted concentrations calculated by Eq. 5.11.

### 3.6 Summary

The results presented here are based on analysis of field experiments conducted in 5 Southern Californian cities. Main highlights of the study are:

Large differences between vector and scalar wind speeds occurred in Los Angeles due to the very low wind speed conditions and large fluctuations of wind direction during the observation periods. The reason for the large temporal variability in wind direction in Los Angeles is because the measurement locations were located deep within the urban canopy and surrounded by tall buildings. In the same way, wind directions observed at street level in Huntington Beach and Anaheim were in agreement with the airport data. Wind directions observed at roof level in Long Beach and Pasadena were also consistent with nearby airport data. With this in mind, for air pollution modeling needs one can rely on routine wind measurements outside of the city, unless the interest is in pollution distribution within deep urban canyons (e.g.  $\lambda_p=0.38$  and  $\lambda_f=0.41$  for Los Angeles). For deep urban canyons local measurements or comprehensive flow modeling are needed.

The calculated mean stabilities,  $z/L$ , for all OPs are between -1 and 0, signifying near neutral and slightly unstable conditions at both surface level and roof level. The friction velocity,  $u_*$ , observed at street level did not vary significantly. In Los Angeles, Huntington Beach and Anaheim the averaged  $u_*$  was 0.25, 0.26 and 0.23 m s<sup>-1</sup>, respectively. However, the average mean wind speeds observed in Los Angeles is about 24% lower than that in Huntington Beach and 32% lower than that in Anaheim which gives normalized frictional velocity,  $u_*/U$  of 1.91 for Los Angeles, 0.38 for Huntington

Beach and 0.46 for Anaheim. This suggests that  $u_*$  is significantly affected by surrounding building geometry. There is no significant difference between  $u_*$  values for Long Beach and Pasadena where data were collected at roof level.

The existing parameterizations for non-dimensional variability of vertical velocity ( $\phi_w$ ) and temperature ( $\phi_T$ ) as functions of  $z/L$  show that the observation data at surface level within the urban canopy has a reasonable agreement with the Monin-Obukhov similarity theory. The estimated  $\sigma_w$  from a shear-generated component and a buoyancy-generated component are correlated to measured  $\sigma_w$ . The coefficient of determination ( $R^2$ ) shows that the data for  $\phi_w$  from three sites (Los Angeles, Huntington Beach and Anaheim) has better correlations with Qian (2010) and Roth ( $R^2=0.70$  for both) or Kaimal and Finnigan ( $R^2=0.73$ ) relationship. At low  $z/L$  (slightly unstable conditions), observed data is higher than predicted by two empirical functions. Observed data of  $\phi_T$  are more consistent with Roth's Eq. ( $R^2=0.48$ ) than Kaimal and Finnigan's ( $R^2=0.37$ ). From this we see that all data in general follows 1/3 law, however, involved constants are function of surrounding geometry.

The generalized additive models of the log-transform of one-minute averaged DTFP concentrations were developed on a wide range of variables, including background concentrations ( $C_{bk}$ ), horizontal mean wind speed ( $WS$ ), vertical mean wind speed ( $W$ ) due to tall building updrafts and downdrafts, wind direction ( $WD$ ), momentum flux ( $F_t = \left( \overline{u'w'^2} + \overline{v'w'^2} \right)^{1/2}$ ), sensible heat flux ( $F_s = \rho C_p \overline{w'T}$ ), turbulent intensity  $\sigma_w$  and traffic count ( $TC$ ) for five cities. The coefficients  $R^2$  for five models were in the range of

0.61 ~ 0.88. The relative importance of urban- or neighborhood-scale background concentrations ( $C_{bk}$ ) in the Anaheim, Long Beach and Los Angeles models were 91.2, 93.3 and 92.5%, respectively. The neighborhood-scale concentration was the most correlated variable with the middle-scale fine particle concentrations. This indicated that turbulence mixing in urban areas dominated the variation of roadside particle concentrations regardless of urban morphometry, which is consistent with descriptive statistics given by Boarnet et al (2011). The distance from local sites to nearby monitoring stations affected model performance when neighborhood- or urban-scale concentrations were used to predict middle-scale concentrations by GAM.

GAM results show that wind direction has effects on DTFP concentrations for Anaheim and Long Beach models. The Long Beach model shows that when mean wind speed was in the range from 0 to  $1.2 \text{ m s}^{-1}$ , mean wind speed has no effect on eliminating pollutions. When mean wind speed was greater than  $1.2 \text{ m s}^{-1}$ , the increasing wind speed resulted in the reduction of pollutions. The cutoff value is a little smaller at street level for the Huntington Beach model. The Los Angeles model shows that increasing vertical velocity fluctuation and vertical mean wind speed reduced DTFP concentrations at street level within the street-canyon-like configurations. The Huntington Beach model shows that a large number of traffic counts have effect on reducing DTFP concentrations. This is probably caused by large traffic induced turbulence when vehicle speeds are very high. The effects of variables other than background concentrations on DTFP concentrations vary with building morphometry.

The LA5 site represented a typical leeward side site within a street canyon. A simple analytical model was built to predict fine particulate concentrations for the LA5 site. The  $R^2$  between predicted concentrations and observed concentrations was 0.76. The estimated fine particle emission factor from Eq. 5.11 was  $0.021 \text{ g vehicle}^{-1}\cdot\text{km}^{-1}$ . The contribution from traffic emissions corresponding to the predicted fine particulate concentrations was  $3.4 \mu\text{g m}^{-3}$ , which was 7.4% of the predicted concentrations.

#### **4 CONCLUSIONS**

The studies in this dissertation are motivated by the need to investigate the flow and dispersion of pollutants in a wider variety of streets in urban areas. The emphasis was on the fine particle matters from traffic emissions in built environments in five Southern Californian cities.

To study the flow within a modeled simple urban setup, Particle Image Velocimetry (PIV) was applied for comprehensive flow measurements. A novel flow feature was lateral channeling, observed and quantitatively measured, within regular  $3 \times 3$  and  $5 \times 5$  arrays of cubes. A sideways mean outflow from the building array is observed behind the first row of buildings followed by the mean inflow in the lee of all succeeding rows of buildings. When the central building in a  $3 \times 3$  array is replaced by a building of double height, due to the strong downdraft caused by this tall building, the lateral outflow becomes significantly more intense. When the central building in a  $5 \times 5$  array is replaced by a building of double height, the building downdraft blocks the lateral inflow to the array. This is the first time that such detailed measurements are available for a mock urban array of finite size – a real three-dimensional case. The pressure analysis



suggested that low pressure in the wake region drew the fluid through the array, which led to formation of the strongest lateral inflow in front of the last row of buildings. As rows are further from the wake region inflow is less intense due to decreased pressure gradient.

A mock urban area with complex building configurations and traffic arterials was built to model flow and dispersion in downtown Los Angeles areas as a development from studies of regular arrays. The purpose is to investigate the influence of an individual building on velocity and concentration fields. The presence of the tall building adding  $0.02H^*$  to building height could lead to  $0.34H^*$  increase in vertical plume spread. The integral time scale of concentration fluctuations  $T_c$  are larger below the characteristic length  $H^*$  than above it. These trends are consistent with Yee's experiments in which vertical profiles of  $T_c$  at different downstream positions in the uniform height array plume were observed in a water channel. The longer integral time scale demonstrates that the speed of concentration decay is slow and the plume is persistent in the canyon because of the presence of obstacle array. Comparing to the case without the tall building, it takes longer for pollutants to escape from the canyon in the case with the tall building. With the tall building, the advective flux of plume dominates the net flux. The removal of plume from the canyon was driven mainly by the advective process.

In order to study the influence of urban morphometry on flow and dispersion of vehicular fine particulate matter emissions, field measurements were performed in major arterials in five Southern Californian cities with different building geometries in the summer of 2008.

Comparing meteorological measurements at street level with the airport data, we concluded that for air pollution modeling needs one can rely on routine wind measurements outside of the city, unless the interest is in pollution distribution within deep urban canyons (e.g.  $\lambda_p = 0.38$  and  $\lambda_f = 0.41$  for Los Angeles). For deep urban canyons local measurements or comprehensive flow modeling are needed.

The existing parameterizations for non-dimensional variability of vertical velocity ( $\phi_w$ ) and temperature ( $\phi_T$ ) as functions of  $z/L$  show that the observation data at surface level within the urban canopy has a reasonable agreement with the Monin-Obukhov similarity theory. The combination of shear-generated  $\sigma_{ws}$  and buoyancy-generated  $\sigma_{wc}$  predicted  $\sigma_w$ , which is consistent with the measured  $\sigma_w$ .

GAMs can be used to investigate the effects of background concentrations, meteorological and traffic-related variables on fine particle concentrations. GAM results for all five cities indicated that the urban- or neighborhood-scale concentration was the most correlated variable with the middle-scale fine particle concentrations. This indicated that turbulence mixing in urban areas dominated the variation of roadside particle concentrations regardless of urban morphometry.

The relationship between fine particle concentrations and other variables, such as mean wind speed, vertical velocity fluctuation and traffic counts are not linear. At street level, when wind speed is greater than a cutoff wind speed, increasing wind speed eliminates pollution from the street. For the Long Beach model, this cutoff wind speed is  $1.2 \text{ m s}^{-1}$ . The Los Angeles model shows that the increasing vertical velocity fluctuation

and vertical mean wind speed reduced DTFP concentrations at street level. The Huntington Beach model shows that a large number of traffic counts have effect on reducing DTFP concentrations. This is probably caused by large traffic induced turbulence when vehicle speeds are very high.

The emission factors from traffic emissions can be estimated with the known urban- or neighborhood- scale concentrations, traffic counts, street width and urban turbulence level (such as vertical velocity fluctuation measured at an relative open area within urban areas). The estimated fine particle emission factor was  $0.021 \text{ g vehicle}^{-1} \cdot \text{km}^{-1}$  in the Los Angeles area. The contribution from traffic emissions was  $3.4 \mu\text{g m}^{-3}$ , which was 7.4% of the predicted fine particle concentrations.

## REFERENCE

- Adrian, R.J., 1988. Review of particle image velocimetry research. In: The symposium on optical methods in flow and particle diagnostics, 6th International Congress on Applications of Lasers and Electro-Optics. Vol. 9, pp. 317-319, San Diego, CA: Optics and Lasers in Engineering.
- Adrian, R.J., 1991. Particle-imaging techniques for experimental fluid-mechanics, *Ann. Rev. Fluid Mech.* 23, 261-304.
- Adrian, R.J., 1997. Dynamic ranges of velocity and spatial resolution of particle image velocimetry, *Meas. Sci. & Tech.* 8(12), 1393-1398.
- Ahmad, K., Khare, M., Chaudhry, K. K., 2005. Wind tunnel simulation studies on dispersion at urban street canyons and intersections-a review. *Journal of Wind Engineering and Industrial Aerodynamics.* 93, 697-717.
- Aldrin, M., Haff, I. H., 2005. Generalised additive modelling of air pollution, traffic volume and meteorology. *Atmos. Environ.* 39, 2145-2155.
- Allwine, K. J., Shinn, J. H., Streit, G., Clawson, K., Brown, M., 2002. Overview of URBAN 2000. *Bulletin of the American Meteorological Society*, 83(4), 521-536.
- Allwine, K. J., Clawson, K. J., Leach, M., Burrows, D., Wayson, R., Flaherty, J., Allwine, E., 2004a. Urban dispersion processes investigated during the Joint Urban 2003 study in Oklahoma City. In: *Proceedings of the 5th AMS Symposium on the Urban Environment*, Vancouver, B.C.
- Allwine, K. J., Leach, M., Stockham, L., Shinn, J. S., Hosker, R. P., Bowers, J. F., Pace, J. C., 2004b. Overview of Joint Urban 2003 - An atmospheric dispersion study in Oklahoma City. *Symposium on Planning, Nowcasting and Forecasting in the Urban Zone*. American Meteorological Society, January 11-15, 2004, Seattle, Washington.
- Allwine, K.J., Flaherty, J.E., 2006. Urban dispersion program MSG05 field study: summary of tracer and meteorological measurements. *Pacific National Laboratory Report, PNNL-15969*, 27p.
- Aly, K. M., Esmail, E., 1993. Refractive index of salt water: effect of temperature. *Opt. Mater.* 2, 195-199.
- Arnold, S.J., ApSimon, H., Barlow, J., Belcher, S., Bell, M., Boddy, J.W., Britter, R., Cheng, H., Clark, R., Colville, R.N., 2004. Introduction to the DAPPLE Air Pollution Project. *Sci. Total Environ.* 332, 139-153.

- Baik, J.-J., Park, R. S., Chun, H. Y., Kim, J. J., 2000. A laboratory model of urban street-canyon flows. *J. Appl. Meteor.* 39, 1592-1600.
- Baik, J.-J., Kim, J.-J., Fernando, H.J.S., 2003. A CFD model for simulating urban flow and dispersion. *J. Appl. Meteor.* 42, 1636-1648.
- Bentham, T., Britter, R., 2003. Spatially averaged flow within obstacle arrays. *Atmospheric Environment* 37(15), 2037-2043.
- Berkowicz, R., Hertel, O., Larsen, S. E., Sorensen, N. N., Nielsen, M., 1997. Modelling traffic pollution in streets. Ministry of Environment and Energy, National Environmental Research Institute. [http://www.mst.dk/NR/rdonlyres/9D313499-E237-4C1A-ADC4D31737E31613/0/A11\\_ModellingTrafficPollutioninStreets.pdf](http://www.mst.dk/NR/rdonlyres/9D313499-E237-4C1A-ADC4D31737E31613/0/A11_ModellingTrafficPollutioninStreets.pdf).
- Berkowicz, R., 2000a. OSPM - a parameterised street pollution model. *Environmental Monitoring and Assessment* 65, 323-331.
- Berkowicz, R.; Ketzel, M.; Jensen, S. S.; Hvidberg, M.; Raaschou-Nielsen, O. 2000b) Evaluation and application of OSPM for traffic pollution assessment for a large number of street locations; *Environmental Modelling & Software* 23, 296-303.
- Boarnet, M.G., Houston, D., Edwards, R., Princevac, M., Ferguson, G., Pan, H., Bartolome, C., 2011. Fine particulate concentrations on sidewalks in five Southern California cities; *Atmos. Environ.* 45, 4025-4033.
- Bottema, M., 1997. Urban roughness modelling in relation to pollutant dispersion. *Atmospheric Environment.* 31(18):3059-3075.
- Britter, R. E. and Hanna, S. R., 2003. Flow and dispersion in urban areas. *Annual Review of Fluid Mechanics.* 35:469-496.
- Brown, M., Lawson, R., DeCroix, D., Lee, R., 2001. Comparison of Centerline Velocity Measurements Obtained Around 2D and 3D Building Arrays in a Wind Tunnel. In: *Proceedings of the Environ. Hydraulics*, Tempe, AZ.
- Carslaw, D. C., Beevers, S.D., Tate, J. E., 2007. Modelling and assessing trends in traffic-related emissions using a generalised additive modelling Approach. *Atmos. Environ.* 41, 5289-5299.
- Castro, I. P., Robins, A. G., 1977. The flow around a surface-mounted cube in uniform and turbulent streams. *Journal of Fluid Mechanics Digital Archive* 79(02): 307-335.

- Cermak, J. E., 1984. Physical modeling of flow and dispersion over complex terrain. *Boundary-Layer Meteorology*, 30, 261-292.
- Cheng, H, Castro I.P., 2002a. Near-wall flow development after a step change in surface roughness. *Boundary-Layer Meteorol.* 105, 411-432.
- Cheng, H, Castro I.P., 2002b. Near-wall flow over urban-like roughness. *Boundary-Layer Meteorol.* 104, 229-259.
- Cheng, W. C., Liu, C.-H., Leung, D. Y. C., 2008. Computational formulation for the evaluation of street canyon ventilation and pollution removal performance. *Atmospheric Environment*. 42, 9041-9051.
- Chung, A., Chang, D.P.Y., Kleeman, M.J., 2001. Comparison of real-time instruments used to monitor airborne particulate matter. *J. Air & Waste Manage. Assoc.* 51, 109-120.
- Coceal, O., Thomas, T. G., Castro, I. P., Belcher S. E., 2006. Mean flow and turbulence statistics over groups of urban-like cubical obstacles. *Boundary-Layer Meteorol.* 121, 491-519.
- Coppeta, J., Rogers, C., 1998. Dual emission laser induced fluorescence for direct planar scalar behavior measurements. *Experimental Fluids* 25(1):1–15.
- Counihan, J., 1971. Wind tunnel determination of the roughness length as a function of the fetch and the roughness density of three-dimensional roughness elements. *Atmospheric Environment* (1967). 5(8):637-642.
- Crimaldi, J., 2008. Planar laser induced fluorescence in aqueous flows. *Experiments in Fluids* 44(6): 851-863.
- Dabberdt, W., Hoydysh, W., 1991. Street canyon dispersion: sensitivity to block shape and entrainment. *Atmos. Environ.* 25A, 1143-1153.
- Davidson, M. J., Snyder, W. H., Lawson, R. E., Hunt, J. C. R., 1996. Wind tunnel simulations of plume dispersion through groups of obstacles. *Atmospheric Environment* 30(22): 3715-3731.
- Dobre. A, Arnold, S. J., Smalley, R. J., Boddy, J. W. D., Tomlin, A. S., Belcher, S. E., 2005. Flow field measurements in the proximity of an urban intersection in London, UK. *Atmospheric Environment*. 39(26):4647-4657.

- Dockery, D. W., Pope III, C. A., 1994. Acute respiratory effects of particulate air pollution. *Annual Review of Public Health*. 15, 107-132.
- Eliasson, I., Offerle, B., Grimmond, C. S. B., Lindqvist, S., 2004. Wind fields and turbulence statistics in an urban street canyon. In: *Proceedings of the 5th AMS Urban Env. Conf.*, Vancouver, B.C.
- EPA, U. S. (2002) Air emission sources. <http://www.epa.gov/air/emissions/pm.htm>.
- Garratt, J. R., 1994. *The atmospheric boundary layer*. Cambridge University Press.
- Gavze, E., Fattal, E., Pistinner, S., 2002. Turbulence properties of the street-roof scale within the urban roughness sub-layer. In: *Proceedings of the 4th AMS Symp. Urb. Env.*, Norfolk, VA.
- Gillies, J.A.; Gertler, A.W.; Sagebiel, J.C.; Dippel, W.A., 2001. On-road particulate matter (PM<sub>2.5</sub> and PM<sub>10</sub>) emissions in the Sepulveda Tunnel, Los Angeles, California. *Environmental Science and Technology*, 35, 1054-1063.
- Gokhale, S.; Raokhande, N., 2008. Performance Evaluation of air quality models for Predicting PM<sub>10</sub> and PM<sub>2.5</sub> concentrations at urban traffic intersection during winter period; *Sci. Total. Environ.*, 394, 9-24.
- Gomes, M. S. d. P., Isnard, A. A., and Pinto, J. M. d. C., 2007. Wind tunnel investigation on the retention of air pollutants in three-dimensional recirculation zones in urban areas, *Atmospheric Environment*, 41(23), 1352-2310.
- Grimmond, C. S. B., Oke, T. R., 1999. Aerodynamic properties of urban areas derived from analysis of surface form. *Journal of Applied Meteorology*. 38(9), 1262-1292.
- Grimmond, C. S. B. and Oke, T. R., 2002. Turbulent heat fluxes in urban areas: observations and a local-scale urban meteorological parameterization scheme (LUMPS). *Journal of Applied Meteorology*. 41(7):792-810.
- Hamlyn, D., Hilderman, T., Britter, R., 2007. A simple network approach to modelling dispersion among large groups of obstacles. *Atmospheric Environment*. 41(28), 5848-5862.
- Hanna, S. R., Chang, J. H., 1992. Boundary-layer parameterizations for applied dispersion modeling over urban areas. *Boundary-Layer Meteorology*. 58, 229-259.

- Hanna, S. R., White, J., Zhou, Y., 2007. Observed winds, turbulence, and dispersion in built-up downtown areas of Oklahoma City and Manhattan. *Boundary-Layer Meteorology*. 125(3), 441-468.
- Hastie, T., Tibshirani, R., 1990. *Generalized Additive Models*. Chapman and Hall, London
- Hosker, R. P., 1980. The effects of buildings on local dispersion, Atmospheric turbulence and diffusion laboratory. National Oceanic and Atmospheric Administration, Oak Ridge, TN 37830.
- Hotchkiss, R. S., Harlow, F. H., 1973. Air pollution transport in street canyons. EPA-R4-73-029.
- Hoydysh, W. G., Dabberdt, W. F., 1988. Kinematics and dispersion characteristics of flows in asymmetric street canyons. *Atmospheric Environment*. 22(12), 2677-2689.
- Hoydysh, W., Dabberdt, W., 1988. Kinematics and dispersion characteristics of flows in asymmetric street canyons. *Atmos. Environ.*, 22, 2677-2689.
- International Towing Tank Conference (ITTC) 2008, Uncertainty Analysis: Particle Image Velocimetry, 7.5-01-03-03, 12 pages, September.
- Johnson, W. B., Ludwig, F. L., Dabberdt, W. F., Allen, R. J., 1973. An urban diffusion simulation model for carbon monoxide. *Journal of Air Pollution Control Association*. 23, 490-498.
- Kaimal, J. C.; Finnigan, J. J. 1994. *Atmospheric Boundary Layer Flows: Their Structure and Measurement*. Oxford University Press US.
- Kanda, M., Moriizumi, T., 2009. Momentum and heat transfer over urban-like surfaces. *Boundary-Layer Meteorology* 131(3), 385-401.
- Kastner-Klein, P., Plate, E., Fedorovich, E., 1997. Gaseous pollutant dispersion around urban-canopy elements: wind-tunnel case studies. *Int. J. Env. & Poll.*, 8, 727-737.
- Kastner-Klein, P., Plate, E., 1999. Wind-tunnel study of concentration fields in street canyons. *Atmos. Environ.* 33(24-25): 3973-3979.
- Kastner-Klein, P., Fedorovich, E., Rotach, M., 2001. A wind tunnel study of organized and turbulent air motions in urban street canyons. *J. Wind Eng. & Ind. Aerodyn.* 89, 849-861.



- Kastner-Klein, P., Rotach, M. W., 2004. Mean flow and turbulence characteristics in an urban roughness sublayer. *Bound. Layer Meteor.* 111(1), 55-84.
- Kastner-Klein, P., Berkowicz, R., Britter, R., 2004. The influence of street architecture on flow and dispersion in street canyons. *Meteorology and Atmospheric Physics*, 87(1-3), 121-131.
- Kingham, S., Durand, M., Aberkane, D., Harrison, J., Wilson, J. G., Epton, M., 2006. Winter comparison of TEOM, MiniVol and DustTrak PM<sub>10</sub> monitors in a woodsmoke environment. *Atmos. Environ.* 40, 338-347.
- Klein, P., Clark, J. V., 2007. Flow variability in a north American downtown street canyon. *Journal of Applied Meteorology and Climatology.* 46(6), 851-877.
- Kumar, P.; Garmory, A.; Ketzler, M.; Berkowicz, R.; Bitter, R., 2009. Comparative study of measured and modeled number concentrations of nanoparticles in an urban street canyon. *Atmospheric Environment* 43, 949-958.
- Lettau, H., 1969. Note on aerodynamic roughness-parameter estimation on the basis of roughness-element description. *Journal of Applied Meteorology.* 8(5):828-832.
- Lien F. S., Yee, E., 2004. Numerical modelling of the turbulent flow developing within and over a 3-D building array, part I: A high-resolution Reynolds-averaged Navier-Stokes approach. *Bound.-Lay. Meteor.* 112 (3), 427-466.
- Lumley, J. L., Panofsky, H., 1964. *The Structure of Atmospheric Turbulence.* John Wiley and Sons.
- Macdonald, R. W., Griffiths, R. F., Cheah, S. C., 1997. Field experiments of dispersion through regular arrays of cubic structures. *Atmospheric Environment.* 31(6), 783-795.
- Macdonald, R. W., Griffiths, R. F., Hall, D., 1998a. A comparison of results from scaled field and wind tunnel modelling of dispersion in arrays of obstacles. *Atmospheric Environment.* 32(22), 3845-3862.
- Macdonald, R. W., Hall, D., Walker, S., A. Spanton, 1998b. Wind tunnel measurements of wind speed in simulated urban arrays, BRE Report CR-243/98, 50 pp.
- Macdonald, R. W., 2000. Modelling the mean velocity profile in the urban canopy layer. *Bound.-Lay. Meteor.* 97, 25-45.

- Macdonald, R. W., Carter, S., Slawson, P. R., 2000a. Measurements of Mean Velocity and Turbulence Statistics in Simple Obstacle Arrays at 1:200 Scale. Thermal Fluids Report.
- Macdonald, R. W., Coulson, B. J., Slawson, P. R., 2000b. Near field dispersion in the urban environment - A hydraulic flume study. Environmental Monitoring and Assessment, 65(1-2), 231-238.
- Macdonald, R. W., Carter, S., Slawson, P., 2002. Physical modeling of urban roughness using arrays of regular roughness elements. Water, Air, & Soil Poll., 2, 541-554.
- Mavroidis, I., Griffiths, R. F., Jones, C. D., Biltoft, C. A., 1999. Experimental investigation of the residence of contaminants in the wake of an obstacle under different stability conditions. Atmospheric Environment. 33(6), 939-949.
- Mensink, C., Colles, A., Janssen, L., Cornelis, J., 2003. Integrated air quality modeling for the assessment of air quality of streets against the council directives. Atmospheric Environment. 37, 5177-5184.
- Mensink, C.; Lefebvre, F.; Janssen, L.; Cornelis, J., 2006. Comparison of three street canyon models with measurements at an urban station in Antwerp, Belgium. Environmental Modelling & Software 21, 514-519.
- Meroney, R. N., Pavageau, M., Rafailidis, S., Schatzmann, M., 1996. Study of line source characteristics for 2-D physical modelling of pollutant dispersion in street canyons. Journal of Wind Engineering and Industrial Aerodynamics 62(1), 37-56.
- Nelson, M. A., Pardyjak, E. R., Klewicki, J. C., Pol, S. U., Brown, M. J., 2007a. Properties of the wind field within the Oklahoma City Park Avenue street canyon. Part I: Mean flow and turbulence statistics. Journal of Applied Meteorology and Climatology. 46(12):2038-2054.
- Nelson, M. A., Pardyjak, E. R., Brown, M., Klewicki, J., 2007b. Properties of the wind field within the Oklahoma City Park Avenue street canyon. Part II: Spectra, cospectra, and quadrant analyses. Journal of Applied Meteorology and Climatology 46(12), 2055-2073.
- Oke, T. R., 1976. The distinction between canopy and boundary layer urban heat islands. Atmosphere. 14, 268-277.
- Oke, T. R., 1987. Boundary Layer Climates, 2nd Edition, Routledge, London.
- Oke, T. R., 1988. The urban energy balance. Progress in Physical Geography. 12, 471-508.

- Pascheke, F., Barlow, J. F., Robins, A., 2008. Wind-tunnel modelling of dispersion from a scalar area source in urban-like roughness. *Boundary-Layer Meteorology*. 126, 103-124.
- Patra, A., Colvile, R., Arnold, S., Bowen, E., Shallcross, D., Martin, D., Price, C., Tate, J., 2008. On street observations of particulate matter movement and dispersion due to traffic on an urban road. *Atmospheric Environment*. 42(17), 3911-3926.
- Pavageau, M., Schatzmann, M., 1999. Wind tunnel measurements of concentration fluctuations in an urban street canyon. *Atmos. Environ.* 33(24-25), 3961-3971.
- Prasad, A.K.; Adrian, R.J.; Landreth, C.C., Offutt, P.W., 1992. Effect of Resolution on the Speed and Accuracy of Particle Image Velocimetry Interrogation, *Experiments in Fluids*, 13(2-3), 105-116.
- Princevac, M., Balk, J-J., Li, X., Pan, H., Park, S-B., 2010. Lateral channeling within rectangular arrays of cubical obstacles. *Journal of Wind Engineering and Industrial Aerodynamics*. 98, 377-385.
- Qian, W., Princevac, M., Venkatram, A., 2010. Using temperature fluctuation measurements to estimate meteorological inputs for modelling dispersion during convective conditions in urban areas. *Boundary-Layer Meteorol.* 135, 269-289.
- R Development Core Team, R: a Language and Environment for Statistical Computing; R Foundation for Statistical Computing, Wood, 2006, Vienna, Austria. ISBN 3-900051-07-0, URL: <http://www.R-project.org>.
- Rafailidis, S., Schatzmann, M., 1995. Concentration measurements with different roof patterns in street canyons with aspect ratios  $B/H=1/2$  and  $B/H=1$ . Report, Universitat Hamburg, Meteorologisches Institut.
- Raffel, M., Willert, C., Wereley, S., Kompenhans, J. 2007. Particle Image Velocimetry: A Practical Guide. Springer-Verlag. ISBN 3-540-72307-2.
- Raupach, M. R., 1994. Simplified expressions for vegetation roughness length and zero-plane displacement as functions of canopy height and area index. *Boundary-Layer Meteorology*. 71(1):211-216.
- Raupach, M. R. and Legg, B. J., 1984. The uses and limitations of flux-gradient relationships in micrometeorology. *Agricultural Water Management*. 8, 119-131.

- Rotach, M. W., Gryning, S.-E., Batchvarova, E., Christen, A., Vogt, R., 2004. Pollutant dispersion close to an urban surface – the BUBBLE tracer experiment. *Meteorology and Atmospheric Physics*. 87(1), 39-56.
- Rotach M.W.L., Vogt R., Bernhofer C., Batchvarova E., Christen A., Clappier A., Feddersen B., Gryning S.E., Martucci G., Mayer H., Mitev V., Oke T.R., Parlow E., Richner H., Roth M., Roulet Y.A., Ruffieux D., Salmond J.A., Schatzmann M., Voogt J.A., 2005. BUBBLE - An urban boundary layer meteorology project, *Theor and Appl. Climat.*, 81(3-4), 231-261.
- Roth, M., 2000. Review of atmospheric turbulence over cities. *Quarterly Journal of the Royal Meteorological Society*. 126, 941-990.
- Richmond-Bryant, J., Saganich, C., Bukiewicz, L., Kalin, R., 2009. Associations of PM<sub>2.5</sub> and black carbon concentrations with traffic, idling, background pollution, and meteorology during school dismissals. *Sci. Total Environ*. 407, 3357-3364.
- Schatzmann, M., Leidl, B., Liedtke, J., 2000. Dispersion in urban environments – Comparison of field measurements with wind tunnel results. *Environmental Monitoring and Assessment*, 65(1-2), 249-257.
- Simoëns, S., Ayrault, M., Wallace, J. M., 2007. The flow across a street canyon of variable width--Part 1: Kinematic description. *Atmospheric Environment*. 41(39), 9002-9017.
- Simoëns, S., Wallace, J. M., 2008. The flow across a street canyon of variable width--Part 2: Scalar dispersion from a street level line source. *Atmospheric Environment* 42(10), 2489-2503.
- Snyder, W. 1981 Guideline for fluid modeling of atmospheric diffusion. EPA report 600/8-81-009.
- Solazzo, E., Britter, R., 2007. Transfer processes in a simulated urban street canyon. *Boundary-Layer Meteorology*. 124(1), 43-60.
- Stewart, L., Oke. T.R., 2009. Newly developed "thermal climate zone" for defining and measuring urban heat island magnitude in the canopy layer. In *Proceeding of The 89th American Meteorological Society Annual Meeting*, Phoenix, AZ, January 11-15, Paper J8.2A.
- Stull, R. B., 1989. *An Introduction to Boundary Layer Meteorology*. Kluwer Academic Publisher, Boston.

- Tay, B. K., McFiggans, G. B., Jones, D. P., Gallagher, M. W., Martin, C., Watkins, P., Harrison, R. M., 2010. Linking urban aerosol fluxes in street canyons to larger scale emissions. *Atmos. Chem. Phys.* 10, 2475-2490.
- Theurer, W., Plate, E.J., Hörschele, K., 1996. Semi-empirical models as a combination of wind tunnel and numerical dispersion modelling. *Atmospheric Environment* 30, 3583-3597.
- Theurer W., 1999. Typical building arrangements for urban air pollution modelling. *Atmospheric Environment* 33: 4057-4066.
- Vardoulakis, S., Vallantis, M., Milner, J., ApSimon, H., 2007. Operational air pollution modelling in the UK--Street canyon applications and challenges. *Atmospheric Environment.* 41(22), 4622-4637.
- Venkatram, A.; Isakov, V.; Seila, R.; Baldauf, R., 2009. Modeling the Impacts of Traffic Emissions on Air Toxics Concentrations Near Roadways; *Atmos. Environ.* 43, 3191-3199.
- Vincont, J.-Y., Simoens, S., Ayrault, M., Wallace, J. M., 2000, Passive scalar dispersion in a turbulent boundary layer from a line source at the wall and downstream of an obstacle. *Journal of Fluid Mechanics.* 424, 127-167.
- Watson, J. G., Chow, J. C., DuBois, D. W., Green, M. C., Frank, N. H., Pitchford, M. L., 1997. Guidance for network design and optimal site exposure for PM<sub>2.5</sub> and PM<sub>10</sub>. Report No. EPA-454/R-99-022. U.S. Environmental Protection Agency: Research Triangle Park, NC. [http:// www.epa.gov/ttn/amtic/pmstg.html](http://www.epa.gov/ttn/amtic/pmstg.html).
- Watson J. G., Chow, J. C., 2001. Estimating middle-, neighborhood- and urban-scale contributions to elemental carbon in Mexico City with a rapid response Aethalometer. *J. Air & Waste Manage. Assoc.* 511, 1522-1528.
- Weber, S., Kuttler, W., Weber, K., 2006. Flow characteristics and particle mass and number concentration variability within a busy urban street canyon. *Atmospheric Environment.* 40(39), 7565-7578.
- Wedding, J., Lombardi, D., Cermak, J., 1977. A wind-tunnel study of gaseous pollutants in city street canyons. *J. Air Poll. Control Assoc.*, 27, 557-566.
- Wood, S. N., Augustin; N. H., 2002. GAMs with integrated model selection using penalized regression splines and applications to environmental modeling. *Ecological Modelling.* 157, 157-177.
- Wood, S.N., 2006. *Generalized Additive Models: An Introduction with R.* Chapman and Hall/CRC, London/Boca Ration, FL.

- Yamartino R. J., Wiegand, G., 1986. Development and evaluation of simple models for the flow, turbulence, and pollutant concentration fields within an urban street canyon. *Atmos. Environ.* 20, 2137-2156.
- Yee, E., Gailis, R. M., Hill, A., Hilderman T., Kiel, D., 2006. Comparison of wind-tunnel and water-channel simulations of plume dispersion through a large array of obstacles with a scaled field experiment. *Bound. Lay. Meteor.* 121, 389-432.
- Zhou, Y., Levy, J.I., 2008. The impact of urban street canyons on population exposure to traffic-related primary pollutants. *Atmos. Environ.* 42, 3087-3098.

## APPENDIX I: Uncertainty analysis for PIV measurements

International Towing Tank Conference proposed the recommended procedures and guidelines for uncertainty analysis of PIV measurements in 2008. The principle of the PIV measurement on flow speed  $u$  can be described by

$$u = \alpha(\Delta X / \Delta t) + \delta u \quad \text{A1.1}$$

where  $\Delta X$  is the displacement of particle images,  $\Delta t$  is the time interval of successive images,  $\alpha$  is the magnification factor and  $\delta u$  is the uncertainty factors of flow visualization.

Table A1.1 shows the principal measurements of  $3 \times 3$  arrays, that consist of four sub-systems: calibration, flow visualization, image detection and data processing.

The error sources come from the following processes: the calibration of  $\alpha$ , the measurement of displacement of particle image  $\Delta X$ , time interval  $\Delta t$ , experimental  $\delta u$ , measurement position of  $x$  and measurement time  $t$ . Table A1.2 gives an example of uncertainty for each variable in velocity measurement. The combined uncertainty is shown in Table A1.3.

Table A1.1 Principal measurements for  $3 \times 3$  arrays

		Symbol	Description	unit
Target flow of measurement	Target flow		2-D water flow	
	measurement facility		circulating water channel	
	measurement area		307×230	mm × mm
	uniform flow speed	$U_{free}$	0.082	m s <sup>-1</sup>
calibration	distance of reference points	$l_r$	100	mm
	distance of reference image	$L_r$	520	pixel
	magnification factor	$\alpha$	0.192	mm pxl <sup>-1</sup>
Flow visualization	tracer particle		Pliolite® particles	
	average diameter	$d_p$	0.05	mm
	Standard deviation of diameter	$s_p$	0.005	mm
	average specific gravity		1.02	
	light source		Double pulse Nd:YAG laser	
	laser power		388	mJ pulse <sup>-1</sup>



	thickness of laser light sheet		1	mm
	time interval	$\Delta t$	1.1	ms
Image Detection	Camera			
	spatial resolution		1600 × 1192	pixel × pixel
	sampling frequency		1	Hz
	gray scale resolution			
	cell size			
	optical system			
	distance from the target	$l_t$	840	mm
	length of focus		50	mm
	F number of lens		f1.8	
	Perspective angle	$\theta$	20.9°	
Data processing	Pixel unit analysis		Cross correlation method	
	correlation area size		32 × 32	pixel × pixel
	search area size		16 x 16	pixel x pixel
	sub-pixel analysis		3 points Gaussian peak fitting	

Table A1. 2 Uncertainty for each variable in velocity measurement

Parameter	Category	Error sources	u(xi)	unit	ci	unit	ciw(xi)	unit	wc
$\alpha$ (mm pxl <sup>-1</sup> )	Calibration	Reference image	0.5	pxl	3.70E-04	mm pxl <sup>-2</sup>	1.85E-04	mm pxl <sup>-1</sup>	
		Physical distance	0.02	mm	1.92E-03	1 pxl <sup>-1</sup>	3.85E-05	mm pxl <sup>-1</sup>	
		Image distortion by lens	2.60	pxl	3.70E-04	mm pxl <sup>-2</sup>	9.62E-04	mm pxl <sup>-1</sup>	
		Image distortion by CCD	0.0056	pxl	3.70E-04	mm pxl <sup>-2</sup>	2.07E-06	mm pxl <sup>-1</sup>	
		Board position	0.5	mm	2.29E-04	1 pxl <sup>-1</sup>	1.14E-04	mm pxl <sup>-1</sup>	
		Parallel board	0.035	rad	0.011	mm pxl <sup>-1</sup>	3.92E-04	mm pxl <sup>-1</sup>	1.061E-03
$\Delta x$ (pxl)	Acquisition	Laser power fluctuation	0.0050	mm	5.21	pxl mm <sup>-1</sup>	0.026	pxl	
		Image distortion by CCD	0.0056	pxl	1.0		0.006	pxl	
	Reduction	particle displacement	0.04	pxl	1.0		0.04	pxl	
		Sub-pixel analysis	n/a		1.0		n/a	pixel	4.806E-02
$\Delta t$ (s)	Acquisition	Delay generator	2.00E-09	s	1.0		2.00E-09	s	
		Pulse time	5.00E-09	s	1.0		5.00E-09	s	5.385E-09
$\delta u$ (mm s <sup>-1</sup> )	Experiment	Particle trajectory	0.008	mm s <sup>-1</sup>	1.0		8.20E-03	mm s <sup>-1</sup>	
		3-D effects	0.15	mm s <sup>-1</sup>	1.0		1.52E-01	mm s <sup>-1</sup>	1.518E-01

Table A1. 3 Combined uncertainty for velocity measurement

Parameter	Category	Error sources	$w_{u(x)}$	$u(x)$	unit	$\frac{\partial u}{\partial \xi}$	ci	unit	$c_{iu(x)}$	unit
$\alpha$ (mm pxl <sup>-1</sup> )	Calibration	Magnification factor	$w_{\alpha}$	0.00106	mm pxl <sup>-1</sup>	$\frac{\partial u}{\partial \alpha}$	427.1	pxl s <sup>-1</sup>	0.45	mm s <sup>-1</sup>
$\Delta x$ (pxl)	Image detection	Image displacement	$w_{\Delta x}$	0.048	pxl	$\frac{\partial u}{\partial \Delta x}$	174.5	mm pxl <sup>-1</sup> s <sup>-1</sup>	8.39	mm s <sup>-1</sup>
$\Delta t$ (s)	Time Interval	Image interval	$w_{\Delta t}$	5.39E-09	s	$\frac{\partial u}{\partial \Delta t}$	74.5	m s <sup>-2</sup>	0.00	mm s <sup>-1</sup>
$\delta u$ (mm s <sup>-1</sup> )	Experiment	Experiment	$w_{\delta u}$	0.152	mm s <sup>-1</sup>	$\frac{\partial u}{\partial \delta u}$	1.0		0.15	mm s <sup>-1</sup>
							Combined uncertainty	Uu	8.40	mm s <sup>-1</sup>
							Percentage uncertainty		10.25	%

**APPENDIX II: Supplemental Field Measurement Figures**

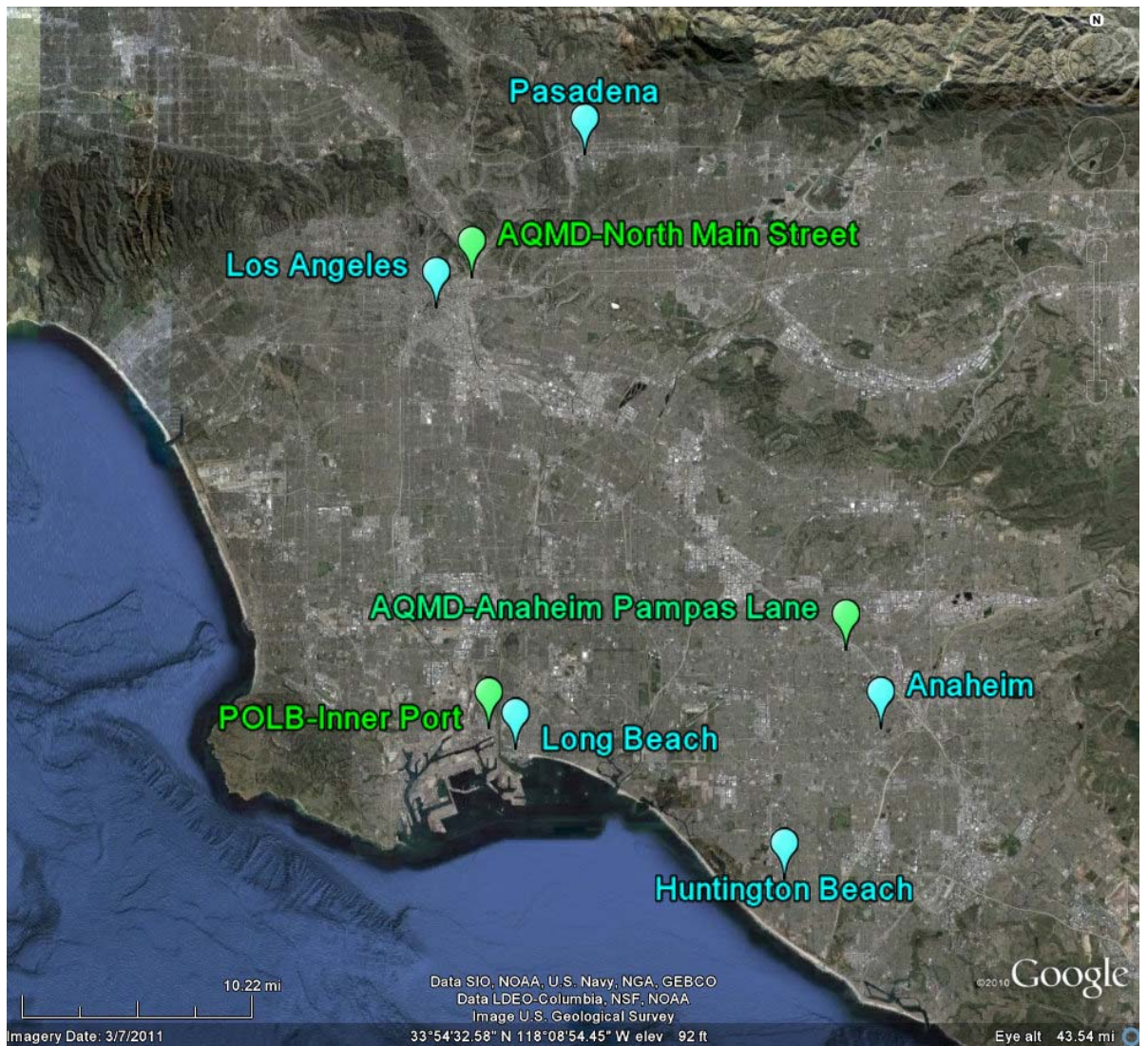


Figure A2.1 Urban- and neighborhood- scale monitoring stations and field measurement cities.

Table A2.1 Specification of each site.

City	Site	Instrument	Arterials	Which side of arterials	Distance to arterials (m)
Anaheim	A1	DustTrak, Camera	Harbor Blvd.	East	3
	A2	DustTrak, Camera	Harbor Blvd.	West	5
	A3	DustTrak, Camera	Lampson Ave.	North	1
	A4	DustTrak	Lampson Ave.	South	1
	A5	DustTrak	Citruswood Ave.	South	1
	A6	DustTrak, Sonic Anemometer	Harbor Blvd.	East	24
Pasadena	P1	DustTrak	El Molino Ave.	West	1
	P2	DustTrak, Camera	Colorado Blvd.	South	1
	P3	DustTrak, Camera	Colorado Blvd.	South	1
	P4	DustTrak, Camera	Colorado Blvd.	North	1
	P5	DustTrak	El Molino Ave.	East	1
	P6 (Roof)	DustTrak, Sonic Anemometer	Green St	East	34
Long Beach	LB1	DustTrak	Ocean Blvd.	North	2

	LB2	DustTrak, Camera	Ocean Blvd.	South	2
	LB3	DustTrak	Broadway	South	1
	LB4	DustTrak, Camera	Pine Ave.	East	1
	LB5	DustTrak, Camera	Broadway	South	1
	LB6 (Roof)	DustTrak, Sonic Anemometer	Pine Ave.	West	60
Los Angeles	LA1	DustTrak, Camera	6 <sup>th</sup> St.	Northeast	1
	LA2	DustTrak, Camera	Grand Ave.	Northwest	1
	LA3	DustTrak, Camera	Grand Ave.	Southeast	1
	LA4	DustTrak, Camera	6 <sup>th</sup> St.	Northeast	1
	LA5	DustTrak	6 <sup>th</sup> St.	Southwest	1
	LA6	DustTrak, Sonic Anemometer	Olive St.	Southeast	50
Huntington	HB1	DustTrak	Garfield Ave.	North	1
Beach	HB2	DustTrak, Camera	Garfield Ave.	South	1
	HB3	DustTrak, Camera	Beach Blvd.	West	1
	HB4	DustTrak, Camera	Beach Blvd.	East	1

---

HB5	DustTrak	Beach Blvd.	West	22
HB6	DustTrak, Sonic Anemometer	Beach Blvd.	East	12

---

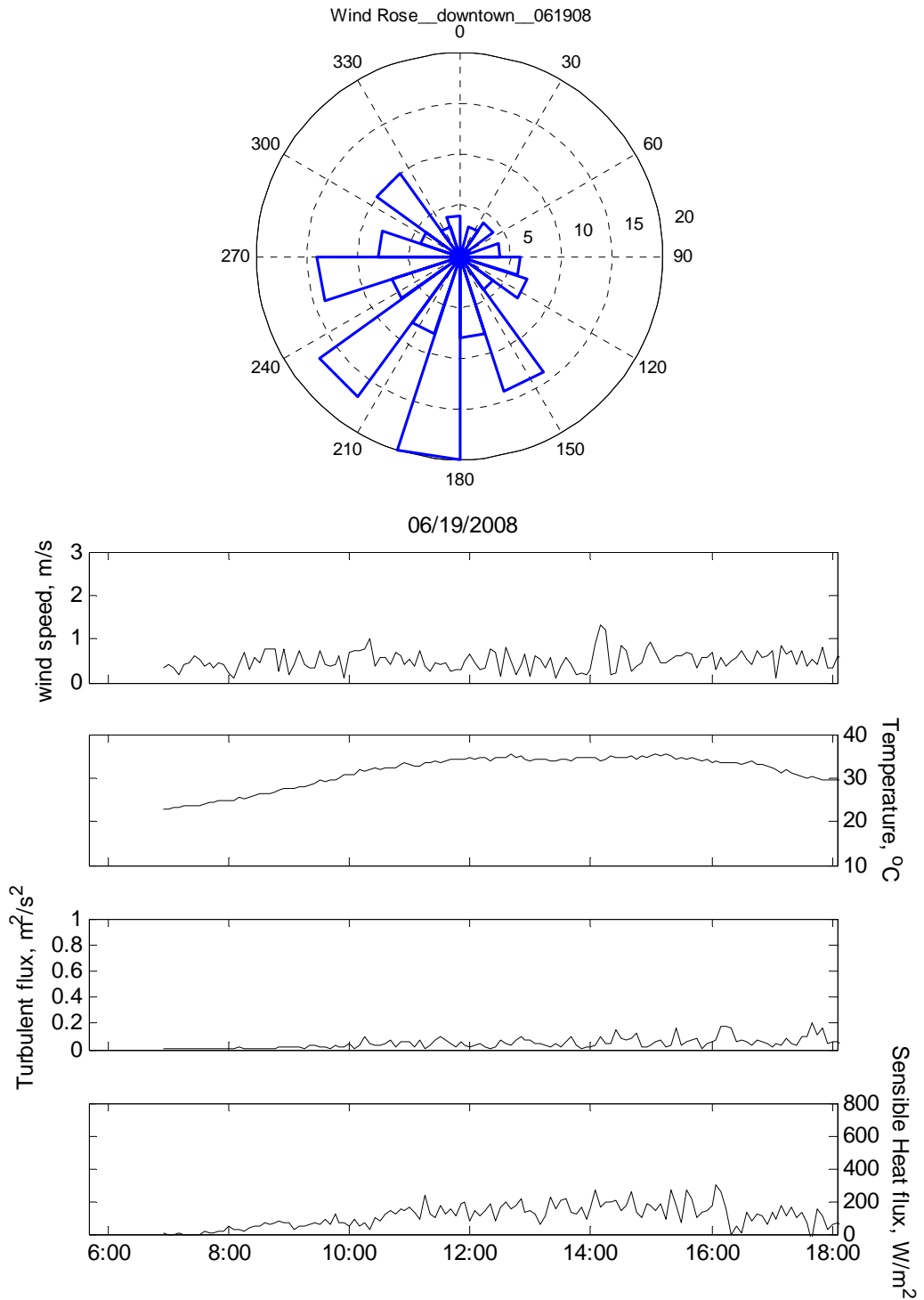


Figure A2.2 Meteorological variables observed in Los Angeles on 06/19/2008.



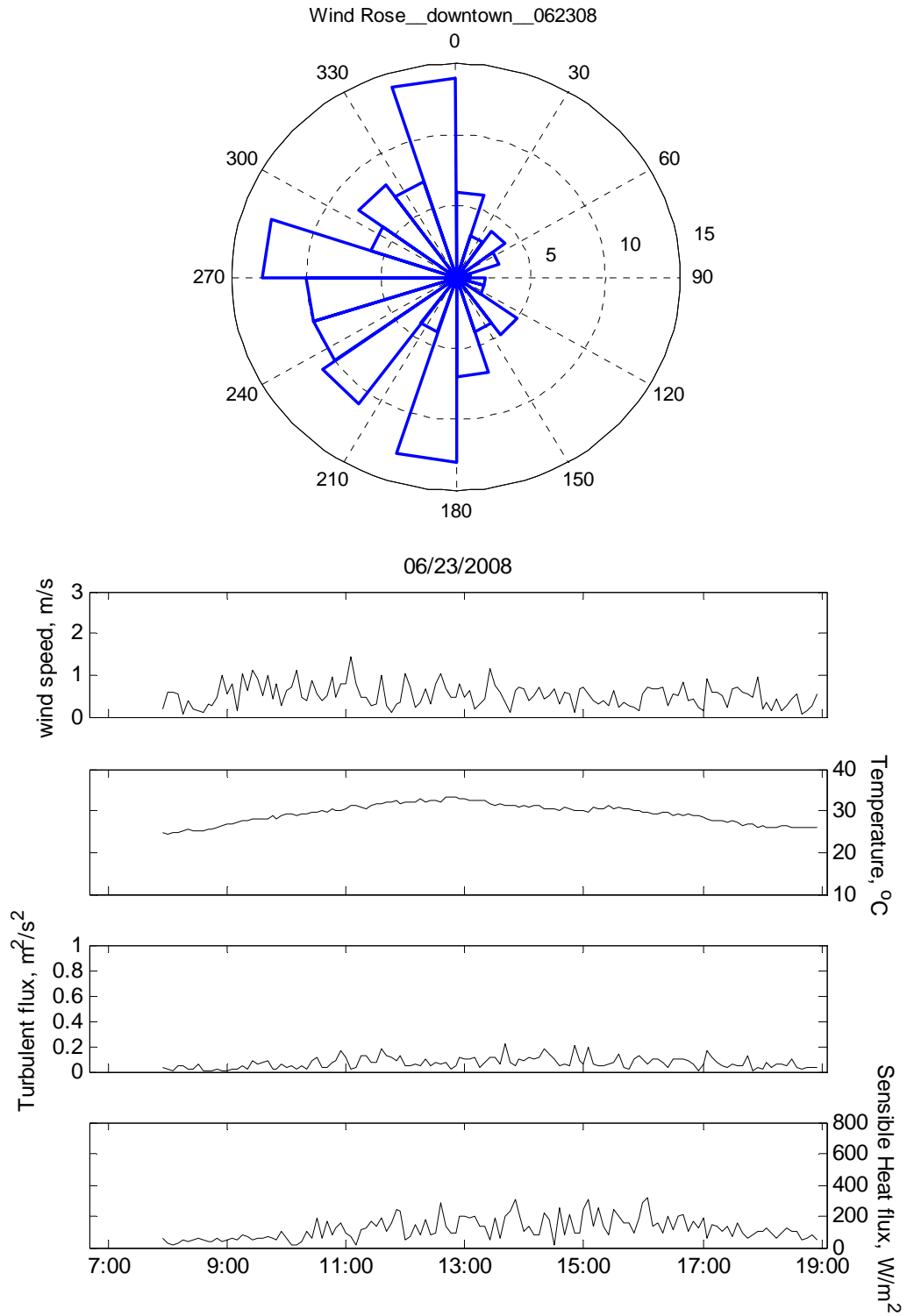


Figure A2.3 Meteorological variables observed in Los Angeles on 06/23/2008.

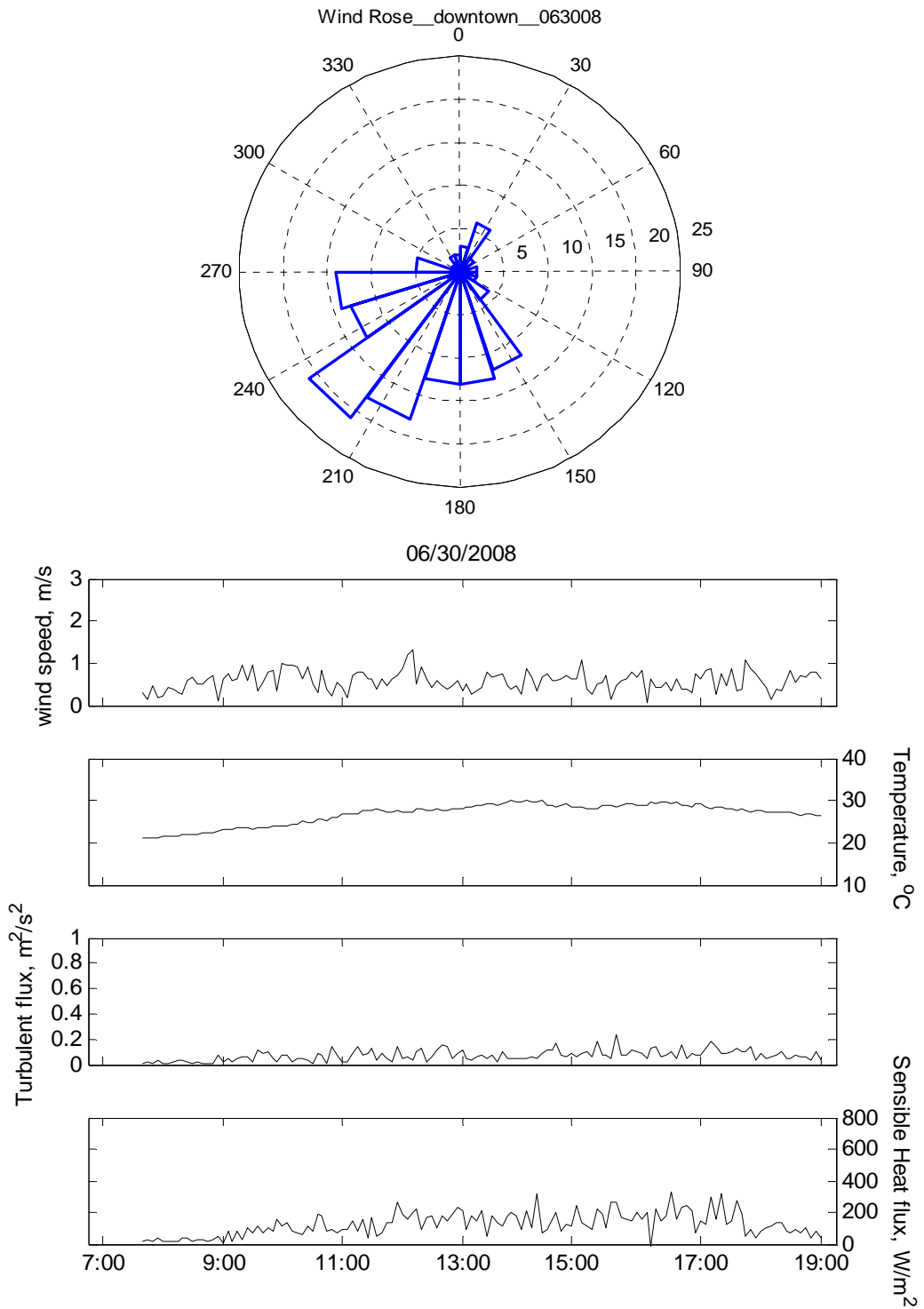


Figure A2.4 Meteorological variables observed in Los Angeles on 06/30/2008.

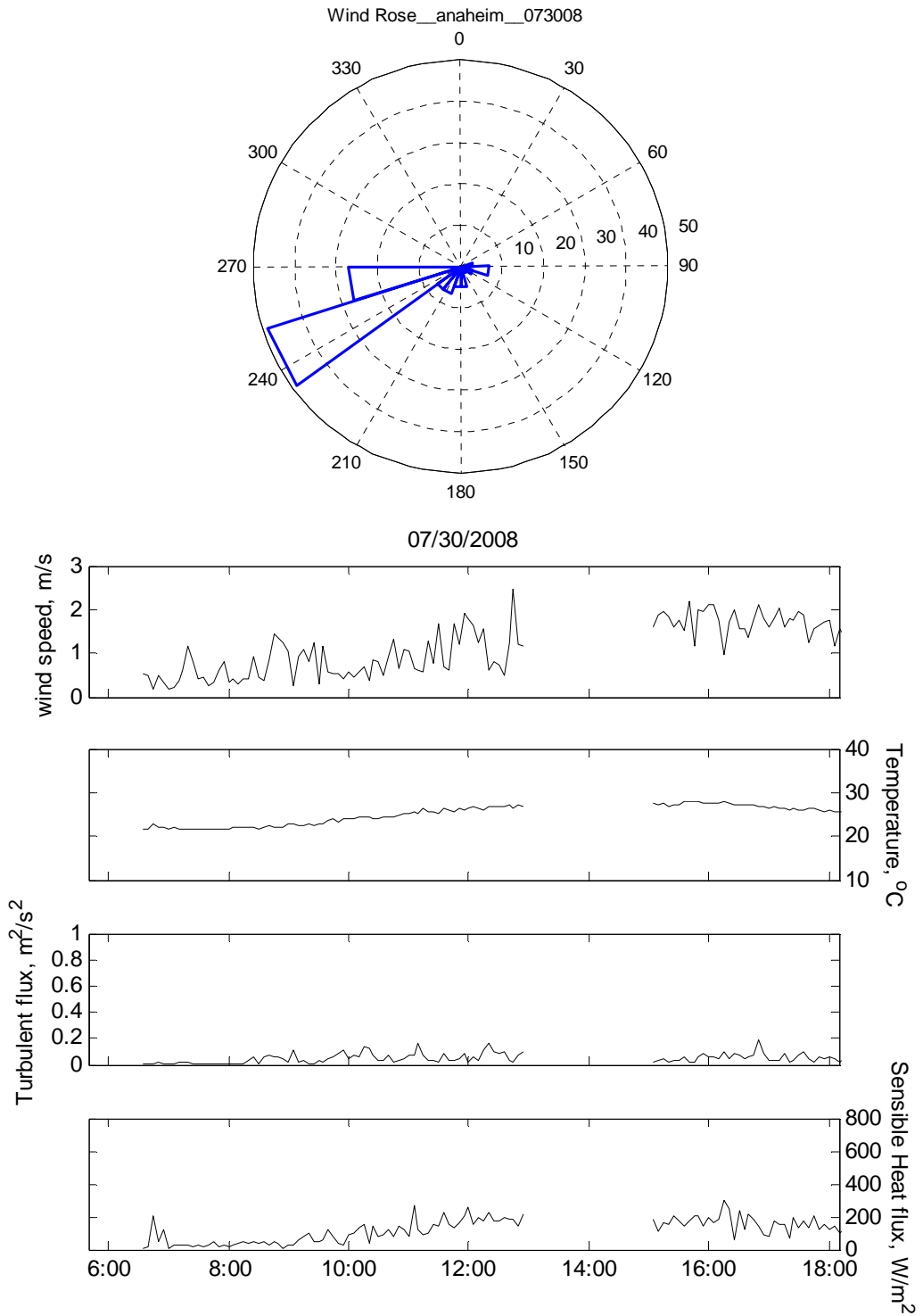


Figure A2.5 Meteorological variables observed in Anaheim on 07/30/2008.

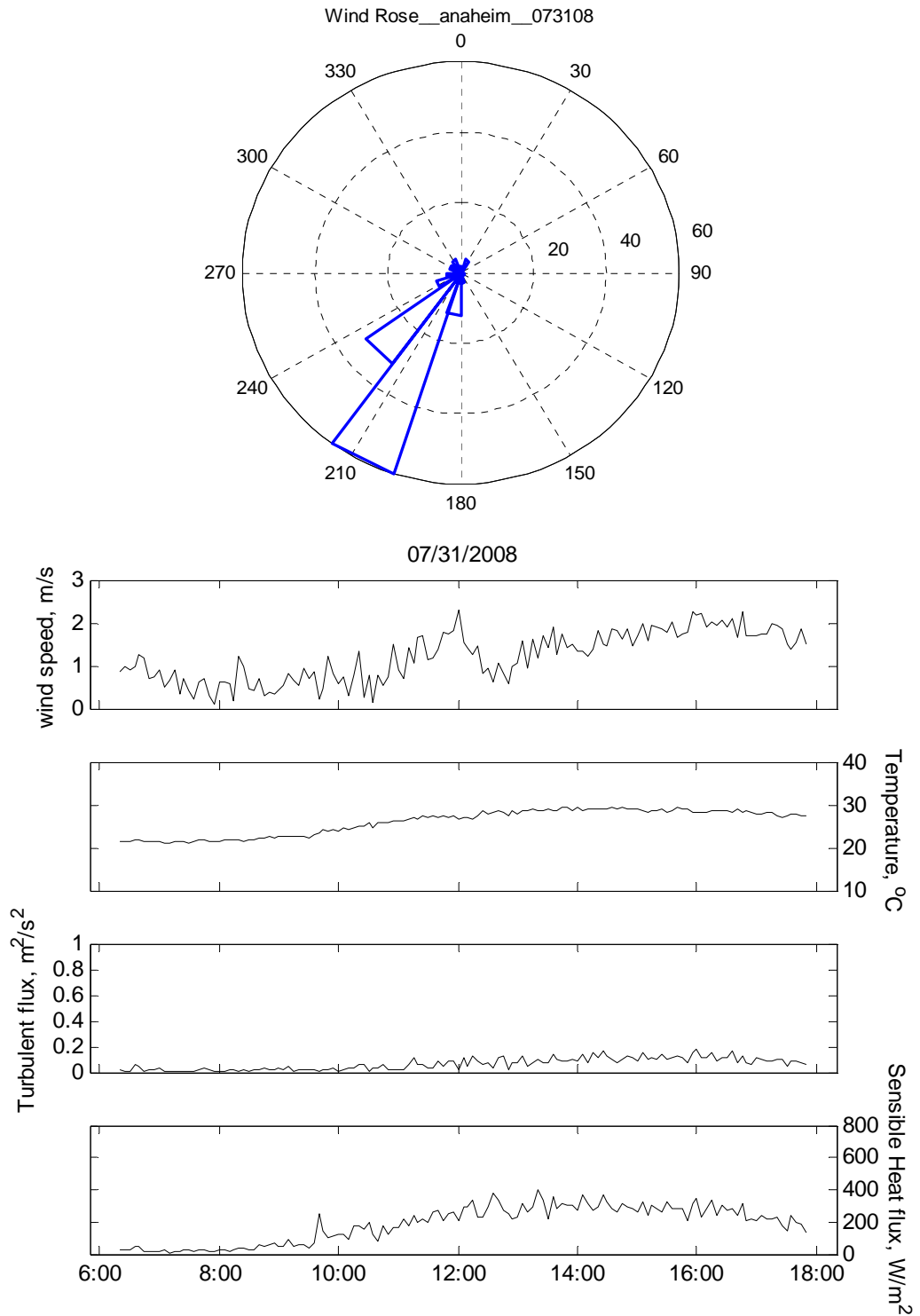


Figure A2.6 Meteorological variables observed in Anaheim on 07/31/2008.

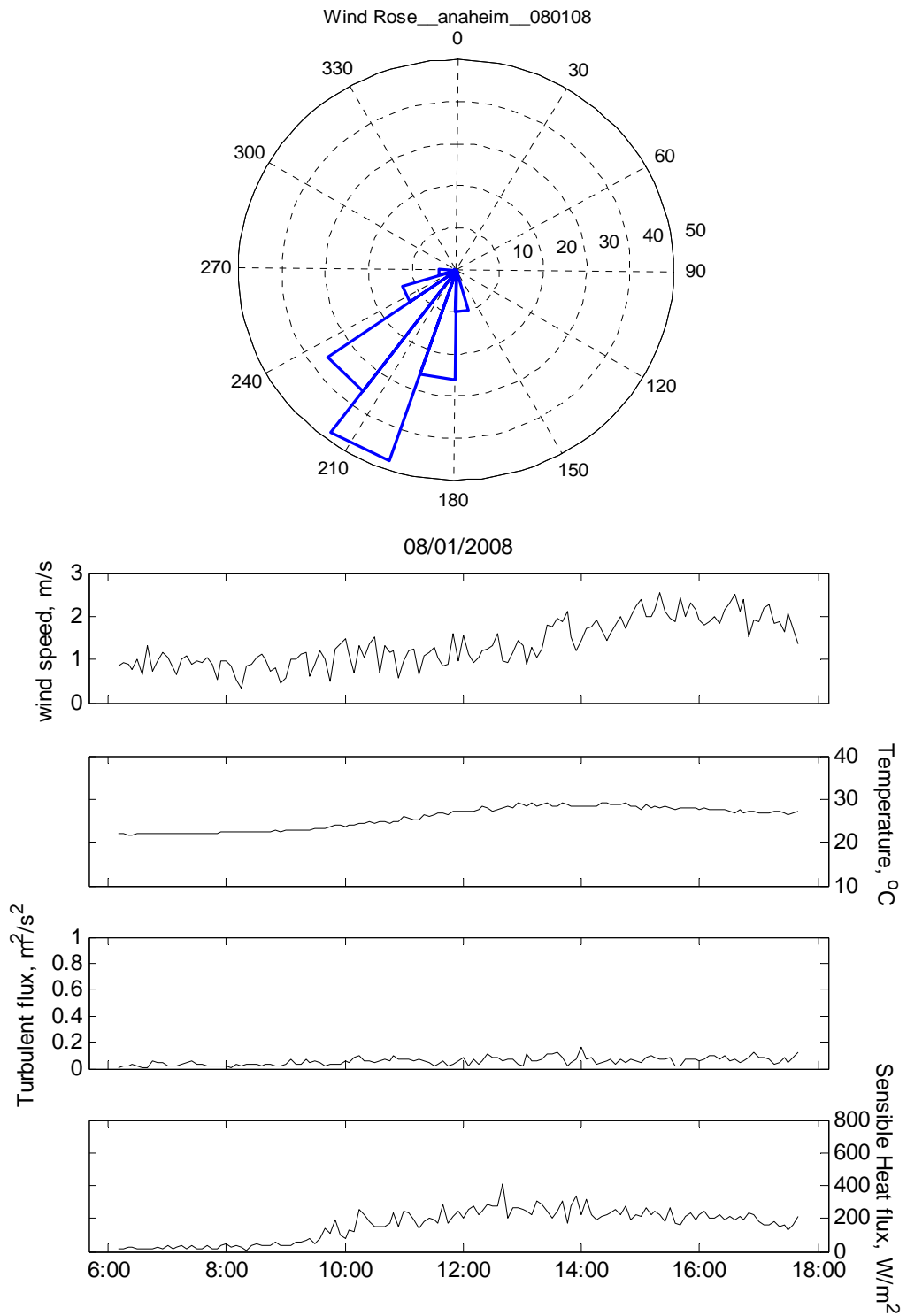


Figure A2.7 Meteorological variables observed in Anaheim on 08/01/2008.

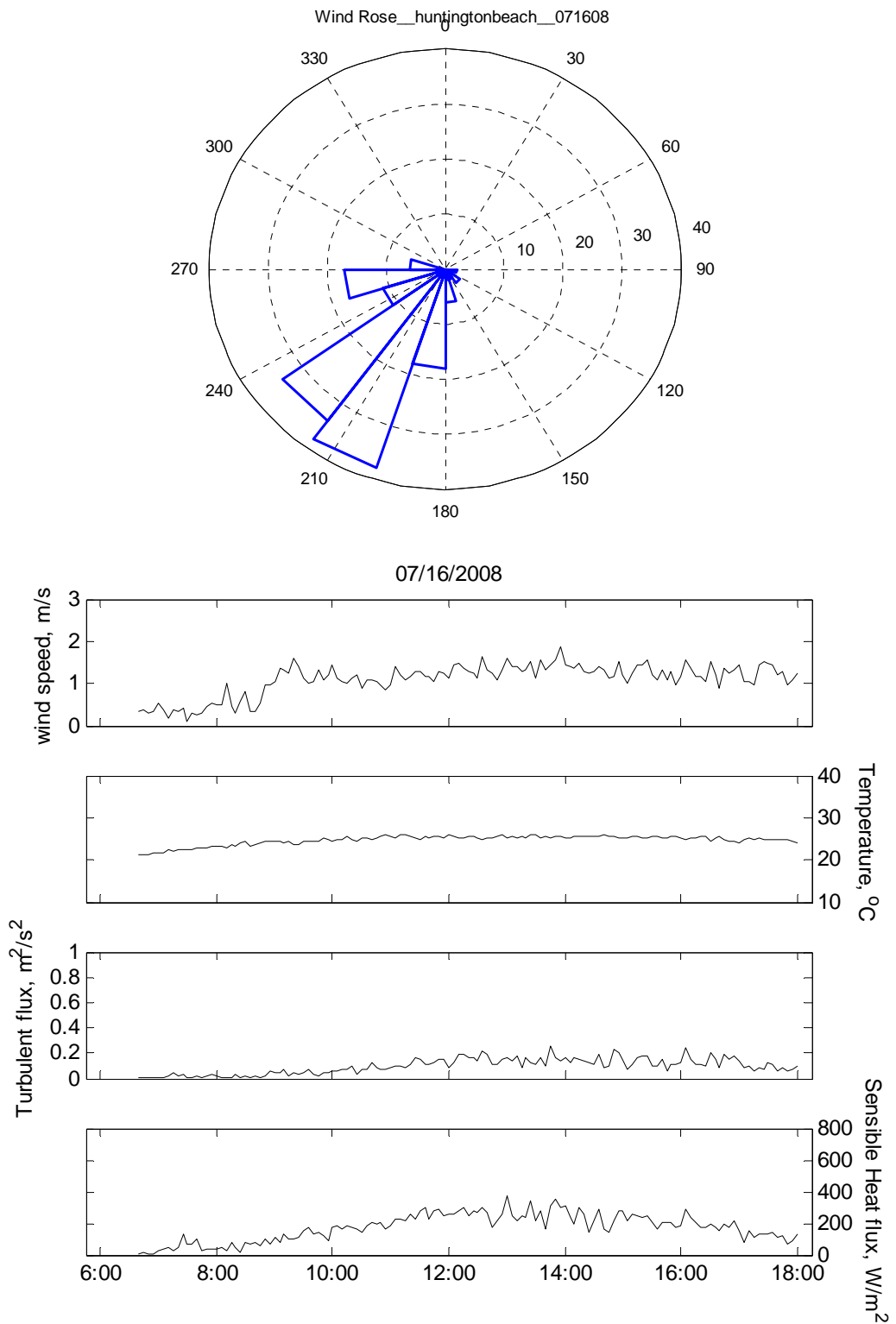


Figure A2.8 Meteorological variables observed in Huntington Beach on 07/16/2008.

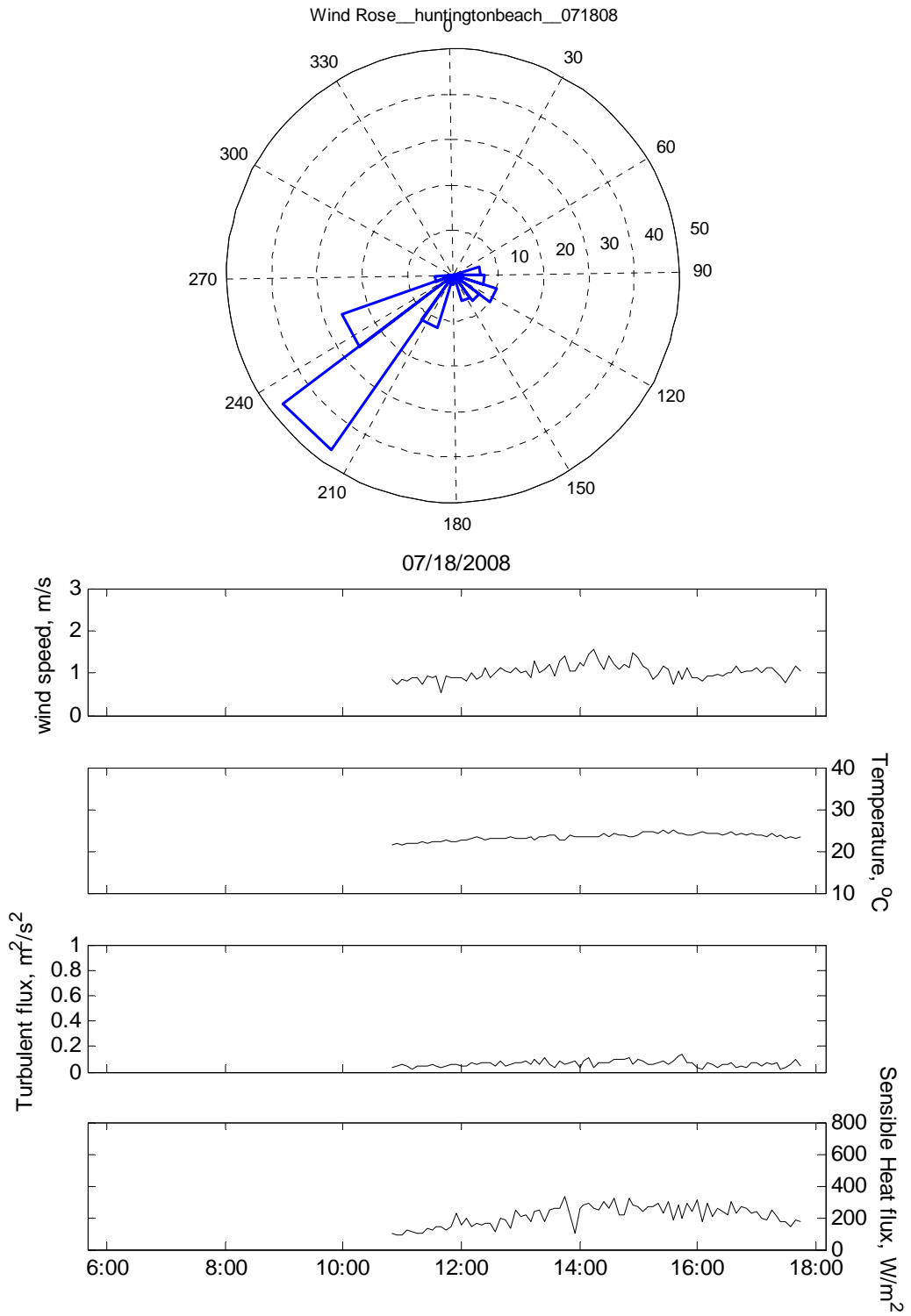


Figure A2.9 Meteorological variables observed in Huntington Beach on 07/18/2008.

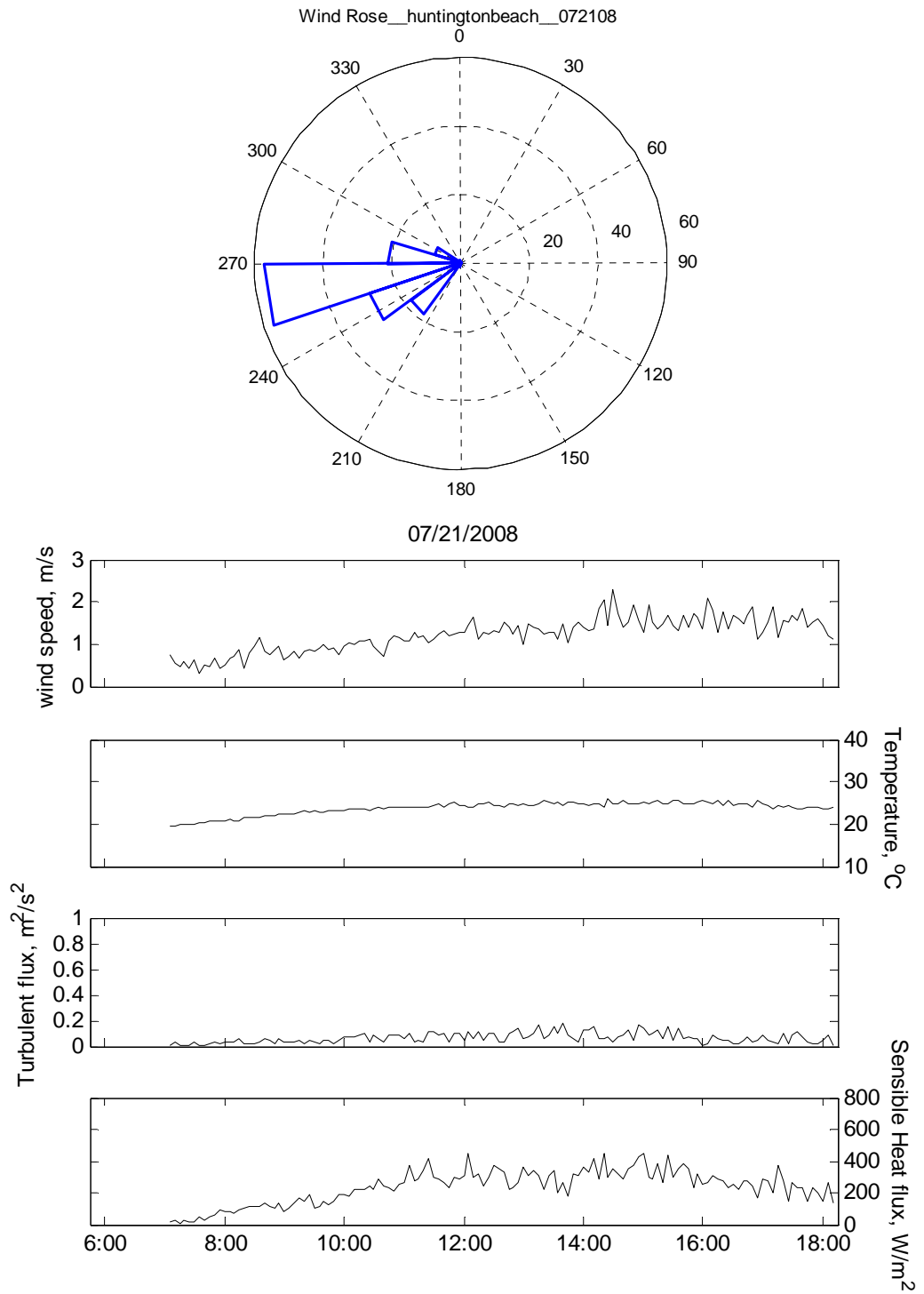


Figure A2.10 Meteorological variables observed in Huntington Beach on 07/21/2008.



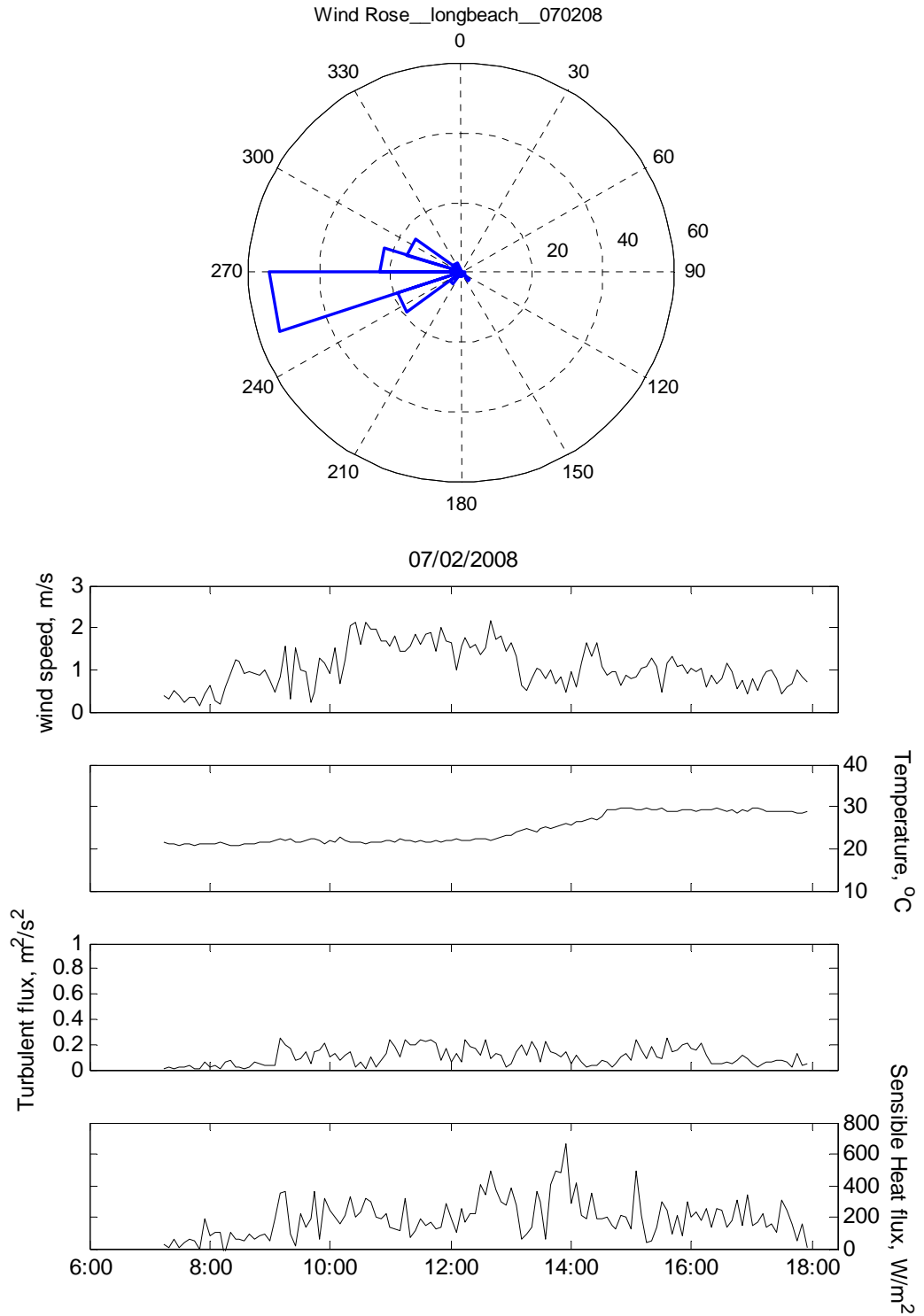


Figure A2.11 Meteorological variables observed in Long Beach on 07/02/2008.

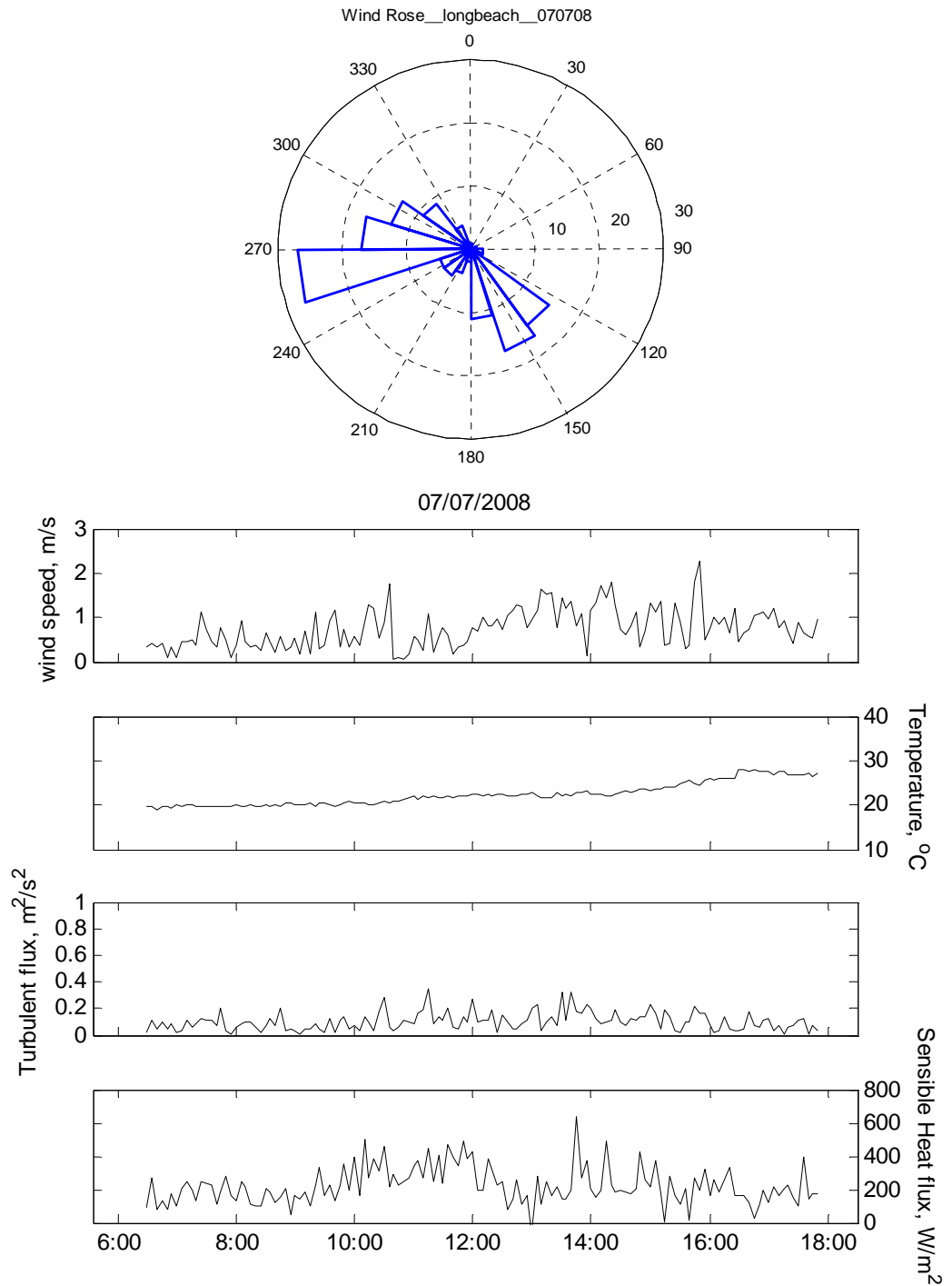


Figure A2.12 Meteorological variables observed in Long Beach on 07/07/2008.

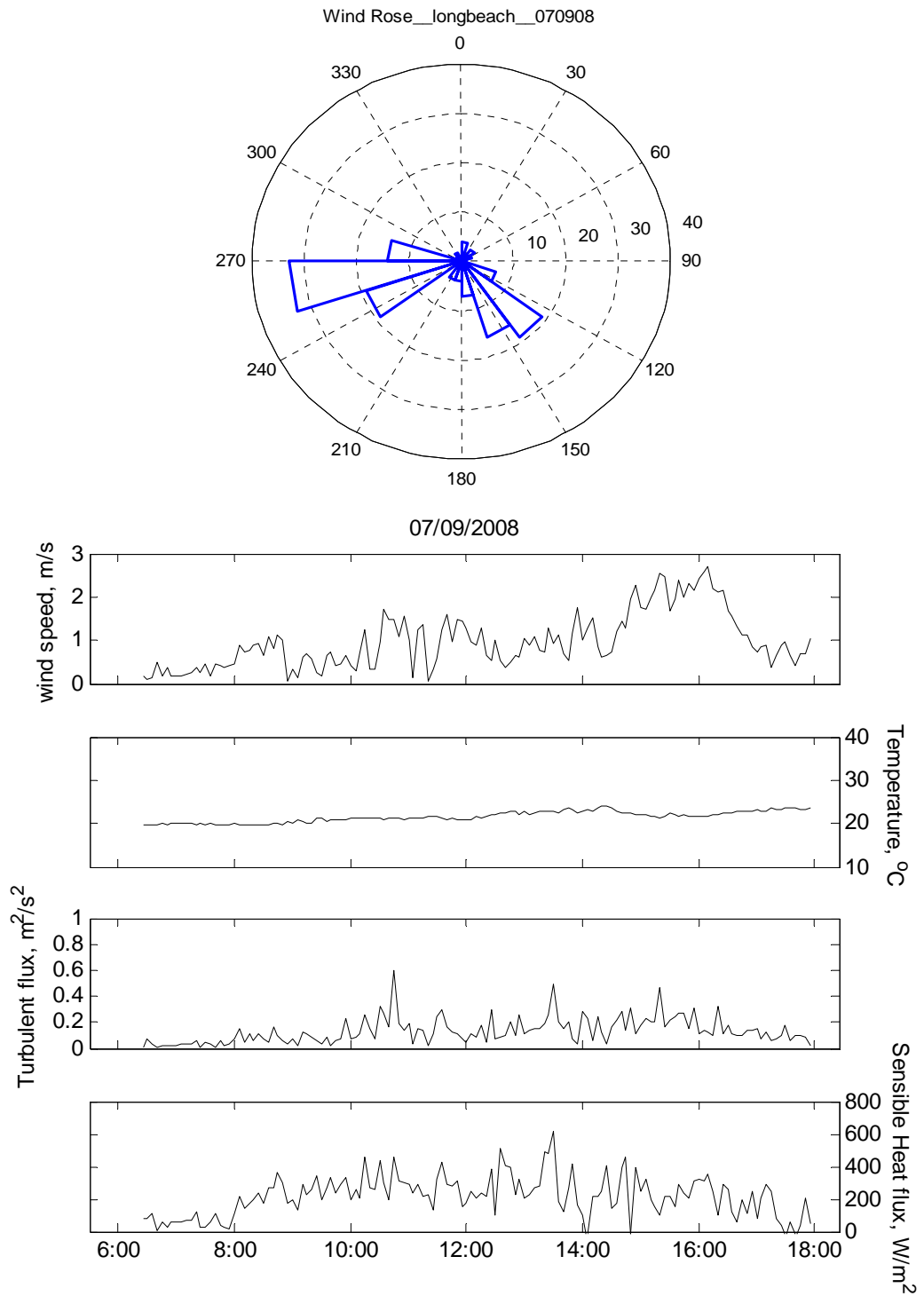


Figure A2.13 Meteorological variables observed in Long Beach on 07/09/2008.

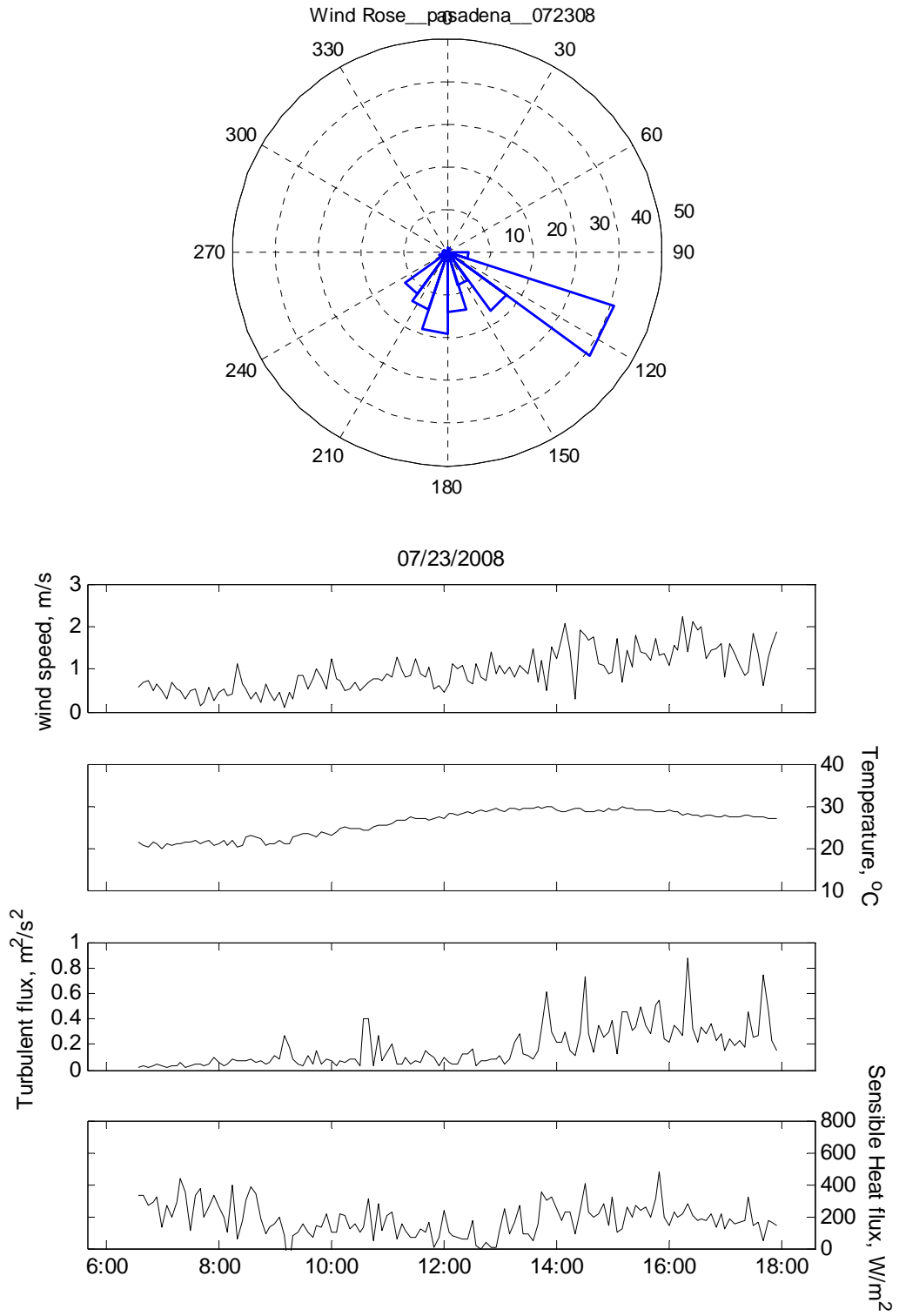


Figure A2.14 Meteorological variables observed in Pasadena on 07/23/2008.

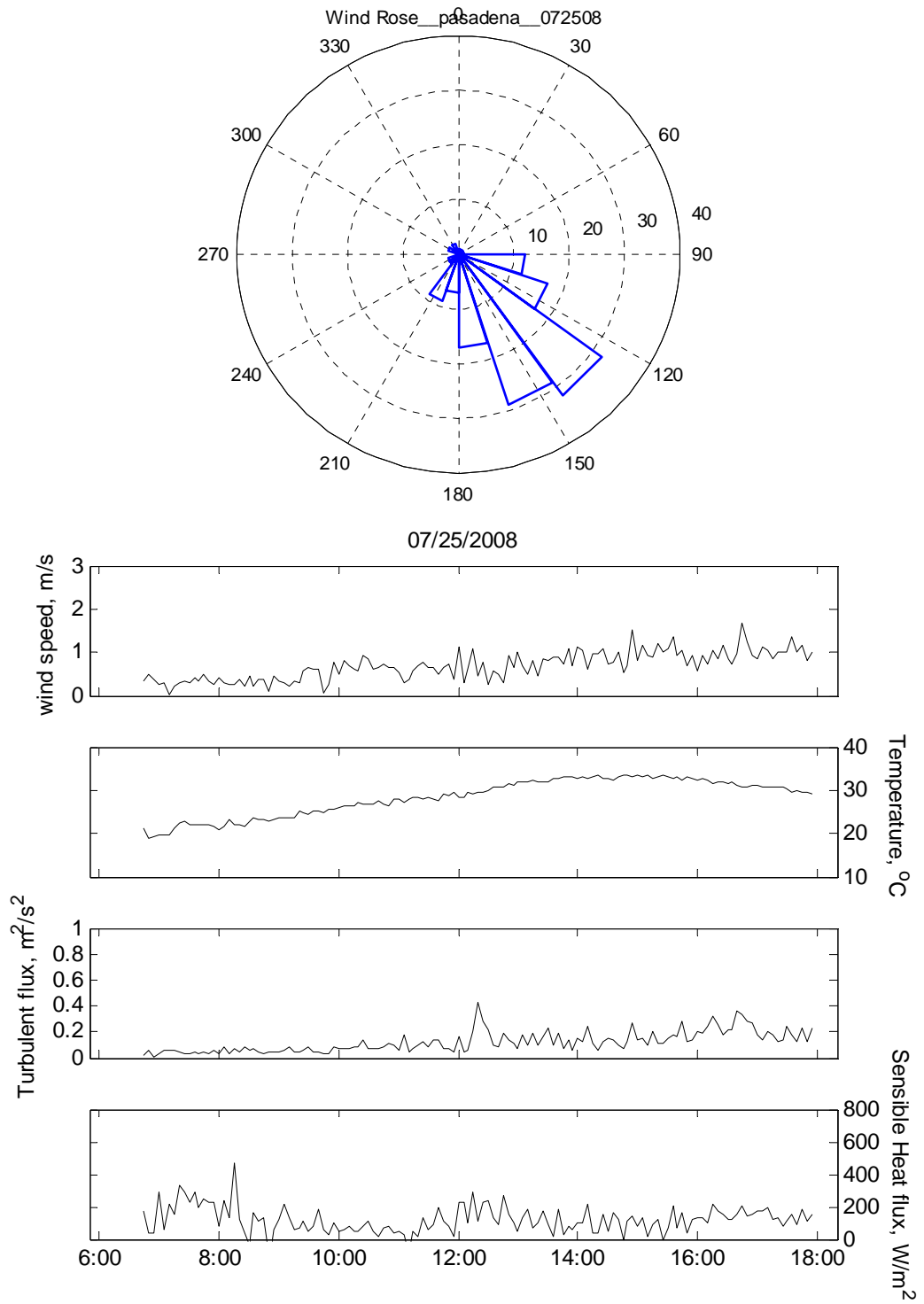


Figure A2.15 Meteorological variables observed in Pasadena on 07/25/2008.

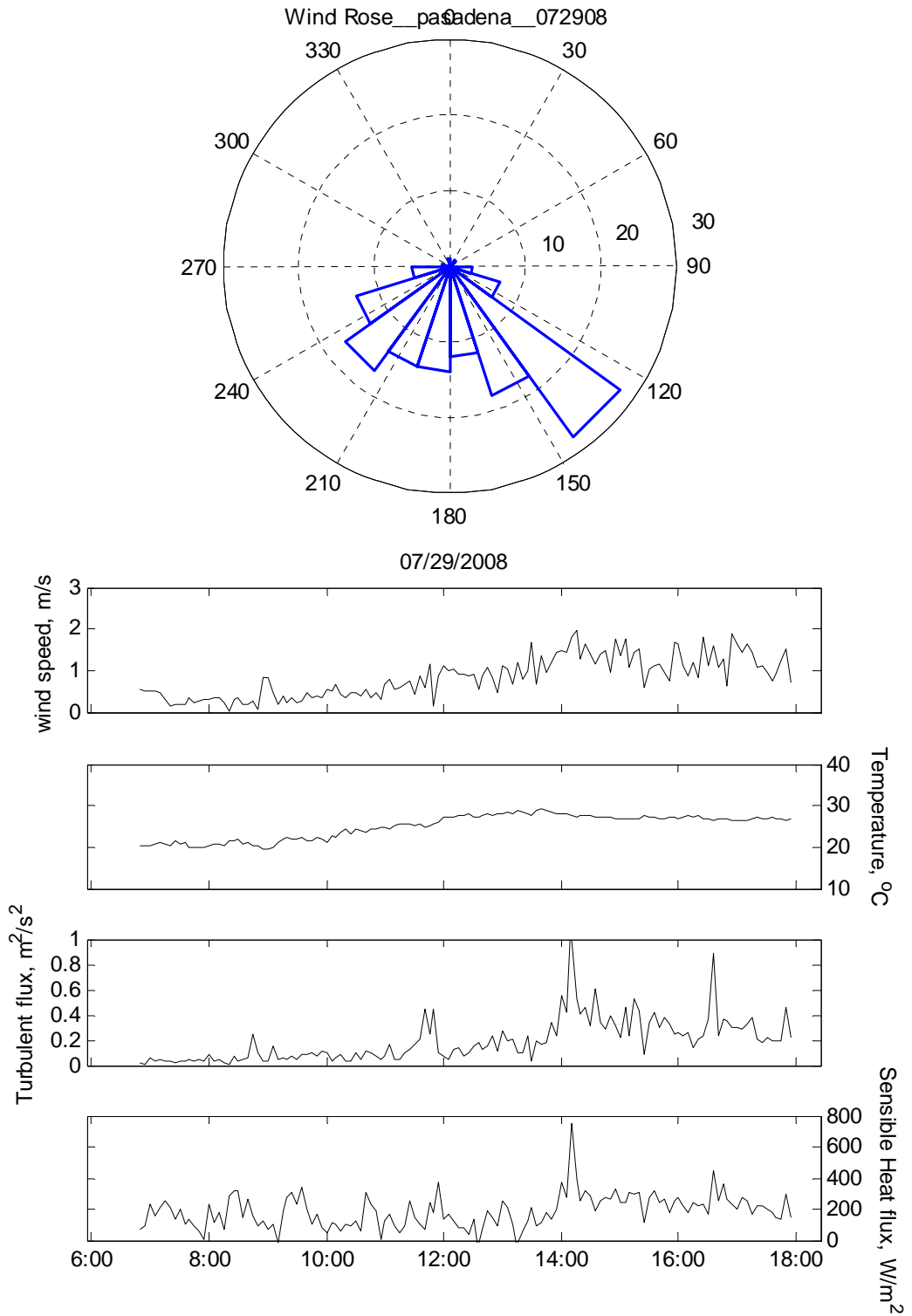


Figure A2.16 Meteorological variables observed in Pasadena on 07/29/2008.

**APPENDIX III: GAM Parameters**

Table A3.1 Parameter coefficients for Intercept and  $C_{bk}$  in GAMs.

City	Term	Estimate	Std.	Error	z value	Pr
LA	Intercept	2.1668318	0.028264	76.66	<2e-16	***
	$C_{bk}$	0.0504052	0.0009005	55.97	<2e-16	***
LB	Intercept	2.071048	0.05477	37.81	<2e-16	***
	$C_{bk}$	0.056171	0.001612	34.85	<2e-16	***
HB	Intercept	3.122691	0.037071	84.23	<2e-16	***
	$C_{bk}$	0.030574	0.001845	16.57	<2e-16	***
PA	Intercept	3.196672	0.0374695	85.31	<2e-16	***
	$C_{bk}$	0.0225776	0.0009801	23.04	<2e-16	***
AN	Intercept	2.305162	0.04132	55.79	<2e-16	***
	$C_{bk}$	0.045901	0.001284	35.74	<2e-16	***

Table A3.2 Parameter coefficients for other variables in GAMs.

City	Variable	edf	Ref. df	Chi.sq	p-value	Significant
LA	$WS$	3.975	5.033	34.302	2.15E-06	***
	$W$	3.724	4.632	24.909	0.000101	***
	$WD$	1.049	1.093	0.012	0.932618	
	$F_t$	2.016	2.575	6.972	0.052203	.
	$F_s$	1.86	2.366	37.546	1.32E-08	***
	$\sigma_w$	1.842	2.354	14.208	0.001286	**
	$TC$	3.975	5.033	34.302	2.15E-06	***
LB	$WS$	3.733	4.65	20.332	0.000795	***
	$W$	1	1	4.325	0.037571	*
	$WD$	3.758	4.688	22.931	0.00026	***
	$F_t$	1.872	2.373	4.42	0.14703	
	$F_s$	1	1	11.859	0.000574	***
	$\sigma_w$	1	1	6.063	0.01381	*



Table A3.2 Parameter coefficients for other variables in GAMs.

		<i>TC</i>					
		3.501	4.399	5.763	0.260767		
HB	<i>WS</i>	2.45	3.146	47.35	3.67E-10	***	
	<i>W</i>	7.926	8.701	40.69	4.41E-06	***	
	<i>WD</i>	6.371	7.549	19.65	0.009	**	
	<i>F<sub>t</sub></i>	2.024	2.58	28.64	1.48E-06	***	
	<i>F<sub>s</sub></i>	4.477	5.618	138.32	2.00E-16	***	
	$\sigma_w$	4.116	5.176	41.93	7.50E-08	***	
	<i>TC</i>	5.939	7.13	71.35	9.25E-13	***	
PA	<i>WS</i>	1	1	0.00024	0.987637		
	<i>W</i>	1	1	0.174	0.677037		
	<i>WD</i>	4.527	5.595	11.52	0.059345	.	
	<i>F<sub>t</sub></i>	1.166	1.306	3.064	0.116707		
	<i>F<sub>s</sub></i>	6.082	7.21	14.72	0.044321	*	

Table A3. 2 Parameter coefficients for other variables in GAMs.

	$\sigma_w$	1	1	0.015	0.902726	
	$TC$	1	1	14.728	0.000124	***
AN	$WS$	1	1	6.902	0.00861	**
	$W$	3.674	4.661	25.82	6.92E-05	***
	$WD$	6.262	7.425	73.512	4.88E-13	***
	$F_t$	1	1	4.163	0.04133	*
	$F_s$	1.867	2.4	3.288	0.2533	
	$\sigma_w$	2.255	2.877	1.866	0.5774	
	$TC$	1	1	0.562	0.45365	

#### **APPENDIX IV: Application of PIV for Flow Measurements around Hovering Hummingbirds**

The flow fields of slowly flying bats and faster-flying birds differ in that bats produce two vortex loops during each stroke, one per wing, and birds produce a single vortex loop per stroke. In addition, the circulation at stroke transition approaches zero in bats but remains strong in birds. It is unknown if these differences derive from fundamental differences in wing morphology or are a consequence of flight speed. Here, we present an analysis of the horizontal flow field underneath hovering Anna's hummingbirds (*Calypte anna*) to describe the wake of a bird flying at zero forward velocity. We also consider how the hummingbird tail interacts with the wake generated by the wings. High-speed image recording and analysis from three orthogonal perspectives revealed that the wing tips reach peak velocities in the middle of each stroke and approach zero velocity at stroke transition. Hummingbirds use complex tail kinematic patterns ranging from in phase to antiphase cycling with respect to the wings, covering several phase shifted patterns. We employed particle image velocimetry to attain detailed horizontal flow measurements at three levels with respect to the tail: in the tail, at the tail tip, and just below the tail. The velocity patterns underneath the wings indicate that flow oscillates along the ventral–dorsal axis in response to the down- and up-strokes and that the sideways flows with respect to the bird are consistently from the lateral to medial. The region around the tail is dominated by axial flows in dorsal to ventral direction. We propose that these flows are generated by interaction between the wakes of the two wings at the end of the upstroke, and that the tail actively deflects flows

to generate moments that contribute to pitch stability. The flow field images also revealed distinct vortex loops underneath each wing, which were generated during each stroke. From these data, we propose a model for the primary flow structures of hummingbirds that more strongly resembles the bat model. Thus, pairs of unconnected vortex loops may be shared features of different animals during hovering and slow forward flight.

#### **A 4.1 Methods for Recording Flow Features in Hovering Hummingbirds**

We measured the flow characteristics of three male Anna's hummingbirds (*C. anna*), captured in Riverside, CA, USA and housed in the vivarium at the University of California Riverside (UCR). The Institutional Animal Care and Use Committee at UCR approved these vertebrate animal procedures.

Prior to each experiment, an individual bird was moved from the vivarium to an experimental flight chamber for 1 day of training in the new setting. The dimensions of the flight chamber were 76 cm × 96 cm × 95 cm high and it was constructed of a PVC frame with walls made of thin plastic sheeting (Figure A4.1). The chamber contained a single perch and one small feeder constructed from a 1-ml syringe. In addition to becoming accustomed to the flight chamber and feeder, we also trained the hummingbirds to feed on command by restricting access to the feeder for 15 min and then only allowing one feeding bout before again restricting access. A feeding bout was defined as a single episode of hovering at the feeder until the bird moved more than approximately two body lengths away in any direction.

Experiments began the day after training and involved the same feeding protocol. A particle image velocimetry (PIV) system was used to measure the instantaneous velocity field in the horizontal plane. The PIV technique measures the velocity in a fluid by correlating images of the particle-seeded flow. For these experiments, atomized food grade olive oil was utilized as the seeding particles. In the minute prior to providing feeder access, we filled the chamber with olive oil mist created using a pressurized oil container equipped with a perforated tube to enable oil-air mixing for adequate atomization.

As the bird approached the feeder, the olive oil particles were illuminated in a plane below the feeder using a horizontal laser sheet with a wavelength of 532 nm (with energy of 388 mJ pulse<sup>-1</sup>) generated by a double-pulsed Nd:YAG laser (Big Sky Laser Technologies, Inc, model CFR400) located 0.5 m from the feeder. The Q-switch was set to 100  $\mu$ s corresponding to approximately medium laser power. The laser beam was expanded into a 20° diverging light sheet using sheet-forming optics, which included a cylindrical lens (-15 mm focal length) and a spherical lens (200 mm focal length). In this way, the beam was transformed into a 200-mm wide and 0.212 mm thick sheet to illuminate seed particles in a horizontal plane close to the bird. In separate experiments, we illuminated three planes: (1) 1 cm above the middle plane, i.e., within the tail, (2) at the tail tip during its cyclical oscillation, and (3) just underneath the tail. A LASERPULSE Synchronizer (TSI Inc.) was utilized to trigger the laser pulse and the camera with correct sequences and timing through a 2.66-GHz dual-processor workstation (Intel® Xeon™). The laser sheet was synchronized with a high-resolution

(1600 × 1192 pixel) POWERVIEW 2M CCD camera (TSI Inc., model 630157) with a 50-mm f/1.8 Nikkor lens and an exposure time of 260  $\mu$ s. Camera aperture was set to 5.6. A total of 15 image pairs per second (15 Hz) were captured. Time difference between the two images in a pair was optimized for the best PIV quality to  $\Delta t = 100 \mu$ s. A grid for the PIV processing was formed using the Nyquist Grid Engine over 64 × 64 pixels interrogation regions. Fast Fourier transform correlation was used with the Gaussian peak engine.

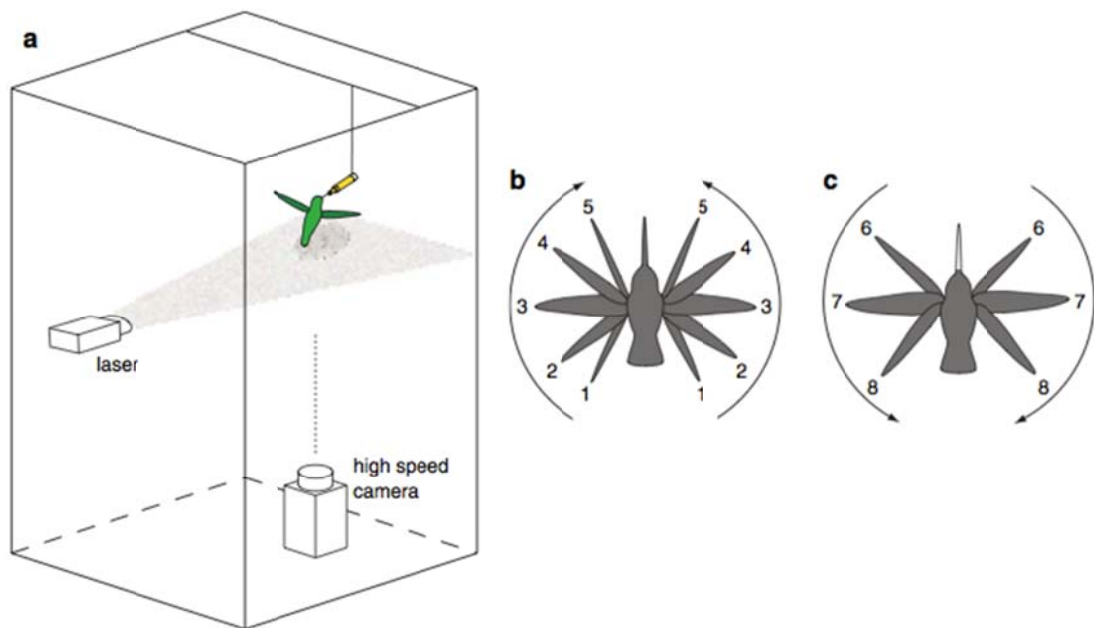


Figure A4.1 a) The experimental chamber used in hummingbird PIV experiments. During different sequences the laser sheet was moved to be either within the tail, at the tail tip, or underneath the tail (shown here). b) The wings were visible in most of the raw images recorded from the camera located underneath the bird. The wing positions were assigned to different numbers indicating the phase within a complete wingbeat cycle. Position 1 corresponds to the wings in the rearward position in the middle of pronation. Positions 2–4 correspond to progressive movement through the downstroke, and position 5 corresponds to the forward position in the middle of supination. c) Positions 6–8 correspond to the wings moving progressively through the upstroke.

We recorded at least ten hovering bouts for each of the hummingbirds, but limited our analysis to the eleven experiments during which the birds maintained constant body orientation through the trial. The instantaneous velocity fields and vorticity were calculated from all image pairs in this group of experiments. The flight chamber was sufficiently large that we could ignore wall influences to the flow because the change in lift per unit wing span due to the chamber walls (Katz and Plotkin 2001)

$$\Delta L = \frac{\pi^2 c^2}{24h^2} \sim 0.01 \ll 1$$

A4.1

where  $h$  is chamber height, and  $c$  is the wing span.

We further narrowed our analysis to the velocity measurements (i.e., image pairs) that could be grouped into one of eight wing positions within a complete wingbeat cycle (see Figure A4.1b, c). This was accomplished by visual assignment of wing positions based upon each raw image. Arranging the measurements by wing position allowed us to compile a stroke sequence of velocity and vorticity profiles even though the images came from separate wingbeats. It is important to note that the wing tip velocity is greatest during mid-stroke and slowest during stroke transition. Therefore the time difference between wing positions (average  $\sim 3$  ms) was not constant.

The different experiments yielded different perspectives of the bird and wake both due to design and behavioral variability. In the former case, we moved the camera either closer to the feeder thereby focusing on the front (ventral) half of the stroke cycle or  $\sim 10$  cm further away from the feeder to focus on the back (dorsal) half of the stroke cycle. In

the latter case, the bird fed at different angles relative to the feeder in the horizontal plane providing either a left or right bias. To facilitate comparisons among these multiple views, we calculated velocity over specific regions of interest (ROI) and along bird-centered axes. The ROIs were constrained to one of three positions: (1) underneath either the left or right wing on the front (ventral) side of the bird, including wing positions 3–7; (2) underneath either the left or the right wing on the back (dorsal) side of the bird, including wing positions 1–3 and 7–8; (3) underneath the tail in a narrow region that covered the full range of tail movement. The original velocity vector components in the  $x$  and  $y$  axes,  $u$  and  $v$ , respectively, were rotated to along the bird component,  $V_s$  (positive from ventral to dorsal) and to a component that is perpendicular to the ventral–dorsal axis,  $V_n$  (positive when moving from the bird’s lateral right to lateral left).

Within a filmed hovering bout, the velocities were averaged over all frames corresponding to the same wing position and the same ROIs were used for all frames. Because the area of the ROIs differed across experiments, we restricted our analysis to within experiment results rather than combining experiments to generate average values.

On average, the measured flow field was 5 cm below the wing stroke plane. We assumed the vertical velocity to be  $U_{vert} \sim 2 \text{ m s}^{-1}$  based upon measurements from similarly sized rufous hummingbirds, *S. rufus* (Warrick et al. 2005). Thus, it is estimated to require an average of 25 ms for the flow structures to be advected from the wing to the measuring plane. Because the wingbeat frequency is  $\sim 40 \text{ Hz}$  (corresponding to a wingbeat period of 25 ms), the measured flow field should be lagging by the full cycle behind the actual wing stroke visible on the raw PIV image.



Another important reason why we avoided combining experiments for analytical purposes is that the vertical distance between the wings and the measuring plane—and thus the time lag—differed across experiments. Within each experiment, the hummingbirds maintained a constant body orientation and the time lag between wake generation and measurement is invariant. However, across experiments, hummingbirds used slightly different body angles, which should produce slight phase shifts in the wingbeat and PIV measurement cycles. Accordingly, we present results for individual experiments and then focus on the common features among experiments to develop a model of the wake of hovering hummingbirds.

#### **A 4.2 Results of Flow Measurements**

A representative trial with a perspective on the bird's ventral, right region is presented in Figure A4.2. Across wing positions the along bird velocity component  $V_s$ , in the wing domain, exhibits a clear pattern of flow reversal from ventral to dorsal. The average  $V_s$  value is close to 0. The perpendicular to bird velocity component  $V_n$ , in the wing domain, indicates net flow from lateral to medial because velocity moving from the lateral right to the lateral left is indicated with positive values.

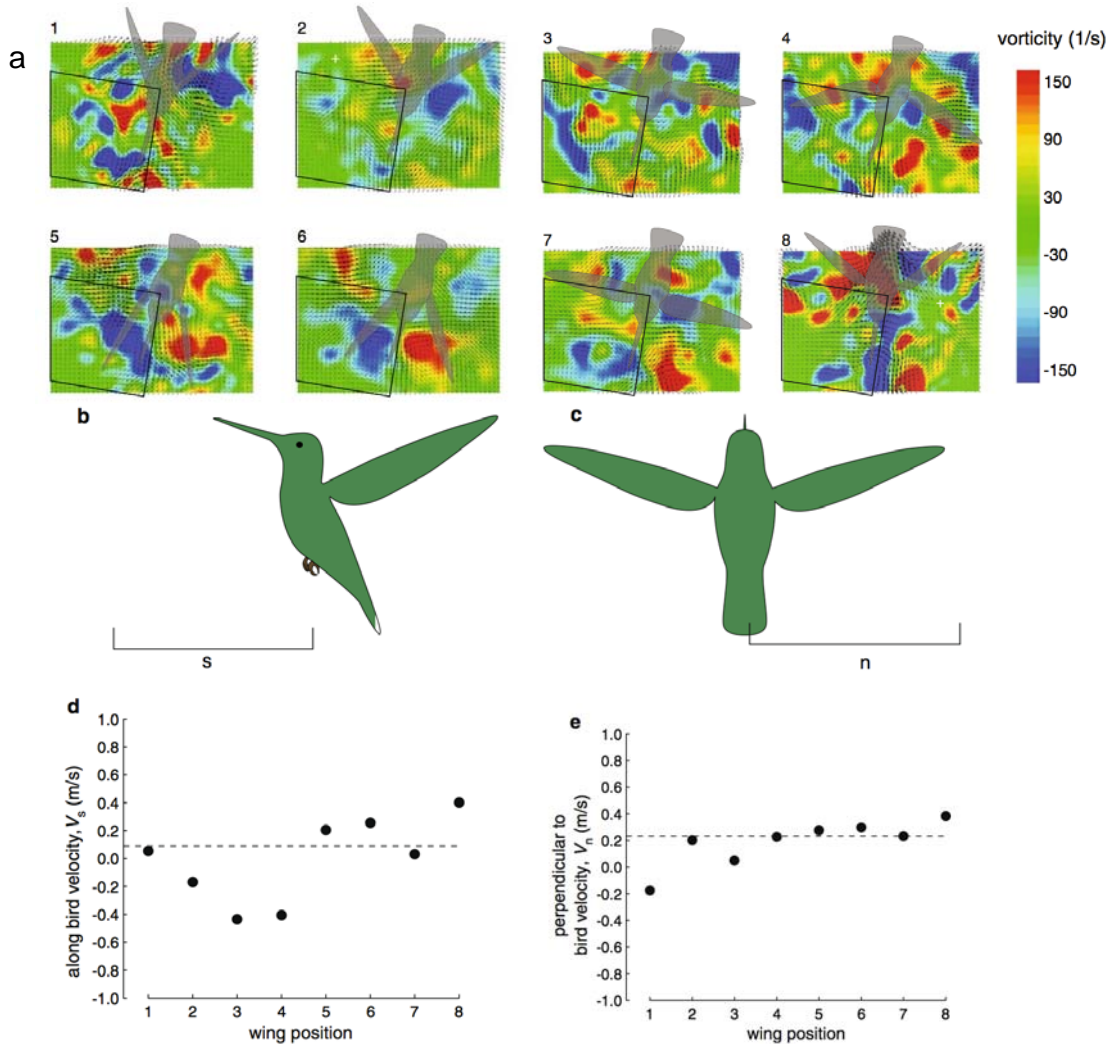


Figure A4.2 Representative analysis of the wake underneath a wing, using experiment 5 as an example. a) The raw images that contained the same wing position image were averaged to produce a color plot containing the vorticity (colors) and velocity vectors (arrows). The eight wing positions are numbered using the system described in Figure A4.1b, c. Within each plot, a black polygon represents the region of interest over which velocity was calculated along the bird ( $V_s$ ) and perpendicular to the bird ( $V_n$ ). A small white cross indicates the center of the vortex loop if present. b) The side view of an idealized hovering hummingbird, with the bottom of the black bracket indicating the planar region quantified in this dimension and the location of the laser sheet underneath the tail. c) The backview of an idealized hummingbird, with the analogous perspective on the region of interest and level of the laser sheet. d) The along bird velocity ( $V_s$ ) across the eight wing positions. The dashed horizontal line indicates the mean velocity across all positions. e) The perpendicular to bird velocity ( $V_n$ ) across the eight wing positions.

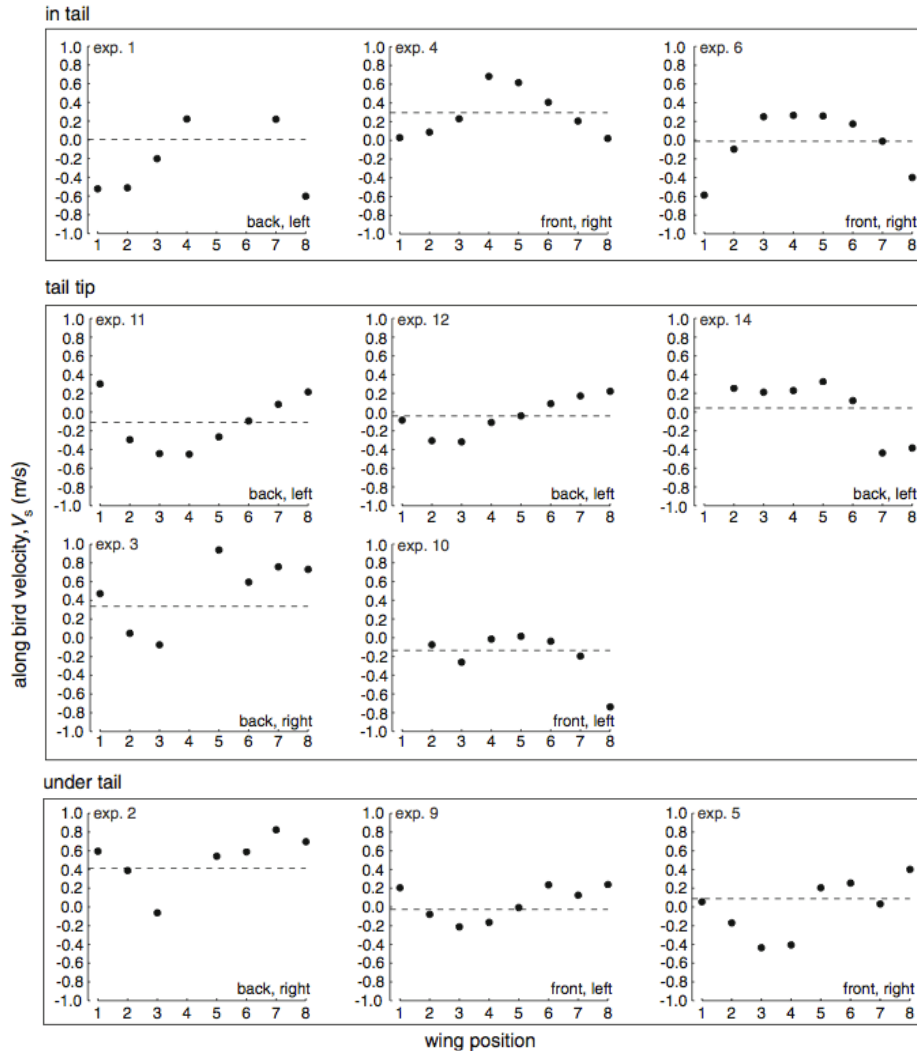


Figure A4.3 Along bird velocity plots in the wing domain. The individual experiments are arranged first by tail position (grouping boxes), then by back to front, and lastly by left to right. Experiments 1–5 come from bird 1. Experiment 6 comes from bird 2. Experiments 9–14 come from bird 3. The wing positions are indicated on the x-axis. The dashed line indicates the mean value across all wing positions

We further calculated the velocity components in the wing domain for all sequences in which the wings could be identified while the birds maintained stable positions. The along bird velocity components in the wing domain for this set of experiments is given in Figure A4.3. Three measuring planes are referred as: in tail

(highest), tail tip (middle) and under tail (lowest). No unique pattern was observed across different experiments, but the hummingbird used different body angles in different experiments and the ROIs were not identical between any two trials. For most of the experiments there is a similar pattern for the same measuring plane. For the highest measurement plane, velocity maxima are observed for wing positions 4–5, and minima are observed for positions 1–2 and 7–8. For the middle and lowest measurement planes, the overall pattern is shifted such that the velocity minima are observed for wing positions 2–3. This apparent change in phase can be attributed to different distances between wing and measuring plane. Flow reversal, from head to tail and from tail to head, is observed in most but not all experiments.

The full experimental results for the normal to the bird velocity component,  $V_n$ , in the wing domain are presented in Figure A4.4. Throughout all experiments, velocity is from lateral to medial, i.e., the values are consistently negative for ROIs on the left side of the birds and consistently positive for ROIs on the right side of the birds.

We further examined the subset of experiments that included complete views of the region around the tail oscillations. A representative sequence is provided in Figure A4.5. The along bird velocities in the tail domain are presented in Figure A4.6. Almost without exception, the velocities are positive across all wing positions, indicating that the net flow is in the ventral to dorsal direction for the region around the tail. In the majority of experiments in the upper and middle planes, the  $V_s$  velocity is minimal at positions 1–2 and 8. Taken together with our assumed lag of the wing wake, these data suggest that the

bird is using its tail to deflect the outgoing flow caused by wings. In the lowest measuring plane for which we have only a single sample, this minimum is phase shifted.

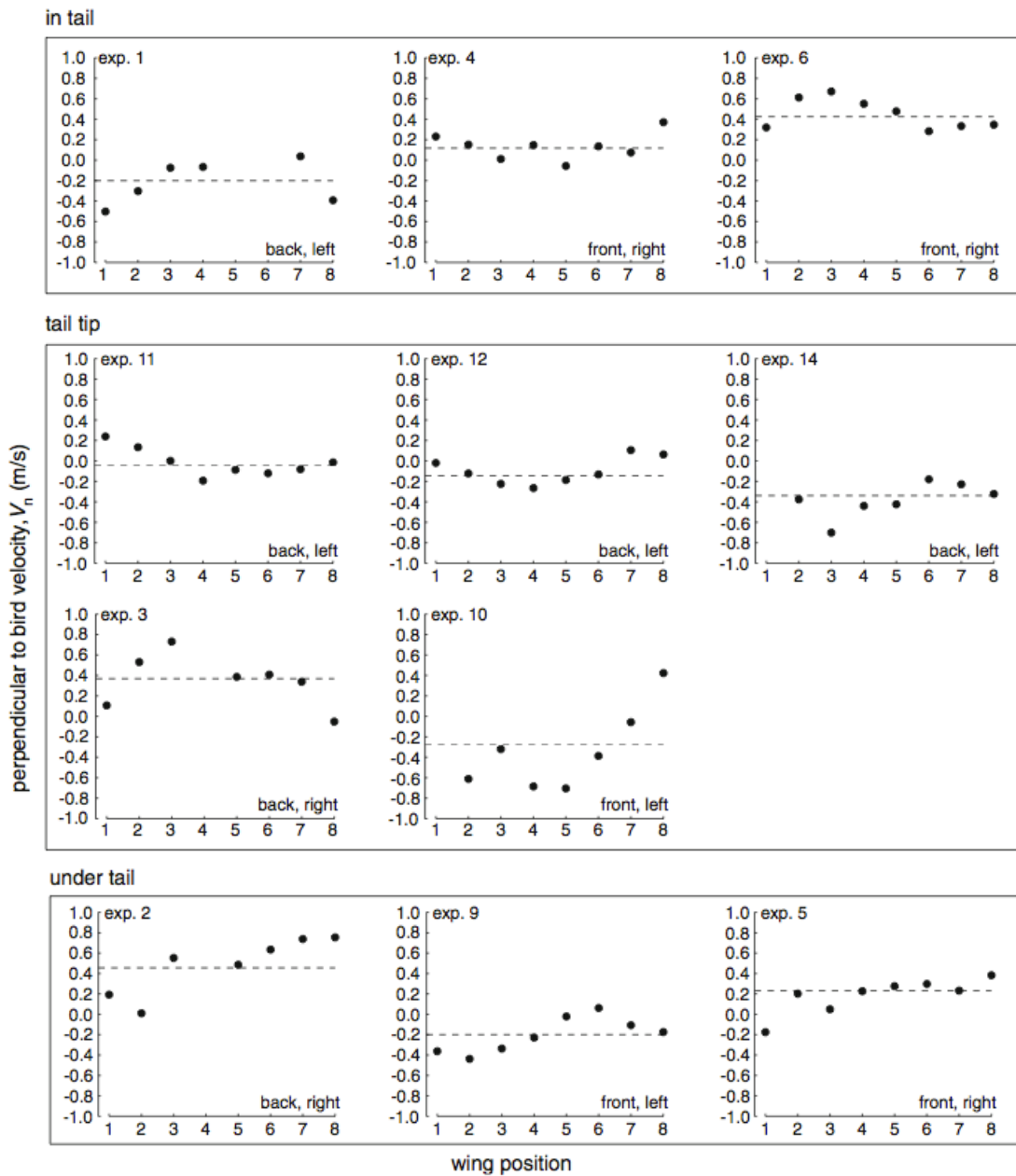


Figure A4.4 Perpendicular to bird velocity plots in the wing domain. Note that all left perspectives have net negative velocities and all right perspectives have net positive

velocities, indicating consistent flow from the periphery toward the bird. Details as in Figure A4.3

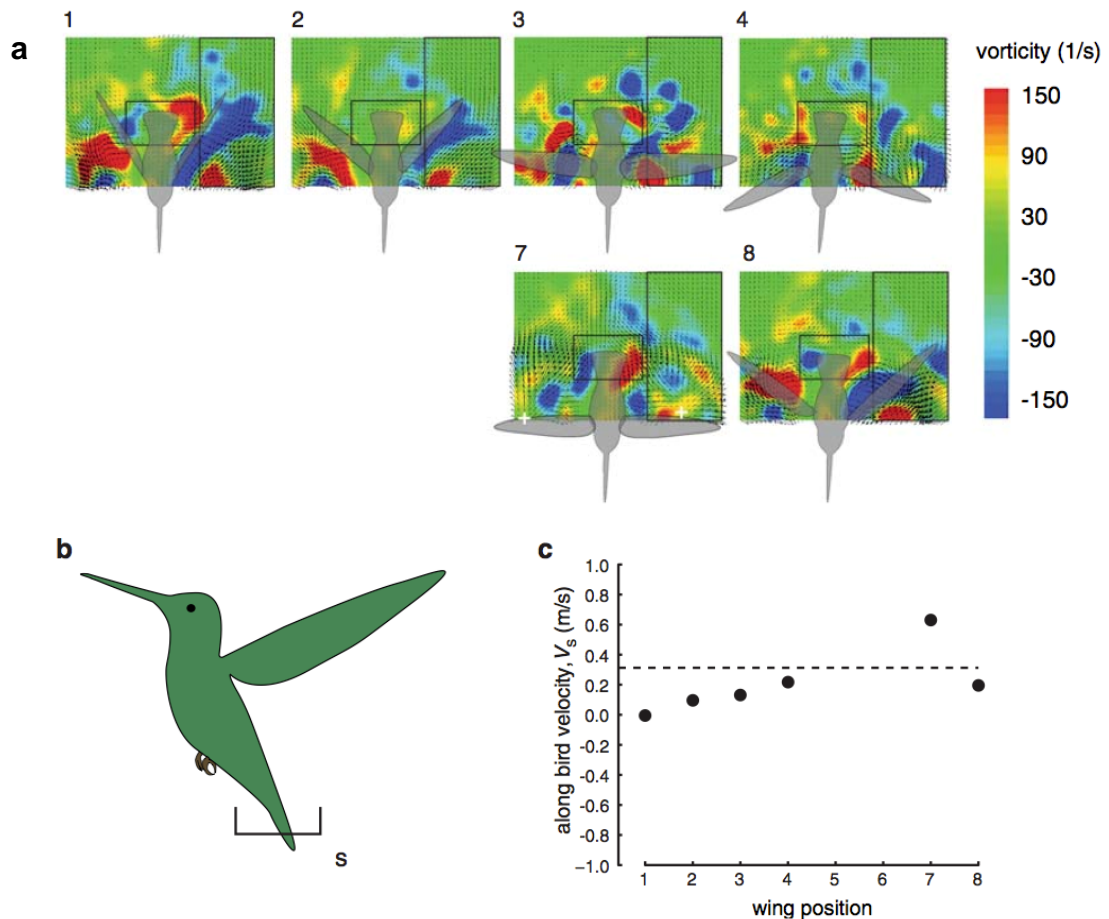


Figure A4.5 Representative analysis of the wake underneath a tail, using experiment 1 as an example. a) The color plots are configured using the same arrangement as in Figure A4.2. However, these images were centered on the tail and wing positions 5 and 6 could not be identified because the both wings were out of view. Velocity was calculated only for the along bird ( $V_s$ ) dimension. A small white cross indicates the center of the vortex loop if present. b) The side view of an idealized hovering hummingbird, with the black bracket indicating the region quantified in this dimension and the location of the laser sheet underneath the tail. c) The along bird velocity ( $V_s$ ) across the six available wing positions. Details as in Figure A4.2d, e.

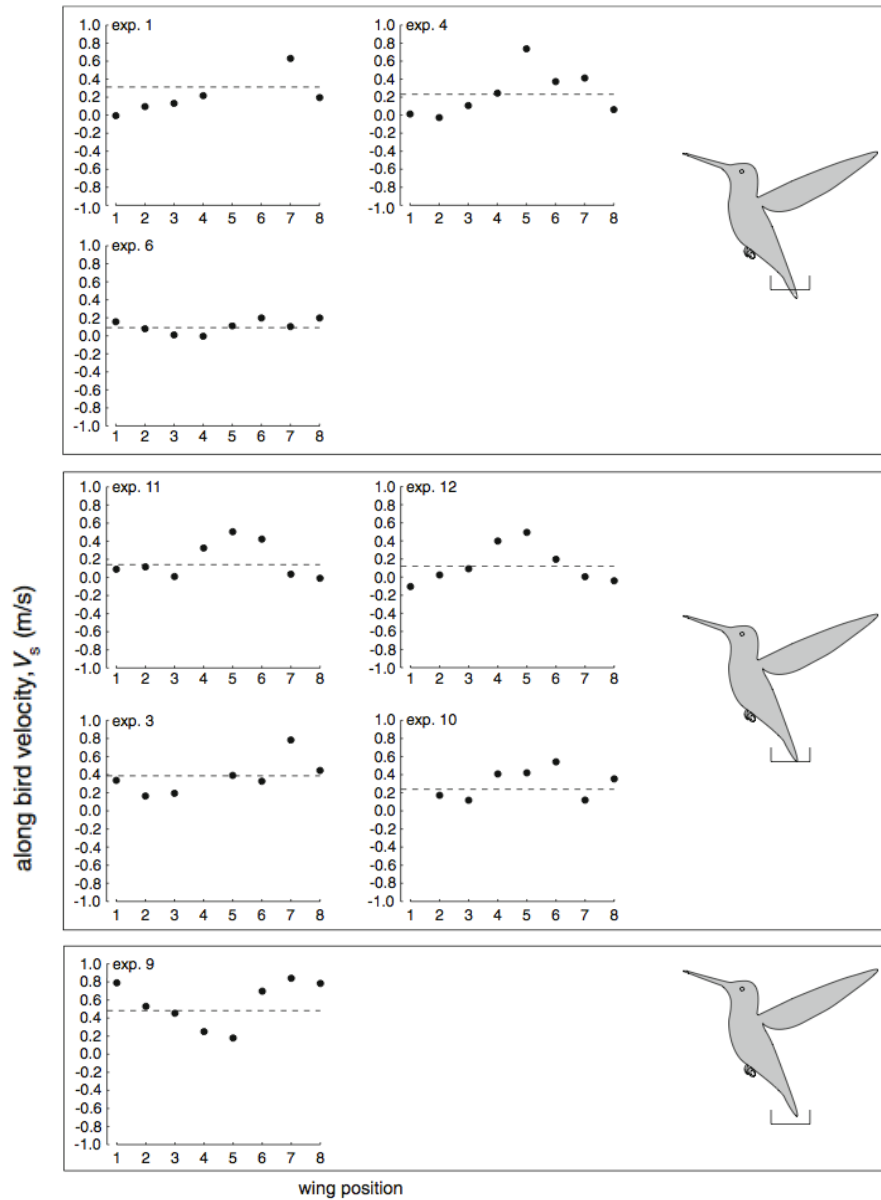


Figure A4.6 Along bird velocity plots in the tail domain. Details as in Figure A4.3.

In addition to measuring the net velocities with the ROIs, we also considered the mass flux over the entire measuring field to identify prominent sites with out of plane flow. These sites are indicated by discrete regions in which velocity emerges in all direction thereby suggesting the center of vortex ring or loop. In every experiment, we



identified at least one, and usually two, wing positions in which there was evidence for vortex loops. Examples can be seen under the right wing for position 2 and under the left wing for position 8, in Figure A4.2. A small white cross indicates the centers of these loops. For experiments in which both sides of the animal were visible, we identified separate vortex loops on either side of the animal. A coarse example of this pattern can be seen in wing position 7 in Figure A4.5. In Figure A4.7 we present a series of representative instantaneous velocity fields from two experiments that clearly indicate the existence of vortex loops that are present during both up- and down-strokes and that are underneath both wings.

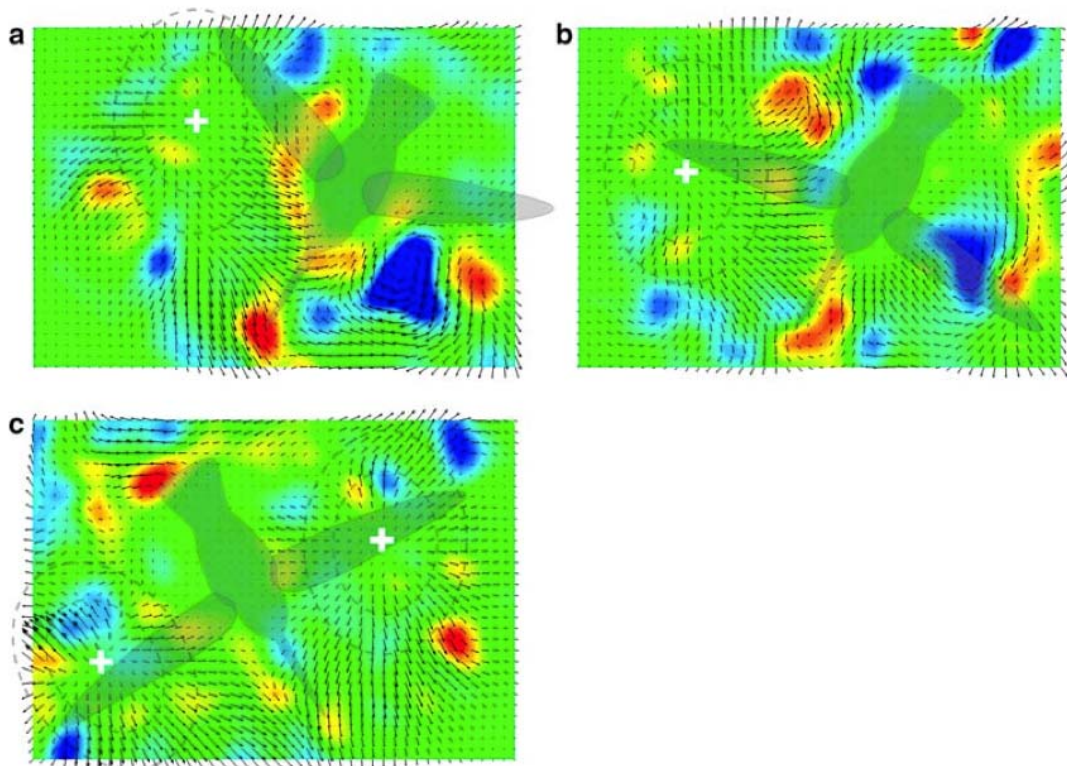


Figure A4.7 Examples of prominent vortex loops. The flow fields in experiment 6 revealed prominent vortex flow structures at bird wing positions 2 (a) and 7 (b), which



presumably correspond to vortices shed during down- and up-strokes respectively. The flow fields from experiment 14 were particularly illustrative of separate flow structures underneath each wing at wing position 7 (c). Note that these images come from single frame pairs and are not averaged across wing positions as was the case in previous flow field plots. The actual positions of the birds and their wing positions are shaded in translucent gray and the hypothesized vortex loops are marked by dashed lines. A small white cross indicates the center of each vortex loop.

### **A 4.3 Discussion**

Measurements of the hovering hummingbird wake in the horizontal plane near the tail revealed three general patterns of flow velocity: (1) Along the ventral–dorsal axis underneath the wings, air flow switches direction more or less sinusoidally indicating the influence of forwards (downstroke) and backwards (upstroke) movement of the wings (Figure A4.3); (2) Perpendicular to this axis, underneath the wings, air flows from the periphery (lateral) in toward to the region underneath the hummingbird’s body (medial) but with varying intensity (Figure A4.4); (3) In a small region around the tail, the air flow is consistently oriented along the head–tail axis and away from the body (Figure A4.6). In addition, we see clear evidence for separate vortex loops that are shed underneath each wing, and separate loops that are shed during down- and up-strokes.

As is the case for other PIV measurements from real flying animals, these flow fields reveal a complex wake that contains many disrupted structures and secondary flows. Furthermore, the patterns of flow reversal do not fit perfect sinusoids as might be expected. However, it is unrealistic to expect invariant flow fields with perfect sinusoids because real hummingbirds exhibit differences in angle of attack, airfoil shape and stroke period between down- and up-strokes (Tobalske et al. 2007; Warrick et al. 2005; D.L.

Altshuler, unpublished data). Additionally, we expect that the animals make rapid adjustments to these and other kinematic features to control stability, which will produce flow fields that vary across wingbeats.

It is not possible to infer the complete three-dimensional structure of the hummingbird's wake from the single perspective described here. Although there are relatively few measurements of the flow fields of different flying animals, we can compare our results with previous studies of forward flight in pigeons (Spedding et al. 1984), passerines (Hedenstroöm et al. 2006; Rosé'n et al. 2007; Spedding et al. 2003) and bats (Hedenstroöm et al. 2007; Muijres et al. 2008). In addition to these vertebrate fliers, the flow fields of numerous insect taxa have been measured during hovering and forward flight (Bomphrey et al. 2005, 2006; Brodsky 1991; Grodnitsky and Dudley 1996; Grodnitsky and Morozov 1992, 1993; Srygley and Thomas 2002; Willmott et al. 1997). Most of these invertebrate studies concerned single vertical perspectives oriented along the body axis and therefore do not provide information about the contributions of bilateral wings to overall flow field structures. However, Bomphrey et al. (2006) constructed a composite view from serial sections and concluded that the Tobacco Hawkmoth (*Manduca sexta*) uses its wings to produce a single vortex loop during downstroke in forward flight.

Wake descriptions from slow-flying bats and faster-flying birds differ in two fundamental aspects: (1) bat wings produce two vortex loops whereas birds produce a single vortex loop per stroke, and (2) bats do not exhibit strong circulation during stroke

transitions unlike birds. Our data indicate that during hovering flight, hummingbirds more strongly resemble the bat pattern. First, we see clear evidence for separate vortex loops for each wing (Figure A4.7). Second, our kinematic results indicate that wingtip velocities approach 0 at stroke transition whereas for other birds during forward flight airstream velocity at the wing tips remains high. Because aerodynamic forces are proportional to the square of velocity, vortex generation should cease as the wings decelerate near stroke transition for hovering hummingbirds. It would be highly informative to consider the flow field patterns of hummingbirds across a wide range of flight speeds.

Combining the results from velocities and vorticity leads to a model for the principal flow structures in hovering hummingbirds (Figure A4. 8). The vortex loops shed during downstrokes move ventrally and loops shed during upstroke move dorsally. As air is sucked into these vortices, the principle mass comes from lateral to the bird because the bird's body acts as a boundary. Thus, the vortex loops move from lateral to medial.

With this model in mind, we can now consider the how the tail interacts with the wing wake. Although the tail oscillates with an approximately sinusoidal motion, the velocities around the actual tail are either 0 or positive, indicating net flow along the body axis but away from the bird. These velocities have high magnitudes and are almost certainly not a consequence of the wake imparted by the tail motion. Instead, these flows are likely the result of wake encounter by the two wings coming toward each other during

the end of the upstroke. We hypothesize that the tail is deflecting these larger flows, although the magnitude of interference with the wake will depend upon the degree of tail spreading and the precise phasing of tail oscillation. Because the magnitude of the pressure force will be proportional to the square of the velocity, the hummingbird should have the capability of generating tail moments of sufficient size to use this structure in maintaining pitch stability.

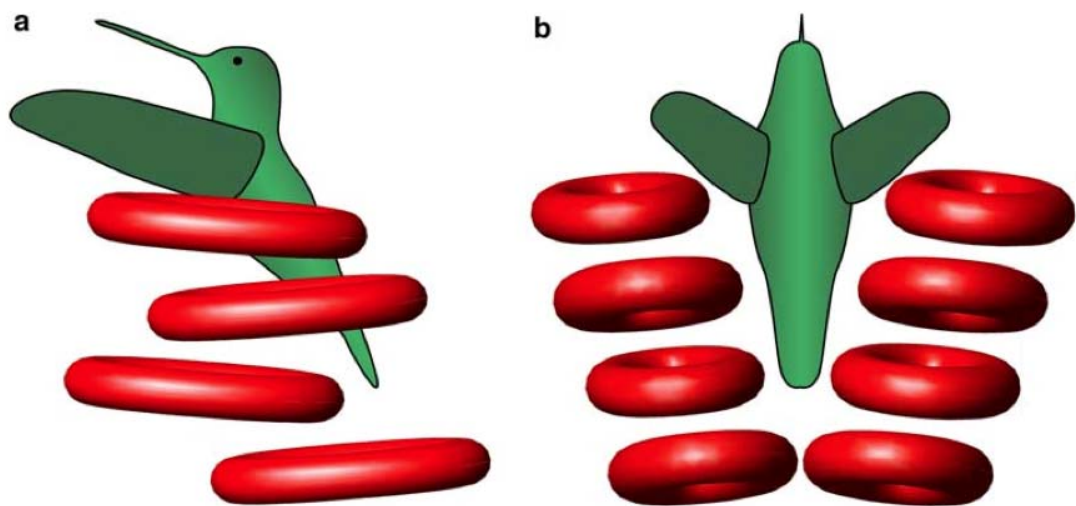


Figure A4. 8 Proposed model for the principal vortex wake structures of hovering Anna's hummingbirds, with left lateral (a) and dorsal (b) views. The vortex loops are elliptical in shape, being longer in the ventral–dorsal than the lateral-medial axis. Two prominent structures are produced during each wingbeat cycle when the wings reach maximum velocity during the up- and down-strokes. The vortices shed during downstrokes move ventrally and vortices shed during upstrokes move dorsally. All vortex loops move from lateral to medial positions after shedding. Other, less prominent flow structures such as cross-stream vorticity are not illustrated.

In this communication, we focus on the analysis of the mean flow patterns for different wing and tail positions. This was done using measured horizontal velocity components in the horizontal plane. Although it is our eventual goal, at this stage we are not attempting to explain the force balance of the hovering bird through momentum or

vorticity analysis because such computations would have to involve doubtful assumptions pertaining to the full three-dimensional flow field surrounding the bird. Dabiri (2005) demonstrated that the spatial velocity distribution in the wake is not sufficient for determination of locomotive forces but has to be combined with the pressure distribution. He proposed a method for accounting for the pressure contribution via wake vortex added-mass in analogy with the added-mass of fluid surrounding solid bodies.

At the present state, computational fluid dynamics and direct numerical simulation cannot be applied with confidence to bird flight. To develop and validate numerical models and to obtain information needed for analytical models (e.g., information to quantify added-mass tensor component proposed by Dabiri 2005) more detailed measurements are required. New technologies for real three-dimensional flow measurements should provide the necessary information, and can be combined with a numerical model to extract the pressure fields needed for full force balance analysis. In addition, such pressure estimates can be validated against existing, limited, pressure measurements (e.g., as in Usherwood et al. 2005). Particle tracking velocimetry can be applied directly to determine the Lagrangian properties of the flow, which can be used to determine the added-mass contributions (Dabiri 2005; Darwin 1953).

**Reference:**

Bomphrey RJ, Lawson NJ, Harding NJ, Taylor GK, Thomas ALR (2005) The aerodynamics of *Manduca sexta*: digital particle image velocimetry analysis of the leading-edge vortex. *J Exp Biol* 208:1079–1094

- Bomphrey RJ, Lawson NJ, Taylor GK, Thomas ALR (2006) Application of digital particle image velocimetry to insect aerodynamics: measurement of the leading-edge vortex and near wake of a Hawkmoth. *Exp Fluids* 40:546–554
- Brodsky AK (1991) Vortex formation in the tethered flight of the peacock butterfly *Inachis io* L. (Lepidoptera, Nymphalidae) and some aspects of insect flight evolution. *J Exp Biol* 161:77–95
- Dabiri JO (2005) On the estimation of swimming and flying forces from wake measurements. *J Exp Biol* 208:3519–3532
- Darwin C (1953) Note on hydrodynamics. *Proc Camb Philos Soc* 49:342–354
- Grodnitsky DL, Dudley R (1996) Vortex visualization during free flight of Heliconiine butterflies (Lepidoptera: Nymphalidae). *J Kans Entomol Soc* 69:199–203
- Grodnitsky DL, Morozov PP (1992) Flow visualization experiments on tethered flying green lacewings *Chrysopa dasyptera*. *J Exp Biol* 169:143–163
- Grodnitsky DL, Morozov PP (1993) Vortex formation during tethered flight of functionally and morphologically two-winged insects, including evolutionary considerations on insect flight. *J Exp Biol* 182:11–40
- Hedenström A, Rose´n M, Spedding GR (2006) Vortex wakes generated by robins *Erithacus rubecula* during free flight in a wind tunnel. *J R Soc Interface* 3:263–276
- Hedenström A, Johansson LC, Wolf M, von Busse R, Winter Y, Spedding GR (2007) Bat flight generates complex aerodynamic tracks. *Science* 316:894–897
- Katz J, Plotkin A (2001) *Low speed aerodynamics*, 2nd edn. Cambridge University Press, Cambridge
- Muijres FT, Johansson LC, Barfield R, Wolf M, Spedding GR, Hedenström A (2008) Leading-edge vortex improves lift in slow-flying bats. *Science* 319:1250–1253
- Rose´n M, Spedding GR, Hedenström A (2007) Wake structure and wingbeat kinematics of a house martin *Delichon urbica*. *J R Soc Interface* 4:659–668
- Spedding GR, Rayner JMV, Pennycuik CJ (1984) Momentum and energy in the wake of a pigeon (*Columba livia*) in slow flight. *J Exp Biol* 111:81–102
- Spedding GR, Rose´n M, Hedenström A (2003) A family of vortex wakes generated by a thrush nightingale in free flight in a

wind tunnel over its entire natural range of flight speeds. *J Exp Biol* 206:2313–2344

Srygley RB, Thomas ALR (2002) Unconventional lift-generating mechanisms in free-flying butterflies. *Nature* 420:660–664

Usherwood JR, Hedrick TL, McGowan CP, Biewener AA (2005) Dynamic pressure maps for wings and tails of pigeons in slow, flapping flight, and their energetic implications. *J Exp Biol* 208:355–369

Warrick DR, Tobalske BW, Powers DR (2005) Aerodynamics of the hovering hummingbird. *Nature* 435:1094–1097

Willmott AP, Ellington CP, Thomas ALR (1997) Flow visualization and unsteady aerodynamics in the flight of the hawkmoth, *Manduca sexta*. *Phil Trans R Soc Lond B* 352:303–316

## **APPENDIX V: Application of PIV for Measurements of Mixing Efficiency of a Micromixer**

Proper mixing of reagents is of paramount importance for an efficient chemical reaction. While on a large scale there are many good solutions for quantitative mixing of reagents, as of today, efficient and inexpensive fluid mixing in the nanoliter and microliter volume range is still a challenge. Complete, i.e., quantitative mixing is of special importance in any small-scale analytical application because the scarcity of analytes and the low volume of the reagents demand efficient utilization of all available reaction components. In this paper we demonstrate the design and fabrication of a novel centrifugal force-based unit for fast mixing of fluids in the nanoliter to microliter volume range. The device consists of a number of chambers (including two loading chambers, one pressure chamber, and one mixing chamber) that are connected through a network of microchannels, and is made by bonding a slab of polydimethylsiloxane (PDMS) to a glass slide. The PDMS slab was cast using a SU-8 master mold fabricated by a two-level photolithography process. This microfluidic mixer exploits centrifugal force and pneumatic pressure to reciprocate the flow of fluid samples in order to minimize the amount of sample and the time of mixing. The process of mixing was monitored by utilizing the planar laser induced fluorescence (PLIF) technique. A time series of high resolution images of the mixing chamber were analyzed for the spatial distribution of light intensities as the two fluids (suspension of red fluorescent particles and water) mixed. Histograms of the fluorescent emissions within the mixing chamber during different stages of the mixing process were created to quantify the level of mixing of the



mixing fluids. The results suggest that quantitative mixing was achieved in less than 3 min. This device can be employed as a standalone mixing unit or may be integrated into a disk-based microfluidic system where, in addition to mixing, several other sample preparation steps may be included.

This work presents the design and fabrication of a centrifugal-based microfluidic unit for continuous mixing of small-scale (up to 30  $\mu$ l) volumes of fluids in a disposable unit made from a polydimethylsiloxane (PDMS) slab and a glass slide as depicted in Figure A5.1c. The unit could be used as a stand-alone micromixer or it could be integrated onto a disk-based microfluidic integrated lab-on a disk system that may incorporate other functionalities, for example, sample lysis, separation of biomaterials, amplification of nucleic acids, detection of biomolecules, and other functions, as determined by the intended use and process flow of the device.

A two-level SU-8 master mold was fabricated using standard photolithographic methods to create shallow features including a mixing chamber and a network of channels, and deep features including two reservoirs for initial storage of the two fluids to be mixed, and another reservoir for storing pneumatic pressure. Centrifugal force (Lai et al., 2004) and the resulting pneumatic pressure accumulated in the system were utilized to propel the two fluids to be mixed into the mixing chamber in a reciprocating manner (Figure A5.1a). In order to be able to follow and quantify the level of mixing, the fluid injected into the first reservoir consisted of an aqueous suspension of fluorescently labeled polystyrene particles in water, while the second fluid was water alone. The

process of mixing was monitored using the planar laser induced fluorescence (PLIF) technique, which is a nonintrusive method for measuring scalar concentration in fluids. In this technique the level of local fluorescence emissions induced by laser excitation is proportional to particle/dye concentration. A time series of high-resolution images of the mixing chamber were analyzed for the spatial distribution of light intensities as the two fluids mixed. The experimental result showed that complete mixing was achieved in less than 3 min.

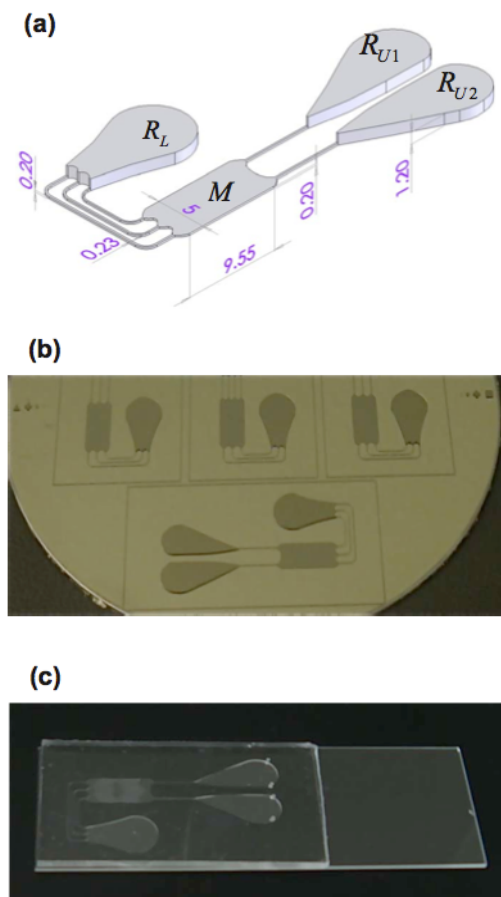


Figure A5.1 Microfluidics mixer cartridge. (a) Schematic illustration of micromixer unit; all units are in millimeters; (b) Photography of the of the SU-8 casting master mold; (c) Photography of the assembled PDMS/ glass slide unit.

## A 5.1 Image System Setup

The PLIF was used for concentration measurements (Crimaldi, 2008; Arratia and Muzzio, 2004). As deployed, the PLIF system consisted of a high resolution charge coupled device (CCD) camera (PowerView 11MP,  $4008 \times 2672$  pixels, 12 bit), 400mJ neodymium doped yttrium aluminum garnet laser (green 532 nm, Blue Sky Research, Milpitas, CA), and a personal computer (PC) workstation (2.66 GHz dual-processor Intel® Xeon™). As a fluorescence indicator, an aqueous suspension of fluorescently labeled polystyrene particles was utilized (1% solids by weight, Cat. No #R25, fluorescent polystyrene micro-sphere suspension, Diagnostics Division, Microgenics Products from Thermo Fischer Scientific, Fremont, CA). The particles contain embedded fluorescence dye within the polystyrene matrix, with an excitation maximum at 542 nm and an emission maximum at 612 nm, with a refractive index of 1.59 and a suspension density of  $1.06 \text{ g cm}^{-3}$ . The suspension of particles was injected into the first reservoir. The second reservoir was filled with distilled water, which does not exhibit fluorescence. A synchronizer (610035, TSI Inc., Shoreview, MN) was utilized to trigger the laser pulse and the camera with correct sequences and timing. A cylindrical lens (-15 mm focal length) was mounted at the end of the laser arm to form a laser light sheet from a laser beam. A Nikon lens -50 mm, f/1.8 was used at the camera with a red pass filter (545AGLP-RED 36297). The exposure time was  $410 \mu\text{s}$  and the aperture was set to 5.6. The Q-switch was set to  $100 \mu\text{s}$  corresponding to approximately 50% of the maximum laser power. A schematic view of the imaging system is displayed in Figure A5.2a. A

total of 600 images were taken to capture three cycles of mixing. Each image covered an area of  $50 \times 60$  mm stored in 30000 data points each corresponding to a block of  $8 \times 8$  pixels. All images (tiff) were preprocessed into ASCII files using INSIGHT 3G (TSI, Inc., Shoreview, MN) and further processed using custom made MATLAB routines.

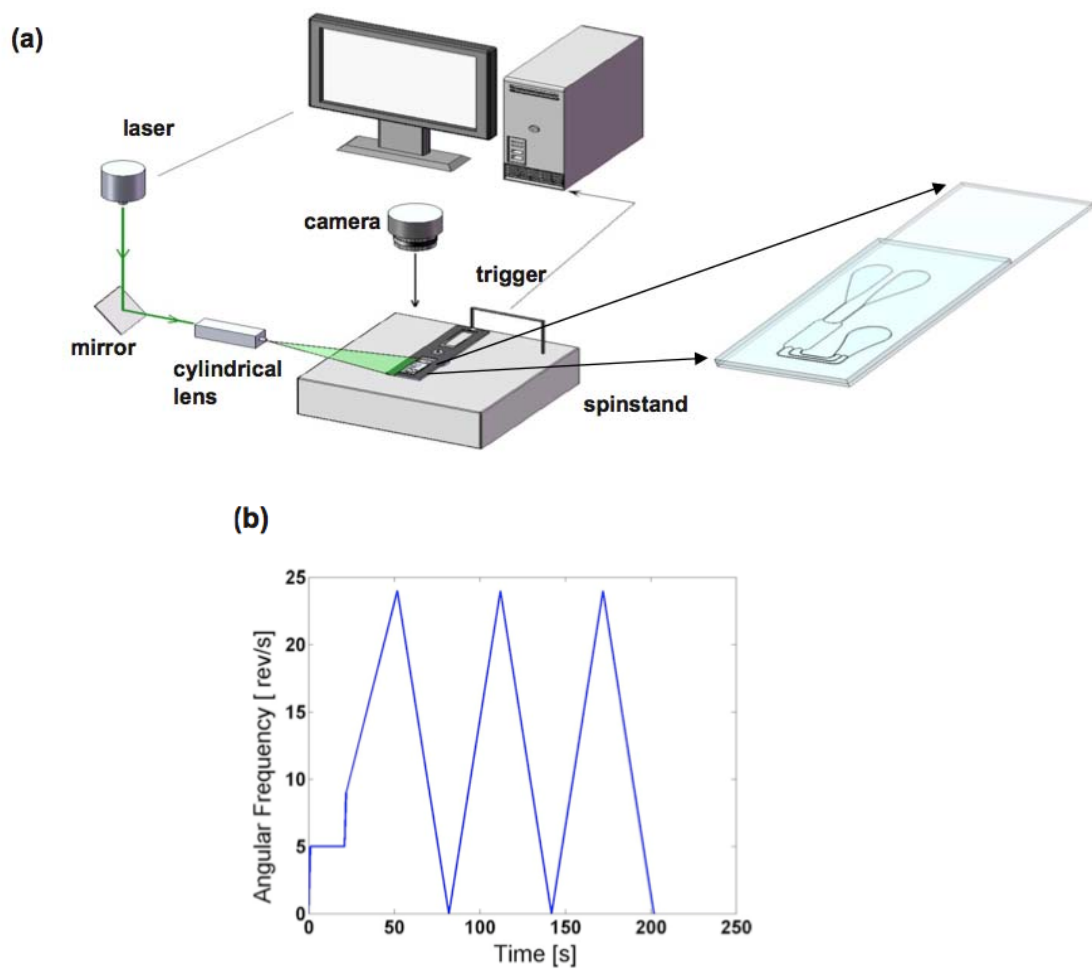


Figure A5.2 Illustration of the experimental setup: a) Schematic illustration of the PLIF imaging system; b) Microfluidics mixer work cycle profile: angular frequency vs time.

## A 5.2 Experimental Procedure

In order to examine changes in concentration gradients in the mixer, 8  $\mu\text{l}$  of purified de-ionized (DI) water and 8  $\mu\text{l}$  of a suspension of red fluorescing polymer microspheres were injected into the top reservoirs  $R_{U1}$  and  $R_{U2}$ , respectively. The loaded PDMS/glass unit was placed on the rectangular platform and immediately mounted onto the spinstand to avoid sample evaporation. The spin program was set according to the angular frequency profile presented in Figure A5.2b. The alignment of the laser was performed at a low angular frequency ( $5 \text{ s}^{-1}$ ) with the spinning time of 20 s. After the alignment was established, the angular frequency was increased up to the “burst frequency,” (Gobby et al. 2009) which is the frequency at which the centrifugal force intensity overcomes the capillary force, advancing the liquid into the microchannels. For our device, the burst frequency was calculated and experimentally verified as  $10 \text{ s}^{-1}$ . Immediately after the burst frequency was reached, the spin speed was further increased to  $24 \text{ s}^{-1}$  for the next 30 s in order to build up the pneumatic pressure in  $R_L$ , and to maintain an average flow rate of  $10 \mu\text{l min}^{-1}$ . At the end of this stage the upper reservoirs  $R_{U1}$  and  $R_{U2}$  were fully emptied. In order to reverse the direction of the flow and thus allow chaotic mixing, angular frequency was decreased to zero in the next 30 s. At the end of this half cycle the lower reservoir,  $R_L$ , was completely empty of fluid. The optimal angular velocities and the timing were experimentally determined using the same sample fluids. A sequence of PLIF images taken during the mixing procedure are presented in Figure A5.3a-e. Images were calibrated to eliminate the false intensity effects due to the proximity of the camera to the mixing chamber M and laser light reflections. To calibrate

the light intensity to concentration, equal parts of fluorescent particles and DI water were mixed thoroughly and injected into inlet holes at  $R_{U1}$  and  $R_{U2}$  and a still image of the mixing chamber was taken after spinning the system for one cycle. For each  $(i,j)$  position in the mixing chamber, calibration was performed according to the following equation

$$I_{i,j,C} = I_{i,j} - \left( I_{c_{i,j}} - I_{MAX} \frac{D_R}{D_M} \right) \quad A5.1$$

where  $I_{i,j,C}$  was the corrected intensity,  $I_{i,j}$  was the measured intensity,  $I_{c_{i,j}}$  was the intensity collected from the calibration image,  $I_{MAX}$  was the maximum possible intensity of 4096,  $D_R$  was the depth of reservoirs (240  $\mu\text{m}$ ), and  $D_M$  was the depth of the mixing chamber (60  $\mu\text{m}$ ).

### A 5.3 Results and Discussion

One of the common ways to estimate the mixing efficiency is to utilize the distribution of the intensity of a fluorescently labeled compound over the mixing area. This can be done either by labeling only one of the two mixing compounds or by using two labels with different colors for both mixing compounds. In this particular case, we decided to label fluid in only one of the chambers. In such arrangement, progression of the mixing process is observed by following spatial and/or temporal variation in fluorescence intensity of the mixture over the defined mixing volume or path. The quantifying factor of mixing efficiency will be a standard deviation of the fluorescence intensity in any particular spot versus the entire studied area or path. Such standard deviation is commonly referred as a mixing index (Liu et al., 2000; Ryu et al., 2004;

Arratia and Muzzio, 2004). Standard deviation or mixing index, as herein defined, is the deviation of the light intensity in the mixing chamber from the mean value of the intensity over its entire area. A lower value of the standard deviation indicates a more homogenous mixture and a higher mixing efficiency. A zero valued standard deviation corresponds to a fully mixed chamber in an ideal situation. However, even in the case of a theoretically perfect mixing device, any practical measurement will show a nonzero standard deviation observed due to systemic error/ fluctuation of pixel intensities of the imaging system.

The Figure A5.3a-e represent histograms of the values of normalized fluorescence intensity as measured over the entire mixing chamber. In the case of our mixer, mixing caused the fluorescence intensity to become more uniformly distributed, resulting in an increasingly narrower peak centered at normalized value of 0.2. Figure A5.4a represents the progression of the mixing index based on the standard deviation versus the cycle number with cycle zero corresponding to  $t=0$  s. We observe a progressive decrease in the standard deviation with each cycle, indicating an increase in fluid mixing with time. Based on the obtained results, it can be concluded that complete mixing of the two fluids is achieved after three complete cycles of flow oscillation.

We hypothesize that fluid mixing in this device is due to the interplay of two different phenomena. First, as seen in Figure A5.3b, at time  $t=30$  s at the end of the first half cycle, the fluorescent particles are deviating from the radial direction as the micromixer spins. This is due to the effect of the Coriolis force that bends the flow in the

negative  $x$  direction as it moves downstream in the mixing chamber. In this experimental setup, the holder rotated in a clockwise direction similar to that in Figure A5.4b, and therefore the Coriolis force acted in the direction shown in the figure, shifting the fluorescent particles opposite to the direction of rotation. As the fluid reversed its direction, the pneumatic pressure forces the two adjacent fluids to mix. Second, observations herein presented suggest that mixing is partially achieved in the mixing chamber due to the flexible nature of PDMS. When the holder was rotated, the mixing chamber deformed by expanding vertically and some of the fluid appeared to travel to the center of the chamber to fill up the area. This effect was verified by measuring the total occupied volume (including the volumes of the microchannels, mixing chamber, and the occupied section of  $R_L$ ) at the end of a half cycle when the angular frequency of rotation was at its peak with the assumption that the PDMS did not deform, and comparing this volume with the volume of the liquid that was initially injected in the inlet holes. The difference in these two values ( $\sim 5 \mu\text{l}$ ) represents the amount of fluid that occupied the deformed section of the mixing chamber,  $M$ , and the lower reservoir  $R_L$ . The deformation or bellowing effect can also be viewed in the image taken at time  $t=30$  s in Figure A5.3a where the color of the fluorescent particles is more intense in the middle of the chamber than closer to the walls. When the angular frequency of rotation was reduced, the chamber contracted and pushed liquid back toward the edges of the chamber. This probably contributed to the mixing.



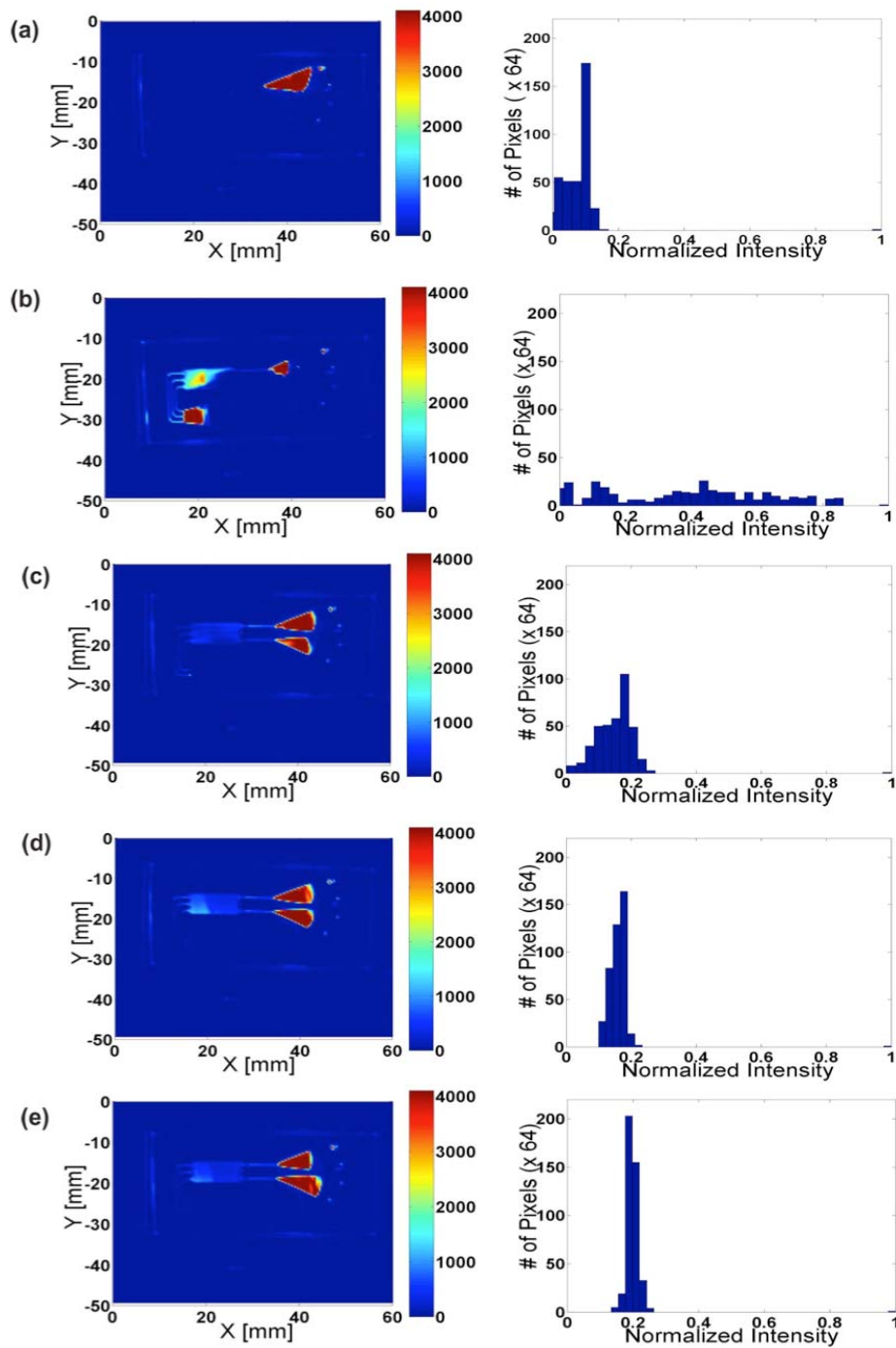


Figure A5.3 Selected sequential planar laser induced fluorescence intensity maps obtained from processed video frames during different stages of mixing and corresponding histograms (a: at time 0 s; b: at time 30 s; c: at time 60 s; d: at time 120 s; e: at time 180 s).

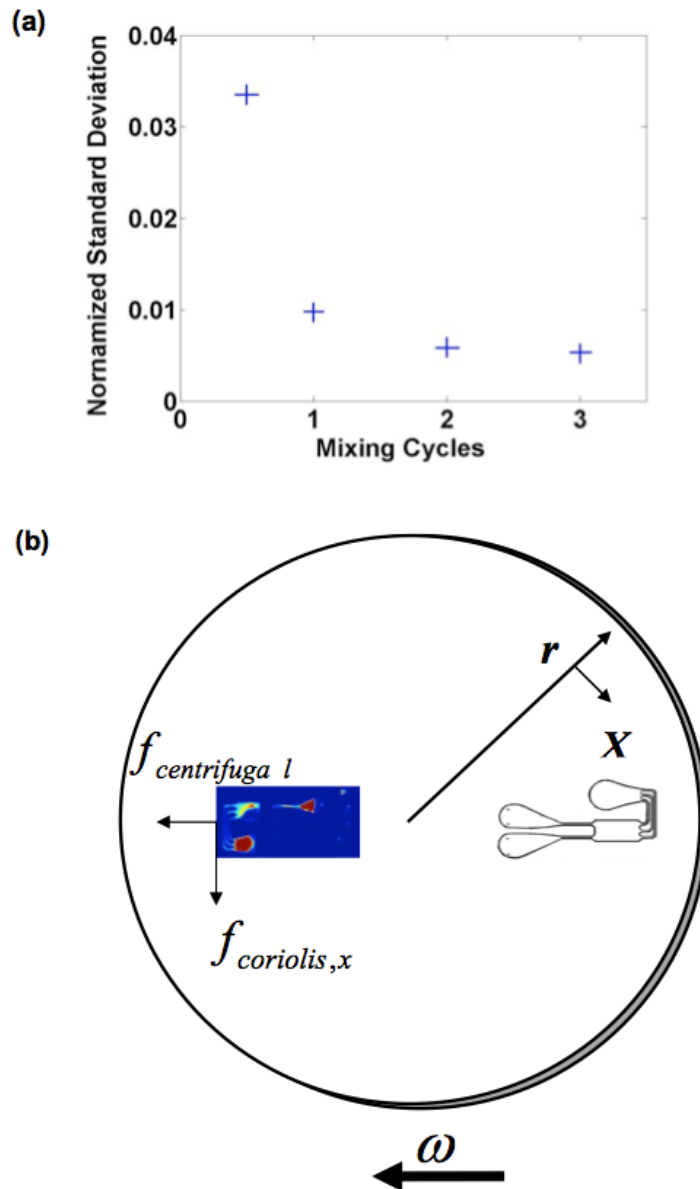


Figure A5.4 a) Progression of the standard deviation of the pixel intensity; b) Schematic of the forces acting on the fluid elements in the mixer.

**Reference:**

Arratia P. E. and Muzzio, F. J., 2004. Ind. Eng. Chem. Res. 43, 6557.

Crimaldi, J. P., 2008. Exp. Fluids 44, 851.

- Duffy, D. C., McDonald, J. C., Schueller, O. J. A. and Whitesides, G. M. *Anal. Chem.* 70, 49741998.
- Gobby, D., Angeli, P., and Gavriilidis, A., 2001. *J. Micromech. Microeng.* 11, 126 40.
- Lai, S., Wang, S. N., Luo, J., Lee, L.J. , Yang, S. T. and Madou, M. J., 2004. *Anal. Chem.* 76, 1832.
- Liu, R. H., Stremmer, M. A., Sharp, K. V., Olsen, M. G., Santiago, J. G., Adrian, R. J., Aref, H., and Beebe, D. J., 2000. *J. Microelectromech. Syst.* 9, 190.
- Ryu, K. S., Shaikh, K., Goluch, E., Fan, Z. F., and Liu, C., 2004. *Lab Chip* 4, 608.

## **APPENDIX VI: Marine Diesel Engine Emission Measurements**

### **A 6.1 Introduction**

Hydrogen is considered as an alternative source of energy for a sustainable system and improved air quality. Hydrogen has some unique features compared to hydrocarbons, such as high mass and thermal diffusivity, wide range of flammability limits, low minimum ignition energy, and high stoichiometric air-to-fuel ratio. With these properties, hydrogen is an ideal fuel to combine with other fuels to potentially improve combustion and emission response (Verhelst and Wallner, 2009). Rakopoulos et al. (2008) pointed out that hydrogen's potential for increased second-law efficiency is possibly one of the most significant advantages.

The application of hydrogen injection control technology in internal combustion engines (ICEs) was proposed in the 1970's. Since then there are numerous hydrogen engine-powered vehicles ranging from two-wheelers to passenger cars, pickup trucks and buses being designed, built and tested over the last decades. Past research has studied technologies that supply hydrogen into diesel fuel ICEs. The objective was to reduce criteria air pollutants and greenhouse gases simultaneously. Varde and Frame (1983) carried out an experimental study on a single cylinder, four-stroke direct injection diesel engine. It was reported that at full load, the brake thermal efficiency increased from 30.53% to 33.68% with approximately 12.5% of the energy supplied by hydrogen. The improved thermal efficiency is due to the increased combustion efficiency. Bika et al. (2008) tested a 1999 Volkswagen 4 cylinder, 1.9 L TDI diesel engine. The results showed that when 10% and 40% of the energy were supplied by hydrogen, PM emissions were

reduced by 10% and 50% respectively. Kumar et al. (2003) investigated the addition of hydrogen into a vegetable oil fuelled compression ignition engine. Results indicated that the brake thermal efficiency was increased from 27.3% to a maximum of 29.3% at 7% of hydrogen mass share at maximum power output. Smoke was reduced from 4.4 to 3.7 Bosch Smoke Unit (BSU) at the best efficiency point. HC and CO emissions were reduced from 130 to 100 ppm and 0.26 – 0.17% by volume respectively at maximum power output. NO level was increased from 735 to 875 ppm at full output due to high combustion rates. Tsolakis et al. (2005) conducted experiments to show that diesel engine exhaust particulate emissions can be reduced by the use of hydrogen-rich gas produced by the catalytic reaction of diesel fuel and exhaust gas. There is also evidence that supplement of H<sub>2</sub> to light-duty diesel engine leads to a reduction in PM emissions when the engine is operated at low, and medium to high load (Varde and Frame, 1982; Tomita et al., 2001; McWilliam et al., 2008; Saravanan and Nagarajan, 2008). Tomita et al. (2001) investigated a four-stroke diesel engine with a single cylinder. The experiments showed that smoke was decreased to almost zero when hydrogen was mixed with inlet air. HC, CO and CO<sub>2</sub> decreased with increasing ratio of the hydrogen. Brake thermal efficiency was slightly smaller than that in ordinary diesel combustion. NO<sub>x</sub> emissions increased or decreased under various conditions. Tomita explained that NO<sub>x</sub> emissions decreased because of lean premixed combustion without the region of high temperature of burned gas such as seen in ordinary diesel operations. He also addressed that such situation happened when the injection timing of diesel oil into the cylinder is extremely advanced.

Recently, some commercial units produce a hydrogen and oxygen ( $H_2/O_2$ ) mixture onboard by water electrolysis (Pan, 2011). Bari et al. (Bari and Esmacil, 2010) investigated the impacts of adding  $H_2/O_2$  mixture on the performance parameters of a diesel engine coupled to generator producing electricity. The engine was tested with the addition of varying amount of  $H_2/O_2$  mixture (1-6%) under three different load levels of 19, 22 and 28 kW. The  $H_2/O_2$  mixture was generated using 24 V external power supply and the power needed to produce the  $H_2/O_2$  mixture is included in the input energy of the engine. The experimental results showed that adding  $H_2/O_2$  mixture with 6.1%, the brake thermal efficiency was increased by 2.6% at 19 kW, 2.9% at 22 kW, and 1.6% at 28 kW. However, beyond 5% addition, no significant effect was found in enhancing the engine performance.

To date, very little research on supplementing  $H_2$  to a modern heavy-duty diesel engine has been conducted especially for off-road applications. In many coastal areas, low-speed marine diesel engines are primary sources of particulate matter (PM) and nitrogen oxides ( $NO_x$ ) (Corbett and Fischbeck, 1997). Hence, the objective of this study was to evaluate and demonstrate hydrogen injection control technology on marine or related diesel engines.

For this study, a two-stroke Detroit diesel engine was tested on a dynamometer for prescribed certification load points and at idles. Each load point was tested for three hydrogen flow rates: 0, 22 and 220 SLPM. A hydrogen flow rate of 0 SLPM represents the baseline condition, 22 SLPM is comparable to the existing commercial products. A hydrogen flow rate of 220 SLPM is ten times the recommended commercial levels and

was selected to ensure that sufficient hydrogen was available to produce measurable effects, while ensuring that the hydrogen-air mixture composition is below the lower flammability limit.

## A 6.2 Experimental Setup

A well-maintained Detroit 12V-71TI marine diesel engine was used as a test engine. The specifications for the engine are summarized in Table A6.1. Ultra low sulfur diesel No. 2 was used for all tests. The engine was mounted on a Taylor heavy-duty water-brake engine dynamometer.

Table A6.1 Engine properties

Basic Engine	12V-71TI
Model	7122-3300 (port) 7122-7300 (starboard)
Description	Turbocharged, Intercooled Pleasure Craft Engine
Engine Type	Two Cycle
Number of Cylinders	12
Bore and Stroke	4 ½ in. × 5 in.
Displacement-Two Cycle (Every Downstroke a Powerstroke)	852 cu. in.
Rated Brake Horsepower	675@2300 RPM
Rated Shaft Horsepower	650@ 2300 RPM

Compression Ratio	17 to 1
Approx. Net Weight (dry) with Standard Equipment	5200 lbs.

Two duty cycles were used to certify marine engines. One cycle assumes engines operate on a fixed-pitch propeller curve (E3), and the other is for propulsion engines that operate at a constant speed (E2). Fixed-pitch propellers are used in most commercial vessels such as tugs, draggers, fishing vessels, and trawlers. In this study, we selected the ISO 8178-E3 four-mode test cycle shown in Table A6.2. The first step involved mounting the engine securely on a water-brake dynamometer and measuring the engine map for the full load range. Selected ISO 8178-E3 four-mode test cycles together with our test conditions is shown in Figure A6.1.

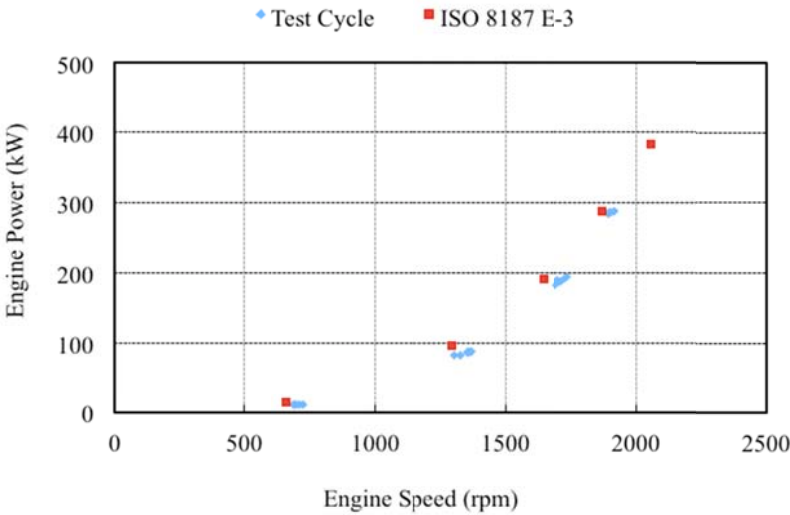


Figure A6.1 Test engine map



Table A6.2 Test modes and weighting factors for marine applications (ISO-8178 E3)

Mode	Power		Speed		Weighting
	kW	%	RPM	%	Factors
	384	100	2053	100	0.2
ISO-8178 E3	288	75	1868	91	0.5
cycle	192	50	1642	80	0.15
	96	25	1293	63	0.15
Idle	15	4	657	32	0

Hydrogen was supplied from a high-pressure six-pack cylinder at 150 bars to an outlet pressure of 1 bar using a hydrogen pressure regulator. A fine control valve was used to adjust the flow rate of hydrogen and flow was measured with a digital mass flow meter (Smart-Trak 2 Series 100, Sierra Instruments). A flame arrestor was installed in the line to suppress a backward flow of the hydrogen. After the flame arrestor, hydrogen was split into two injection ports to improve mixing of hydrogen with air in the intake.

Schematic of hydrogen injection system and emissions sampling is provided in Figure A6.2. During the test, the hydrogen-air mixture and exhaust are collected into sampling bags and later analyzed for the volume percentage of hydrogen in air by Residual Gas Analyzer (RGA).

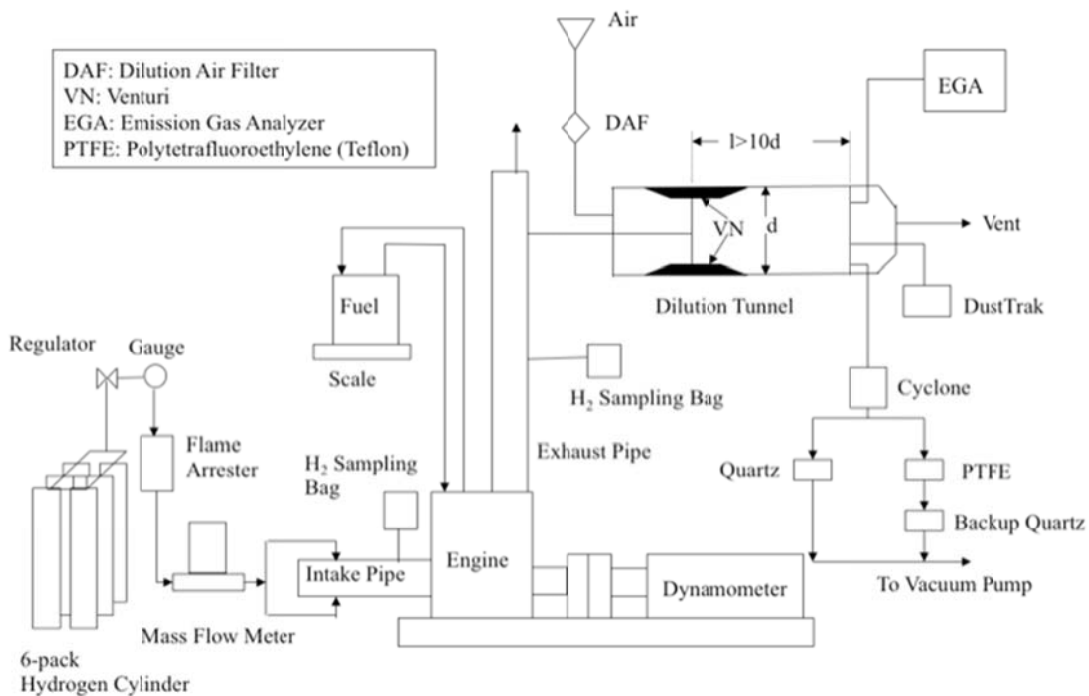


Figure A6.2 Flow diagram of the hydrogen injection system and the sampling system

The sampling and analysis of gases and particulate matter (PM) conforms to ISO 8178-1. The concentrations of CO<sub>2</sub> or NO<sub>x</sub> were measured in the raw exhaust gas and the diluted gas in the dilution tunnel using the exhaust gas analyzer (EGA), to determine the dilution ratio. More details about the sampling, emission measurements of different gases, PM<sub>2.5</sub> mass, elemental and organic carbon could be found in Agarwal et al.'s study (2008).

Emissions were measured under various operating modes and the emission factors for those modes are reported directly. For the overall emission factors of NO<sub>x</sub>, CO<sub>2</sub>, and PM, we used weighting factors listed in ISO 8178 E-3 as

$$A_{WM} = \frac{\sum_{i=1}^n (g_i \times WF_i)}{\sum_{i=1}^n P_i \times WF_i} \quad \text{A 6.1}$$

where  $A_{WM}$  is weighted mass emission level (HC, CO, CO<sub>2</sub>, PM, or NO<sub>x</sub>) in g/kW-hr,  $g_i$  is mass flow in grams per hour,  $P_i$  is power measured during each mode (includes auxiliary loads), and  $WF_i$  is effective weighting factor for an ISO E3 cycle (Table A6.2).

### A 6.3 Results and Discussion

The emissions measured during hydrogen injection are compared with the baseline. The results are also compared with the Tier 2 certification standards. Data were taken in duplicate and average values for each mode are presented in the following sections.

#### A6.3.1 Gaseous emissions

Emissions of gases, CO, CO<sub>2</sub> and NO<sub>x</sub> were measured over the modes identified in the ISO 8178 E-3 cycle. CO<sub>2</sub> emissions were analyzed first in order to make sure that the repeatability of the data was within expected limits.

During testing, CO<sub>2</sub> emissions increased linearly with load as expected with coefficients of determination  $R^2$  in the range from 0.986 to 0.997. This finding is consistent with the linear relationship of the amount of fuel consumed and the output shaft power. The linear relationships were also used to estimate CO<sub>2</sub> emissions at 100% load. The variation of CO<sub>2</sub> emissions with the percentage of H<sub>2</sub> is shown in Figure A6.3. At 50% load, CO<sub>2</sub> emissions reduced 7% with H<sub>2</sub> flow rate of 22 SLPM and 12% with H<sub>2</sub>

flow rate of 220 SLPM. At idle, the reductions of CO<sub>2</sub> emissions were 21% and 37% with H<sub>2</sub> flow rate of 22 and 220 SLPM respectively. At high load (75% load), CO<sub>2</sub> emissions increased 2% with H<sub>2</sub> flow rate of 22 SLPM, and there was no change in CO<sub>2</sub> emissions at H<sub>2</sub> flow rate of 220 SLPM. Dividing the emission by the power for each load gives EF<sub>CO<sub>2</sub></sub> (g/kW-hr) as presented together with the overall weighted emission factors in Figure A6.4.

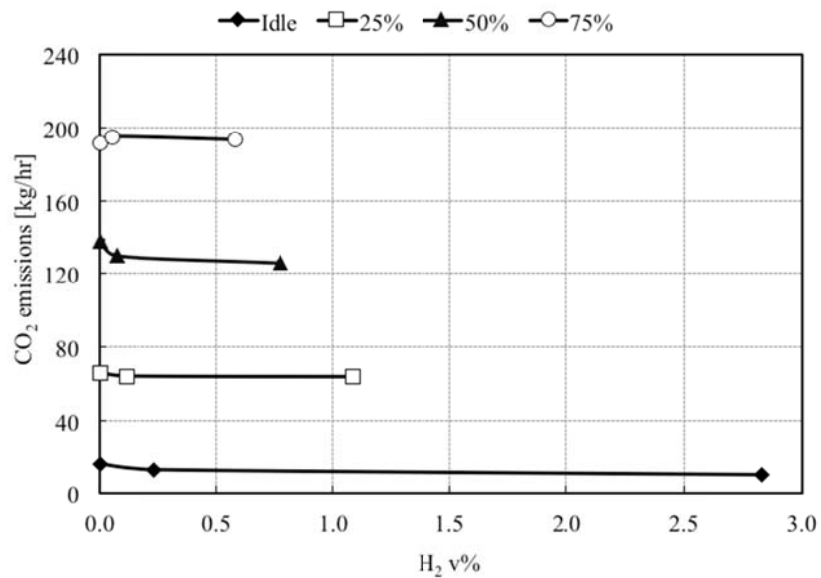


Figure A6.3 CO<sub>2</sub> emissions vs. H<sub>2</sub> volume percentage.

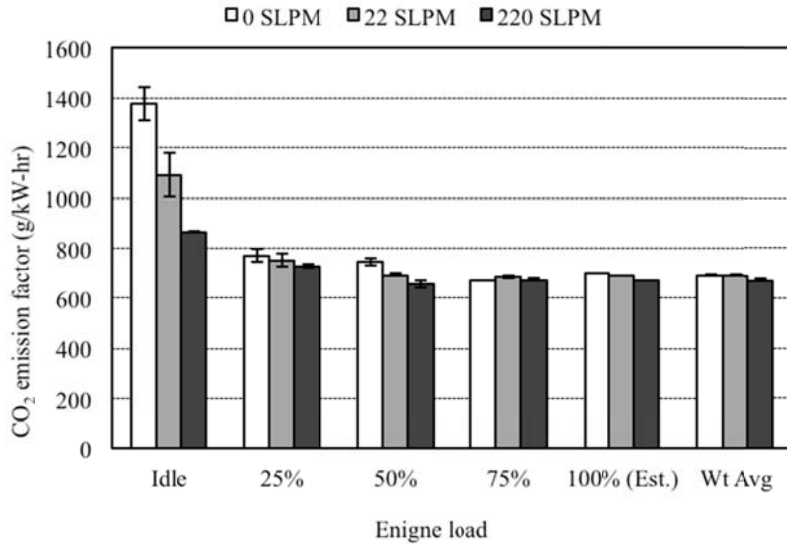


Figure A6.4 Modal and overall emission factors for CO<sub>2</sub>.

Hydrogen has a wide range of flammability, hydrogen engines can run on A/F ratios of anywhere from 34:1 (stoichiometric) to 180:1 (College of the Desert, 2001). References (Heywood, 1988) showed that the critical equivalence ratio ( $\Phi$ ) for NO formation in high-temperature high-pressure burned gases is close to 1 for both a gasoline engine and a diesel engine, where  $\Phi$  is equal to the stoichiometric A/F ratio divided by the actual A/F ratio. Our results in Figure A6.5 showed the increased NO<sub>x</sub> curve relative to  $\Phi$  when hydrogen was injected into a diesel engine. At 75% loads, equivalence ratios were around 1 and NO<sub>x</sub> emissions were about 3.3 kg/hr.

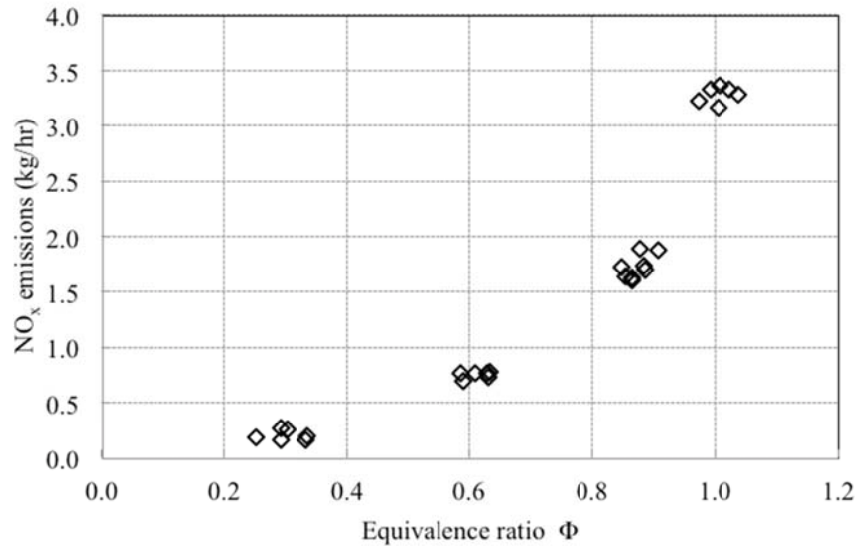


Figure A6.5  $\text{NO}_x$  emissions vs. equivalence ratio.

As discussed by Heywood (1988), for a compression-ignition engine, the peak NO concentrations occurs when burned gas temperatures are at a maximum, which is between the start of combustion and shortly after the occurrence of peak cylinder pressure. After that, burned gas temperatures decrease due to cylinder gas expansion and mixing of high-temperature gas with air (Kerley and Thurston, 1962). The cooler burned gas freezes the NO chemistry resulting in a decrease of NO concentrations. Heywood (1988) also investigated the ratio of local NO concentration to exhaust NO concentration. It was found that almost all of the NO forms within the  $20^\circ$  crank angle degrees following the start of combustion (Muranaka et al. 1987). The retarded injection timing could cause the retarded combustion process. Hence, NO formation occurs later and peak temperatures are lower so that the NO concentrations are lower.

Figure A6.6 shows the variation of  $\text{NO}_x$  emissions with varying  $\text{H}_2$  volume percentage. At 75% load,  $\text{NO}_x$  emissions increased 3% when  $\text{H}_2$  flow rate was 22 SLPM.

The increasing NO<sub>x</sub> emissions were probably caused by increased flame temperature when burning hydrogen as Heywood (1988) pointed that the burned gas temperature of close-to-stoichiometric mixture is overriding important in determining NO<sub>x</sub> emissions. However, at lower load, results show decreasing NO<sub>x</sub> emissions with injection of H<sub>2</sub>. For example, at 50% load, NO<sub>x</sub> emissions reduced 10% and 15% at 50% load and 28% and 41% at idle with H<sub>2</sub> flow rates of 22 and 220 SLPM respectively. This is probably because H<sub>2</sub> additions performed as diluents reducing burned gas temperatures rather than burning fuels increasing flame temperatures. Note that the heat capacity of H<sub>2</sub> per mole at the temperatures relevant to diesel combustion is a little higher than that of N<sub>2</sub>.

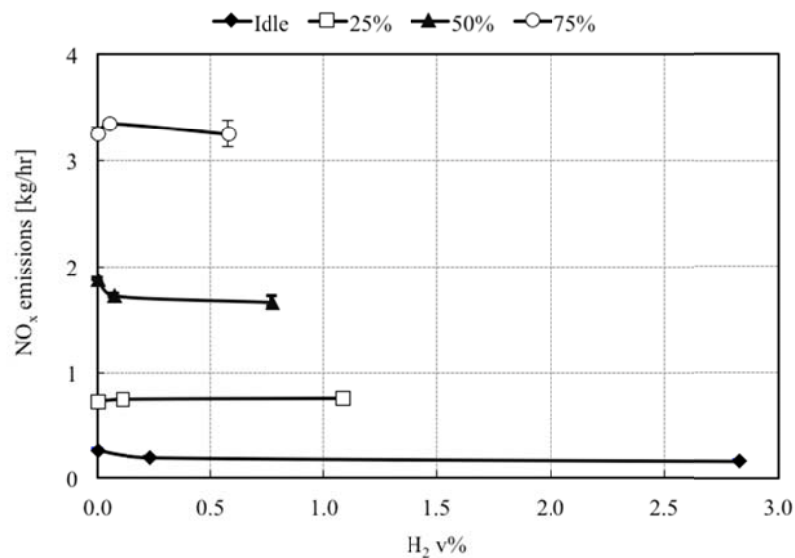


Figure A6.6 NO<sub>x</sub> emissions vs. H<sub>2</sub> volume percentage.

Figure A6.7 represents  $EF_{NO_x}$  at idle, ISO load points and overall weighted for all H<sub>2</sub> flow rates. Nitric oxide emissions were measured at each mode and each power setting allowing us to calculate its emission rate and emission factor. The correlation obtained between the NO<sub>x</sub> emission rates and loads was good with  $R^2 \sim 0.95$ .

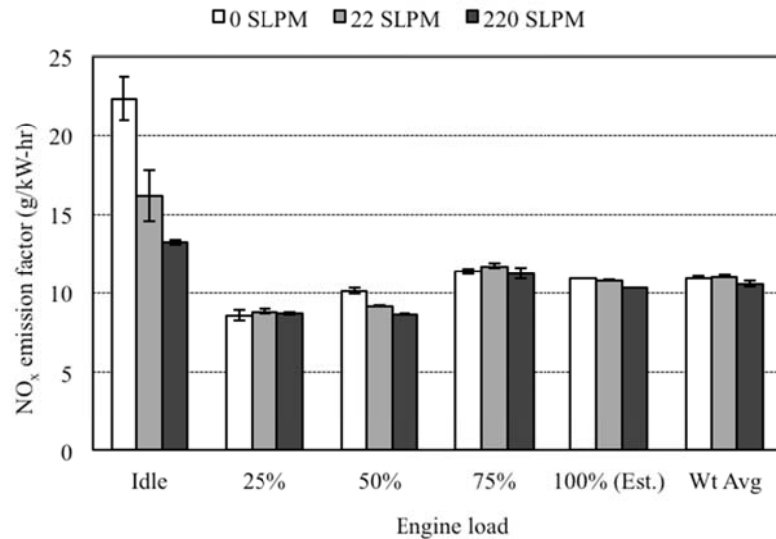


Figure A6.7 Modal and overall emission factors for NO<sub>x</sub>

As shown in Figure A6.7, hydrogen injection has an obvious effect on NO<sub>x</sub> emission factors at idle. At a H<sub>2</sub> flow rate of 22 SLPM, which is about 0.24 volume %, NO<sub>x</sub> emission factor reduced by 28% from the baseline condition. At H<sub>2</sub> flow rate of 220 SLPM, which is about 2.8 volume %, NO<sub>x</sub> emission factor reduced by 41% from the baseline condition. NO<sub>x</sub> weighted emission factors were unchanged compared to the baseline condition.

The variation of carbon monoxide emissions with hydrogen volume percentage are shown in Figure A6.8. At 75% load, CO emissions increased 10% and 14% with hydrogen flow rates of 22 and 220 SLPM. At idle, CO emissions decreased 22% and 47% with hydrogen flow rates of 22 and 220 SLPM. The measured CO emissions at each mode and each power setting allowing us to calculate its emission rates as shown in Figure A6.9.



A6.3.2. Particulate matter (PM<sub>2.5</sub>) emissions.

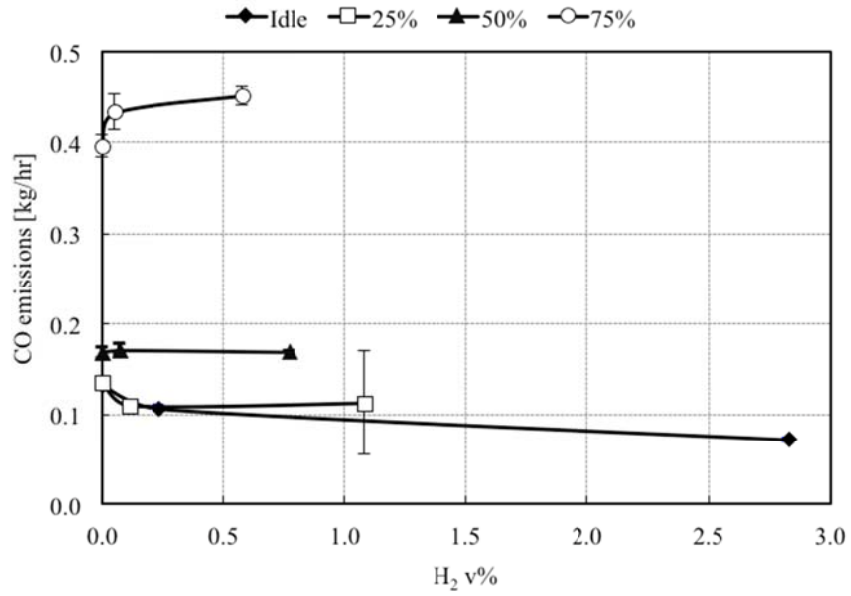


Figure A6.8 CO emissions vs. H<sub>2</sub> volume percentage.

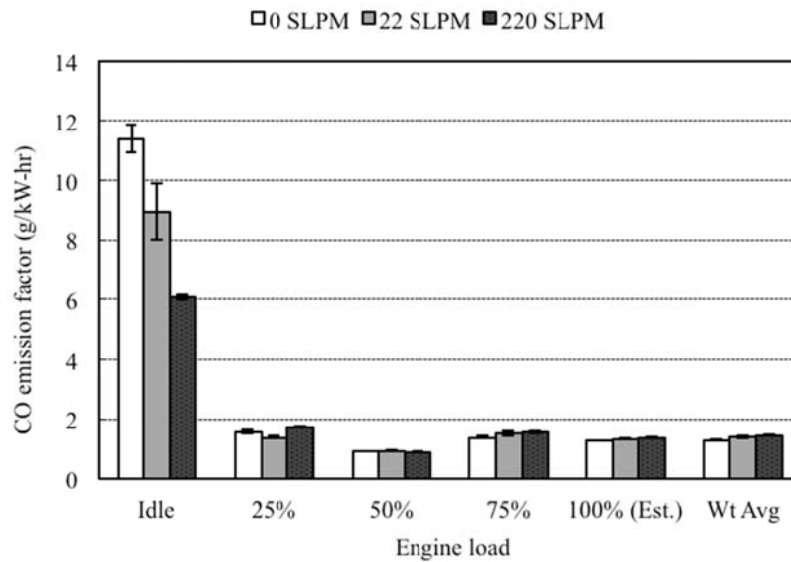


Figure A6.9 Modal and overall emission factors for CO.

PM<sub>2.5</sub> mass was measured by two independent methods to assure the quality of the data. One method measures the PM<sub>2.5</sub> mass collected on a Teflon filter, and the other

simultaneously sums the total elemental and organic carbon mass collected on a quartz filter. Real-time particulate matter concentrations were measured by TSI DustTrak 8520 (TSI, Inc.). A linear correlation was observed between DustTrak and mass collected on Teflon filter with  $R^2 \sim 0.78$ , but as expected DustTrak under predicts PM by a factor of 2 to 3 (Kingham et al., 2006).

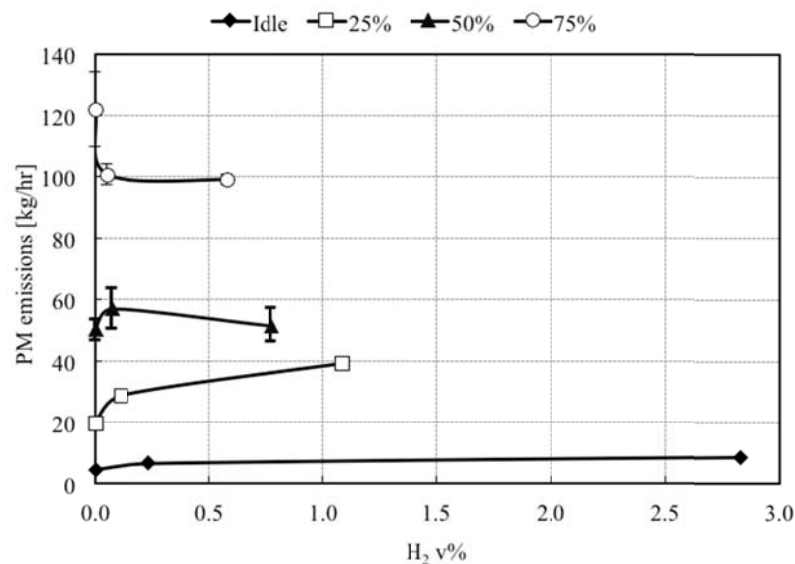


Figure A6.10 PM emissions vs. H<sub>2</sub> volume percentage.

The correlation coefficient of a linear fit between PM emission rates and loads are greater than 0.90. Compared to NO<sub>x</sub> emissions PM emissions show opposite trend at idle and 75% as shown in Figure A6.10. At 75%, PM emissions decreased 16% and 19% with H<sub>2</sub> flow rates of 22 and 220 SLPM. As we discussed before, hydrogen additions increased flame temperature at high load which improved the combustion of hydrocarbon and inhibited the formation of PM. While at idle, hydrogen additions worked as diluents that reduced the burned gas temperature and caused incomplete combustion of

hydrocarbon. The results in Figure A6.10 shows that at idle, PM emissions increased 41% and 86% with H<sub>2</sub> flow rates of 22 and 220 SLPM respectively.

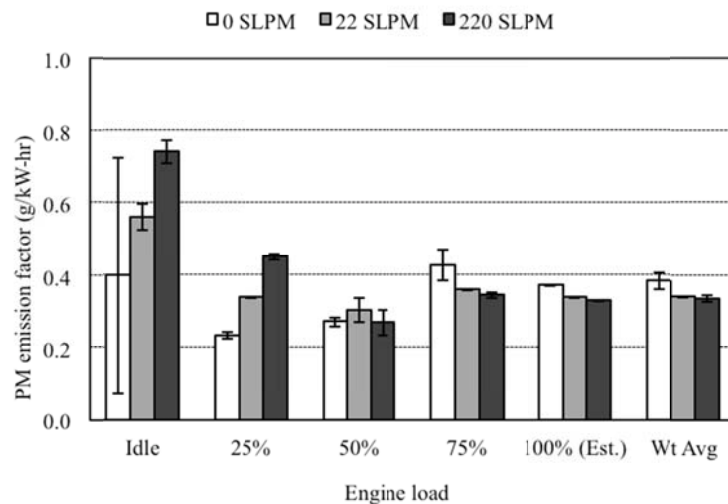


Figure A6.11 Modal and overall emission factors for weighted PM.

As shown in Figure A6.11, with H<sub>2</sub> flow rate of 22 SLPM, PM emission factor increased by 50% from the baseline condition at idle. With H<sub>2</sub> flow rate of 220 SLPM, PM emission factor increased by 75% from the baseline condition. However, the error at idle with H<sub>2</sub> flow rate of 0 SLPM is about 75%. Hence, further investigation is needed to explain the trend of PM emission at idle. Since idle is not included in weighted emission factors, this large uncertainty does not affect overall results of the present study. At 25% load, PM emission factors also increased with H<sub>2</sub> injection. The weighted emission factors with H<sub>2</sub> flow of 22 and 220 SLPM decreased by 11% from the baseline condition. This is because emission factors at 75% also decreased and 75% load is the most weighted (weighting factor of 0.5) in the overall weighted emission factor calculation.

### A6.3.3. Unburned hydrogen measurements

A previous study (Li et al. 2009) reported that the H<sub>2</sub> present outside of the diesel spray plume might survive the main combustion process due to the lack of a propagating flame. This survived hydrogen will exit diesel engine as unburned fuel. However, we believe that any hydrogen in the exhaust mostly appears as a consequence of thorough cylinder flushing with the fresh mixture of air and hydrogen during exhaust/intake stroke. In any case, for this study, hydrogen volume percentage was measured in both intake mixture and exhaust to analyze any unburned hydrogen.

Hydrogen volume percentage measurements are provided in Table 3. Set points are calculated hydrogen v% based on the flow rates of hydrogen and air. RGA measured H<sub>2</sub> are corrected by a CO<sub>2</sub> correlation factor, which is the ratio of EGA CO<sub>2</sub> to RGA CO<sub>2</sub>. In most cases H<sub>2</sub> in the exhaust was at the noise level with the exception of a few settings (see Table A6. 3) where measurable amount was noticed.

Table A6. 3 Hydrogen measurements

Load	Baseline (0 SLPM)		Commercial Value (22 SLPM)				High Level (220 SLPM)		
	H <sub>2</sub> in Intake Mixture [%]	Unburned H <sub>2</sub> in Exhaust [%]	H <sub>2</sub> in Intake Mixture [%]		Unburned H <sub>2</sub> in Exhaust [%]		H <sub>2</sub> in Intake Mixture [%]		Unburned H <sub>2</sub> in Exhaust [%]
			Set	Measured	Set	Measured	Set	Measured	
IDLE	n/a	0.23	0.23	0.23	0.01		2.83	1.94	0.20
25%	n/a	0.11	0.11	0.43	UDL <sup>a</sup>		1.08	1.58	0.05
50%	n/a	0.07	0.07	0.09	0.03		0.77	1.09	0.34

---

75%	0.09	0.05	0.05	0.09	0.01	0.58	1.21	0.04
-----	------	------	------	------	------	------	------	------

---

#### A6.3.4 Overall Weighted Emission Factors under E3 Cycle

The overall weighted emission factors are calculated based on the equations presented in Section 2.5. Figure A6.12 indicates the overall weighted emission factor for gases and PM for the engine along with the certification values for Tier 2 and Tier 3 engines. With H<sub>2</sub> flow rates of 22 SLPM and 220 SLPM, NO<sub>x</sub> weighted emission factors increased by 1% and reduced by 4%. PM weighted emission factors reduced by 11% for both H<sub>2</sub> flow rates.

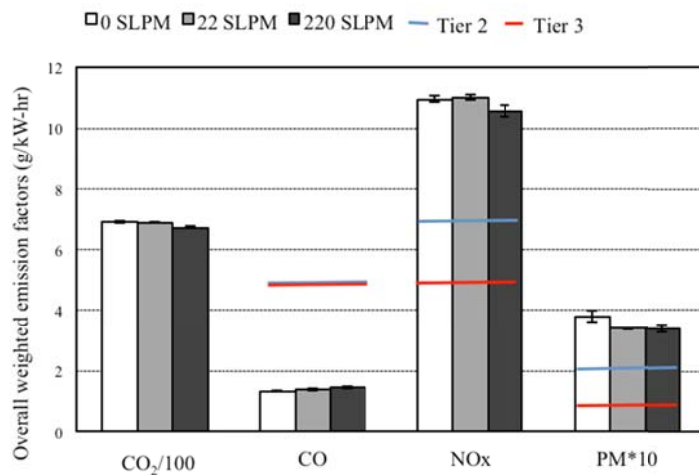


Figure A6.12 Overall weighted average emission factors for gases and PM<sub>2.5</sub> with hydrogen flow rates of 0, 22 and 220 SLPM under the test cycle of E3. Note that Tier 2 and Tier 3 standards on the NO<sub>x</sub> bars Represent NO<sub>x</sub> + THC.

#### A6.3.5 Energy Efficiency

Energy input in a diesel engine is converted to: 1) useful brake output power; 2) energy transferred to cooling water; 3) energy transferred to the exhaust gas; 4)

uncounted losses due to friction, radiation, heat transfer to surroundings, operating auxiliary equipment, etc., (Al-Najem and Diab, 1992).

The efficiency of useful brake output power or diesel engine efficiency  $\eta$  is:

$$\eta = \frac{1}{BSFC[\text{kW} \cdot \text{h}] \times LHV[\text{kW} \cdot \text{h/g}]} \quad \text{A6.2}$$

Here brake specific fuel consumption, BSFC [ $\text{g J}^{-1}$ ] is calculated as

$$BSFC = r/P \quad \text{A6.3}$$

where  $r$  is the fuel consumption rate [ $\text{g s}^{-1}$ ],  $P$  is the power produced [W]. The power is calculated as  $P = \tau\omega$ , with  $\omega$  being the shaft angular velocity [ $\text{rad s}^{-1}$ ], and  $\tau$  is the engine torque [Nm]. Figure A6.13 shows engine power efficiency at various loads.

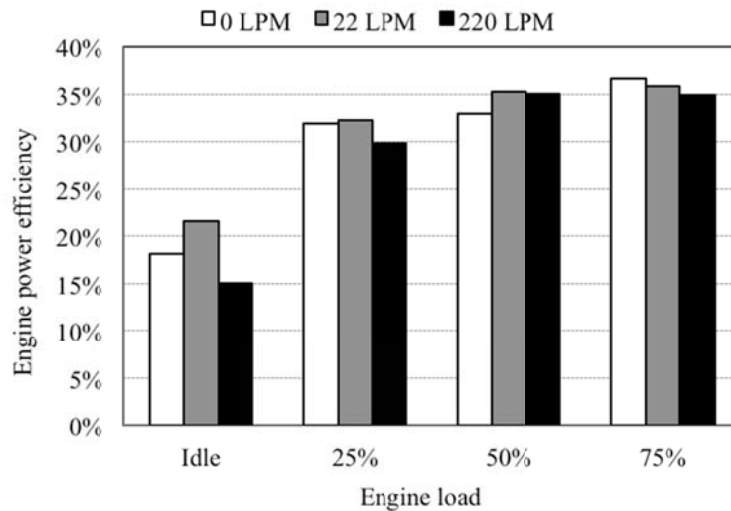


Figure A6.13 Engine power efficiency vs. loads.

#### A6.3.6 Enthalpy of Combustion

Since hydrogen was supplied to the intake air, the overall enthalpy of combustion increases. Added energy to the combustion is calculated by assuming diesel formula to

be  $C_{10.8}H_{18.7}$  and lower heating value (LHV) of stoichiometric combustion of diesel is considered to be  $6.4 \times 10^6$  KJ/Kmol (College of the Desert, 2001). The stoichiometric combustion of diesel with theoretical air is given as:



Figure A6.14 provides the calculated results of enthalpy of combustion. With hydrogen flow rate of 22 and 220 SLPM, the energy added to the combustion is negligible for loads greater than 25%. However, at idle, the energy added from hydrogen increased by 6% and 93% for 22 and 220 SLPM respectively. This could be a reasonable explanation for the observed reduction of  $CO_2$  emissions since when no  $CO_2$  results from  $H_2$  combustion. As we noticed,  $CO_2$  emissions reduced by 37% as energy added increased by 93%. Furthermore,  $CO_2$  emissions have a linear relationship with fuel economy as seen in Figure A6.15.

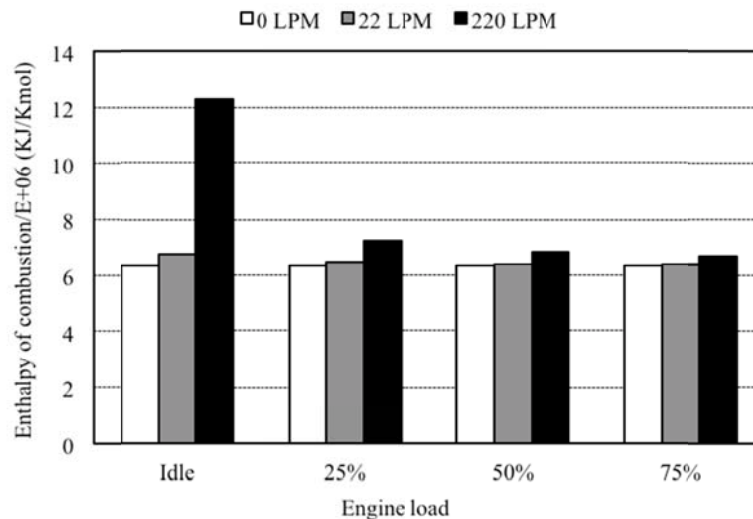


Figure A6.14 Enthalpy of combustion vs. loads.

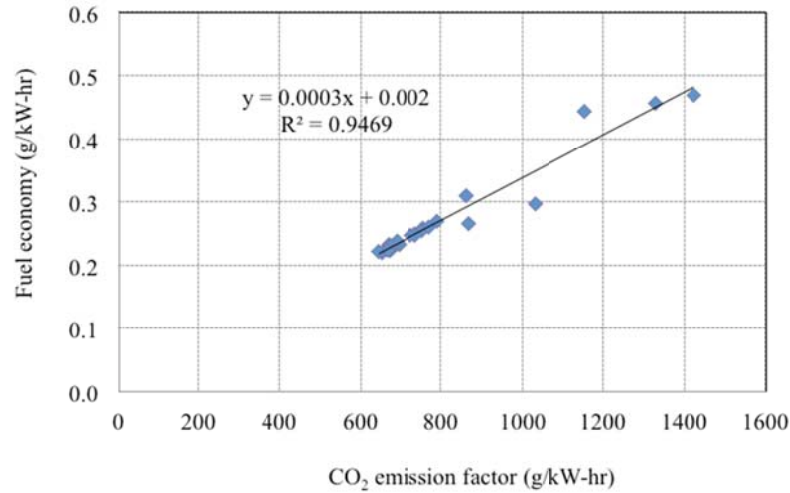


Figure A6.15 Fuel consumption vs. CO<sub>2</sub> emission factors.

#### A6.3.7 Increase in Fuel Consumption due to Electrolysis Producing Hydrogen

Gutierrez-Martin et al. (2009) discussed the electrolysis process and the energy consumption of a typical process. A typical electrolysis process consumes:

$$W_u \approx 46 \text{ [kWh/kg}_{\text{H}_2}\text{]} \quad \text{A6.5}$$

For the reaction of water decomposition at low temperatures, with a standard efficiency of conventional electrolysis at low current densities:  $\eta=70\%$ . For a commercial product, such as HES 210, at a practical current density of about  $2 \text{ A/cm}^2$  the cell voltage is about  $2 \text{ V}$ , the efficiency would be  $74\%$ , computed according to Gutierrez-Martin's method.

Using Eqn. A6.5 and hydrogen density ( $8.38 \times 10^{-5} \text{ kg/l}$ ), power consumptions of the water electrolyzer at H<sub>2</sub> flow rates of 22 and 220 SLPM were calculated to be  $5.1 \text{ kW}$  and  $51 \text{ kW}$  respectively. Based on the linear curves of fuel consumption according to



engine power loads under varying hydrogen flow rates, with the hydrogen flow rate of 22 SLPM, a 5.1 kW of power load will increase the fuel consumption by 1.75 kg/hr. With the hydrogen flow rate of 220 SLPM, the potential increase in fuel consumption is 11.7 kg/hr. The percentage of potential increased fuel consumption in measured fuel consumption for engine loads ranged from 75% to idle is listed in Table 4. For example, at 75% engine load, hydrogen production of 22 SLPM will increase 2.6% in fuel consumption, and hydrogen production of 220 SLPM will increase 17.7 in fuel consumption. The increased fuel consumption will also increase CO<sub>2</sub> emission factors. The net effect of hydrogen injection on CO<sub>2</sub> emission factors is listed in Table A6.4. For commercial H<sub>2</sub> flow rates change in CO<sub>2</sub> emission factors is within 5%.

Table A6.4 Percentage of increased fuel consumptions due to the increased electrical load of electrolysis for each engine load

Engine Load	Commercial Value (22 SLPM)		High Level (220 SLPM)	
	Net Effect on CO <sub>2</sub> Emission Factors [%]	Increased Fuel Consumption [%]	Net Effect on CO <sub>2</sub> Emission Factors [%]	Increased Fuel Consumption [%]
75%	3.8	2.6	18.1	17.7
50%	-4.6 <sup>a</sup>	3.9	11.7	27.1
25%	3.0	8.0	45.3	53.8
Idle	0.6	39.8	163.0	339.4

#### A6.3.8 Effect of Hydrogen on Operation at Idle

Figure A6.16 and Figure A6.17 show results of continuous monitoring of engine power and speed during idle testing. It is obvious that engine stability is improved with hydrogen injection. During idle, additional hydrogen improves very low diesel combustion efficiency, which is also evident from the reduction of CO in Figure A6.8. This improved combustion efficiency leads to more uniform engine output. In regimes other than idle, pure diesel combustion efficiency is already high so that additional hydrogen even had adverse effect.

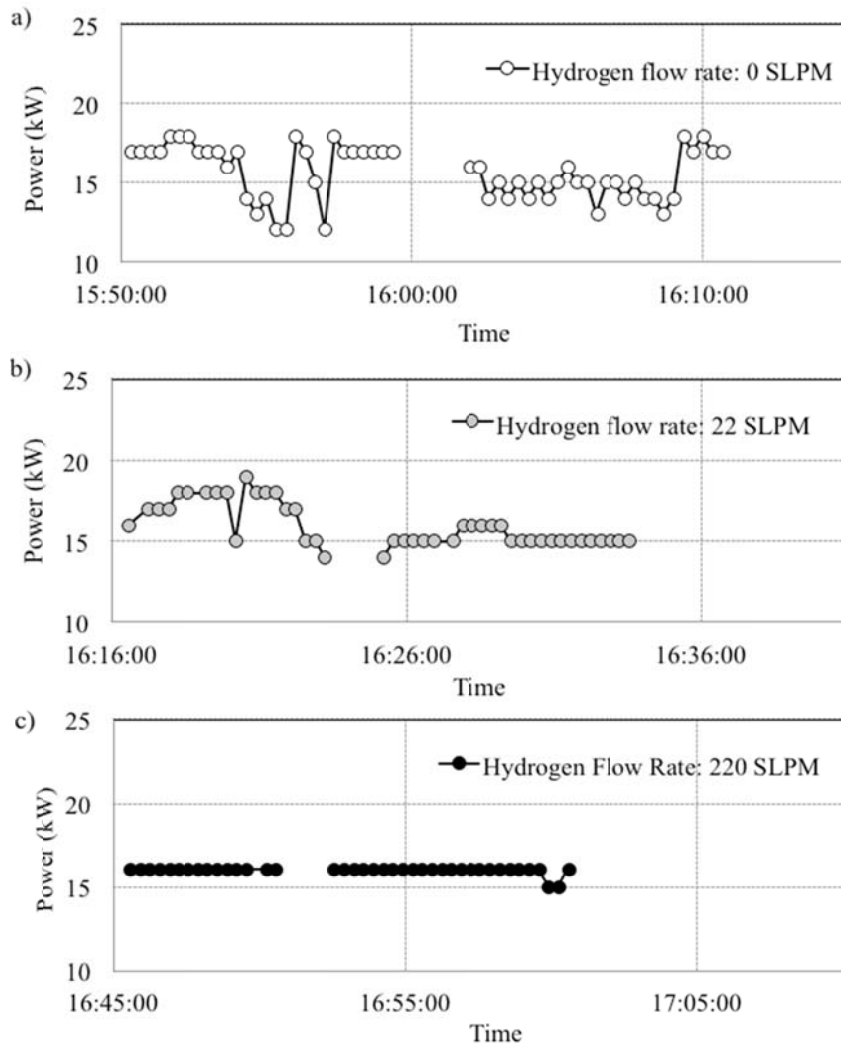


Figure A6.16 Continuous monitoring of power during idle modes with hydrogen flow rates of a) 0 SLPM, b) 22 SLPM and c) 220 SLPM.

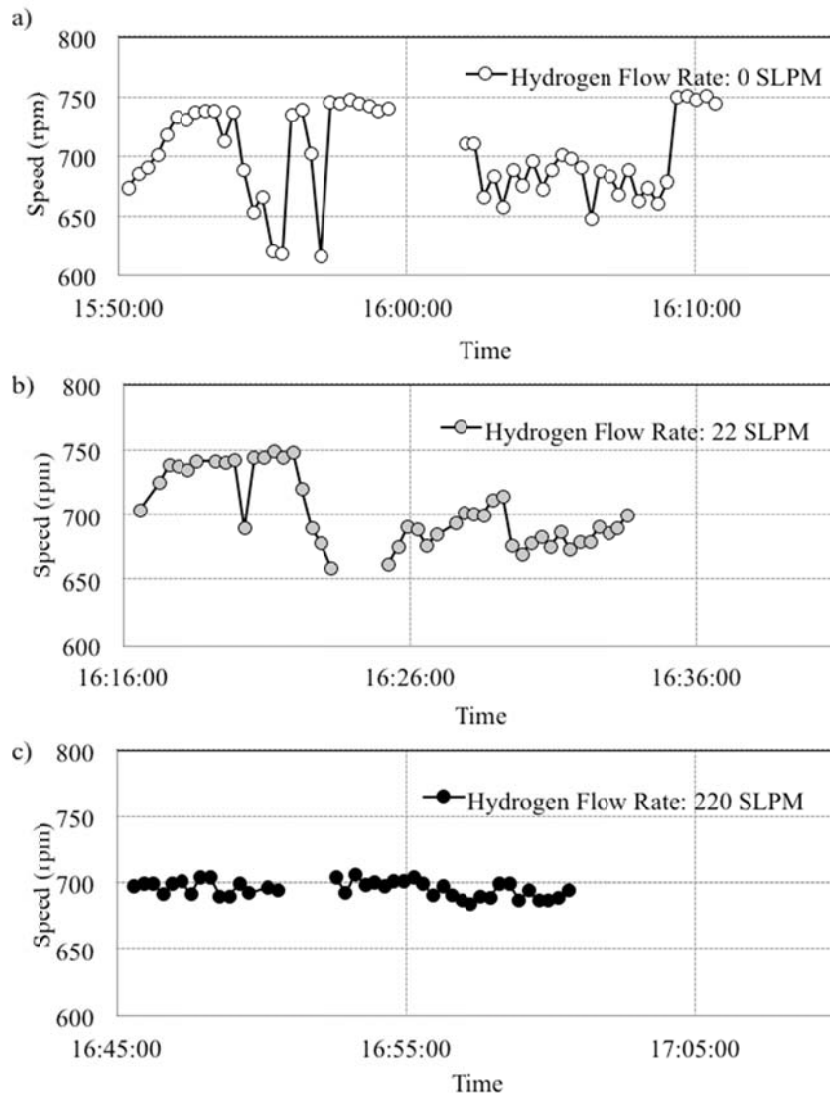


Figure A6.17 Continuous monitoring of speed during idle modes with hydrogen flow rates of a) 0 SLPM, b) 22 SLPM and c) 220 SLPM.

**Reference:**

Agrawal H, Malloy QGJ, Welch B, Miller W, Cocker DR. In-use gaseous and particulate matter emissions from a modern ocean going container vessel. *Atmospheric Environment* 2008; 42:5504-5510.

Al-Najem NM, Diab JM. Energy-exergy analysis of a diesel engine. *Heat Recovery Systems & CHP* 1992; 12:525-529.

- Bari S, Esmail MM. Effect of H<sub>2</sub>/O<sub>2</sub> addition in increasing the thermal efficiency of a diesel engine. *Fuel* 2010; 89:378-383.
- Bika AS, Franklin LM, Kittelson DB. Emission effects of hydrogen as a supplement fuel with diesel and bio-diesel. SAE Paper 2008; 2008-01-0648.
- College of the Desert, Hydrogen use in internal combustion engines. 2001. <http://www1.cere.energy.gov>
- Corbett JJ, Fischbeck PS. Emissions from ships. *Science* 1997;278 (5339):823-824.
- Gutierrez-Martin F, Garcia-De Maria JM, Bairi A, Laraqi N. Management strategies for surplus electricity loads using electrolytic hydrogen. *International Journal of Hydrogen Energy* 2009; 34:8468-8475.
- Heywood JB, *Internal Combustion Engine Fundamentals*, McGraw-Hill, 1988.
- Kerley RV, Thurston KW. The indicated performance of Otto-Cycle engine. *SAE Trans.* 1962; 70:5-30.
- Kingham S, Durand M, Aberkane D, Harrison J, Wilson JG, Epton M. Winter comparison of TEOM, MiniVol and DustTrak PM10 monitors in a woodsmoke environment. *Atmospheric Environment* 2006; 40: 338-347.
- Kumar MS, Ramesh A, Nagalingam B. Use of hydrogen to enhance the performance of a vegetable oil fuelled compression ignition engine. *International Journal of Hydrogen Energy* 2003; 28:1143–1154.
- Li H, Shade B, Clark N, Thompson G, Wayne S, Gautam, M. An experimental evaluation of NO<sub>x</sub> reductions from H<sub>2</sub> enhanced diesel combustion. Review Report 2009.
- McWilliam L, Megaritis T, Zhao H. Experimental investigation of the effects of combined hydrogen and diesel combustion on the emissions of a HSDI diesel engine. SAE paper 2008-01-0156; 2008.
- Muranaka S, Takagi Y, Ishida T. Factors limiting the improvement in thermal efficiency of S.I. engine at higher compression ratio. SAE paper 870548.
- Pan H, Princevac M, Mahalingam S, Miller W, Khan Y, Jayaram V, Welch B. Effect of hydrogen injection on emissions from a marine diesel engine. Report to California Air Resources Board. 2011 Contract #08-421.

- Rakopoulos CD, Scott MA, Kyritsis DC, Giakoumis EG. Availability analysis of hydrogen/natural gas blends combustion in internal combustion engines. *Energy* 2008; 33:248-255.
- Saravanan N, Nagarajan G. An experimental investigation of hydrogen as a dual fuel for diesel engine system with exhaust gas recirculation technique. *International Journal of Hydrogen Energy* 2008; 33:422-427.
- Shirk MG, McGuire TP, Neal GL, Haworth DC. Investigation of a hydrogen-assisted combustion system for a light-duty diesel vehicle. *Int. J. of Hydrogen Energy*; 33:7237-7244.
- Tomita E, Kawahara N, Piao Z, Fujita S, Hamamoto Y. Hydrogen combustion and exhaust emissions ignited with diesel oil in a dual fuel engine. SAE Paper 2001-01-3503; 2001.
- Tsolakis A, Hernandez JJ, Megaritis A, Crampton M. Dual fuel diesel engine operation using H<sub>2</sub>. Effect on particulate emissions. *Energy & Fuels* 2005; 19:418-425.
- Varde KS, Frame GA. Hydrogen aspiration in a direct injection type diesel engine-its effects on smoke and other engine performance parameters. *Int. J. Hydrogen Energy* 1982; 8:549-555.
- Varde KS, Frame GA. Hydrogen aspiration in a direct injection type diesel engine-its effects on smoke and other engine performance parameters. *International Journal of Hydrogen Energy* 1983; 8 (7):549-555.
- Verhelst S, Wallner T. Hydrogen-fueled internal combustion engines. *Progress in Energy and Combustion Science* 2009; 35:490-527.